Fault-tolerant control of non-sinusoidal multiphase permanent magnet synchronous machine drives under constraints on current and voltage for automotive applications

Duc Tan Vu

HESAM UNIVERSITÉ

Arts et Métiers Sciences et Technologies

ÉCOLE DOCTORALE SCIENCES DES MÉTIERS DE L'INGÉNIEUR
[L2EP – Campus de Lille]

THÈSE

présentée par : **Duc Tan VU**

soutenue le : **24 novembre 2020**

pour obtenir le grade de : **Docteur d'HESAM Université**

préparée à : **École Nationale Supérieure d'Arts et Métiers**

Spécialité : **Génie électrique**

Fault-tolerant control of non-sinusoidal multiphase permanent magnet synchronous machine drives under constraints on current and voltage for automotive applications

THÈSE dirigée par :
[M. Eric SEMAIL]

et co-encadrée par :
[M. Ngac Ky NGUYEN]

Jury

M. Mohamed BENBOUZID, Professeur des universités, IRDL, Université de Bretagne Occidentale		Président
M. Franck BETIN, Professeur des universités, LTI, Université de Picardie Jules Verne		Rapporteur
M. Johan GYSELINCK, Professeur des universités, BEAMS, Université Libre de Bruxelles		Rapporteur
Mme. Carole HENAUX, Maître de conférences HDR, LAPLACE-UPS-INPT, Université de Toulouse		Examinatrice
M. Eric SEMAIL, Professeur des universités, L2EP, Arts et Métiers Sciences et Technologies/ENSAM		Examinateur
M. Ngac Ky NGUYEN, Maître de conférences, L2EP, Arts et Métiers Sciences et Technologies/ENSAM		Examinateur

THÈSE

Acknowledgments

This thesis has been carried out for three years and nine months, under the supervision of M. Eric SEMAIL and M. Ngac Ky NGUYEN. I can say that I am a very lucky student as my supervisors have been always available for discussions regardless of their busy schedules. Thus, there are a lot of things that I have learned from them. Without their support, I would not have been able to finish this research. I do not think that I could have found better supervisors for my PhD study. Therefore, I would like to express my special gratitude to M. Eric SEMAIL and M. Ngac Ky NGUYEN for their guidance, support, patience, and encouragement.

I would like to acknowledge the jury of my thesis defense. Despite the pandemic, all members of the jury have spent their time to give me their insightful comments and hard questions which have incented me to widen my research from various perspectives. I would like to thank M. Mohamed BENBOUZID, professor at Université de Bretagne Occidentale, France for being the president of the jury. I would like to thank M. Franck BETIN, professor at Université de Picardie Jules Verne, France, and M. Johan GYSELINCK, professor at Université Libre de Bruxelle, Belgium for being the reviewers of my thesis. I would like to thank Mme. Carole HENAUX, associate professor at Université de Toulouse, France for being the examiner of my thesis.

I would like to thank M. Alain BOUSCAYROL, head of the control team in L2EP laboratory for his valuable advice. I would like to thank Mme. Betty SEMAIL, director of L2EP laboratory, for her support from my early days in the laboratory. I also would like to thank all professors, colleagues, and staffs of L2EP as well as those at ENSAM, including laboratories LISPEN and LMFL.

I would like to express my gratitude to the Ministry of Education and Training, a representative of the Vietnamese government, for the four-year scholarship. I also would like to thank Campus France, a representative of the French government, together with ENSAM and CE2I project for their valuable support. My sincere thanks go to my dear colleagues at Thai Nguyen University of Technology for favorable conditions enabling me to pursue my PhD study.

I have experienced one of the most memorable periods in my life, as a PhD student, thanks to my wonderful friends. I am thankful to anh Kỳ, chị Xiaoxiao, Noé, Thùy Anh, Hai Long, anh Long, chị Thủy, anh Châu, Bảo Huy, Chi, Tiago, Hussein, Youssouf, Jinlin, Lamine, Keitaro, and all members of football team Les Ch'tis.

Last but not least, my profound gratitude goes to my family for supporting me unconditionally. This thesis is dedicated to my family, including my grandparents, my parents, my brothers, my sisters, especially my wife Vân Anh and my little daughter Hoàng Mai.

Abstract

The electrification of transportation has been considered as one of solutions to tackle the shortage of fossil energy sources and air pollution. Electric drives for electrified vehicles, including pure electric and hybrid electric vehicles, need to fulfil some specific requirements from automotive markets such as high efficiency, high volume power and torque densities, low-cost but safe-to-touch, high functional reliability, high torque quality, and flux-weakening control. In this context, multiphase permanent magnet synchronous machine (PMSM) drives have become suitable candidates to meet the above requirements.

The main objective of this doctoral thesis is to propose and refine fault-tolerant control strategies for non-sinusoidal multiphase PMSM drives that require less constraints on their design. In addition, constraints on current and voltage defined by the inverter and the machine are considered to optimize the machine control under the non-sinusoidal condition without exceeding their allowable limits. Therefore, the system sizing is guaranteed, especially in flux-weakening operations. The proposed fault-tolerant control strategies, based on the mathematical model of multiphase drives, enrich the control field of multiphase drives by providing various control options. The selection of one of the proposed control options can be a trade-off between a high quality torque but a low average value and a high average torque but a relatively high ripple. The control and torque performances of the drives can be refined by using artificial intelligence with a simple type of artificial neural networks named ADALINE (ADAptive LInear NEuron). With self-learning ability, fast convergence, and simplicity, ADALINEs can be applied to industrial multiphase drives. All proposed control strategies in this doctoral thesis are validated with an experimental seven-phase PMSM drive. The non-sinusoidal back electromotive force (back-EMF) of the experimental seven-phase PMSM is complex with the presence of multi-harmonics. Experimental results verify the effectiveness of the proposed strategies, and their applicability in a multiphase machine with a complex non-sinusoidal back-EMF.

Keywords: Multiphase machine, seven-phase machine, non-sinusoidal back-EMF, fault-tolerant control, optimal control under constraint, artificial intelligence, adaptive linear neuron, ADALINE.

Résumé

L'électrification des transports a été considérée comme l'une des solutions pour lutter contre la pénurie de sources d'énergie fossile et la pollution de l'air. Les entraînements électriques pour les véhicules électrifiés, y compris les véhicules électriques purs et électriques hybrides, doivent répondre à certaines exigences spécifiques des marchés automobiles, tels qu'un rendement élevé, des densités volumiques élevées de puissance et de couple, un coût faible avec une protection contre les risques électriques, une fiabilité fonctionnelle élevée, une qualité de couple élevée, et un contrôle de défluxage. Dans ce contexte, les entraînements de machines synchrones à aimants permanents (PMSM) polyphasées sont devenus des candidats appropriés pour répondre aux exigences citées ci-dessus.

L'objectif principal de cette thèse de doctorat vise à proposer et affiner des stratégies de commandes tolérantes aux défauts pour les entraînements de machines PMSM polyphasées non-sinusoïdales qui requièrent moins de contraintes lors de leur conception. Par ailleurs, les contraintes de courant et de tension définies par l'onduleur et la machine sont prises en compte pour optimiser en régime non-sinusoïdal le contrôle de la machine sans dépasser les limites admissibles. Cela permet idéalement un dimensionnement au plus juste et cela tout particulièrement dans la zone de défluxage. Les stratégies proposées de commandes tolérantes aux défauts, basées sur le modèle mathématique des entraînements polyphasés, enrichissent le domaine de contrôle des entraînements polyphasés en offrant de diverses options de contrôle. Le choix de l'une des options proposées de commande peut être un compromis entre un couple de haute qualité mais avec une valeur moyenne faible, et un couple moyen élevé mais avec une ondulation relativement élevée. Les performances de contrôle et de couple peuvent être affinées en utilisant l'intelligence artificielle avec un type simple de réseaux de neurones artificiels nommé ADALINE (neurone linéaire adaptatif). Grâce à leur capacité d'auto-apprentissage, à leur convergence rapide, et à leur simplicité, les ADALINE peuvent être appliqués aux entraînements polyphasés industriels. Toutes les stratégies de contrôle proposées dans cette thèse de doctorat sont validées avec un entraînement d'une machine PMSM à sept phases. La force électromotrice non-sinusoïdale de la machine PMSM à sept phases, relevée expérimentalement, est complexe avec la présence de plusieurs harmoniques. Les résultats expérimentaux vérifient l'efficacité des stratégies proposées, et leur applicabilité dans une machine polyphasée avec une force électromotrice non-sinusoïdale complexe.

Mots clés : Machine polyphasée, machine à sept phases, force électromotrice non-sinusoïdale, commande tolérante aux défauts, commande optimale sous contrainte, intelligence artificielle, neurone linéaire adaptatif, ADALINE.

Contents

Nomenclature

Abbreviations

AC	Alternating Current
ADALINE	ADAptive LInear NEuron
AI	Artificial Intelligence
ANN	Artificial Neural Network
BEV	Battery Electric Vehicle
CBPWM	Carrier Based Pulse Width Modulation
CCS-MPC	Continuous Control Set Model-based Predictive Control
CE2I	The Intelligent Integrated Energy Converter project
DC	Direct Current
DoF	Degrees of Freedom
DTC	Direct Torque Control
EMF	Electromotive Force
EMR	Energetic Macroscopic Representation
ES	Electrical Source
est, *est*	estimated
EV	Electrified Vehicle
exp, *exp*	experimental or experiment
FCV	Fuel Cell Vehicle
FL	Fuzzy Logic
FM	Fictitious Machine
FOC	Field-Oriented Control
FS-MPC	Finite Set Model-based Predictive Control
HEV	Hybrid Electric Vehicle
HM	Healthy Mode
ICE	Internal Combustion Engine
IGBT	Insulated-Gate Bipolar Transistor
IM	Induction Machine
L2EP	Laboratory of Electrical Engineering and Power Electronics

LMS	Least Mean Square
mea, *mea*	measured
MMF	Magnetomotive Force
MPC	Model-based Predictive Control
MS	Mechanical Source
MTPA	Maximum Torque Per Ampere
OC	Open Circuit
opt, *opt*	optimal or optimization
PI	Proportional Integral
PIR	Proportional Integral Resonant
PMSM	Permanent Magnet Synchronous Machine
pu	per unit
PWM	Pulse Width Modulation
PWM-DTC	Pulse Width Modulation Direct Torque Control
RCA	Robust Control Approach
ref, *ref*	reference
RMS	Root Mean Square
SC	Short Circuit
SCL	Similar Copper Losses
ST-DTC	Switching Table Direct Torque Control
SVPWM	Space Vector Pulse Width Modulation
VSI	Voltage Source Inverter
ZM	Zero-sequence Machine

Parameters, variables, matrices, and vectors

$\left[\boldsymbol{T}_{\boldsymbol{Clarke}}^{\boldsymbol{fault}}\right]$	*7*-by-6 Clarke transformation matrix when phase *A* is opened
$\left[\boldsymbol{T}_{\boldsymbol{Clarke}}^{\boldsymbol{1}}\right], \left[\boldsymbol{T}_{\boldsymbol{Park}}^{\boldsymbol{1}}\right]$	6-by-6 new Clarke and Park matrices for the first harmonic of current
$\left[\boldsymbol{T}_{\boldsymbol{Clarke}}^{\boldsymbol{3}}\right], \left[\boldsymbol{T}_{\boldsymbol{Park}}^{\boldsymbol{3}}\right]$	6-by-6 new Clarke and Park matrices for the third harmonic of current
$\boldsymbol{[L]}$	*n*-by-*n* inductance matrix in natural frame
$\boldsymbol{[L_{dq}]}$	*n*-by-*n* inductance matrix in the rotor reference (d-q) frames

$\mathbf{[L_{\alpha\beta}]}$	*n*-by-*n* inductance matrix in the decoupled stator reference (α-β) frames
$\mathbf{[T_{Clarke}]}$	*n*-by-*n* Clarke transformation matrix
$\mathbf{[T_{Park}]}$	*n*-by-*n* Park transformation matrix
ΔT	Torque ripple
A, *B*, *C*, *D*, *E*, *F*, *G*	Names of phases of a 7-phase machine
$\underline{e}$	*n*-dimensional back-EMF vector in natural frame
$\underline{e}_{dq}$	*n*-dimensional back-EMF vector in the rotor reference (d-q) frames
$\underline{e}_{dqj}$	2-dimensional back-EMF vector of two-phase fictitious machine *j* in the rotor reference (d-q) frames
E_{n1}, E_{n3}	Amplitudes of the first and third harmonics of a speed-normalized back-EMF in natural frame, respectively
$e_{nA} \ldots e_{nG}$	Speed-normalized back-EMFs of phases *A* to *G*
E_y	The squared error of the ADALINE output
$\underline{e}_{\alpha\beta}$	*n*-dimensional back-EMF vector in the decoupled stator reference (α-β) frames
f_m	Friction coefficient of the rotor load bearings
$\underline{i}$	*n*-dimensional phase current vector in natural frame
I_{DC}	DC-bus current
$\underline{i}_{dq}$	*n*-dimensional current vector in the rotor reference (d-q) frames
$\underline{i}_{dqj}$	2-dimensional current vector of two-phase fictitious machine *j* in the rotor reference (d-q) frames
I_{peak_lim}	Limit of the peak phase currents
I_{RMS}	Highest RMS current among all phases
I_{RMS_j}	RMS current of phase *j*
I_{RMS_lim}	Limit of the RMS phase currents
$\underline{i}_{\alpha\beta}$	*n*-dimensional current vector in the decoupled stator reference (α-β) frames
J	Cost function in MPC
J_m	Moment of inertia of the electric drive and mechanical load
$\underline{k}_R$	Repartition coefficient vector
L	Self-inductance of one phase
L_1	Inductance of the first fictitious machine

L_2	Inductance of the second fictitious machine
L_3	Inductance of the third fictitious machine
L_z, L_{z1}, L_{z2}	Inductances of the zero-sequence machines
M_1	Mutual inductance between two phases shifted an angle of $2\pi/n$
M_2	Mutual inductance between two phases shifted an angle of $4\pi/n$
M_3	Mutual inductance between two phases shifted an angle of $6\pi/n$
n	The number of phases of an electric machine
$\mathbb{N}$, $\mathbb{N}_0$	Sets of natural numbers without zero and with zero
p	Number of pole pairs
P_{em}	Output mechanical power
P_{loss}	Total copper loss
R_s	Stator winding resistance of one phase
s	Laplace operator
s_j, $\bar{s}_j$	Switches of leg j of an inverter,
$\underline{s}_{1,n}$	Switching signal vector for n phases
t	Time
T_1	Torque of the first fictitious machine
T_2	Torque of the second fictitious machine
T_3	Torque of the third fictitious machine
T_{ave}	Average torque
T_{em}	Electromagnetic torque
T_{em_exp}	Experimental electromagnetic torque
T_{em_opt}	Optimal electromagnetic torque from the offline optimizations
T_{load}	Load torque
T_z	Torque of the zero-sequence machine
$\underline{v}$	n-dimensional phase voltage vector in natural frame
V_{DC}	DC-bus voltage
$\underline{v}_{dq}$	n-dimensional voltage vector in the rotor reference (d-q) frames
$\underline{v}_{dqj}$	2-dimensional voltage vector of two-phase fictitious machine j in the rotor reference (d-q) frames
v_{j_dead}, v_{x_dead}	"Dead-time" voltages in phase j (A to G) and axis x (d_1, q_1, d_9, q_9, d_3, q_3)

V_{lim}	Limit of the peak phase voltages in experiments
V_{lim_opt}	Limit of the peak phase voltages for the offline optimization
V_{peak}	Highest peak phase voltage among all phases
$\underline{v}_{\alpha\beta}$	*n*-dimensional voltage vector in the decoupled stator reference (α-β) frames
$\underline{w}$	Weight vector of an ADALINE
w_k	The k^{th} weight of an ADALINE
$\underline{x}$	A general *n*-dimensional vector of machine parameters in natural frame
x	One of machine parameters (current *i*, back-EMF *e*, or voltage *v*), or one of axes (d_1, q_1, d_9, q_9, d_3, q_3) in d-q frames
$\underline{x}_{dq}$	A general *n*-dimensional vector of machine parameters in the rotor reference (d-q) frames
$\underline{x}_{in}$	Input vector of an ADALINE
x_{ink}	The k^{th} input of an ADALINE
$\underline{x}_{\alpha\beta}$	A general *n*-dimensional vector of machine parameters in the decoupled stator reference (α-β) frames
y	Output of an ADALINE
δ	Spatial angular displacement of two adjacent phases (equal to $2\pi/n$ for a *n*-phase machine)
η	Learning rate of an ADALINE
θ	Electrical position
Ω	Rotating speed
Ω_{base}	Base speed
Ω_{max}	Maximum speed
Φ	Stator flux

List of figures

List of tables

Introduction

In 1830s, the idea of using electric machines for the traction of vehicles, known as Electrified Vehicles (EVs), was introduced. However, constraints on production costs, volume, and mass of batteries hindered their commercialization process. In recent decades, fossil energy sources have been sharply declining, and environmental pollution has been becoming a serious global problem. Meanwhile, significant improvements on batteries have been achieved. Therefore, since 1990s, EVs have been slowly emerging and becoming an effective commercial solution to deal with the energy and environmental crises. An EV can be either a combination of an electric drive and a thermal engine in a hybrid electric vehicle (HEV) or a pure electric vehicle. The pure electric vehicle can be a fuel cell vehicle (FCV) or a battery electric vehicle (BEV). BEVs and FCVs with zero emission have constraints on production costs and technology. Meanwhile, HEVs with low emission become more interesting in automotive industry because the rate of hybridization can be adjusted [1].

In general, an EV is a sophisticated combination of electrical and automotive engineering. Regarding electrical engineering, electric drives play an important role in operations of EVs. They generally consist of electric machines, power electronics converters, energy supplies, control systems, and energy management strategies. The electric drive technologies applied to EVs are mainly dependent on the electric machine technologies: DC, AC induction (IM), and AC synchronous. It is noted that DC technology is no longer attractive due to its maintenance requirements and mechanical limitations. Currently, permanent magnet synchronous machines (PMSMs) are more found in HEVs in which spatial constraints are important. Meanwhile, IMs and DC-excited synchronous machines, without high-cost permanent magnets, are more observed in BEVs [2].

There have been several main requirements for electric drives to guarantee high-performance electromechanical conversions of EVs at variable speeds and variable torques. These requirements will be explained in the following paragraphs as follows:

High efficiency

Electric drives for EVs are required to have high efficiency for optimal energy consumption. In fact, the use of electric drives in vehicles increases the system efficiency because the efficiency of electric machines is higher than that of Internal Combustion Engines (ICEs). In addition, electric drives can recover the regenerating braking energy. However, at the present time, the electric energy storage for EVs is a challenge and therefore high-efficiency electric drives can increase the driving range or reduce the need for a huge battery capacity in EVs. Using PMSMs can be a solution [3].

High volume densities

High volume power density (kW/m^3) and high volume torque density (Nm/m^3), collectively known as high volume densities, are important criteria for electric drives of EVs, especially of HEVs. In the limited space of EVs, these high volume densities can reduce the size of electric drives. The high volume torque density is mainly important at low speed for accelerations and uphill climbs. Meanwhile, the high volume power density is crucial in the constant power range of EVs. These requirements can be satisfied by using PMSMs with higher volume densities than IMs, DC-excited synchronous machines and DC machines with the same torque and power [1, 3-5].

Low-cost but safe-to-touch

To meet the first and second criteria about high efficiency and high volume densities, PMSMs are considered as a high potential candidate. However, the use of permanent magnets results in high-cost machines, making PMSMs less interesting than IMs. For the mass market of EVs, low production costs can ensure an affordable price of EVs, making them become more attractive to customers. Therefore, a compromise between a low cost, high efficiency and high volume densities need to be made.

Besides the low-cost criterion, EVs need to be safe for humans. In this case, a low-voltage standard (< 48 V) can be a solution for the electrical safety margin. Low-voltage drives can avoid the high-voltage electric shock as well as expensive complex requirements for circuit insulations and powerful electronic devices. Therefore, protection costs are decreased. In addition, the battery management can be easier because the number of battery cells in series is reduced, facilitating the degradation detection of battery cells through variations of cell voltages. In recent years, 48 V electric drives have significantly drawn the attention of EV researchers [6-12]. Nevertheless, for a given power, currents in DC bus and phase windings in the low-voltage electric drives are obviously much higher than conventional drives, leading to a big challenge of electric drives.

High functional reliability

High functional reliability is a prime consideration in electric transportation systems [13, 14] in which electric drives have ability to tolerate faults in power converters or electric machine windings. Specifically, power converter components including power semiconductors, gate drives, and capacitors have been reported as the most fragile elements in electric drives [15]. Faults in power converters are hardly predicted even when several improvements have been proposed in [16]. Therefore, the fault-tolerant capability for electric machines and power converters has become a solution to avoid breakdowns or even damage of EVs, increasing their functional reliability. Besides, voltages and currents of electric machines in EVs are required to respect their limits in all operating modes such as healthy, faulty, accelerating and decelerating. The possibility of operating well with a derated power under a defective condition makes post-fault electric drives more acceptable, avoiding a costly safety margin in the context of a mass market.

High torque quality

An operation with a low-ripple torque is an important criterion in all electric drives, especially in automotive applications, to ensure smooth accurate driving, especially at low speed [5]. Torque ripples severely deteriorate the EV performances when producing undesirable mechanical vibrations and acoustic noise, decreasing control precision of drivers [17, 18]. Therefore, torque ripples need to be reduced even eliminated in electric drives for automotive applications in all operating modes. It means that electric drives can operate in healthy and faulty conditions with constant or low-ripple torques. Therefore, the technologies for electric machines as well as electric drives with corresponding control strategies need to be properly chosen to improve the performance quality of EVs.

Flux-weakening control

EVs need to operate at high speed in many circumstances, for example a drive on highways. Therefore, electric drives for EVs are required to operate in the flux-weakening region, known as the constant power region [1]. In fact, an EV can reach a high speed if its power is high enough. However, the use of the flux-weakening strategy can avoid the oversizing of electric drives. In flux-weakening control, the tractive torque is reduced when the rotating speed is above the base speed. Therefore, limits of current and voltage are respected, especially at high speed. In classical three-phase drives, the flux-weakening strategy can be analytically presented.

The above requirements for electric drives used in EVs can be summarized as follows:

1) High efficiency for optimal consumption of embedded energy supply.
2) High volume power and torque densities due to limited spaces in EVs.
3) Low-cost for affordable EVs in the mass market but safe for human touches.
4) High functional reliability with fault-tolerant ability and respect for electrical limits.
5) High torque quality for smooth EVs with low vibrations and acoustic noise.
6) Flux-weakening control for high-speed driving without oversized electric drives.

These requirements are considered as challenges that can be contradictory with the classical solutions. Therefore, flexible compromises need to be made. To alleviate these contradictions, the research on new solutions with more degrees of freedom (DoF) is of interest. In this doctoral thesis, electric drives with n phases ($n > 3$), known as multiphase drives, having more DoF for control and design compared to classical three-phase drives, will be considered.

This thesis will be presented in three chapters. **Chapter 1** will discuss several distinct properties that open up opportunities for multiphase drives in automotive applications. Indeed, despite some drawbacks, multiphase drives are considered as a suitable candidate for EVs. After modeling a general multiphase drive, recent studies in the control field of multiphase drives will be categorized and analyzed. These analyses combined with the six above requirements for electric drives allow to address objectives of this doctoral thesis.

Chapter 2 will present the modeling and control strategies of a specific multiphase drive in healthy mode and especially under a single-phase open-circuit (OC) fault. Control strategies for two-phase OC faults are briefly presented in **Appendix B.** These control strategies are based on the mathematical model of the drive in which a seven-phase PMSM is used for illustrations. The approaches in this doctoral thesis can be applied to other electric drives with different numbers of phases. In addition, constraints on current and voltage are always imposed in control schemes to guarantee high functional reliability and flux-weakening operations of the multiphase drives.

In **Chapter 3**, the performances, either in healthy mode or faulty mode, of the considered multiphase drive with the strategies proposed in **Chapter 2** will be improved by using artificial intelligence. As a result, current control and torque quality will be enhanced regardless of uncertainties and imperfections of the multiphase drive. Moreover, the knowledge of harmonic components in signals of the drives allows a fast response of control (fast convergence) and avoids the calculation burden. Therefore, the applicability of the proposed strategies to industrial electric drives is improved.

Chapter 1. Multiphase Drives: Opportunities and State of the Art

1.1. Multiphase drives for automotive applications

1.1.1. Multiphase drives: a suitable candidate for EVs

The use of classical machines with only three coupling phases, or rather the use of Voltage Source Inverters (VSIs) with only three legs, is a limitation imposed by the past. It is noted that these electric drives cannot work properly when one phase is not supplied. This historical property induces an important constraint on the safety margin for VSIs and electric machines. To release this constraint, electric drives of which VSIs have more than three legs will be considered in this doctoral thesis. These electric drives are called multiphase drives. Owing to more legs as well as phases, multiphase drives have more DoF for design and control. In this subsection, multiphase drives will be compared with different existing solutions regarding the requirements for electric drives in the EV mass market presented in the **Introduction** of this doctoral thesis.

A general multiphase drive with n phases ($n > 3$) fed by a n-leg VSI and DC-bus voltage in automotive applications is described in Fig. 1.1. The electric drive provides a traction force to an EV (wheel and chassis) through a gearbox. The first study of a multiphase drive, a five-phase IM fed by a VSI, was proposed in 1969 [19]. However, at that time, the attention to this proposed five-phase machine was still limited. The interest in multiphase machines for variable-speed electric drives has only been growing significantly in recent decades. It is thanks to evolutions in some specific areas such as power electronics converters and digital signal processors. Another reason for this emergence is that the in-depth knowledge about multiphase drives has been significantly advanced [20-23].

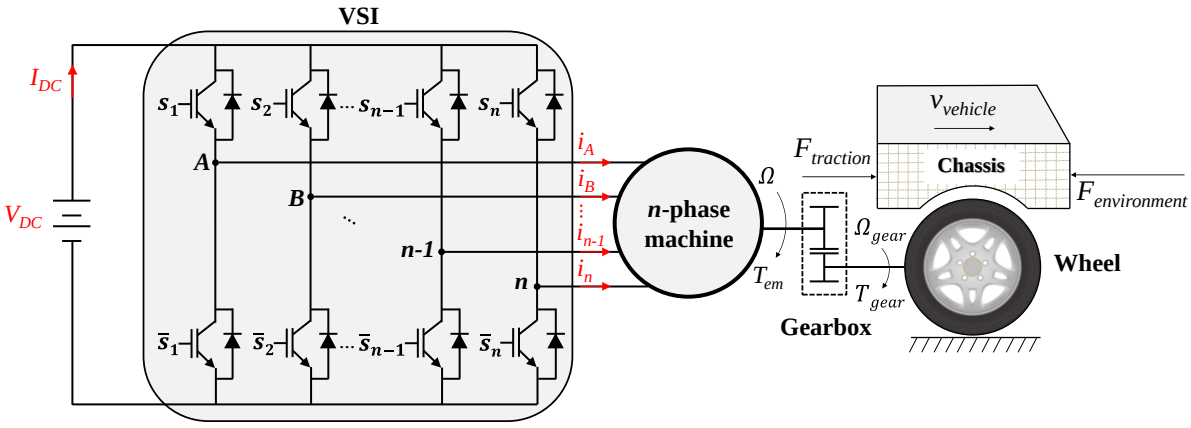

Fig. 1.1. A n-phase machine fed by a n-leg VSI in an EV.

Based on the spatial displacement between two adjacent phases, multiphase machines can be divided into symmetrical (with a spatial phase shift angle of $2\pi/n$) and asymmetrical machines (with several sets of phases such as 2 sets of three phases for a six-phase machine) [24, 25]. If the rotor construction is considered, there are mainly induction and synchronous multiphase

machines. An induction machine using a squirrel-cage rotor has been interesting due to low-cost materials. Meanwhile, a synchronous multiphase machine can be with PM excitation, with field windings, or of reluctance type [21, 26, 27]. Like three-phase PMSMs, multiphase PMSMs are interesting due to their advantages such as high efficiency and high volume densities. Therefore, multiphase PMSMs can meet the first two requirements for electric drives in EVs (see **Introduction**) but using high-cost PMs is one of their drawbacks.

The other requirements can be met by exploiting the following distinct properties of multiphase drives.

1.1.1.A. *Low power per phase rating for safe EVs*

As analyzed in the third requirement of EVs (see **Introduction**), a safe-to-touch EV is supplied by a low voltage. Consequently, the current per phase rating becomes higher than that of an EV supplied by a higher voltage with the same power. Therefore, several transistors with a given commercial affordable rating can be used in parallel to make a synthetic transistor with a higher rating. However, the synchronization of these parallel transistors during their lifetime is a challenge since their aging is not the same. As a failure of a single transistor induces higher currents in the remaining healthy transistors, a safety margin becomes needful to ensure a sufficient reliability. Consequently, the oversizing of the transistors is practically necessary. For example, when a phase of a three-phase machine is obtained by putting k windings in parallel, it is possible to supply the machine with k three-phase star windings by k three-leg VSIs [28]. As a result, a $3k$-phase machine is then obtained with the same properties of a three-phase machine. The requirement is a perfect synchronization of all three-leg VSIs. On the other hand, circulations of parasitic currents are observed between the windings of different three-phase star windings. Moreover, in case of a fault in one winding of one three-phase star winding, the supply of the entire corresponding three-phase winding is removed. This approach is quite simple and used in industrial solutions. A huge power loss in case of a fault of one transistor and the complicated transistor synchronization are its main drawbacks. Therefore, we will not consider this kind of machines in our work.

Eventually, it is concluded that the use of multiphase machines to split the power across a high number of phases and inverter legs is interesting. The current per phase rating of converters and machine windings is lower compared to conventional three-phase drives with the same DC-bus voltage and power [21, 22]. Therefore, it is possible to use two power electronics switches per leg instead of a set of parallel switches, improving the reliability of the electric drives [29]. This feature of multiphase drives enables EVs to be supplied by a low voltage such as 48 V with a power greater than 10 kW, the minimum power for hybridization. As a result, safe-to-touch EVs become more feasible with multiphase drives [30].

1.1.1.B. *Fault-tolerant ability for high functional reliability*

Fault tolerance is one of the major advantages of multiphase machines [21-23, 27, 31] that can meet the fourth requirement of EVs about high functional reliability (see **Introduction**). There are various faults including Open Circuit (OC) and Short Circuit (SC) faults that can suddenly happen in power converters (switches), phase lines, or stator windings. These faults can

dramatically interrupt or even damage electric drives. The fault tolerance of multiphase drives is due to having more DoF for control than conventional three-phase drives. This feature, as first presented in [13], allows to preserve a persistent operation of electric drives without any additional hardware. Indeed, the reconfiguration in post-fault operations of multiphase drives only defines new current references to obtain constant or low-ripple torques.

1.1.1.C. *Low ripple torques for smooth EVs*

A three-phase machine is usually designed with distributed stator windings, inducing a sinusoidal back-EMF. As a result, a constant torque is generated when sinusoidal currents are imposed. Then, time-constant d-q currents are simply obtained. The more recent PMSM generation with tooth concentrated stator windings is interesting for EVs due to lower production costs with short end-windings [32, 33]. In this case, a sinusoidal back-EMF, required for a constant torque with sinusoidal currents, can be obtained by a special design of rotor.

With a multiphase machine, this design requirement is relaxed as the number of phases is high. Indeed, according to the multi-reference frame approach [34, 35], a n-phase symmetrical machine is characterized by $(n+1)/2$ (if n is odd) and $(n+2)/2$ (if n is even) characteristic planes, known as reference frames. One frame is associated with a group of harmonics. A constant torque can be ideally obtained when only a single harmonic of currents and back-EMFs exists in each reference frame (except the zero-sequence frames). Therefore, an increase in the number of phases results in more reference frames, permitting to have more harmonics in back-EMFs. Consequently, in a well-designed multiphase machine, the torque generated by non-sinusoidal back-EMFs can be constant even in a transient operation by imposing constant d-q currents in each reference plane. This property is not available in a three-phase machine. In conclusion, with a multiphase machine, it is possible to obtain a constant torque by imposing constant d-q currents in different reference planes. Meanwhile, a three-phase machine requires the classical constraint on sinusoidal back-EMFs and currents. Therefore, a multiphase machine leads to less constraints on design than a three-phase machine.

As discussed in [29, 36-40], an electric drive with a high number of phases generates lower torque ripples than a conventional three-phase drive. Indeed, with a n-phase drive, the lowest harmonic order of torque ripples is $2n$ if n is odd, and its back-EMF contains only odd harmonics. For example, the lowest harmonic orders of torque ripples in 3-phase, 5-phase, and 7-phase drives are 6, 10, and 14, respectively. When n is even, the lowest harmonic order of torque ripples in symmetrical machines is n while that in asymmetrical machines is $2n$. For example, the lowest harmonic order of torque ripples in a 6-phase symmetrical machine is 6, equivalent to a 3-phase machine. The lowest harmonic order of torque ripples in a 6-phase asymmetrical machine is 12, equivalent to a 12-phase symmetrical machine. Therefore, an increase in the number of phases results in higher-frequency torque ripples. This feature is interesting since the mechanical resonance of an electric drive at high frequency is eliminated. As a result, the torque of a multiphase drive can be smoother than that of a three-phase drive.

This feature of multiphase drives meets the fifth requirement of EVs (see **Introduction**) about high torque quality for smooth driving, especially at low speed.

1.1.1.D. *More possibilities of stator winding configurations*

When an inverter is defined with a given maximum current and bus voltage, the connection changes of the machine windings allow to vary the torque-speed characteristic with an approach of flux-weakening. Combinations of the flux-weakening techniques [41-44] and different connections of stator windings can enlarge the speed range. Indeed, the maximum voltages that can be applied to the terminals of a phase winding are different for different configurations. A higher maximum phase voltage (a wider speed range) results in a smaller phase current (a lower torque) and vice versa.

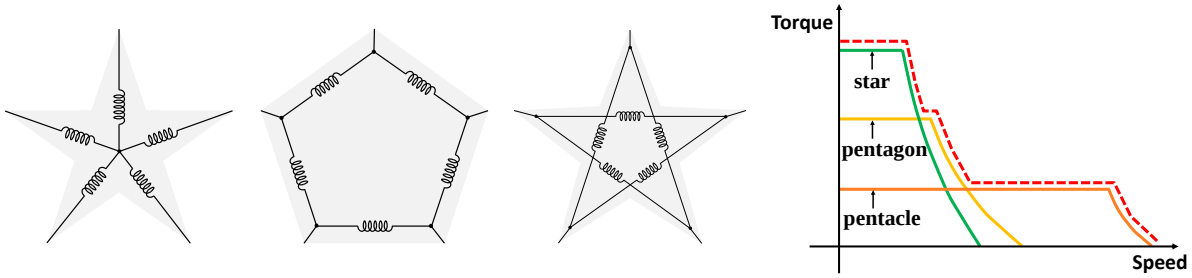

Fig. 1.2. Different possibilities of stator winding configurations for five-phase machines: star (a), pentagon (b), pentacle (c), and corresponding torque-speed characteristics (d) [45, 46].

Multiphase drives have more options of stator winding configurations for high speed operations. Generally, with a *n*-phase machine, there are (*n*+1)/2 possibilities to connect stator windings. For example, with a 3-phase machine, there are only 2 connecting possibilities: delta and star [47]. If the number of phases increases to 5, there will be 3 connecting options including star, pentagon, and pentacle as shown in Fig. 1.2a, b, and c, respectively. Among these connecting options, the pentacle gives the widest speed range and lowest torque while the star connection has the shortest speed range and highest torque as presented in Fig. 1.2d [45, 46]. It is understood that the pentacle makes possible to obtain the highest voltage while the maximum current is smallest.

1.1.1.E. *Electromagnetic pole changing by imposing harmonics of current*

The payload of torque-speed characteristics is specified and characterized by limits that are defined by maximum torque at low speed and maximum power at high speed (above the base speed). To find an optimal solution for a complex payload, a high number of DoF in multiphase drives can applied.

The basic principle of the classical pole changing is that a decrease in the number of pole pairs can extend the speed range. In three-phase drives, the pole changing methods are implemented by switching different winding configurations as discussed in [48-51]. An appropriate connection of stator windings results in a magnetomotive force (MMF) in the air gap corresponding to the desired number of pole pairs. However, these pole changing methods are physically implemented by electronic devices with a high number of switches.

In a multiphase drive, the principle to extend its speed range is inherited from the classical pole changing methods. However, multiphase machines can work on multiple polarities by injecting different harmonic components of current, called electromagnetic pole changing. This pole

changing is implemented without any winding reconfigurations, reducing switching losses as presented in [52-55]. This distinct feature is only possessed by multiphase machines. Indeed, by using the multi-reference frame approach [34, 35], a *n*-phase machine is decomposed into (*n*+1)/2 (*n* is odd) or (*n*+2)/2 (*n* is even) fictitious machines with corresponding characterized frames. Each frame is associated with a given group of harmonic components. In healthy mode, these harmonics of current can be independently controlled to obtain a constant torque. Compared to a three-phase machine, a high number of phases in a multiphase machine allows to use more than one harmonic of current to generate constant torques.

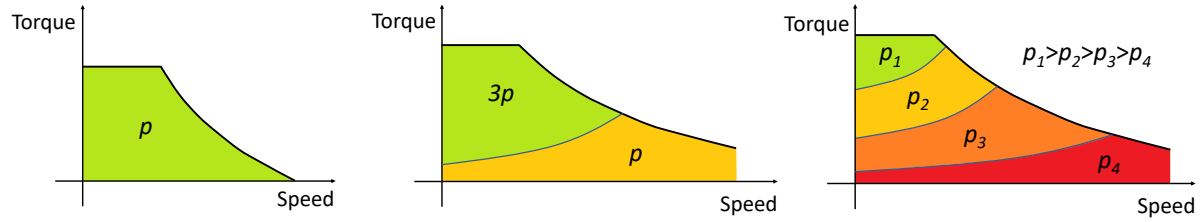

(a) (b) (c)

Fig. 1.3. Electromagnetic pole changing in multiphase drives for speed range extensions: *p* pole pairs (a), a combination of *p* and *3p* pole pairs (b), and a more general case (c).

For example, a five-phase machine, with *p* pole pairs, is decomposed into 2 fictitious two-phase machines and one zero-sequence machine. The first fictitious machine associated with the first harmonic is equivalent to *p* pole pairs while the second fictitious machine associated with the third harmonic is equivalent to *3p* pole pairs. If only the currents of the first machine with *p* pole pairs are used to generate torque, the speed range is presented in Fig. 1.3a. When the currents of the first and third machines are imposed, a wider speed range is derived in Fig. 1.3b. At the starting stage (low speed), the first and second machines contribute to the torque generation with *3p* pole pairs, whereas the torque is mainly produced by the main machine with *p* pole pairs at high speed. A more general torque-speed characteristic using the electromagnetic pole changing with decreases in the number of pole pairs from p_1 to p_4 is shown in Fig. 1.3c.

In conclusion, in an EV using a multiphase drive, its mechanical gearbox can be replaced by an electromagnetic gearbox, not only reducing switching losses and but also increasing the efficiency and reliability of the EV. In addition, a more comfortable driving can be obtained with the electromagnetic gearbox.

1.1.2. Opportunities for multiphase drives in automotive applications

According to the six requirements for electric drives in EVs (see **Introduction**), the five special properties in **section 1.1.1** enable multiphase drives to possibly become a favored choice for automotive applications. Especially, multiphase PMSMs are more interesting than multiphase IMs due to their high efficiency, high volume torque and power densities. The last two properties of multiphase drives can be combined with flux-weakening strategies to extend the speed range. Different from three-phase drives, flux-weakening strategies cannot be analytically expressed in multiphase drives due to too many currents in d-q frames. Therefore, flux-weakening operations in multiphase drives can be implemented by imposing constraints on current and voltage.

However, to fully replace their three-phase counterparts being widely used in EVs, multiphase drives, especially multiphase PMSM drives, need to overcome several drawbacks. There are also possible solutions for these drawbacks in the below discussions.

1) One of the disadvantages of multiphase drives is an increase in the calculation burden for design and control. It is the reason why the potential for the multiphase machines has only been progressively exploited over the past twenty years. This problem has been tackled by using more powerful microprocessors in combination with adapted modeling and control.
2) Another inconvenience of multiphase drives is an increase in the number of inverter legs and the number of wires connecting multiphase machines and VSIs. When the number of phases is not a multiple of three, it is difficult to use previous standards developed for three-phase drives. Therefore, special VSIs must be designed for the multiphase drives. In this case, if transistors in parallel are unnecessary, the number of drivers and heatsink components increases and so do production costs. However, the mass production could cut down these costs. In addition, as the current in each leg is lower, the quantity of Silicon and switch losses in multiphase drives are not intrinsically higher compared to three-phase drives.
3) Time constants of fictitious machines in a multiphase machine may not be of the same order, especially a machine with classical distributed windings (an integer number of slots per pole per phase). If the classical Pulse Width Modulation (PWM) is used, the smallest time constant imposes the carrier frequency for PWM. Consequently, the switching frequency is high with corresponding switching losses [56]. Using Space Vector PWM (SVPWM) can be a solution to tackle this problem. Indeed, low-amplitude voltage vectors can be used for fictitious machines with small time constants. Specifically, zero-amplitude voltage vectors can be used if no torque is required in the fictitious machine associated with the smallest time constant (or zero-sequence machines in the case of an open-winding configuration). Another solution is to choose stator windings which induce equal time constants. It is the case of fractional windings such as tooth concentrated windings. In addition, with new high-frequency wide-bandgap components, this problem could vanish.
4) Another drawback is an occurrence of parasitic currents that do not contribute to the torque generation. It is possible when the control of a n-phase drive ($n > 3$) is obtained by an adaptation of the classical three-phase drive control. For example, when only the main harmonic of currents is considered for the torque production, only two components of the n-dimensional voltage vector are mainly considered to control two d-q currents associated with the main harmonic. In fact, it is also necessary to take care of (n-2) other components of the voltage vector to avoid the occurrence of parasitic currents. Consequently, the control of a multiphase drive is more complex than a three-phase drive.
5) Social inertia is one of existing obstacles preventing multiphase drives from being popularized in industry. The development of these complex electric drives requires long-term human investments. In a society with market profit rules and short-term

shareholding companies, risks from developing a drive with complex knowledge in the field of energy are high. Therefore, a change from industrial three-phase drives to multiphase drives is a challenge.

1.1.3. Recent projects on multiphase drives

In recent years, there have been several projects on multiphase drives for multiple applications such as project "MotorBrain" in Germany and "Intelligent Integrated Energy Converter (CE2I)" in France. The common points of these projects are an attempt to design converter-integrated multiphase machines with a high power density. EVs can be one of high potential applications of these motor drives. In addition, another integrated drive with a seven-phase modular brushless wound rotor synchronous machine is described in [57].

The two projects MotorBrain and CE2I are briefly summarized as follows:

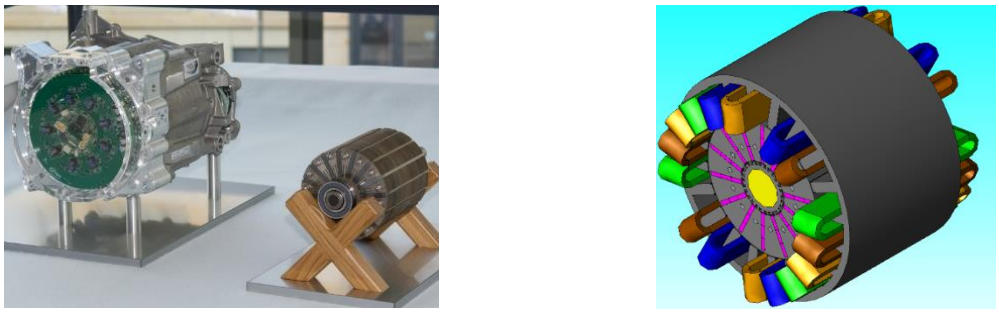

(a) (b)

Fig. 1.4. The highly compact electric motor prototype without using rare earth metals in MotorBrain project [58] (a), and the model of an integrated machine in CE2I project [59] (b).

1.1.3.A. *MotorBrain project*

The MotorBrain project started in 2011 with Infineon and a total of 30 partners from nine European countries. The MotorBrain prototype is a highly integrated electric motor that unifies the most important components of the powertrain for an electric vehicle. The interdisciplinary team represents all development and production sectors relevant to electromobility. The team includes universities, non-university research facilities, semiconductor manufacturers, electric motor builders, automobile component suppliers and automobile manufacturers. The main challenge is to develop a low-cost integrated drive for automotive applications. Without taking fault tolerance into consideration, the constraint on integration leads to the choice of multiphase machines, giving more DoF for design. Therefore, six-phase and nine-phase prototypes have been developed. The first one is a pure reluctance machine while the latter one is composed of ferrite magnets as shown in Fig. 1.4a. The integration of a motor, a gearbox, and an inverter, with the use of newly developed ferrite magnets, allows to build an engine with a reduced weight about 15%, from 90 kg to 77 kg [58] in comparison with the reference non-integrated three-phase drive. It is interesting to note that in this project, the number of phases higher than three does not come from the fault tolerance requirement.

1.1.3.B. *CE2I project*

The smart energy converter project CE2I [59] is undertaken by Laboratory of Electrical Engineering and Power Electronics (L2EP) cooperated with other laboratories and industrial partners in the north region of France from 2015 to 2020. The project is to address interdisciplinary issues related to integrated drives. One of the target outcomes is a low-voltage (< 48 V) electromagnetic actuator with integrated VSIs using wide-bandgap components. To maximize the profit of an imposed safe low voltage of 48 V, an open-winding configuration is chosen for the machine. Therefore, 48 V will be the maximum peak voltage imposed on one phase. GaN transistor used in VSIs is a wide-bandgap component fitted for low voltages. Considering limited available currents for GaN and associated thermal constraints, a multiphase tooth concentrated winding PM machine (Fig. 1.4b) with H-bridge supply is chosen, allowing tolerance for OC and SC faults of power components. Specifically, two axial multi-leg VSIs, one at each axial extremity of the machine, will supply twenty coils of the machine. The final choice of the number of phases from five to twenty will be made according to a compromise between spatial constraints in the VSIs and the machine, and computational constraints for the control and thermal dissipation [59].

1.1.4. Section summary

Section 1.1 has manly delivered several distinct properties, opening up opportunities for multiphase drives in automotive applications regardless of some drawbacks. Before further discussions about the existing control issue, a general model of a multiphase machine will be discussed in the next section. As previously analyzed, compared to multiphase IMs, multiphase PMSMs possess functional advantages such as high efficiency, high volume torque and power densities. Therefore, for the sake of simplicity, this thesis will focus on the modeling and control of multiphase PMSMs.

1.2. General model of a multiphase PMSM

The schematic diagram of a *n*-phase PMSM is shown in Fig. 1.5 with several assumptions: *n* phases (*A*, *B*, *C*, …, *n-1*, *n*) are equally shifted with a spatial phase shift angle $\delta=2\pi/n$ in the stator; the rotor is non-salient; θ is the electrical position; Ω is the rotating speed of the machine; the magnet circuit saturation is not considered in the back-EMF and flux calculations; and iron losses are not considered.

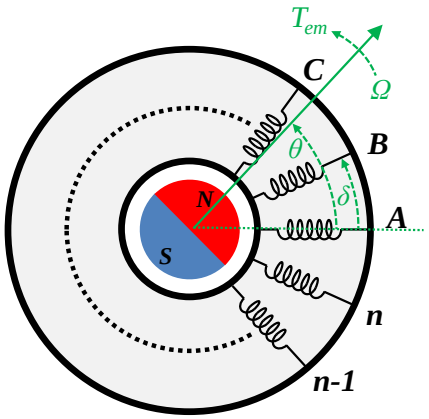

Fig. 1.5. The schematic diagram of a *n*-phase multiphase PMSM.

1.2.1. Natural frame model

The voltage and electromagnetic torque of a *n*-phase PMSM are given by:

$$\underline{v} = R_s \underline{i} + [\boldsymbol{L}] \frac{d\underline{i}}{dt} + \underline{e} \tag{1.1}$$

$$T_{em} = \frac{P_{em}}{\Omega} = \frac{\underline{e}^T \underline{i}}{\Omega} \tag{1.2}$$

where $\underline{v}$, $\underline{i}$, and $\underline{e}$ are the *n*-dimensional vectors of phase voltages, phase currents and back-EMFs, respectively; R_s is the resistance of the stator winding of one phase; $[\boldsymbol{L}]$ is the *n*-by-*n* stator inductance matrix; L is the self-inductance of one phase; M_j is the mutual inductance between two phases shifted an angle of $(2\pi j/n)$ with $j \in [1, (n\text{-}1)/2] \subset \mathbb{N}$ if *n* is odd, and $j \in [1, n/2] \subset \mathbb{N}$ if *n* is even; T_{em} and P_{em} are the electromagnetic torque and power of the machine, respectively.

$$\underline{v} = \begin{bmatrix} v_A \\ v_B \\ v_C \\ \vdots \\ v_{n-1} \\ v_n \end{bmatrix}; \ \underline{i} = \begin{bmatrix} i_A \\ i_B \\ i_C \\ \vdots \\ i_{n-1} \\ i_n \end{bmatrix}; \underline{e} = \begin{bmatrix} e_A \\ e_B \\ e_C \\ \vdots \\ e_{n-1} \\ e_n \end{bmatrix}; [\boldsymbol{L}] = \begin{bmatrix} L & M_1 & M_2 & \cdots & M_3 & M_2 & M_1 \\ M_1 & L & M_1 & \cdots & M_4 & M_3 & M_2 \\ M_2 & M_1 & L & \cdots & M_5 & M_4 & M_3 \\ \vdots & \vdots & \vdots & \ddots & \vdots & \vdots & \vdots \\ M_3 & M_4 & M_5 & \cdots & L & M_1 & M_2 \\ M_2 & M_3 & M_4 & \cdots & M_1 & L & M_1 \\ M_1 & M_2 & M_3 & \cdots & M_2 & M_1 & L \end{bmatrix}$$

1.2.2. Decoupled stator reference frame model

The decoupled stator reference frames are virtual frames obtained by the Clarke (or Concordia) transformation. The machine parameters (back-EMFs, currents, and voltages) in natural frame are converted into the decoupled stator reference frames as follows:

$$\underline{x}_{\alpha\beta} = [\boldsymbol{T}_{\boldsymbol{Clarke}}] \underline{x} \tag{1.3}$$

$$\underline{x}_{\alpha\beta} = \begin{bmatrix} x_{\alpha 1} \\ x_{\beta 1} \\ \vdots \\ x_{\alpha k} \\ x_{\beta k} \\ x_{z1} \\ x_{z2} \end{bmatrix}; \ \underline{x} = \begin{bmatrix} x_A \\ x_B \\ x_C \\ \vdots \\ x_{n-1} \\ x_n \end{bmatrix}; [\boldsymbol{T}_{\boldsymbol{Clarke}}] = \sqrt{\frac{2}{n}} \begin{bmatrix} 1 & \cos(\delta) & \cos(2\delta) & \cdots & \cos((n-2)\delta) & \cos((n-1)\delta) \\ 0 & \sin(\delta) & \sin(2\delta) & \cdots & \sin((n-2)\delta) & \sin((n-1)\delta) \\ \vdots & \vdots & \vdots & \ddots & \vdots & \vdots \\ 1 & \cos(k\delta) & \cos(k2\delta) & \cdots & \cos(k(n-2)\delta) & \cos(k(n-1)\delta) \\ 0 & \sin(k\delta) & \sin(k2\delta) & \cdots & \sin(k(n-2)\delta) & \sin(k(n-1)\delta) \\ 1/\sqrt{2} & 1/\sqrt{2} & 1/\sqrt{2} & \cdots & 1/\sqrt{2} & 1/\sqrt{2} \\ 1/\sqrt{2} & -1/\sqrt{2} & 1/\sqrt{2} & \cdots & 1/\sqrt{2} & -1/\sqrt{2} \end{bmatrix}$$

where $\underline{x}$ is the *n*-dimensional vector of a parameter in natural frame; $\underline{x}_{\alpha\beta}$ is the *n*-dimensional vector of the parameter in the decoupled stator reference frames; k is the number of two-dimensional stator reference frames (α-β); $k=(n\text{-}1)/2$ if *n* is odd, and $k=(n\text{-}2)/2$ if *n* is even; x_{z1} and x_{z2} are parameters in one-dimensional zero-sequence frames (z_1, z_2); $[\boldsymbol{T}_{\boldsymbol{Clarke}}]$ is the *n*-by-*n* Clarke transformation matrix; x_{z2} in $\underline{x}_{\alpha\beta}$ and the last row of $[\boldsymbol{T}_{\boldsymbol{Clarke}}]$ only exist if *n* is even; coefficient $\sqrt{2/n}$ in $[\boldsymbol{T}_{\boldsymbol{Clarke}}]$ is to preserve the power in the new reference frames.

In other words, according to [35], after the Clarke transformation, the real *n*-phase machine is mathematically decomposed into (*n*+1)/2 (if *n* is odd) or (*n*+2)/2 (if *n* is even) fictitious machines as presented in Figs. 1.6 and 1.7, respectively. Specifically, there are *k* two-phase fictitious machines with *k* two-dimensional reference frames from (α_1-β_1) to (α_k-β_k). In addition, there is only 1 zero-sequence machine with 1 one-dimensional reference frame (z_1) if *n* is odd. When *n* is even, there are 2 zero-sequence machines with 2 one-dimensional frames (z_1, z_2).

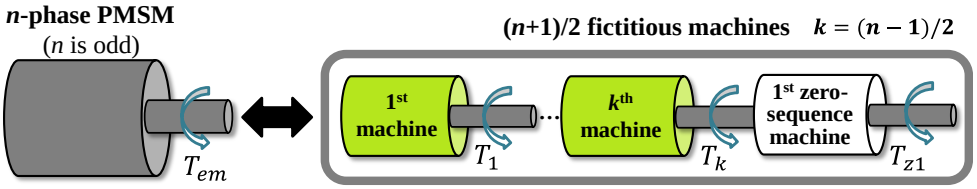

Fig. 1.6. Equivalent fictitious machines of a *n*-phase machine when *n* is odd.

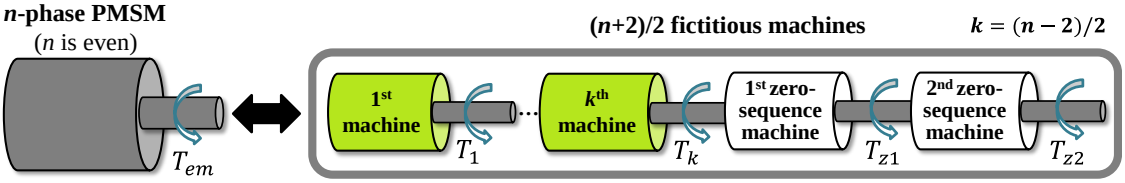

Fig. 1.7. Equivalent fictitious machines of a *n*-phase machine when *n* is even.

A fictitious machine with its corresponding decoupled reference frame is associated with a given group of harmonics as presented in Table 1.1.

Table 1.1. Fictitious machines, reference frames, and associated harmonics of a *n*-phase machine.

Fictitious machine	Reference frame	Associated harmonic
1st fictitious machine	α_1-β_1	$nj \pm 1$
2nd fictitious machine	α_2-β_2	$nj \pm 2$
kth fictitious machine	α_k-β_k	$nj \pm k$
1st zero-sequence machine	z_1	nj
2nd zero-sequence machine (if *n* is even)	z_2	$n(j \pm 1/2)$

with $j \in \mathbb{N}_0$, k=(n-1)/2 if *n* is odd, k=(n-1)/2 if *n* is even.

The voltages in the decoupled stator frames are given by:

$$\underline{v}_{\alpha\beta} = R_s \underline{i}_{\alpha\beta} + [\boldsymbol{L}_{\boldsymbol{\alpha\beta}}] \frac{d\underline{i}_{\alpha\beta}}{dt} + \underline{e}_{\alpha\beta} \tag{1.4}$$

where $\underline{v}_{\alpha\beta}$, $\underline{i}_{\alpha\beta}$ and $\underline{e}_{\alpha\beta}$ are the *n*-dimensional vectors of voltages, currents and back-EMFs in the decoupled stator frames, respectively; for a non-salient machine, the inductance matrix $[\boldsymbol{L}_{\alpha\beta}]$ in the decoupled stator frames is diagonal and expressed as follows:

$$[\boldsymbol{L}_{\alpha\beta}] = [\boldsymbol{T}_{Clarke}][\boldsymbol{L}][\boldsymbol{T}_{Clarke}]^T = \begin{bmatrix} L_1 & 0 & \cdots & 0 & 0 & 0 & 0 \\ 0 & L_1 & \cdots & 0 & 0 & 0 & 0 \\ \vdots & \vdots & \ddots & \vdots & \vdots & \vdots & \vdots \\ 0 & 0 & \cdots & L_k & 0 & 0 & 0 \\ 0 & 0 & \cdots & 0 & L_k & 0 & 0 \\ 0 & 0 & \cdots & 0 & 0 & L_{z1} & 0 \\ 0 & 0 & \cdots & 0 & 0 & 0 & L_{z2} \end{bmatrix} \tag{1.5}$$

where L_j ($j \in [1, k] \subset \mathbb{N}$), L_{z1} and L_{z2} are the inductances of fictitious machine j, zero-sequence machine z_1 and z_2, respectively. If the rotor presents any saliency, all elements of $[\boldsymbol{L}_{\alpha\beta}]$ need to be calculated with the electrical position of the machine.

It is noted that the natural frame model does not allow an easy development of the control system due to the magnetic coupling between phase windings, representing in $[\boldsymbol{L}]$ from (1.1). By using the Clarke transformation, the inductance matrix $[\boldsymbol{L}]$ becomes $[\boldsymbol{L}_{\alpha\beta}]$ in (1.5), allowing the magnetic decoupling between phase windings in the new reference frames.

All row vectors of $[\boldsymbol{T}_{Clarke}]$ are orthogonal to each other. An important property of the Clarke matrix regardless of the even or odd number of phases is that the inversion of the Clarke matrix is equal to its transpose:

$$[\boldsymbol{T}_{Clarke}]^T = [\boldsymbol{T}_{Clarke}]^{-1} \tag{1.6}$$

The electromagnetic torque of the machine is equal to the sum of torques generated by all fictitious machines as follows:

$$T_{em} = \left\{ \sum_{j=1}^{k} T_j \right\} + T_{z1} + T_{z2} \tag{1.7}$$

1.2.3. Rotor reference frame model

The rotor reference frames are virtual frames in which the sinusoidal parameters of the machine in the decoupled stator reference frames are converted to constant signals by using the Park transformation. The general Park transformation is given by:

$$\underline{x}_{dq} = [\boldsymbol{T}_{Park}]\underline{x}_{\alpha\beta} = [\boldsymbol{T}_{Park}][\boldsymbol{T}_{Clarke}]\underline{x} \tag{1.8}$$

$$\underline{x}_{dq} = \begin{bmatrix} x_{d1} \\ x_{q1} \\ \vdots \\ x_{dk} \\ x_{qk} \\ x_{z1} \\ x_{z2} \end{bmatrix}; \underline{x}_{\alpha\beta} = \begin{bmatrix} x_{\alpha1} \\ x_{\beta1} \\ \vdots \\ x_{\alpha k} \\ x_{\beta k} \\ x_{z1} \\ x_{z2} \end{bmatrix}; \underline{x} = \begin{bmatrix} x_A \\ x_B \\ x_C \\ \vdots \\ x_{n-1} \\ x_n \end{bmatrix}; [\boldsymbol{T}_{Park}] = \begin{bmatrix} \cos(h_1\theta) & \sin(h_1\theta) & \cdots & 0 & 0 & 0 & 0 \\ -\sin(h_1\theta) & \cos(h_1\theta) & \cdots & 0 & 0 & 0 & 0 \\ \vdots & \vdots & \ddots & \vdots & \vdots & \vdots & 0 \\ 0 & 0 & \cdots & \cos(h_k\theta) & \sin(h_k\theta) & 0 & 0 \\ 0 & 0 & \cdots & -\sin(h_k\theta) & \cos(h_k\theta) & 0 & 0 \\ 0 & 0 & \cdots & 0 & 0 & 1 & 0 \\ 0 & 0 & \cdots & 0 & 0 & 0 & 1 \end{bmatrix}$$

where $\underline{x}_{dq}$ is the n-dimensional vector of the machine parameters in the rotor reference frames; k is the number of 2-dimensional rotating frames (d-q); k=(n-1)/2 if n is odd, and k=(n-2)/2 if n is even; x_{z1} and x_{z2} are parameters in one-dimensional zero-sequence frames; $[\boldsymbol{T}_{Park}]$ is the n-by-n Park transformation matrix with harmonics $h_1\theta$ to $h_k\theta$ that are determined from associated harmonics in Table 1.1. It is noted that x_{z2} in $\underline{x}_{dq}$ and $\underline{x}_{\alpha\beta}$, and the last row of $[\boldsymbol{T}_{Park}]$ only exist in case of the even number of phases.

The voltages in a d-q frame k can be expressed as follows:

$$\begin{cases} v_{dk} = R_s i_{dk} + L_{dk}\dfrac{di_{dk}}{dt} - p\Omega L_{qk} i_{qk} + e_{dk} \\ v_{qk} = R_s i_{qk} + L_{qk}\dfrac{di_{qk}}{dt} + p\Omega L_{dk} i_{dk} + e_{qk} \end{cases} \tag{1.9}$$

where (v_{dk}, v_{qk}), (i_{dk}, i_{qk}), and (e_{dk}, e_{qk}) are the voltages, currents, and back-EMFs in d-q frame k, respectively; p is the number of pole pairs; (L_{dk}, L_{qk}) are inductances in d-q frame k.

In a non-salient machine, the inductance matrix in the rotor reference frames $\mathbf{[L_{dq}]}$, equal to matrix $\mathbf{[L_{\alpha\beta}]}$ in (1.5), can be proved as follows:

$$\begin{aligned} [\boldsymbol{L_{dq}}] &= ([\boldsymbol{T_{Park}}][\boldsymbol{T_{Clarke}}])[\boldsymbol{L}]([\boldsymbol{T_{Park}}][\boldsymbol{T_{Clarke}}])^T = [\boldsymbol{T_{Park}}]([\boldsymbol{T_{Clarke}}][\boldsymbol{L}][\boldsymbol{T_{Clarke}}])^T [\boldsymbol{T_{Park}}]^T \\ &= [\boldsymbol{T_{Park}}][\boldsymbol{L_{\alpha\beta}}][\boldsymbol{T_{Park}}]^T = \begin{bmatrix} L_1 & 0 & \cdots & 0 & 0 & 0 & 0 \\ 0 & L_1 & \cdots & 0 & 0 & 0 & 0 \\ \vdots & \vdots & \ddots & \vdots & \vdots & \vdots & \vdots \\ 0 & 0 & \cdots & L_k & 0 & 0 & 0 \\ 0 & 0 & \cdots & 0 & L_k & 0 & 0 \\ 0 & 0 & \cdots & 0 & 0 & L_{z1} & 0 \\ 0 & 0 & \cdots & 0 & 0 & 0 & L_{z2} \end{bmatrix} = [\boldsymbol{L_{\alpha\beta}}] \end{aligned} \tag{1.10}$$

where L_j ($j \in [1, k] \subset \mathbb{N}$), L_{z1} and L_{z2} are the inductances of fictitious machine j, zero-sequence machine z_1 and z_2, respectively. Therefore, we have (L_{dk}=L_{qk}= L_k).

In the rotor reference frames, the machine model inherits the magnetic decoupling property from the decoupled stator reference frames. Ideally, the machine parameters such as currents in the rotor reference frames are time-constant for control.

1.3. State of the art in the control field of multiphase drives

To derive a general and systematic view of studies on the control of multiphase drives, the state of the art is organized as follows. First, control techniques for multiphase drives in healthy mode are presented. Then, existing studies on fault-tolerant control are analyzed.

1.3.1. Existing control techniques of multiphase drives in healthy mode

As analyzed in [21-23, 26, 31, 60-62], control techniques for multiphase drives can be generally categorized in three main types: Field-Oriented Control (FOC), Direct Torque Control (DTC) and Model-based Predictive Control (MPC). The inner loop for current, torque, and flux control is considered because the outer loop for speed control in the three control techniques is the same.

1.3.1.A. *FOC*

FOC, early proposed in [63, 64], has become the most popular control technique with the use of orthogonal transformation matrices. To understand the principle of FOC, the FOC-based current control loop of a n-phase PMSM fed by a VSI is described in Fig. 1.8. As previously mentioned, matrices [$\boldsymbol{T_{Clarke}}$] and [$\boldsymbol{T_{Park}}$] are applied to decompose the n-phase machine into

(n+1)/2 or (n+2)/2 fictitious machines (decoupled reference frames). Therefore, the control of flux and torque can be decoupled by independently regulating constant currents in rotor reference frames. Reference voltages $\underline{v}_{dq\_ref}$, mostly calculated by proportional integral (PI) controllers and estimated back-EMF compensations $\underline{e}_{dq\_est}$ (optional), are converted into natural frame $\underline{v}_{ref}$. These voltages are reference values to determine the duty cycle for the generation of switching signals of VSI ($\underline{s}_{1,n}$). Specifically, $\underline{v}_{ref}$ is compared with carrier signals, called Carrier Based PWM (CBPWM), or it is used to define different adjacent space vectors applied in different time periods, called Space Vector PWM (SVPWM).

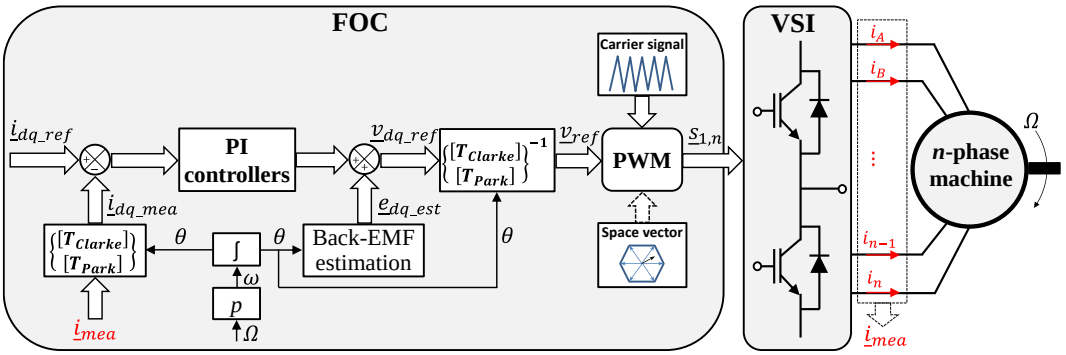

Fig. 1.8. The inner control loop of a n-phase PMSM drive based on FOC technique.

In the early 2000s, methodologies to generally study multiphase drives by using space vector approach have been proposed [35, 65]. The geometrical and graphical properties of the space vector are generalized and adapted for multiphase systems with advancements of matrix calculations. Power converters including PWM voltages and current source inverters are characterized by space vectors. The methodologies can be generalized to various inverters with different numbers of legs. Then, the formalism is first applied to three-phase machines before being verified in five-phase induction machines.

Some recent studies on FOC-based control of multiphase drives can be summarized as follows:

1) Five phase and dual three-phase induction machines with sinusoidal MMFs have been studied in [66-68]. Due to more DoF than three-phase counterparts, non-sinusoidal MMFs in multiphase induction machines can be properly controlled in [69-74]. The injection of current harmonics allows to improve torque quality.
2) Studies based on FOC for three-phase, five-phase, dual three-phase and seven-phase PMSMs with different stator winding topologies have been proposed in [29, 46, 53-55, 75-90]. In these studies, most of these machines have non-sinusoidal back-EMF waveforms, enabling to increase the torque density. Especially, a bi-harmonic five-phase PMSM with a dominant third harmonic of back-EMF is introduced in [55, 83]. This special machine can easily exploit corresponding current harmonics to have an electromagnetic gearbox, extending the speed range without using physical electronics switches. Meanwhile, studies [87] calculate current references to obtain maximum torque-speed characteristic by considering limits of peak values of phase currents and voltages for a sinusoidal five-phase PMSM.

1.3.1.B. *DTC*

An alternative to FOC is DTC that was introduced in [91-93]. In general, DTC is based on the modeling to estimate the magnetic flux and torque. The control of the magnetic flux and torque is implemented in decoupled stator reference frames without the inner current control loop. DTC techniques are categorized by the way to define the stator voltages. The stator voltages can be either obtained by an optimal Switching Table (ST-DTC) or by a constant switching frequency (PWM-DTC).

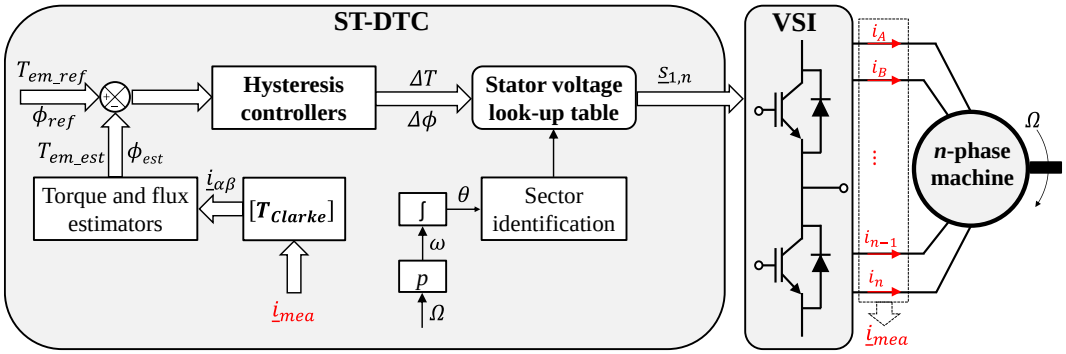

Fig. 1.9. The inner control loop of a *n*-phase PMSM drive based on ST-DTC technique.

The inner loop of a *n*-phase PMSM drive using ST-DTC is described in Fig. 1.9. The ST-DTC is to compare the estimated and reference values of the stator flux (ϕ_{est} and ϕ_{ref}) as well as of the electromagnetic torque (T_{em_est} and T_{em_ref}). Then, stator voltage vectors are selected from a look-up table to define switching signals of VSI ($\underline{s}_{1,n}$). With ST-DTC, hysteresis controllers are usually applied to force the controlled variables to rapidly track their reference values without PWM. This feature makes ST-DTC simple with a fast torque response. However, ST-DTC leads to variable switching frequencies and parasitic high-frequency components in currents, resulting in higher-ripple torques than FOC [23]. In addition, the number of voltage space vectors is exponentially proportional to the number of phases, making the size of the look-up table dramatically increase [60]. Study [94] proposes a general ST-DTC method for the odd number of phases more than three. However, the ST-DTC technique has not been extended yet to any phase number higher than six.

1) Some studies on ST-DTC for five-phase and asymmetrical six-phase induction machines are introduced in [95-97]. Specifically, the stator voltages in the secondary plane are reduced to minimize the stator current components that do not generate the torque.
2) Meanwhile, studies on ST-DTC for five-phase PMSM drives using the multi-machine multi-converter system concept have been proposed in [98, 99].

Alternatively, PWM-DTC technique imposes constant switching frequencies and requires a PWM as described in Fig. 1.10. Specifically, DTC algorithm in PWM-DTC is used to generate voltage references before PWM defines inverter switching states. This algorithm is based on the deadbeat solution in which reference values of the stator flux and electromagnetic torque are obtained in just one sampling time [100]. This method has several advantages compared to ST-DTC with variable switching frequencies such as lower torque ripples and smaller high-

frequency components in currents. However, because of controlling in decoupled stator reference frames, PWM-DTC requires a high switching frequency to guarantee a good performance. In addition, as ST-DTC, the calculation burden is a drawback of PWM-DTC. An application of PWM-DTC can be found in [101] for a dual three-phase induction motor drive.

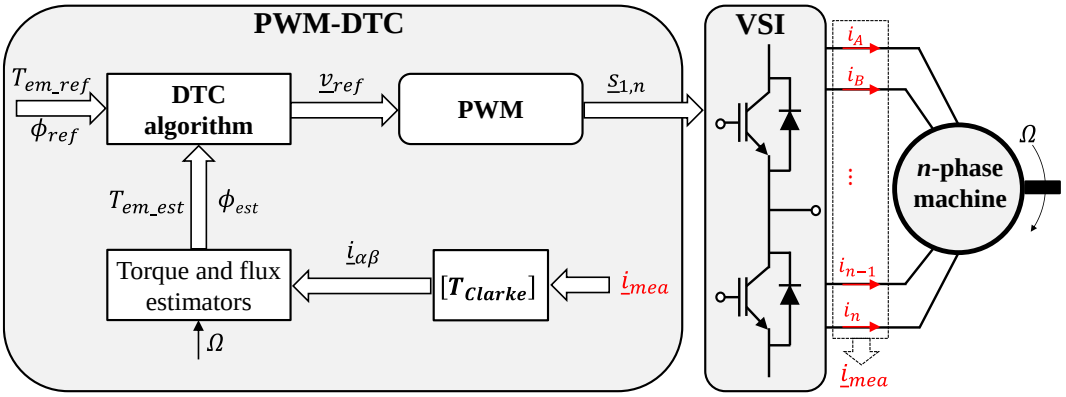

Fig. 1.10. The inner control loop of a *n*-phase PMSM drive based on PWM-DTC technique.

1.3.1.C. *MPC*

Although first developed in the 1970s, MPC has recently become one of the most promising and widely used techniques [23, 102]. This approach can be considered as an improvement of DTC. According to the optimization and control actions, MPC techniques can be divided into two types, including Continuous Control Set MPC (CCS-MPC) and Finite Control Set MPC (FCS-MPC). CCS-MPC applies an average model of the system with continuous reference signals and a fixed frequency. Meanwhile, FCS-MPC uses the finite number of switching states in the inverter, and it has variable switching frequencies. Indeed, the FCS-MPC scheme for a *n*-phase PMSM drive in Fig. 1.11 shows that it is based on the accuracy of the system model to predict future behaviors of the system variables ($i_{\alpha\beta}^{k+1}$). The anticipation with a minimization of a cost function ($min(J)$) allows to define the optimal VSI switching states ($\underline{s}_{1,n}$). It is noted that FCS-MPC can easily add extra control objectives such as copper losses or constraints on current and voltage.

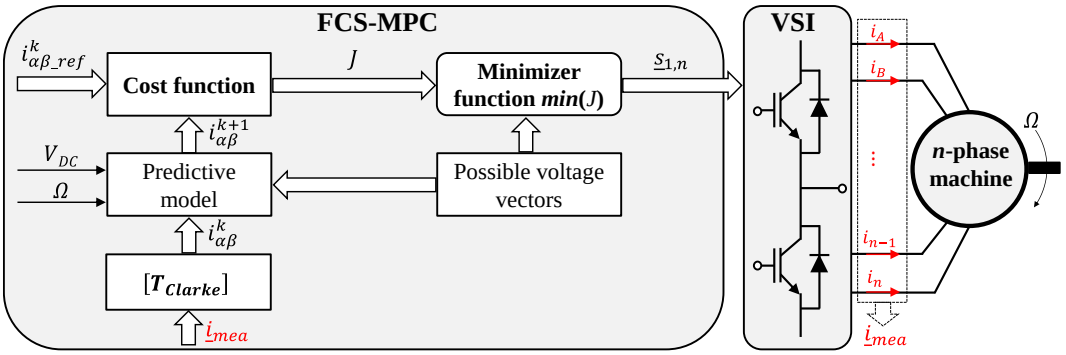

Fig. 1.11. The inner control loop of a *n*-phase PMSM drive based on FCS-MPC technique.

In general, MPC has a faster response than FOC and a more flexible control structure than DTC. However, it still possesses high computational costs due to a high number of iterations and high switching frequencies. Importantly, MPC requires accurate knowledge of the system for the model prediction [23].

1) General MPC schemes for power electronics and devices are categorized in [102]. MPC-based control structures are described in [103, 104] for asymmetrical six-phase induction machines, and in [105-107] for five-phase induction machines.
2) Studies for five-phase PMSMs are conducted in [108, 109], taking into account limits of current and voltage.

1.3.2. Existing control strategies for post-fault operations

1.3.2.A. *Possible faults in multiphase drives*

To analyze existing fault-tolerant control strategies, possible electric faults may happen in multiphase drives should be presented. In Fig. 1.12, different types of faults in a multiphase drive include SC or OC in inverter switches, phase windings or connecting lines between the machine and the inverter. Among them, OC faults have been more reported than SC faults in electric drives [31, 110] since a SC fault normally leads to an OC fault with the inner protection of the corresponding switches [111]. Therefore, this present doctoral thesis will mainly focus on OC faults in multiphase drives.

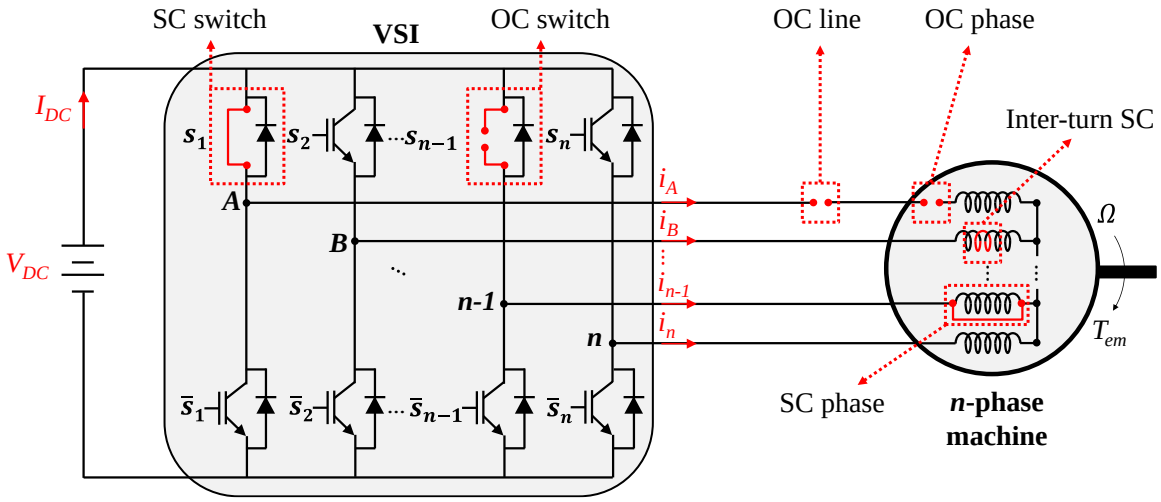

Fig. 1.12. Different types of faults in a *n*-phase drive.

When a fault happens in an electric drive, detections, diagnoses, and fault isolations of the fault need to take place, avoiding possible damages of the electric drive. There have been many studies on fault diagnoses, detections and isolations such as [14, 112-118] by exploiting special characteristics of multiphase drives.

In healthy mode, multiphase drives are properly controlled with smooth torques by the control techniques as presented in the previous subsection. Their phase currents have the same waveform with rated RMS values. In post-fault operations, the number of active phases is lower, and the remaining phases are no longer symmetrical. If the pre-fault current references are not changed, there will have uncontrollable currents and pulsating torques [78, 118-121]. Specifically, there are two main consequences of the fault occurrence in a multiphase drive as follows:

1) Limits of peak or Root Mean Square (RMS) currents may not be respected. In other words, current waveforms of remaining healthy phases of the drive are deteriorated in post-fault operations. The peak current limit is based on the instantaneous peak currents during a short-time operation, and it is related to VSI components. Meanwhile, RMS current limit is mainly defined from the thermal limits of the stator windings.
2) Smooth electromagnetic torques cannot be guaranteed. In general, the uncontrolled healthy phase currents create uncircular rotating MMFs per reference frame, generating torque ripples. These torque ripples can cause noises and vibrations, reducing the operating quality of the drive.

1.3.2.B. *Categorization based on criteria of new current references for fault-tolerant operations*

From the consequences in the previous subsection, new current references need to be defined when one or more phases are open-circuited, called the reconfiguration or fault-tolerant control. New current references are required to generate smooth torques and comply some of the several additional criteria as follows:

1) Constraints on current limit: the remaining healthy phase currents need to respect their RMS or peak value limits [61, 87, 122, 123].
2) Constraints on voltage limit: the peak phase voltages are required to be within their limits to avoid inverter saturation. In other words, flux-weakening operations can be guaranteed in faulty modes [61, 74, 87].
3) Copper loss optimization: the remaining healthy phase currents are designed to obtain either minimum total copper losses [120, 121, 124-136] or equal copper losses in the healthy phases [124, 126-135, 137, 138].

The above criteria can be combined with each other in a fault-tolerant strategy. For example, the first and second criteria can guarantee high functional reliability in low-speed and flux-weakening operations for post-fault multiphase drives.

1.3.2.C. *Categorization based on types of MMFs for fault-tolerant operations*

The principle of a fault-tolerant strategy is based on fault types and characteristics of multiphase drives such as the number of phases and machine design. One of the first attempts [13] shows that the number of stator phases and the type of excitation waveforms (sinusoidal or non-sinusoidal) affect degrading performances. Accordingly, fault-tolerant control studies can be classified into two groups according to types of MMFs for IMs and PMSMs as follows:

1) Sinusoidal multiphase machines: Fault-tolerant strategies for sinusoidal multiphase machines have been found in [87, 119, 123, 126-133, 137-141]. These machines have more DoF for control because high-order harmonics of back-EMF do not exist, allowing the presence of high-order harmonics of current for optimization purposes.

Fault-tolerant control strategies for sinusoidal machines cannot be simply applied to non-sinusoidal machines due to torque ripples.

2) Non-sinusoidal multiphase machines: Studies [61, 120-122, 124, 125, 134-136, 142-149] have been proposed fault-tolerant strategies for non-sinusoidal multiphase machines. These strategies are often more complicated than those of sinusoidal machines. However, these non-sinusoidal multiphase machines have several advantages such as easy-to-manufacture, lower production costs, higher torque densities, lower copper losses (if concentrated windings with short end-windings are chosen), and the ability for electromagnetic pole changing (see **section 1.1.1.E**).

1.3.2.D. *Categorization based on modeling of multiphase drives for fault-tolerant operations*

The modeling of a multiphase drive in post-fault conditions can be derived by the vector space decomposition [150], or the multi-reference frame theory with generalized space vectorial formalism [34, 35, 65]. As discussed in the general modeling (see **section 1.2**), using Clarke transformation [$\boldsymbol{T_{Clarke}}$] allows to decompose a *n*-phase machine into several decoupled fictitious machines (reference frames). There are (*n*+1)/2 reference frames for the odd number of phases and (*n*+2)/2 reference frames for the even number of phases. In these reference frames, currents and voltages are independently controlled in healthy mode. However, in faulty modes, the decoupling property no longer exists. Therefore, there have been two options for the modeling as follows:

1) Clarke transformation of healthy mode [$\boldsymbol{T_{Clarke}}$] is preserved but current references in rotor reference frames need to be redefined [87, 120, 123, 138]. The control structure is unchanged in faulty modes, making these strategies simpler. New d-q current references of fictitious machines that create most of the torque are designed to be constant. Consequently, other d-q currents in other fictitious machines are time-variant.
2) Reduced-order transformation matrices [126-129, 132-135, 149] with dimensions equivalent to the number of healthy phases are applied. Indeed, when a *n*-phase drive loses one phase, the machine in this post-fault condition can be considered as an asymmetric (*n*-1) phase machine. Hence, the post-fault drive can be mathematically re-modeled with (*n*-1) phases in which new (*n*-1)-dimensional Clarke and Park matrices are defined with the aim of preserving MMFs under the OC fault. In new decoupled reference frames, new d-q current references with optimization options are determined to obtain constant torques.

1.3.2.E. *Categorization based on control techniques for fault-tolerant operations*

A popular control technique for a post-fault multiphase drive is FOC in which the speed control loop is regulated by a proportional or PI controller to generate torque references [31]. Meanwhile, the inner loop controller for current can be one of the following options:

1) PI: Studies [87, 120] apply the classical FOC scheme with PI controllers because main d-q current references, generating most of the torque, are designed to be constant.
2) MPC and DTC: With a faster response than FOC, the use of MPC has been found in [109, 128, 151, 152] while some studies [136, 148] have been conducted with DTC. The MPC scheme is also flexible to apply constraints on current and voltage. However, MPC and DTC possess some drawbacks as described in the control techniques (see **section 1.3.1**).
3) Hysteresis control: To deal with time-variant current references in natural frame, studies [121, 122, 125, 153, 154] apply hysteresis controllers for current control. However, noises, losses and variable switching frequencies can be considered as several drawbacks of the control.
4) Dual PI: Studies [123, 135, 138, 149, 155] use dual PI or proportional integral resonant (PIR) controllers for time-variant current references. Demands for multiple parameter adjustments and the knowledge of frequencies are some drawbacks of this approach.
5) Robust control: A FOC-based control scheme with a robust controller for speed or current such as a fuzzy logic (FL) controller and a sliding mode controller has been found in [139, 156, 157]. This scheme can enhance the fault-tolerant ability of the drive in various types of faults (OC faults in inverter switches or lines between inverters and machines).

1.4. Objectives of the doctoral thesis

This doctoral thesis is dedicated to enriching control methods of multiphase drives with the aim of highlighting advantages of multiphase drives in automotive applications. Multiphase drives can meet the six requirements for electric drives in EVs (see **Introduction**) only when these drives are properly controlled under a variety of operating conditions. For example, an EV driven by multiphase drives with two driving modes is described in Fig. 1.13. The torque reference can be generated by either the accelerator pedal (controlled by the driver) or the speed controller (an autonomous operation, for example). Economical mode generally enables EVs to work with high efficiency in the low-torque region of the torque-speed characteristic. Meanwhile, high-performance mode allows EVs to operate with maximum torques at each speed for accelerations. A switch between these two driving modes is made when the required torque results in an excess of electrical limits (currents and voltages). This doctoral thesis will focus on high-performance mode under healthy or faulty conditions. The electromagnetic torque will be maximized under limits of currents and voltages.

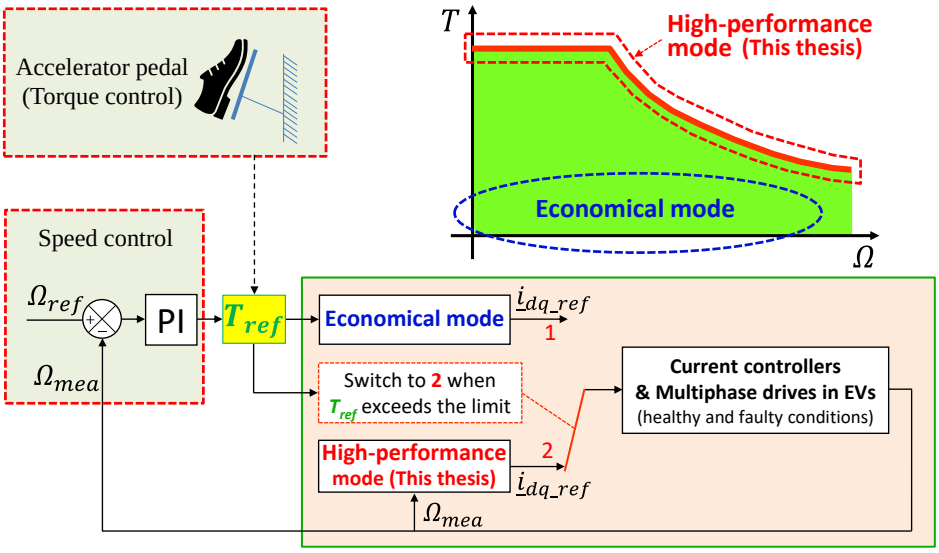

Fig. 1.13. Multiphase drives in EVs with two driving modes.

Therefore, according to the above analyses and state of the art in the control field of multiphase drives (see **section 1.3**), the main objective of this doctoral thesis is to propose control strategies for non-sinusoidal multiphase PMSM drives under OC faults (see **section 1.3.2.A**). Importantly, constraints on current and voltage will be always considered in all operating modes. Another objective of this doctoral thesis is to enhance performances, including the control and torque quality, under impacts of uncertainties and imperfections of the electric drives by using artificial intelligence.

Several main points of these objectives of this doctoral thesis can be justified and more explained as follows:

1) Regarding the type of electric machine, non-sinusoidal multiphase PMSMs are the controlled object in this doctoral thesis. As analyzed in **section 1.1.2**, besides the general properties of the multiphase concept, multiphase PMSMs are chosen for this doctoral thesis due to their high efficiency and high volume densities. These advantages meet the first two requirements of EVs. In addition, non-sinusoidal back-EMFs are considered due to several advantages such as easy-to-manufacture, low production costs, high torque densities, and the ability for the electromagnetic pole changing (see **section 1.1.1.E**). The control of non-sinusoidal machines is more challenging and interesting due to high-order back-EMF harmonics.
2) Regarding the control technique in this doctoral thesis, proposed control strategies in all operating modes will be based on FOC technique and PI controllers as healthy mode. Besides the recent techniques MPC and DTC, the classical FOC technique with PI controllers is still interesting, especially for industry due to its quality, simplicity, and robustness (less dependent on the machine model). In addition, this classical FOC has been widely used in industry. Therefore, the proposed control strategies in this thesis are derived from the mathematical model using the multi-reference frame theory [35]. Currents in rotating reference frames are expected to either be constant or slowly vary, especially currents generating most of the torque.

3) Regarding constraints on current and voltage, these constraints guarantee high functional reliability and flux-weakening operations of the drives. From the state of the art (see **section 1.3**), few studies considering fault-tolerant control and non-sinusoidal back-EMFs under constraints on current and voltage have been conducted, except [61] with MPC and DTC techniques for 5-phase machines.
4) Regarding enhancements of control and torque performances under impacts of uncertainties and imperfections of electric drives by artificial intelligence, ADALINE (ADAptive LInear NEuron), a simple type of artificial neural networks, is chosen. One of the uncertainties can be "dead-time" voltages (the inverter nonlinearity) while the presence of multi-harmonics in back-EMFs causes an imperfection in machine design. ADALINEs are chosen in this doctoral thesis thanks to their self-learning ability and easy implementation. Moreover, the knowledge of harmonic components in signals of the drives allows a fast response of control (fast convergence) and avoids the calculation burden, increasing their applicability to industrial electric drives. Indeed, this knowledge is easily obtained and generally proportional to the number of phases. ADALINEs just need to find the right amplitudes of these harmonics. These advantages make ADALINEs more favorable compared to other approaches such as FL, PIR, and so on. FL control requires experience of experts while PIR control requires multiple parameter adjustments and the knowledge of frequencies. By using ADALINEs, quality of torque and current control will be significantly improved in either healthy mode or faulty mode.

1.5. Conclusions

According to the requirements presented in the **Introduction** of this doctoral thesis, **section 1.1** of **Chapter 1** has presented several distinct advantages and some possible drawbacks of multiphase drives. Thanks to these important advantages of multiphase drives, EVs driven by multiphase drives, especially PMSM drives, have high potential to be commercialized in near future. However, there have been some drawbacks of multiphase drives regarding the calculation burden, high electronics drive costs for a high number of VSI legs, the complexity of modeling and control, and social inertia. These drawbacks can be overcome by advances in microprocessors, mass productions, enhancements in power electronics technologies as well as long-term investments of industrial companies and so on. In addition, the modeling of a general multiphase PMSM has been briefly described in **section 1.2**. This modeling has facilitated the analyses of recent studies on control strategies of multiphase drives in healthy and faulty modes in **section 1.3**. High-performance driving mode of EVs can be feasible if the objectives of this doctoral thesis presented in **section 1.4** are achieved. Then, justifications and explanations of the objectives have been delivered to clarify the purposes of this work.

Chapter 2. Modeling and Control of Multiphase Drives

This chapter is dedicated to presenting the modeling and control of multiphase drives under heathy and faulty modes. The healthy-mode issues are discussed in **section 2.1** in which the modeling and a control scheme under constraints on current and voltage are introduced. In this scheme, FOC technique and PI controllers are used. Current references are calculated by an optimal strategy that maximizes torques under the considered constraints. **Section 2.2** describes critical problems of post-fault operations without reconfigurations through analytical expressions and experimental results. Especially, **section 2.3** proposes three main fault-tolerant control methods by exploiting mathematical models of multiphase drives. The control scheme is almost the same as healthy mode with on FOC technique and PI controllers. The critical problems in post-fault operations including ripple torques and electrical limit excesses are solved. Therefore, torque-speed characteristics with flux-weakening operations of post-fault multiphase drives will be verified by numerical and experimental results. Conclusions of the chapter are presented in **section 2.4.**

2.1. Modeling and control of a multiphase drive in healthy mode

This section presents the modeling and control of a multiphase machine in healthy mode. To effectively illustrate characteristics of the multiphase drive, a seven-phase PMSM drive is considered as a case study. Compared to a five-phase machine, the seven-phase machine possesses more DoF for control.

2.1.1. The case study: a seven-phase PMSM

The schematic diagram of a seven-phase PMSM is described in Fig. 2.1 with rotating speed Ω, electrical position θ, and electromagnetic torque T_{em}.

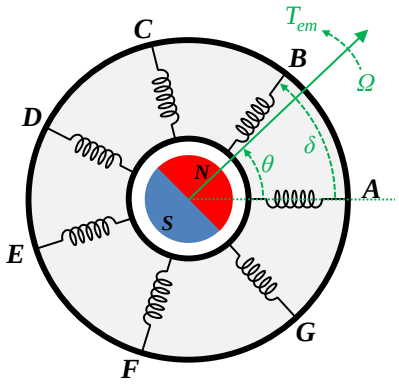

Fig. 2.1. Schematic diagram of a seven-phase PMSM.

To model the machine, several assumptions are considered as follows:

1) Seven phases of the machine are equally shifted with the spatial angular displacement δ equal to $2\pi/7$.

2) The machine has a non-salient rotor; hence, the inductances in fictitious machines can be easily calculated from Clarke transformation matrix as in (1.5).
3) The saturation of the magnetic circuits is not considered in the calculations of the back-EMFs and the fluxes.

To simplify the control scheme, machine parameters are converted from natural frame into the decoupled α-β and d-q frames for the seven-phase machine as follows:

$$\begin{aligned}\left[x_{d1}\ x_{q1}\ x_{d9}\ x_{q9}\ x_{d3}\ x_{q3}\ x_z\right]^T &= \left[\boldsymbol{T_{Park}}\right]\left[x_{\alpha 1}\ x_{\beta 1}\ x_{\alpha 2}\ x_{\beta 2}\ x_{\alpha 3}\ x_{\beta 3}\ x_z\right]^T \\ &= \left[\boldsymbol{T_{Park}}\right]\left[\boldsymbol{T_{Clarke}}\right]\left[x_A\ x_B\ x_C\ x_D\ x_E\ x_F\ x_G\right]^T\end{aligned} \tag{2.1}$$

with

$$\left[\boldsymbol{T_{Clarke}}\right] = \sqrt{\frac{2}{7}}\begin{bmatrix} 1 & \cos(\delta) & \cos(2\delta) & \cos(3\delta) & \cos(4\delta) & \cos(5\delta) & \cos(6\delta) \\ 0 & \sin(\delta) & \sin(2\delta) & \sin(3\delta) & \sin(4\delta) & \sin(5\delta) & \sin(6\delta) \\ 1 & \cos(2\delta) & \cos(4\delta) & \cos(6\delta) & \cos(8\delta) & \cos(10\delta) & \cos(12\delta) \\ 0 & \sin(2\delta) & \sin(4\delta) & \sin(6\delta) & \sin(8\delta) & \sin(10\delta) & \sin(12\delta) \\ 1 & \cos(3\delta) & \cos(6\delta) & \cos(9\delta) & \cos(12\delta) & \cos(15\delta) & \cos(18\delta) \\ 0 & \sin(3\delta) & \sin(6\delta) & \sin(9\delta) & \sin(12\delta) & \sin(15\delta) & \sin(18\delta) \\ 1/\sqrt{2} & 1/\sqrt{2} & 1/\sqrt{2} & 1/\sqrt{2} & 1/\sqrt{2} & 1/\sqrt{2} & 1/\sqrt{2} \end{bmatrix}$$

$$\left[\boldsymbol{T_{Park}}\right] = \begin{bmatrix} \cos(\theta) & \sin(\theta) & 0 & 0 & 0 & 0 & 0 \\ -\sin(\theta) & \cos(\theta) & 0 & 0 & 0 & 0 & 0 \\ 0 & 0 & \cos(9\theta) & \sin(9\theta) & 0 & 0 & 0 \\ 0 & 0 & -\sin(9\theta) & \cos(9\theta) & 0 & 0 & 0 \\ 0 & 0 & 0 & 0 & \cos(3\theta) & \sin(3\theta) & 0 \\ 0 & 0 & 0 & 0 & -\sin(3\theta) & \cos(3\theta) & 0 \\ 0 & 0 & 0 & 0 & 0 & 0 & 1 \end{bmatrix}$$

where x is an arbitrary parameter of the machine such as current, back-EMF and voltage; $\boldsymbol{[T_{Clarke}]}$ is the 7 by 7 Clarke transformation matrix; $\delta = 2\pi/7$ is the spatial angular displacement; θ is the electrical position; $\boldsymbol{[T_{Park}]}$ is the 7 by 7 Park transformation matrix in which the 1st (θ), 9th (9θ), and 3rd (3θ) harmonic components are considered. The selection of these harmonic components in the Park matrix depends on main harmonics existing in the back-EMFs of the machine. In this study, the 5th harmonic is much smaller than the 9th one; hence, 9θ is used instead of 5θ.

In the new decoupled reference frames, the real machine is decomposed into 4 fictitious machines including 3 two-phase fictitious machines (FM1, FM2, FM3) and 1 zero-sequence machine (ZM) as described in Fig. 2.2. Each fictitious machine with a corresponding reference frame is associated with a given group of harmonics as shown in Table 2.1. Specially, the d-q reference frame for the second fictitious machine is denoted by (d_9-q_9) because the ninth harmonic is considered in the back-EMFs.

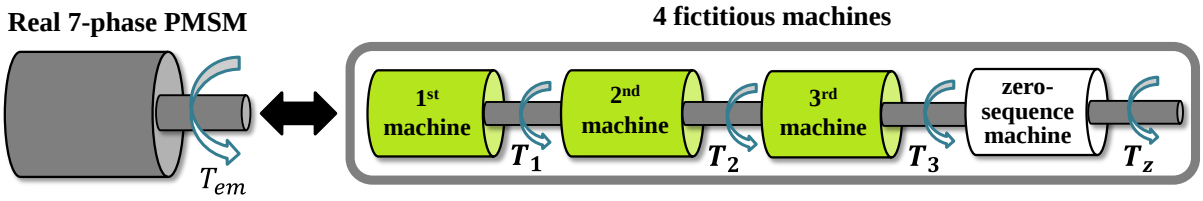

Fig. 2.2. Decomposition of a seven-phase machine into four fictitious machines.

Table 2.1. Four fictitious machines with corresponding reference frames and associated harmonics of a seven-phase machine (only odd harmonics).

Fictitious machine	Reference frame	Associated harmonic
The first machine (FM1)	d_1-q_1	1, 13, 15,…,$7j \pm 1$
The second machine (FM2)	d_9-q_9	5, 9, 19, …, $7j \pm 2$
The third machine (FM3)	d_3-q_3	3, 11, 17,…, $7j \pm 3$
Zero-sequence machine (ZM)	z	7, 21,…, $7j$

with $j \in \mathbb{N}_0$

The electromagnetic torque T_{em} of the real machine is equal to the sum of torques generated by all its fictitious machines as expressed in (2.2).

$$T_{em} = T_1 + T_2 + T_3 + T_z \tag{2.2}$$

2.1.2. Energetic Macroscopic Representation for modeling and control

2.1.2.A. *The representation of the electric drive model*

Energetic Macroscopic Representation (EMR) is a functional description originally developed in the control team of L2EP laboratory in 2000s to analyze an energetic system [158, 159]. In other words, EMR is a graphical tool using block diagrams to easily organize the model and facilitate the control of an energetic system. In addition, the number of DoF are pointed out for the control. This point is particularly important for multiphase machines whose number of DoF is high in comparison with three-phase machines.

In fact, there have been existing other graphical approaches based on the facilitation of visual human sense. The idea is to choose a graphical approach which is adapted at first for the deduction of control and then for energetic system. Two of other tools for system model representations are Bond Graph (1959) and Causal Ordering Graph (COG 1996). Bond Graph is based on the derivative causality while the integral causality is used in COG. As COG, EMR is based on the integral causality. Consequently, the control scheme is deduced from the model representation by the principle of inversion in which the control is considered as a functional inversion of the model. As Bond Graph, EMR can point out power flows. Therefore, it is thus well adapted to the graphical representation of an energetic system as electrical drives. From the above reasons, EMR is chosen to represent multiphase drives in this doctoral thesis. Thanks to EMR, the modeling and control of a complex system such as a multiphase drive become more synthetic.

More descriptions about EMR elements are presented in **Appendix A** of this doctoral thesis. To understand the representation of a system model by EMR, the case study with the considered seven-phase drive is described in Fig. 2.3.

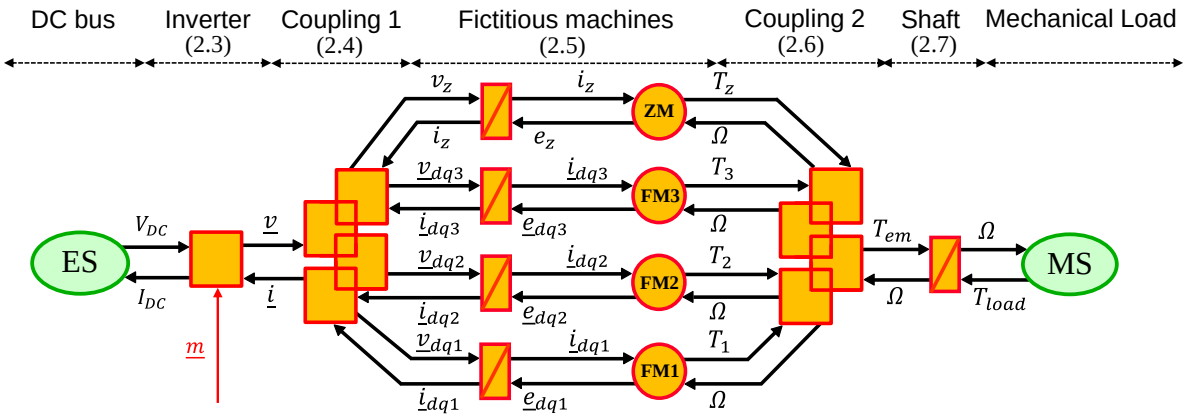

Fig. 2.3. Representation of the model of a seven-phase PMSM drive using EMR.

Two adjacent elements of EMR are connected by two arrows with two opposite directions, representing the action and reaction between them. This connection is based on causality principle (integral). EMF helps to highlight controlled variables of the system such as a duty cycle (conversion factor) for an inverter. In addition, EMF can determine either the power flow or the control path. Four main elements of EMR can be generally described as follows:

1) Energy sources (oval green pictograms) represent the environment of the studied system, delivering or receiving energy. In Fig. 2.3, the electric source (ES) is a DC-bus voltage V_{DC} to feed an inverter while the mechanical source (MS) represents the mechanical load of the drive system.
2) Accumulation elements (rectangle orange pictograms with diagonal lines) represent the energy storage because the transfer functions of these elements include integral operators. In Fig. 2.3, the accumulation elements present in the fictitious machines and in the rotor shaft.
3) Conversion elements (square orange pictograms for mono-physical conversions or circle orange pictograms for multi-physical conversions) convert energy without any energy accumulations. In Fig. 2.3, the mono-physical conversion element is the inverter while the multi-physical conversion elements are the electromechanical elements in the fictitious machines.
4) Coupling elements (overlapped orange pictograms) are for energy distributions. In Fig. 2.3, the first coupling element is the Clarke transformation (or combined with Park transformation). The second coupling element is to calculate the electromagnetic torque from four fictitious machines.

Specifically, mathematical descriptions for all elements in Fig. 2.3 are expressed in (2.3)-(2.7).

Inverter (conversion element):

$$\begin{cases} \underline{v} = \underline{m}\, V_{DC} \\ I_{DC} = \underline{m}^T \underline{i} \end{cases} \tag{2.3}$$

with $\underline{v} = \left[v_A\ v_B\ v_C\ v_D\ v_E\ v_F\ v_G\right]^T$

$\underline{i} = \left[i_A\ i_B\ i_C\ i_D\ i_E\ i_F\ i_G\right]^T$

$$\underline{m} = \begin{bmatrix} m_A & m_B & m_C & m_D & m_E & m_F & m_G \end{bmatrix}^T$$

where $\underline{v}$ and $\underline{i}$ are the 7-dimensional phase voltage and current vectors; $\underline{m}$ is the conversion factor vector; V_{DC} and I_{DC} are the voltage and current of the DC bus, respectively.

Coupling 1 (coupling element):

$$\begin{cases} \underline{v}_{dq} = \left[\boldsymbol{T}_{\boldsymbol{Park}}\right]\left[\boldsymbol{T}_{\boldsymbol{Clarke}}\right]\underline{v} \\ \underline{i} = \left[\boldsymbol{T}_{\boldsymbol{Clarke}}\right]^{-1}\left[\boldsymbol{T}_{\boldsymbol{Park}}\right]^{-1}\underline{i}_{dq} \end{cases} \tag{2.4}$$

with

$$\underline{v}_{dq} = \begin{bmatrix} v_{d1} & v_{q1} & v_{d9} & v_{q9} & v_{d3} & v_{q3} & v_z \end{bmatrix}^T$$

$$\underline{v}_{dq1} = \begin{bmatrix} v_{d1} & v_{q1} \end{bmatrix}^T;\ \underline{v}_{dq2} = \begin{bmatrix} v_{d9} & v_{q9} \end{bmatrix}^T;\ \underline{v}_{dq3} = \begin{bmatrix} v_{d3} & v_{q3} \end{bmatrix}^T$$

$$\underline{i}_{dq} = \begin{bmatrix} i_{d1} & i_{q1} & i_{d9} & i_{q9} & i_{d3} & i_{q3} & i_z \end{bmatrix}^T$$

$$\underline{i}_{dq1} = \begin{bmatrix} i_{d1} & i_{q1} \end{bmatrix}^T;\ \underline{i}_{dq2} = \begin{bmatrix} i_{d9} & i_{q9} \end{bmatrix}^T;\ \underline{i}_{dq3} = \begin{bmatrix} i_{d3} & i_{q3} \end{bmatrix}^T$$

where $\underline{v}_{dq}$ and $\underline{i}_{dq}$ are the 7-dimensional voltage and current vectors in d-q frames, respectively; ($\underline{v}_{dq1}$, $\underline{v}_{dq2}$, $\underline{v}_{dq3}$) and ($\underline{i}_{dq1}$, $\underline{i}_{dq2}$, $\underline{i}_{dq3}$) are the 2-dimensional voltage and current vectors of fictitious machines FM1, FM2 and FM3 in d-q frames, respectively; v_z and i_z are the voltage and current of zero-sequence ZM, respectively.

Fictitious machines (accumulation and conversion elements):

$$\begin{cases} \underline{i}_{dqj} = \left(\underline{v}_{dqj} - \underline{e}_{dqj}\right)\dfrac{1}{L_j s + R_s} \\ T_j = \dfrac{\underline{i}_{dqj}\,\underline{e}_{dqj}^T}{\Omega} \\ i_z = \left(v_z - e_z\right)\dfrac{1}{L_z s + R_s} \\ T_z = \dfrac{i_z e_z}{\Omega} \end{cases} \quad \text{with } j \in [1,3] \subset \mathbb{N}_0 \tag{2.5}$$

with

$$\underline{e}_{dq} = \begin{bmatrix} e_{d1} & e_{q1} & e_{d9} & e_{q9} & e_{d3} & e_{q3} & e_z \end{bmatrix}^T$$

$$\underline{e}_{dq1} = \begin{bmatrix} e_{d1} & e_{q1} \end{bmatrix}^T;\ \underline{e}_{dq2} = \begin{bmatrix} e_{d9} & e_{q9} \end{bmatrix}^T;\ \underline{e}_{dq3} = \begin{bmatrix} e_{d3} & e_{q3} \end{bmatrix}^T$$

where $\underline{e}_{dq}$ is the back-EMF vector in d-q frames; L_j and L_z are the inductances of the fictitious machines in d-q frames calculated as in (1.5); R_s is the stator winding resistance of one phase; s is the Laplace operator; T_j and T_z are the torques of the fictitious machines; Ω is the rotating speed of the machine.

Coupling 2 (coupling element):

$$T_{em} = T_1 + T_2 + T_3 + T_z \tag{2.6}$$

where the electromagnetic torque of the machine T_{em} is equal to the sum of torques of the fictitious machines (T_1, T_2, T_3, T_z).

Shaft (accumulation element):

$$\Omega = (T_{em} - T_{load}) \frac{1/f_m}{(J_m/f_m)s + 1} \tag{2.7}$$

where T_{load} is the load torque applied to the machine; f_m is the friction coefficient of the rotor-load bearings; J_m is the moment of inertia of the electric drive and mechanical load.

2.1.2.B. *The representation of the electric drive control*

The control scheme will be designed according to the model representation with the principle of inversion. Indeed, the control elements are determined based on the inversion of their corresponding models with three inversion rules as follows:

1) Conversion elements are directly inverted from their corresponding models.
2) Accumulation elements require closed-loop controls with controllers. The pictograms of these controllers are light blue parallelograms with oblique lines.
3) Inversions of coupling elements may require criterion inputs which lead to a strategy of the energy management (in blue parallelograms).

The control structure of the studied seven-phase drive with speed and current control is described in Fig. 2.4 where all control elements are presented in light blue parallelograms. More descriptions about EMR elements are presented in **Appendix A** of this doctoral thesis.

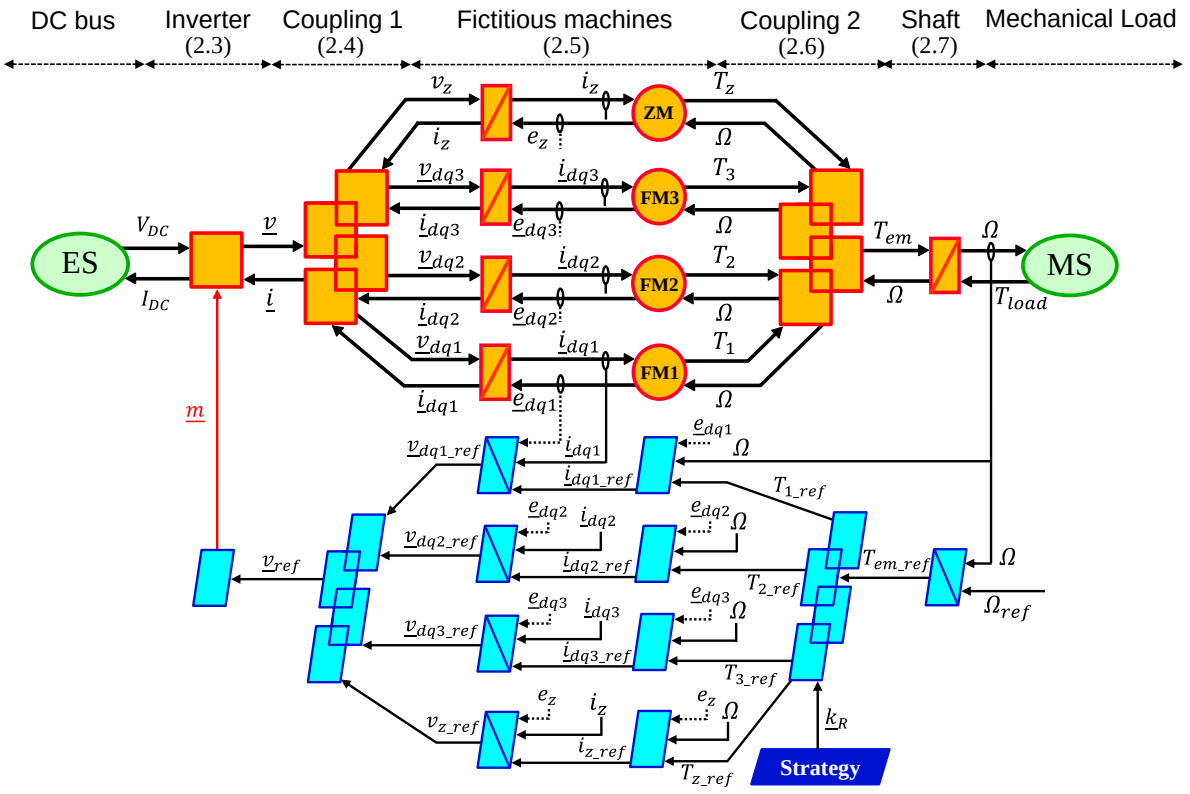

Fig. 2.4. The general control scheme of a seven-phase PMSM drive with speed and current control represented by EMR.

The close-loop control of speed and currents can be implemented with PI or other advanced controllers. From the speed reference Ω_{ref}, torque reference T_{em_ref} is calculated by the speed controller.

When no electrical constraints on voltage and current are considered, current references can be generally calculated as in (2.8) by using the vectorial approach, also called Maximum Torque Per Ampere (MTPA), as introduced in [121]. Then, current references for each fictitious machine can be determined as follows:

$$\underline{i}_{ref} = \frac{T_{em\_ref}\,\Omega}{\|\underline{e}\|^2}\underline{e} \tag{2.8}$$

$$\underline{i}_{dq\_ref} = [\boldsymbol{T_{Park}}][\boldsymbol{T_{Clarke}}]\underline{i}_{ref} \tag{2.9}$$

with

$$\underline{i}_{dq\_ref} = \begin{bmatrix} i_{d1\_ref} & i_{q1\_ref} & i_{d9\_ref} & i_{q9\_ref} & i_{d3\_ref} & i_{q3\_ref} & i_{z\_ref} \end{bmatrix}^T$$

$$\underline{i}_{dq1\_ref} = \begin{bmatrix} i_{d1\_ref} & i_{q1\_ref} \end{bmatrix}^T;\ \underline{i}_{dq2\_ref} = \begin{bmatrix} i_{d9\_ref} & i_{q9\_ref} \end{bmatrix}^T;\ \underline{i}_{dq3\_ref} = \begin{bmatrix} i_{d3\_ref} & i_{q3\_ref} \end{bmatrix}^T$$

where $\|\underline{e}\|$ is the norm of the back-EMF vector $\underline{e}$ in natural frame.

In other words, the total torque reference T_{em_ref} is distributed to fictitious machines (T_{1_ref}, T_{2_ref}, T_{3_ref}, T_{z_ref}) according to the MTPA strategy with repartition coefficient vector $\underline{k}_R$ as follows:

$$\begin{cases} \begin{bmatrix} T_{1\_ref} & T_{2\_ref} & T_{3\_ref} & T_{z\_ref} \end{bmatrix}^T = \underline{k}_R T_{em\_ref} \\ \underline{k}_R = \begin{bmatrix} k_{r1} & k_{r2} & k_{r3} & k_{rz} \end{bmatrix}^T \end{cases} \tag{2.10}$$

$$k_{r1} = \frac{E_1^2}{E_1^2 + E_9^2 + E_3^2 + E_7^2} \tag{2.11}$$

$$k_{r2} = \frac{E_9^2}{E_1^2 + E_9^2 + E_3^2 + E_7^2} \tag{2.12}$$

$$k_{r3} = \frac{E_3^2}{E_1^2 + E_9^2 + E_3^2 + E_7^2} \tag{2.13}$$

$$k_{rz} = \frac{E_7^2}{E_1^2 + E_9^2 + E_3^2 + E_7^2} \tag{2.14}$$

where E_h is the amplitude of h^{th} harmonic of the back-EMFs; the 1st harmonic of the back-EMFs is considered in the first fictitious machine; the 9th harmonic is considered in the second machine instead of the 5th harmonic; the 3rd harmonic is in the third machine while the 7th harmonic is in the zero-sequence machine.

Then, current references for all fictitious machines in d-q frames are given by:

$$\begin{cases} \underline{i}_{dqj\_ref} = \dfrac{T_{j\_ref}\,\Omega}{\left\|\underline{e}_{dqj}\right\|^2}\,\underline{e}_{dqj} \\ i_{z\_ref} = \dfrac{T_{z\_ref}\,\Omega}{e_z} \end{cases} \quad \text{with } j \in [1,3] \subset \mathbb{N}_0 \tag{2.15}$$

where $\left\|\underline{e}_j\right\|$ is the norm of the back-EMF vector $\underline{e}_j$ of the fictitious machine j.

In variable torque/speed applications such as automotive, the determination of the electromagnetic torque reference depends on constraints (limits of currents and voltages, for example) and optimizations (high efficiency, high torque quality, and minimum copper losses, for example). Therefore, in this study, the torque generation with the current control loop at each rotating speed is considered. In a multiphase machine, as the torque is the sum of torques generated by fictitious machines, a strategy of the torque repartition that considers the above constraints and optimizations must be defined by $\underline{k}_R$, as described in Fig. 2.5.

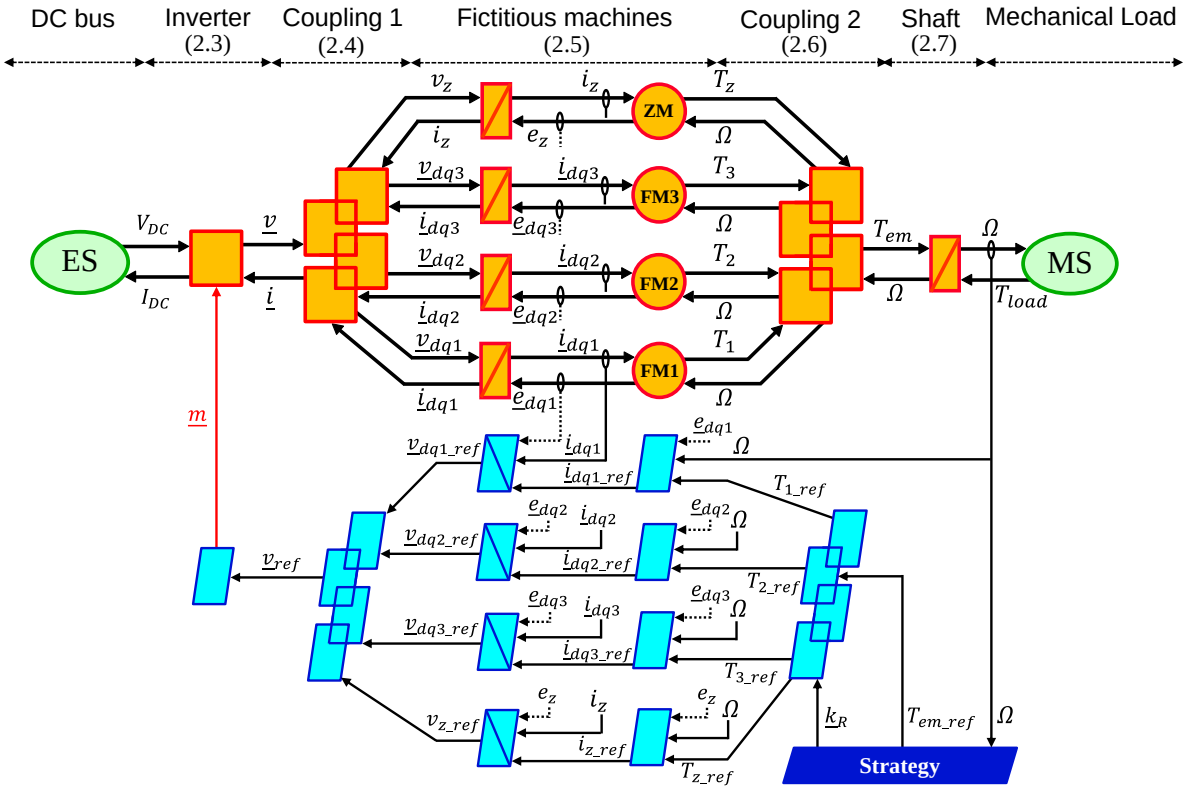

Fig. 2.5. The control scheme of a seven-phase PMSM drive with current control represented by EMR.

2.1.3. Control scheme with an optimal control strategy under constraints on RMS current and peak voltage in healthy mode

Developed from the control scheme in Fig. 2.5, an optimal strategy in which the electromagnetic torque is maximized under constraints on current and voltage is considered to determine current references. In fact, the constraint on peak phase currents has been considered in [87] for five-phase sinusoidal machines. The peak current limit can be defined from rated parameters of VSI components. However, in this doctoral thesis, the concern about the RMS current limit is preferred for a long-term operation of the drive for good efficiency without any

overheated machine windings. The thermal issue is more important when the drive is covered and placed in a limited space of EVs. By using this optimal control strategy, flux-weakening operations are also guaranteed. The details of the optimal strategy are described as follows:

$$\begin{cases} Maximize(T_{em}) \\ v_j(t) \le V_{lim} \\ RMS\{i_j(t)\} \le I_{RMS\_lim} \end{cases} \quad \text{with } j = [A, B, C, D, E, F, G] \tag{2.16}$$

where $v_j(t)$ and $i_j(t)$ are the instantaneous voltage and current of phase j; V_{lim} is the limit of peak phase voltages; I_{RMS_lim} is the limit of RMS phase currents.

Determinations of V_{lim} and I_{RMS_lim} can be explained as follows:

1) Conventionally, in a wye-connected stator winding machine, the limit of the peak phase voltages V_{lim} is roughly equal to a half of the DC-bus voltage in the PWM technique. In an open-end winding configuration (H-bridge), V_{lim} can be equal to the DC-bus voltage. The voltage limit for the offline optimization, denoted by V_{lim_opt}, can be chosen to be smaller than the value of V_{lim} due to the imperfection of the experimental systems.
2) RMS current limit I_{RMS_lim} is associated with the maximum thermal limit of stator windings and permanent magnets. Thus, I_{RMS_lim} can be defined from the rated RMS current. If the RMS current limit is respected in all phases, the winding insulation will be guaranteed for a long-term operation of the drive.

The control scheme with the optimal strategy in (2.16) to maximize torques under constraints on RMS current and peak voltage for healthy mode is described in Fig. 2.6. The details of the optimal strategy are explained as follows:

1) A current calculation method (MTPA, for example) providing the way to define current references is combined with an offline optimization.
2) The offline optimization with *fmincon* function is used to determine proper current references that generate maximal torques under constraints on current and voltage as described in (2.16). The *fmincon* function is a nonlinear programming solver in MATLAB to find the minimum or maximum value of a constrained nonlinear multivariable function [160].
3) After calculations in the offline optimization, optimal d-q current references $\underline{i}_{dq\_opt}$ are stored in a look-up table with their corresponding rotating speed Ω. These stored current references will be selected for current control according to the rotating speed of the drive.

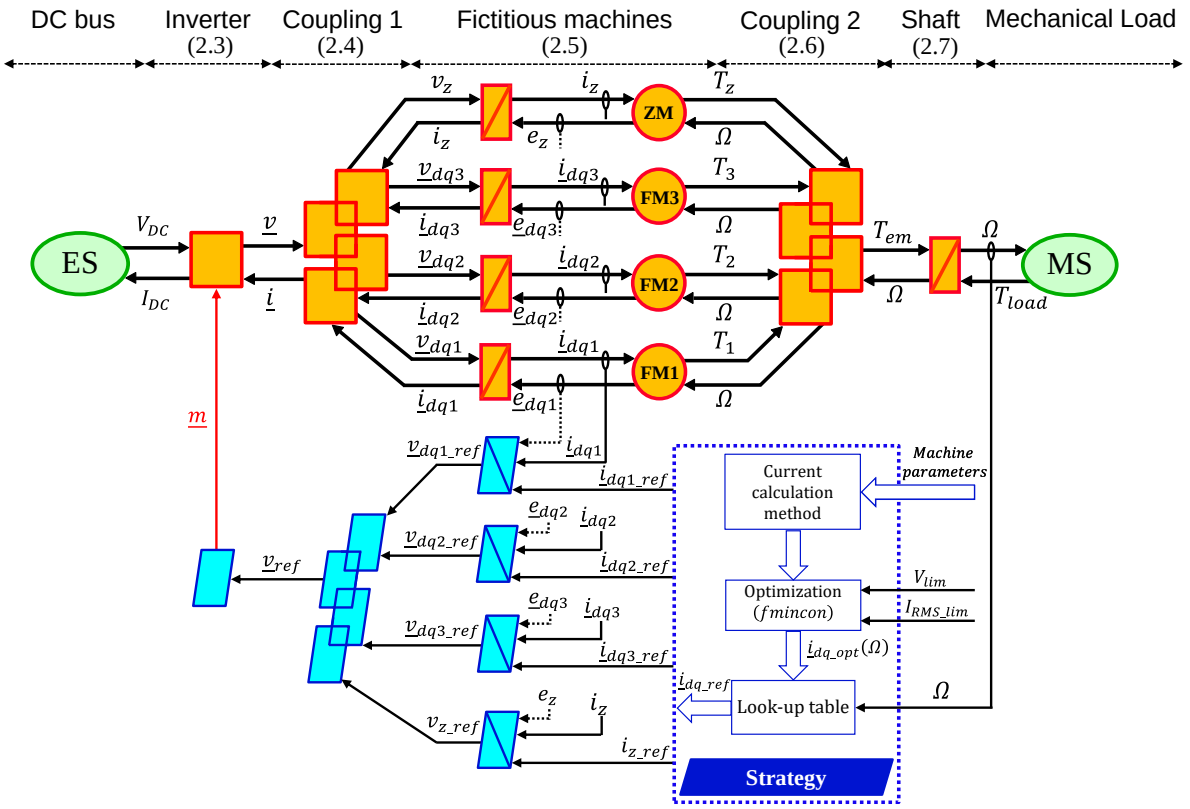

Fig. 2.6. The control scheme of a seven-phase PMSM drive in healthy mode with the optimal control strategy under constraints on RMS current and peak voltage, represented by EMR.

2.1.4. Control performances of a seven-phase PMSM drive in healthy mode

2.1.4.A. *Assumptions and experimental setup descriptions*

To control in healthy mode, there are several assumptions for the considered seven-phase PMSM drive as follows:

1) The machine windings are wye-connected; hence, the current control of the zero-sequence machine is unnecessary because its current is always zero.
2) The control scheme in Fig. 2.6 is used with the aim of maximizing the electromagnetic torque under constraints on RMS current and peak voltage. PI controllers are used for the current control loop. MTPA strategy combined with the offline optimization is applied to calculate current references.
3) The saturation of magnetic circuits is not considered in calculations of back-EMFs and fluxes.

The control scheme in Fig. 2.6 is verified by an experimental electric drive as shown in Fig. 2.7. Electrical parameters of the drive are described in Table 2.2. The experimental seven-phase PMSM is mechanically connected to a load drive that is an industrial three-phase synchronous machine. The load drive is controlled to tune the speed of the seven-phase machine. A voltage source inverter (VSI) with seven legs of Insulated Gate Bipolar Transistor (IGBT) is used to supply the seven-phase machine. A dSPACE 1005 board with I/O interface is used to transfer PWM signals (10 kHz) to the IGBT driver of the inverter and collect measured data of speed and currents.

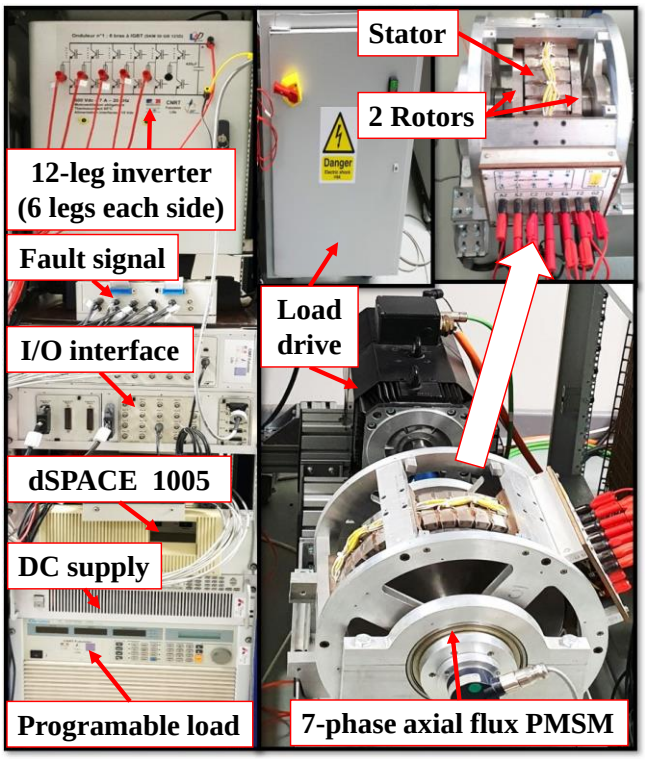

Fig. 2.7. Experimental test bench of the seven-phase PMSM drive.

Table 2.2. Electrical parameters of the experimental seven-phase PMSM drive.

Parameter	**Unit**	**Value**
Stator resistance R_s	Ω	1.4
Self-inductance L	mH	14.7
Mutual inductance M_1	mH	3.5
Mutual inductance M_2	mH	-0.9
Mutual inductance M_3	mH	-6.1
1st harmonic of the speed-normalized back-EMF	V/rad/s	1.265
3rd harmonic of back-EMF over 1st harmonic	%	32.3
9th harmonic of back-EMF over 1st harmonic	%	12.5
Number of pole pairs p		3
Rated RMS current of seven-phase PMSM	A	5.1
DC-bus voltage V_{DC}	V	200
Maximum calculation time	µs	350
PWM frequency	kHz	10
The friction coefficient of the rotor-load bearings f_m	Nm/(rad/s)	0.1
The moment of inertia of the electric drive and mechanical load J_m	kg.m^2	0.02

The experimental seven-phase PMSM is introduced in [161, 162]. This machine has an axial flux with double rotors. Different configurations of the double rotors result in several back-EMF waveforms. For example, when the two rotors have different numbers of poles and spatially shifted an angle of 7 degrees, the back-EMF waveform and its harmonic spectrum are presented in Fig. 2.8. Besides the 1st harmonic of the back-EMFs, the 9th and 3rd harmonics account for the highest proportions (12.5 and 32.3% of the 1st harmonic, respectively). Each of these harmonics present in one fictitious machine. Several minor harmonics in fictitious machines can be described as follows:

1) In FM1, besides the 1st harmonic, the 13th harmonic is equal to 5.02% of the 1st harmonic.
2) In FM2, besides the 9th harmonic, the 19th harmonic is equal to 1.98% of the 1st harmonic.

3) In FM3, besides the 3rd harmonic, the 11th harmonic is equal to 10.3% of the 1st harmonic. Proportions of other harmonics are trivial.
4) In ZM, the 7th and 21st harmonics are equal to 9.4 and 3.2% of the 1st harmonic. If the machine windings are wye-connected, these harmonics have no effects on currents and torques.

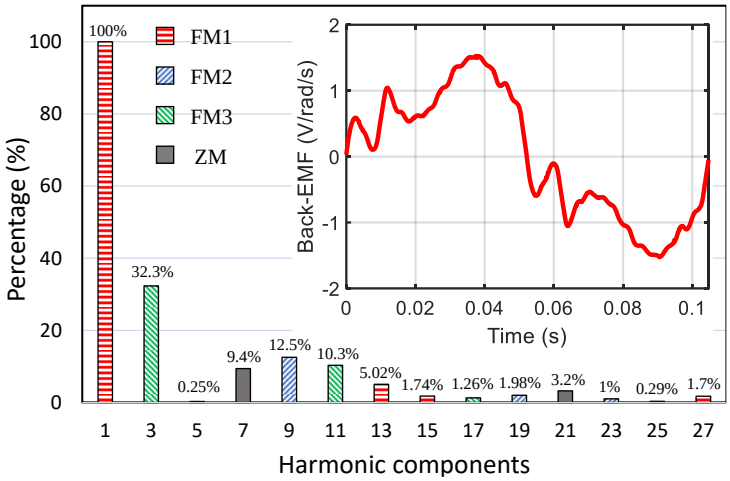

Fig. 2.8. The measured speed-normalized back-EMF and harmonic spectrum of the experimental seven-phase PMSM.

2.1.4.B. *Optimal calculations under constraints on RMS current and peak voltage*

In the control scheme in Fig. 2.6, the offline optimization based on (2.16) considers only the main harmonics of the back-EMFs including 1st, 3rd, and 9th. Therefore, the calculated (optimal) torque in healthy mode is constant when the 1st, 3rd, and 9th harmonics of current are imposed.

The constraints on RMS current and peak voltage can be specified based on parameters of the considered drive (see Table 2.2) as follows:

1) The rated RMS phase current is 5.1 A; hence, the RMS current limit I_{RMS_lim} is selected to be 5.1 A.
2) The VSI is fed by a DC-bus voltage V_{DC} of 200 V; hence, the limit of phase voltage references V_{lim} is 100 V, equal to a half of V_{DC}. However, high-order harmonics of the considered experimental back-EMFs (11th, 13th, and 19th, for example) may cause additional values to phase voltage references. Therefore, to respect the peak voltage limit V_{lim} in experiments, the peak voltage limit for the offline optimization V_{lim_opt} is selected to be 75 V based on simulation assessments.

The optimal torque-speed characteristic is shown in Fig. 2.9a with a speed range from 0 to 73 rad/s and the base speed of 38 rad/s. The torque before the base speed is 33.3 Nm and reduces after the base speed to respect the considered constraints.

In healthy mode, phase currents as well as phase voltages are identical in all phases. Therefore, the RMS currents of all phases at a speed are equal to the highest RMS current among all phases, denoted by I_{RMS}. Thanks to the offline optimization, current references are determined so that I_{RMS} is equal to I_{RMS_lim} (5.1 A) at every speed as shown in Fig. 2.9b. In addition, the peak voltages of all phases at a speed are equal to the highest peak voltage among all phases, denoted

by V_{peak}. The value of V_{peak} is less than or equal to voltage limit V_{lim_opt} even at high speed as shown in Fig. 2.9c. Therefore, a flux-weakening operation of the drive can be performed.

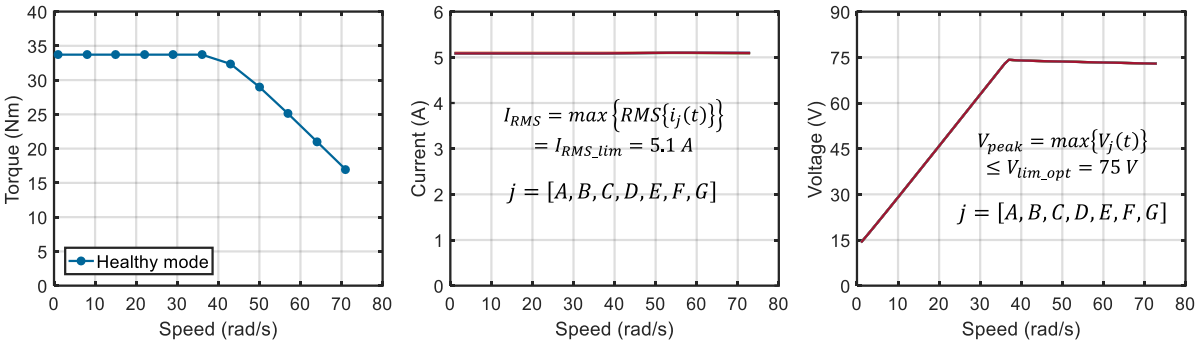

(a) (b) (c)

Fig. 2.9. (Calculated result) Optimal torque-speed characteristic (a), all RMS phase currents (b), and all peak phase voltages (c) in terms of speed under constraints on RMS current and peak voltage in healthy mode.

2.1.4.C. *Verification with experimental results for healthy mode*

2.1.4.C.1. Current control performance:

To obtain the torque-speed characteristic as the optimal result in Fig. 2.9a, six d-q currents obtained from seven measured phase currents need to properly track their constant references at every speed. These current references are calculated from the offline optimization in Fig. 2.6 as discussed in **section 2.1.4.B**. Currents in (d_1-q_1) frame that create most of the torque are well controlled as described in Fig. 2.10.

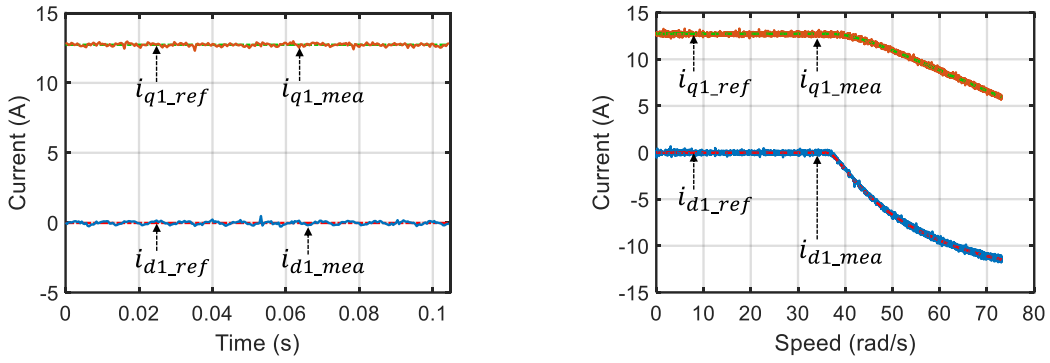

(a) (b)

Fig. 2.10. (Experimental result) Currents in (d_1-q_1) frame in terms of time at 20 rad/s with i_{d1_ref}=0 A and i_{q1_ref}=12.7 A (a), and in terms of speed (b) in healthy mode.

However, in Figs. 2.11-2.12, measured currents in both (d_9-q_9) and (d_3-q_3) frames, generating minor torques, are time-variant with a main frequency of 14θ even though their references are constant. These current harmonics in (d_9-q_9) and (d_3-q_3) frames are generated by unwanted harmonics (11^{th} and 19^{th}, for example) of the experimental back-EMF and by the inverter nonlinearity. This issue will be more explained in **sections 3.2.1** and **3.2.2** of **Chapter 3** of this doctoral thesis.

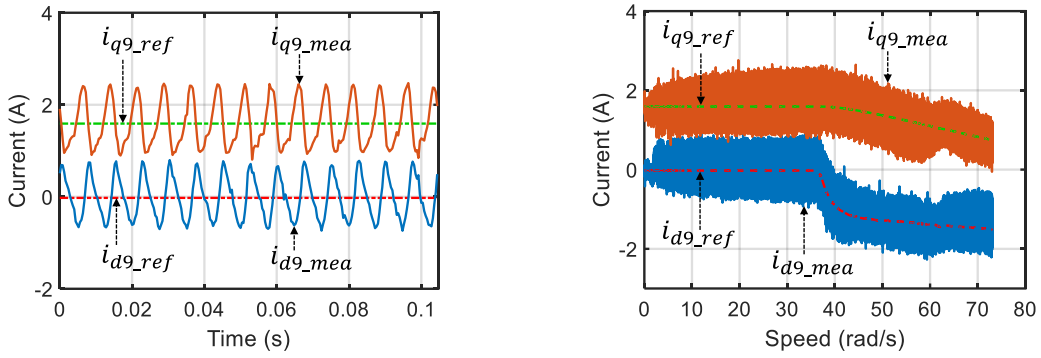

(a) (b)

Fig. 2.11. (Experimental results) Currents in (d_9-q_9) frame in terms of time at 20 rad/s with i_{d9_ref}=0 A and i_{q9_ref}=1.6 A (a), and in terms of speed (b) and in healthy mode.

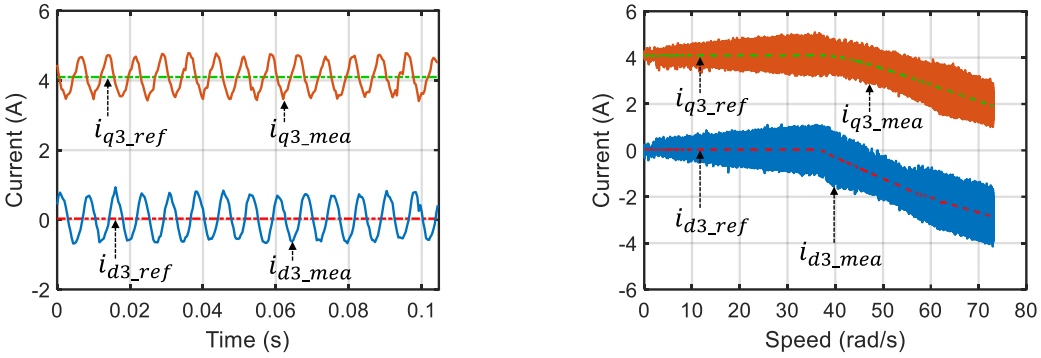

(a) (b)

Fig. 2.12. (Experimental result) Currents in (d_3-q_3) frame in terms of time at 20 rad/s with i_{d3_ref}=0 A and i_{q3_ref}=4.1 A (a), and in terms of speed (b) in healthy mode.

2.1.4.C.2. Torque performance:

In healthy mode, the total torque is mainly generated by three dominant harmonic components of back-EMFs (1st, 3rd, and 9th) and corresponding current harmonics. If the back-EMF values are ideally constant in d-q frames, the constant torque will be generated by constant d-q currents. It means that the back-EMFs should contain only one harmonic per reference frame for the best performance [35]. However, the considered experimental back-EMFs contain more than one harmonic per frame (see Fig. 2.8), causing torque ripples in healthy mode. In this doctoral thesis, a torque ripple ΔT is given by:

$$\Delta T = \frac{max(T_{em}) - min(T_{em})}{T_{ave}} 100\% \tag{2.17}$$

where $max(T_{em})$ and $min(T_{em})$ are maximum and minimum values of the instantaneous electromagnetic torque T_{em}, respectively; T_{ave} is the average torque.

In addition, in this doctoral thesis, experimental torques are estimated values calculated from measured currents and estimated back-EMFs, denoted by T_{em_exp}. Meanwhile, optimal torques are calculated values obtained from the offline optimization as shown in Fig. 2.9a of **section 2.1.4.B**, denoted by T_{em_opt}.

The total torque and the fictitious machine torques at 20 rad/s in healthy mode are shown in Fig. 2.13a. The optimal torque (T_{em_opt}) is constant at 33.3 Nm while the experimental total torque (T_{em_exp}) has an average value of 33.5 Nm and a ripple of 12% at a main frequency of

14θ. These ripples are caused by the interactions between current harmonics and unwanted back-EMF harmonics. For example, the 1st harmonic of currents interacts with the 13th harmonic of back-EMFs, and the 3rd harmonic of currents interacts with the 11th harmonic of back-EMFs. A ripple-free torque can be possible by applying the MTPA strategy as described in (2.8). However, all d-q current references for control are no longer constant, possibly making PI controllers less effective at high speed. A viable solution with an ADALINE will be presented in **section 3.2.3** of **Chapter 3** of this doctoral thesis. In Fig. 2.13a, the torques in first, second and third fictitious machines (T_{1_exp}, T_{2_exp}, T_{3_exp}) are proportional to their amplitudes in the back-EMF harmonic spectrum. Therefore, FM1 generates the highest torque (T_{1_exp}) then FM3 (T_{3_exp}).

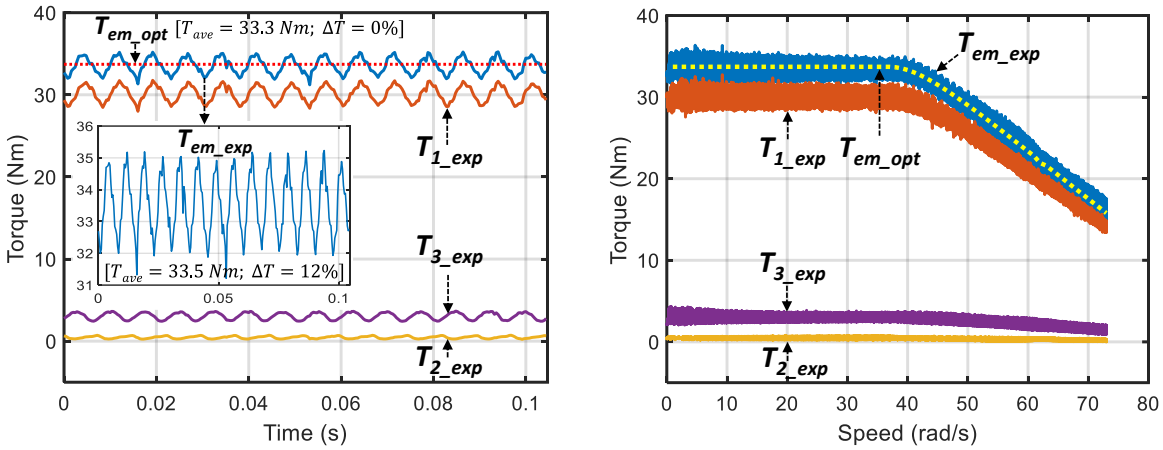

Fig. 2.13. (Experimental result) Torques in terms of time at 20 rad/s (a), and torque-speed characteristics (b) in healthy mode.

Fig. 2.13b presents the torque-speed characteristic in a speed range from 0 to 73 rad/s with the base speed at 38 rad/s. The experimental torque T_{em_exp} is in good accordance with the optimal value T_{em_opt} as obtained in **section 2.1.4.B** and equal to the sum of fictitious machine torques.

2.1.4.C.3. Constraints on RMS current and peak voltage:

In Fig. 2.14, all measured phase currents always respect their constraint even in the flux-weakening region (38 to 73 rad/s). Indeed, the RMS current of all phases (I_{RMS}) that is directly calculated from the measured phase currents in real time is stably controlled at 5.1 A, equal to I_{RMS_lim}. It means that the local thermal limit of each phase winding can be guaranteed in a long-term speed-variable operation. Fig. 2.14 also shows a variation of the measured current waveform before and after the base speed of 38 rad/s. Current waveforms at two investigated speeds (20 and 55 rad/s) are totally different but have the same RMS value.

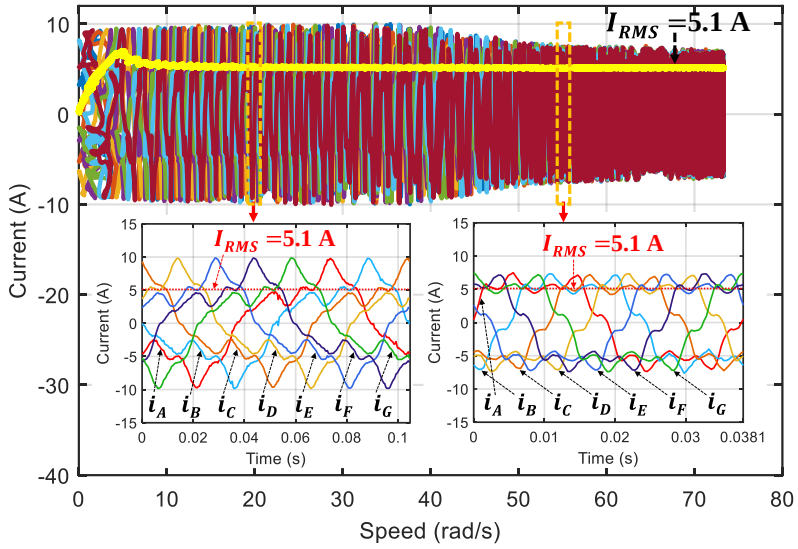

Fig. 2.14. (Experimental result) Phase currents in terms of speed, and current waveforms at 20 and 55 rad/s in healthy mode.

Similarly, Fig. 2.15 shows that experimental voltage references, known as output signals of current controllers, respect their limit (V_{lim}=100 V) at high speed. It is noted that the voltage limit (V_{lim_opt}=75 V) used for the offline optimization is suitable. Fig. 2.15 shows a change in the voltage reference waveform before and after the base speed (20 and 55 rad/s).

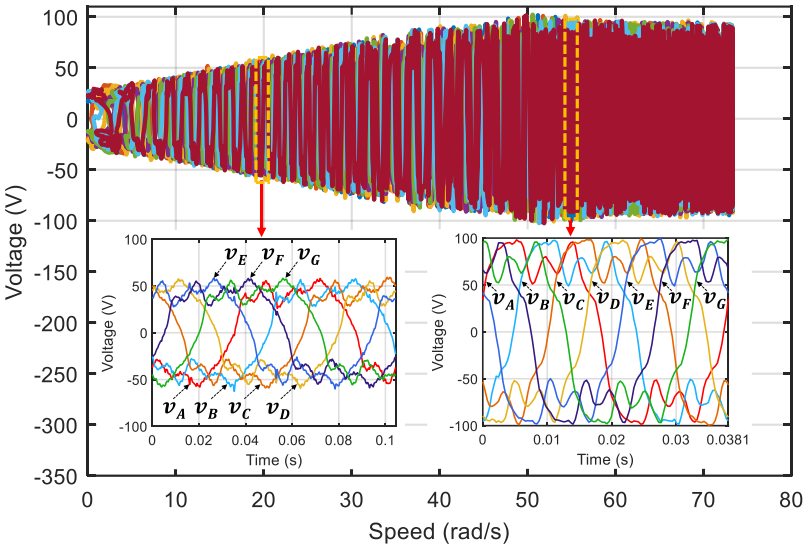

Fig. 2.15. (Experimental result) Phase voltage references in terms of speed, and voltage reference waveforms at 20 and 55 rad/s in healthy mode.

2.1.4.C.4. Comparative summary:

The general comparisons between optimal and experimental results at 20 rad/s are described in Table 2.3. It is noted that the experimental results are in good accordance with the optimal values in terms of the RMS current and total copper loss. The optimal results are obtained from numerical calculations of the offline optimization (see **section 2.1.4.B**). In addition, the experimental average torque is like the optimal average torque. However, the experimental instantaneous torque has a ripple of 12% while the optimal instantaneous torque is time-constant, as previously discussed in the torque performance section.

Notably, in Table 2.3, the experimental peak voltage reference is higher than its optimal value due to extra voltages generated by high-order harmonics in the experimental back-EMFs. This point can verify the necessity of using the peak voltage limit V_{lim_opt}=75 V for the offline optimization instead of V_{lim}=100 V.

Table 2.3. Comparisons between optimal and experimental results in healthy mode under constraints on RMS current and peak voltage at 20 rad/s.

Type of results	**RMS current I_{RMS}**	**Torque T_{em}**		**Peak voltage V_{peak}**	**Total copper loss P_{loss}**
	(A)	T_{ave} (Nm)	ΔT (%)	(V)	(W)
Optimal (numerical)	5.1	33.3	0	45.9	255
Experimental	5.1	33.5	12	60	255.2

2.2. Control of a multiphase drive in an OC fault without reconfigurations

2.2.1. An OC fault in a seven-phase PMSM drive

In general, an electric drive under OC faults is modeled by considering more constraints on the stator windings of its electric machine [116]. For example, Fig. 2.16 describes three situations causing an OC fault in phase *A* of a seven-phase PMSM drive. The first two situations are when either the line cable or the phase-*A* winding is opened. The last situation is when two switches (s_1 and $\bar{s}_1$) in the inverter leg of phase *A* are simultaneously opened[1].

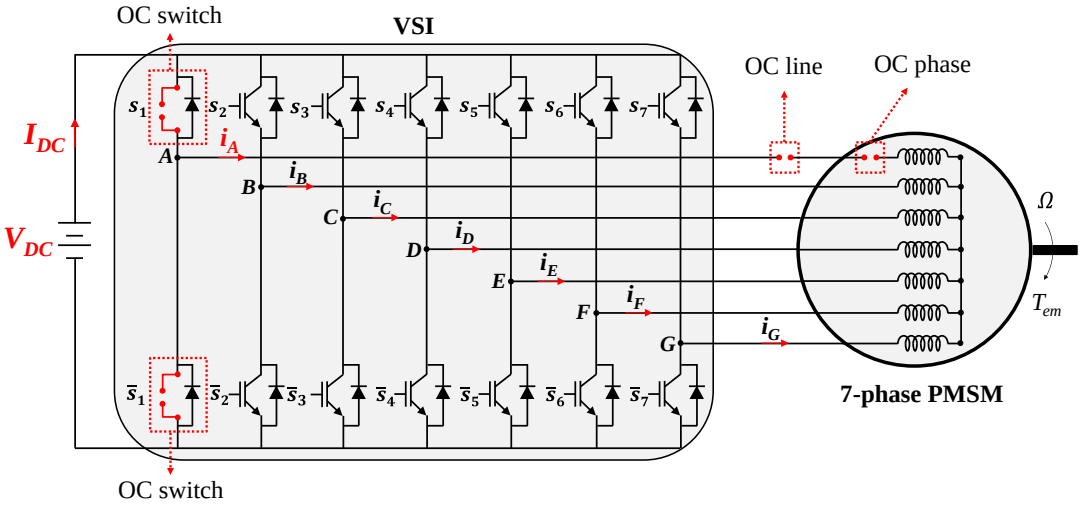

Fig. 2.16. An OC fault happens in phase *A* of a seven-phase PMSM drive.

When the OC fault happens in phase *A*, the current of phase *A* must be zero. The fault reduces the number of DoF of the drive for control. The number of DoF means the number of independent variables that can be used for control. In this work, these variables are phase currents or currents in decoupled reference frames. The decrease in the number of DoF can be explained either in natural frame or in α-β frames (or d-q frames) as follows:

1) In natural frame, the number of DoF is 7 for a seven-phase machine when there are no constraints on stator windings. It means that 7 current references of the seven phases can be independently imposed. If the stator windings are wye-connected, the sum of the seven phase currents must be zero. Therefore, the number of DoF is reduced to 6 in this case. When phase *A* is open-circuited, i_A must be zero, making the number of DoF become 5.
2) In α-β frames, the number of DoF can be explained according to (2.1) for currents. Without any constraints on stator windings, the number of DoF is 7. It means that 7 currents in α-β frames can be independently imposed. When the stator windings are wye-connected, the zero-sequence current i_h must be zero. Therefore, only 6 α-β currents can be independently imposed, reducing the number of DoF to 6. If an OC fault happens in phase *A*, i_A must be zero; hence, after applying the inversion property of Clarke matrix in (1.6), the current transformation in (2.1) becomes:

[1] SC faults of switches normally lead to OC faults with the inner protection of the switches [111] as discussed in **section 1.3.2.A** of **Chapter 1**.

$$\begin{bmatrix} 0 \\ i_B \\ i_C \\ i_D \\ i_E \\ i_F \\ i_G \end{bmatrix} = \sqrt{\frac{2}{7}} \begin{bmatrix} 1 & 0 & 1 & 0 & 1 & 0 & 1/\sqrt{2} \\ \cos(\delta) & \sin(\delta) & \cos(2\delta) & \sin(2\delta) & \cos(3\delta) & \sin(3\delta) & 1/\sqrt{2} \\ \cos(2\delta) & \sin(2\delta) & \cos(4\delta) & \sin(4\delta) & \cos(6\delta) & \sin(6\delta) & 1/\sqrt{2} \\ \cos(3\delta) & \sin(3\delta) & \cos(6\delta) & \sin(6\delta) & \cos(9\delta) & \sin(9\delta) & 1/\sqrt{2} \\ \cos(4\delta) & \sin(4\delta) & \cos(8\delta) & \sin(8\delta) & \cos(12\delta) & \sin(12\delta) & 1/\sqrt{2} \\ \cos(5\delta) & \sin(5\delta) & \cos(10\delta) & \sin(10\delta) & \cos(15\delta) & \sin(15\delta) & 1/\sqrt{2} \\ \cos(6\delta) & \sin(6\delta) & \cos(12\delta) & \sin(12\delta) & \cos(18\delta) & \sin(18\delta) & 1/\sqrt{2} \end{bmatrix} \begin{bmatrix} i_{\alpha 1} \\ i_{\beta 1} \\ i_{\alpha 2} \\ i_{\beta 2} \\ i_{\alpha 3} \\ i_{\beta 3} \\ i_z \end{bmatrix} \tag{2.18}$$

$$0 = \sqrt{\frac{2}{7}} \left(i_{\alpha 1} + i_{\alpha 2} + i_{\alpha 3} + \frac{1}{\sqrt{2}} i_z \right) \tag{2.19}$$

Therefore, the currents in α-β frames must respect (2.19). It means that another constraint on α-β currents has been imposed on the drive. As a result, the number of DoF decreases from 6 to 5 as previously explained in natural frame.

In this faulty condition, if current references for the post-fault operation are kept as in healthy mode, the current control will be no longer guaranteed due to the coupling between currents in fictitious machines.

2.2.2. Control performances in an OC fault without reconfigurations

It is assumed that an OC fault happens in phase *A* as discussed in the previous subsection. To see impacts of the OC fault, the experimental drive in **section 2.1.4.A** is used. The OC fault of phase *A* is safely created by sending an interrupting signal from a control interface to the inverter of the drive. This signal helps open simultaneously two IGBTs of the VSI leg of phase *A*, disconnecting phase *A* from the power source.

2.2.2.A. *Current control performance*

As analyzed in **section 2.2.1**, the current control cannot be guaranteed due to the coupling between currents in d-q frames. Current responses in three d-q frames cannot properly track their references at 20 rad/s as presented in Fig. 2.17. Therefore, fault detections and reconfigurations are necessary.

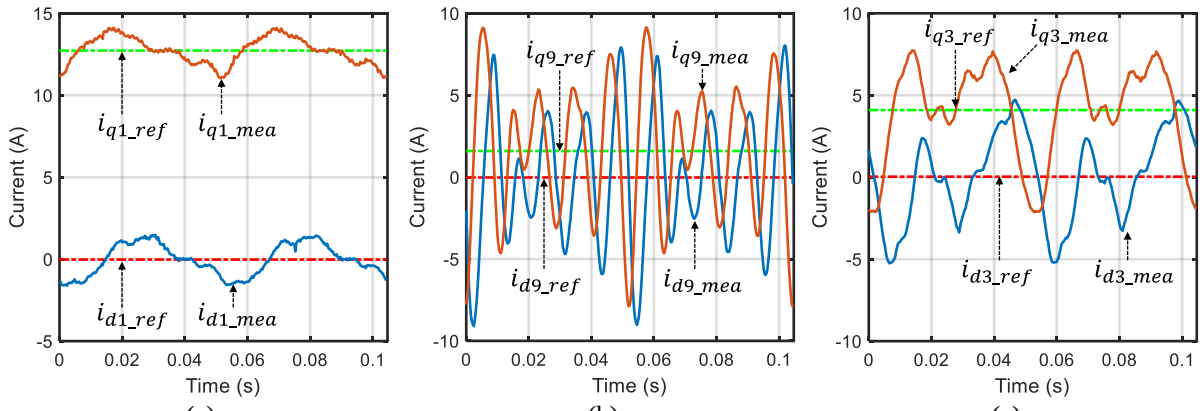

(a) (b) (c)

Fig. 2.17. (Experimental result) Measured currents in (d_1-q_1) frame (a), (d_9-q_9) frame (b), and (d_3-q_3) frame (c) when phase *A* is open-circuited without any reconfigurations at 20 rad/s.

2.2.2.B. *Torque performance*

The distortion of current control reduces the torque quality of the drive. As described in Fig. 2.18, although the average torques are similar, the experimental OC torque ($T_{em\_est\_OC\_No}$) without reconfigurations has a ripple of 50%, much higher than that of the healthy torque ($T_{em\_est\_HM}$) with only 12%.

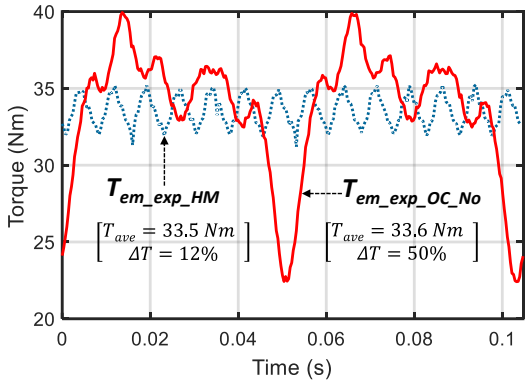

Fig. 2.18. (Experimental result) Torques in healthy mode and when phase *A* is open-circuited without any reconfigurations at 20 rad/s.

2.2.2.C. *Constraints on RMS current*

The post-fault current waveforms of the remaining healthy phases are deteriorated and no longer identical as shown in Fig. 2.19, leading to unequal RMS currents in the remaining phases as shown in Table 2.4. The highest RMS current appears in phase *B* (I_{RMS_B}), increasing about 1.55 times from 5.1 A (Fig. 2.19a) to 7.9 A (Fig. 2.19b). In other words, the RMS current limit I_{RMS_lim} is not respected in the post-fault operation when new current references are not imposed.

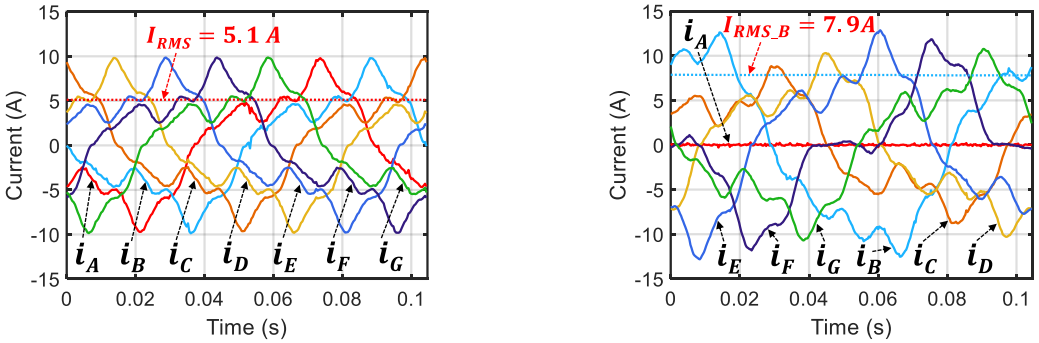

(a) (b)

Fig. 2.19. (Experimental result) Measured phase currents in healthy mode (a), and when phase *A* is open-circuited without any reconfigurations (b), at 20 rad/s.

Table 2.4. Experimental RMS currents in all phases when phase *A* is open-circuited without any reconfigurations at 20 rad/s.

Operating mode	RMS current (A)						
	A	*B*	*C*	*D*	*E*	*F*	*G*
Phase *A* is opened without reconfigurations	0.1	7.9	5	5.7	6.8	5.7	5.8

2.2.2.D. *Comparative summary*

The comparative summary of healthy mode and a faulty mode with an OC fault in phase *A* without reconfigurations is described in Table 2.5. Per unit (pu) based on parameters of healthy mode is applied to evaluate the increase in corresponding parameters under the post-fault operation compared to healthy mode. It is noted that per unit is not used for the torque ripple value because the torque ripple in healthy mode, as a base, can be zero. As previously analyzed, the fault occurrence dramatically increases all important parameters such as the torque ripple (12 to 50%), the highest RMS current (1.55 pu), the highest peak voltage reference (1.74 pu), and the total copper loss (1.27 pu). Therefore, a reconfiguration of the control for the post-fault drive, called fault-tolerant control, is necessary.

Table 2.5. Comparisons between experimental results in healthy mode and when phase *A* is open-circuited without any reconfigurations at 20 rad/s.

Operating mode	**Highest RMS current I_{RMS}**		**Torque T_{em}**			**Highest peak voltage V_{peak}**		**Total copper loss P_{loss}**	
	(A)	(pu)	T_{ave} (Nm)	T_{ave} (pu)	ΔT (%)	(V)	(pu)	(W)	(pu)
Healthy mode	5.1	1	33.5	1	12	60	1	255.2	1
OC fault without reconfigurations	7.9	1.55	33.6	1	50	104.1	1.74	323.7	1.27

pu: per unit where the base values are parameters of healthy mode.

2.3. Fault-tolerant control for a multiphase drive

2.3.1. Introduction to proposed fault-tolerant control methods

From the analyses in **section 2.2**, new current references for post-fault operations need to be defined to avoid the oversizing of the drive. Before proposing fault-tolerant control methods, several assumptions of the considered seven-phase machine are described as follows:

1) Phase windings of the machine are symmetrically distributed in the stator. Constraints on stator winding configurations (such as a wye connection in healthy mode) are removed to have general analyses of fault-tolerant control.
2) In the offline optimization for fault-tolerant control, only the 1st and 3rd harmonics of the back-EMFs are considered to facilitate the offline optimization with theoretical smooth torques. Indeed, the number of DoF for control in the post-fault condition is reduced from 7 to 6 (no constraint on stator winding configurations), or from 6 to 5 (wye-connected stator windings) (see **section 2.2.1**). Therefore, only 4 d-q currents in the first and third fictitious machines that generate most of the torque are usually imposed as constants. Meanwhile, d-q currents in the second fictitious machines are consequently time-variant. As a result, the harmonics of back-EMFs in the second fictitious machine (9th) should not be considered in the offline optimization to theoretically obtain smooth torques.
3) The saturation of magnetic circuits is not considered in calculations of back-EMFs and fluxes.

Owing to the equal spatial displacement of phases, phase *A* is assumed to be open-circuited without loss of generality. Therefore, the current of phase *A* is always equal to zero (i_A=0). Because there are no constraints on stator windings, the number of DoF becomes 6, compared to 7 in healthy mode. In other words, only 6 currents can be independently imposed either in natural frame or decoupled α-β and d-q frames when phase *A* is open-circuited. Similarly, when two phases are open-circuited, there will be 5 currents that can be independently imposed. Fault-tolerant control strategies for two-phase OC faults are presented in **Appendix B**. This chapter will focus on an OC fault in one phase (phase *A*).

Under the considered fault, the transformation of phase currents from natural frame into the decoupled frames is similar to (2.1), (2.4), and (2.9) as follows:

$$\begin{bmatrix} i_{d1} \\ i_{q1} \\ i_{d9} \\ i_{q9} \\ i_{d3} \\ i_{q3} \\ i_z \end{bmatrix} = [\boldsymbol{T}_{\boldsymbol{Park}}] \begin{bmatrix} i_{\alpha 1} \\ i_{\beta 1} \\ i_{\alpha 2} \\ i_{\beta 2} \\ i_{\alpha 3} \\ i_{\beta 3} \\ i_z \end{bmatrix} = [\boldsymbol{T}_{\boldsymbol{Park}}][\boldsymbol{T}_{\boldsymbol{Clarke}}] \begin{bmatrix} 0 \\ i_B \\ i_C \\ i_D \\ i_E \\ i_F \\ i_G \end{bmatrix} \tag{2.20}$$

In this doctoral thesis, new current references in single-phase OC faults are derived by exploiting the transformation equation in (2.20). The general scheme of three methods (I), (II),

and (III) is described in Fig. 2.20 where α-β and d-q frames are equivalent. The principles of these methods are explained as follows:

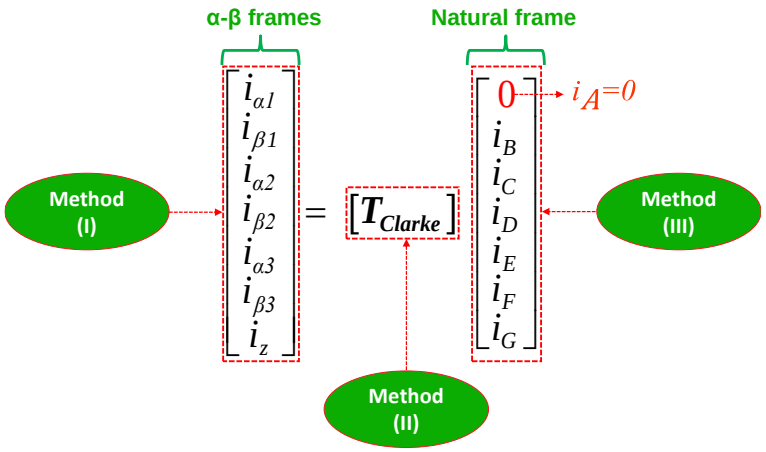

Fig. 2.20. General scheme of the proposed fault-tolerant control methods when phase *A* is open-circuited.

1) *Method (I):* New current references are determined from decoupled α-β or d-q frames to obtain smooth post-fault torques. As a result, currents in natural frame are derived from the determined currents in the decoupled frames. Method (I) is similar to the study in [120] where the current references are calculated from the decoupled α-β frames. However, in this doctoral thesis, method (I) with different possible options is systematically described.
2) *Method (II):* New current references are determined by finding new transformation matrices with a 6-by-6 dimension to obtain smooth post-fault torques. Two current design options will be proposed to provide either control robustness or similar distributions of copper losses in the remaining healthy phases. Method (II) is developed based on the principle in [134] where five-phase non-sinusoidal machines are considered.
3) *Method (III):* New current references are directly determined from natural frame to obtain the waveform uniformity of healthy phase currents, resulting in higher average torques compared to methods (I) and (II) under current limits. Another purpose of method (III) is to distribute equally copper losses to the remaining heathy phases. However, torque ripples with method (III) are inevitable. Method (III) is developed from a solution in [137] where sinusoidal machines are considered with a various number of phases. However, the approach of method (III) in this doctoral thesis is different from the existing study with analytical expressions and more proposed solutions.

Especially, different from [120, 134, 137], in this doctoral thesis, new current references with methods (I), (II) and (III) are required to maximize electromagnetic torques and respect constraints on current and voltage as described in (2.16). Therefore, a control scheme with the optimal strategy under constraints on RMS current and peak voltage for faulty modes in Fig. 2.21 is applied. In fact, the scheme in Fig. 2.21 for faulty mode is developed from the control scheme in Fig. 2.6 for heathy mode by adding fault information (types and positions of faults), and by using method (I), (II) or (III) to calculate current references. Then, new current

references stored in a look-up table can be selected according the fault information and rotating speed. However, the fault detection issue is not within the scope of this doctoral thesis.

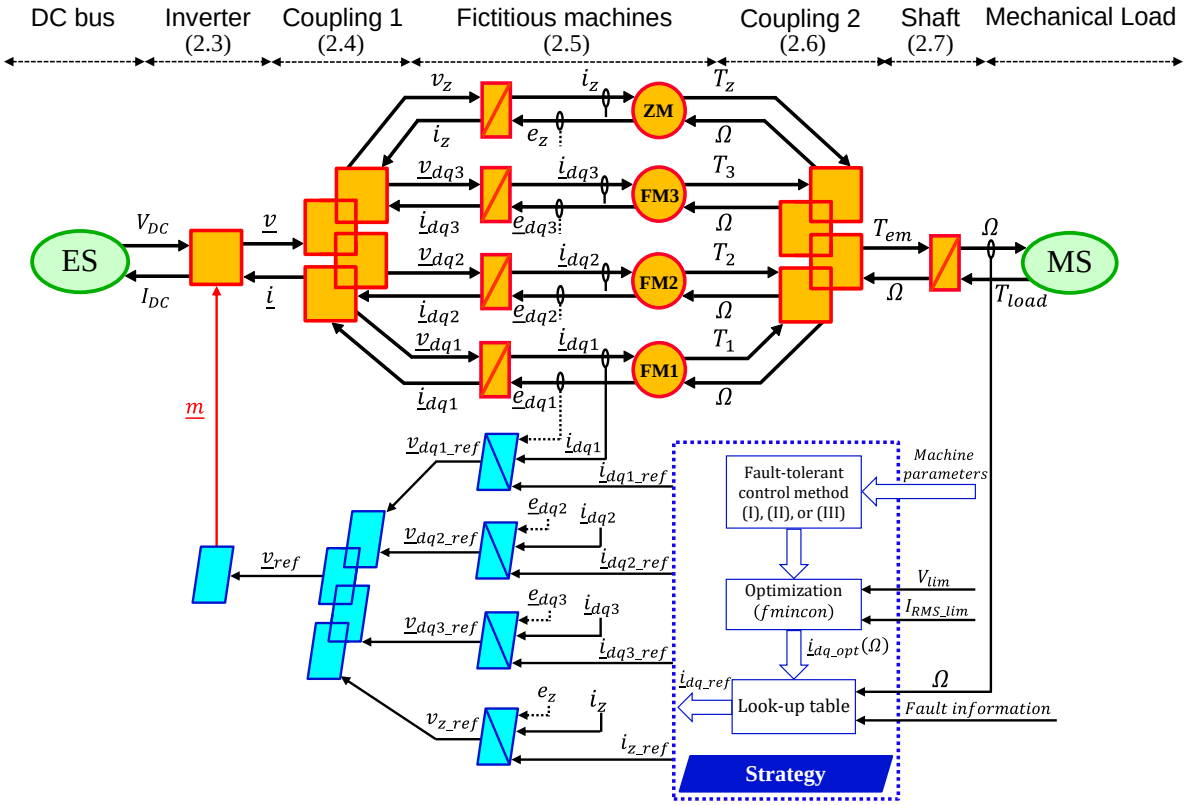

Fig. 2.21. The control scheme of a seven-phase PMSM drive for faulty modes with an optimal control strategy under constraints on current and voltage, represented by EMR.

2.3.2. Method (I): new current references determined from decoupled reference frames

2.3.2.A. *Principle of method (I)*

When phase *A* is open-circuited, six of seven currents in decoupled frames ($i_{\alpha 1}$, $i_{\beta 1}$, $i_{\alpha 2}$, $i_{\beta 2}$, $i_{\alpha 3}$, $i_{\beta 3}$, i_z) or (i_{d1}, i_{q1}, i_{d9}, i_{q9}, i_{d3}, i_{q3}, i_z) can be independently determined, and the last current is consequently derived. Thanks to the relationship between phase currents and decoupled frames in (2.20), currents of the remaining healthy phases can be derived from currents in the decoupled frames.

In the considered non-sinusoidal seven-phase machine, it is assumed that the 1st and 3rd harmonics of the back-EMFs account for the highest proportions, presenting in the first and third fictitious machines, respectively. Other harmonics, 9th for example, exist in small proportions. Therefore, in method (I), the determination of currents in decoupled frames should be based on the following principles:

1) The 1st and 3rd harmonic currents ($i_{\alpha 1}$, $i_{\beta 1}$) and ($i_{\alpha 3}$, $i_{\beta 3}$), creating most of the torque, are chosen to be sinusoidal in α-β frames. Equivalently, these corresponding currents in d-q frames (i_{d1}, i_{q1}) and (i_{d3}, i_{q3}) are constant, facilitating the control with conventional PI controllers at high speed. Therefore, 4 currents ($i_{\alpha 1}$, $i_{\beta 1}$, $i_{\alpha 3}$, $i_{\beta 3}$), equivalent to (i_{d1},

i_{q1}, i_{d3}, i_{q3}), in the first and third machines have been determined. In other words, the first and third harmonic sinusoidal MMFs are guaranteed in each fictitious machine.

2) Among three currents ($i_{\alpha 2}$, $i_{\beta 2}$, i_z), equivalent to (i_{d9}, i_{q9}, i_z), only 2 of the three currents can be independently imposed. The last current is consequently derived from previously determined currents.

From (2.20), the relationship between currents ($i_{\alpha 1}$, $i_{\beta 1}$, $i_{\alpha 3}$, $i_{\beta 3}$) and (i_{d1}, i_{q1}, i_{d3}, i_{q3}) is given by:

$$\begin{bmatrix} i_{\alpha 1} \\ i_{\beta 1} \\ i_{\alpha 3} \\ i_{\beta 3} \end{bmatrix} = \begin{bmatrix} \cos(\theta) & -\sin(\theta) & 0 & 0 \\ \sin(\theta) & \cos(\theta) & 0 & 0 \\ 0 & 0 & \cos(3\theta) & -\sin(3\theta) \\ 0 & 0 & \sin(3\theta) & \cos(3\theta) \end{bmatrix} \begin{bmatrix} i_{d1} \\ i_{q1} \\ i_{d3} \\ i_{q3} \end{bmatrix} \tag{2.21}$$

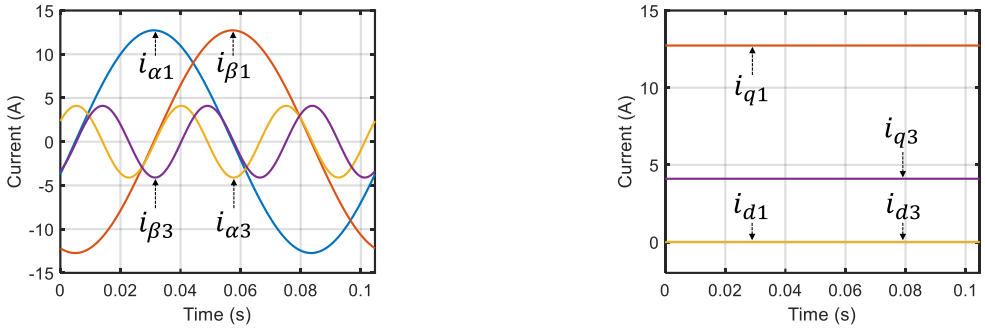

(a) (b)

Fig. 2.22. Desired currents ($i_{\alpha 1}$, $i_{\beta 1}$, $i_{\alpha 3}$, $i_{\beta 3}$) (a), and (i_{d1}, i_{q1}, i_{d3}, i_{q3}) (b), at 20 rad/s with (i_{d1}=0 A, i_{q1}=12.7 A, i_{d3}=0 A, i_{q3}=4.1 A).

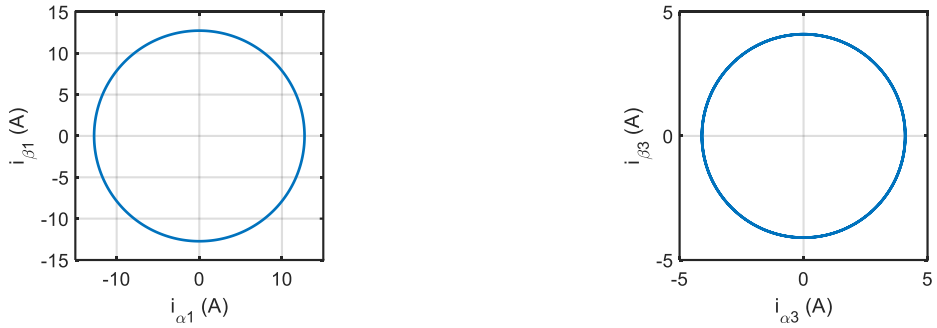

(a) (b)

Fig. 2.23. Circles created by desired currents ($i_{\alpha 1}$, $i_{\beta 1}$) (a), and ($i_{\alpha 3}$, $i_{\beta 3}$) (b).

According to the first principle, desired currents (i_{d1}, i_{q1}, i_{d3}, i_{q3}) are constant, enabling desired currents ($i_{\alpha 1}$, $i_{\beta 1}$, $i_{\alpha 3}$, $i_{\beta 3}$) to be sinusoidal. Indeed, the desired currents ($i_{\alpha 1}$, $i_{\beta 1}$, $i_{\alpha 3}$, $i_{\beta 3}$) and (i_{d1}, i_{q1}, i_{d3}, i_{q3}) are described in Fig. 2.22a and Fig. 2.22b, respectively. Consequently, desired sinusoidal currents ($i_{\alpha 1}$, $i_{\beta 1}$) and ($i_{\alpha 3}$, $i_{\beta 3}$) create two circles as presented in Fig. 2.23. These circular relationships are to describe the first and third harmonic sinusoidal MMFs, creating constant torques.

Finally, there are 3 remaining currents ($i_{\alpha 2}$, $i_{\beta 2}$, i_z) or (i_{d9}, i_{q9}, i_z) to be defined. When the 9th harmonic is considered in the second fictitious machine, the relationship between ($i_{\alpha 2}$, $i_{\beta 2}$, i_z) and (i_{d9}, i_{q9}, i_z) can be expressed by:

$$\begin{bmatrix} i_{d9} \\ i_{q9} \\ i_z \end{bmatrix} = \begin{bmatrix} \cos(9\theta) & \sin(9\theta) & 0 \\ -\sin(9\theta) & \cos(9\theta) & 0 \\ 0 & 0 & 1 \end{bmatrix} \begin{bmatrix} i_{\alpha 2} \\ i_{\beta 2} \\ i_z \end{bmatrix} \tag{2.22}$$

According to the second principle, the number of currents that can be independently imposed is 6, leading to only 2 remaining currents to be imposed. Therefore, only two of three currents ($i_{\alpha 2}$, $i_{\beta 2}$, i_z) can be independently imposed, and the last current will be consequently derived.

Table 2.6. Description of the three options in method (I).

Option	Current design description			Objective
	$i_{\alpha 2}$	$i_{\beta 2}$	i_z	
Method (I)-1	0	0	≠0	Reduce copper losses
Method (I)-2	≠0	0	0	Reduce copper losses
Method (I)-3	≠0	≠0	0	A simple dual three phase system ($i_B+i_D+i_F=0$) and ($i_C+i_E+i_G=0$)

Therefore, in method (I), three options are proposed to define currents ($i_{\alpha 2}$, $i_{\beta 2}$, i_z) as described in Table 2.6. These proposed options can be specified as follows:

1) *Method (I)-1:* Currents in the second machine ($i_{\alpha 2}$, $i_{\beta 2}$) are imposed to be zero, aiming at reducing copper losses. Consequently, the zero-sequence current (i_z) is different from zero. It means that this option is feasible in two cases [163]. The first case is when there is a neutral line connecting the neutral point of the stator windings and the power source. The second one is when the stator windings are configured in an open-end topology.
2) *Method (I)-2:* β-axis current in the second machine ($i_{\beta 2}$) and zero-sequence current (i_z) are imposed to be zero, enabling to reduce copper losses [163]. As a result, α-axis current in the second machine ($i_{\alpha 2}$) is different from zero. This option can be applied without adding the neutral line connection or changing the stator winding topology. The study in [120] applies the vectorial approach to obtain the current references ($i_{\alpha 2}$, $i_{\beta 2}$) with the aim of reducing copper losses. The current references in [120] and method (I)-2 of this doctoral thesis are similar when phase *A* is open-circuited. When other phases are opened, study [120] uses non-zero current references ($i_{\alpha 2}$, $i_{\beta 2}$). In addition, the study in [120] does not consider any constraints on current and voltage as well as flux-weakening operations.
3) *Method (I)-3:* Only zero-sequence current (i_z) is imposed to be zero. The currents ($i_{\alpha 2}$, $i_{\beta 2}$) in the second machine are determined according to a simple dual three phase system ($i_B+i_D+i_F=0$ and $i_C+i_E+i_G=0$) [164, 165]. Like method (I)-2, this option can be applied without adding the neutral line connection or changing the stator winding topology.

It is worth noting that an option with currents ($i_{\alpha 2}= i_z=0$) is an impossible solution due to the coupling in the post-fault condition developled from (2.18)-(2.19) as follows:

$$0=\sqrt{\frac{2}{7}}\left[\left(i_{\alpha 1}+i_{\alpha 3}\right)+\left(i_{\alpha 2}+\frac{1}{\sqrt{2}}i_z\right)\right] \tag{2.23}$$

where $i_{\alpha 1}$ and $i_{\alpha 3}$ are previously imposed as sinusoidal currents; hence, $i_{\alpha 2}$ and i_z cannot be zero at the same time.

The details of methods (I)-1, (I)-2, and (I)-3 will be presented in the following subsections.

2.3.2.B. *Method (I)-1*

With ($i_{\alpha 2}$=$i_{\beta 2}$=0), the current transformation in (2.20) becomes:

$$\begin{bmatrix} 0 \\ i_B \\ i_C \\ i_D \\ i_E \\ i_F \\ i_G \end{bmatrix} = \sqrt{\frac{2}{7}} \begin{bmatrix} 1 & 0 & 1 & 0 & 1 & 0 & 1/\sqrt{2} \\ \cos(\delta) & \sin(\delta) & \cos(2\delta) & \sin(2\delta) & \cos(3\delta) & \sin(3\delta) & 1/\sqrt{2} \\ \cos(2\delta) & \sin(2\delta) & \cos(4\delta) & \sin(4\delta) & \cos(6\delta) & \sin(6\delta) & 1/\sqrt{2} \\ \cos(3\delta) & \sin(3\delta) & \cos(6\delta) & \sin(6\delta) & \cos(9\delta) & \sin(9\delta) & 1/\sqrt{2} \\ \cos(4\delta) & \sin(4\delta) & \cos(8\delta) & \sin(8\delta) & \cos(12\delta) & \sin(12\delta) & 1/\sqrt{2} \\ \cos(5\delta) & \sin(5\delta) & \cos(10\delta) & \sin(10\delta) & \cos(15\delta) & \sin(15\delta) & 1/\sqrt{2} \\ \cos(6\delta) & \sin(6\delta) & \cos(12\delta) & \sin(12\delta) & \cos(18\delta) & \sin(18\delta) & 1/\sqrt{2} \end{bmatrix} \begin{bmatrix} i_{\alpha 1} \\ i_{\beta 1} \\ 0 \\ 0 \\ i_{\alpha 3} \\ i_{\beta 3} \\ i_z \end{bmatrix} \tag{2.24}$$

where the spatial angular displacement δ is $2\pi/7$. Therefore, calculations of zero-sequence current i_z and phase currents (i_B, i_C, i_D, i_E, i_F, i_G) from four main currents ($i_{\alpha 1}$, $i_{\beta 1}$, $i_{\alpha 3}$, $i_{\beta 3}$) are given by:

$$\begin{cases} i_z = -\sqrt{2}\{i_{\alpha 1} + i_{\alpha 3}\} \\ i_B = \sqrt{\frac{2}{7}}\left\{i_{\alpha 1}\cos(\delta) + i_{\beta 1}\sin(\delta) + i_{\alpha 3}\cos(3\delta) + i_{\beta 3}\sin(3\delta) + \frac{1}{\sqrt{2}}i_z\right\} \\ i_C = \sqrt{\frac{2}{7}}\left\{i_{\alpha 1}\cos(2\delta) + i_{\beta 1}\sin(2\delta) + i_{\alpha 3}\cos(6\delta) + i_{\beta 3}\sin(6\delta) + \frac{1}{\sqrt{2}}i_z\right\} \\ i_D = \sqrt{\frac{2}{7}}\left\{i_{\alpha 1}\cos(3\delta) + i_{\beta 1}\sin(3\delta) + i_{\alpha 3}\cos(9\delta) + i_{\beta 3}\sin(9\delta) + \frac{1}{\sqrt{2}}i_z\right\} \\ i_E = \sqrt{\frac{2}{7}}\left\{i_{\alpha 1}\cos(4\delta) + i_{\beta 1}\sin(4\delta) + i_{\alpha 3}\cos(12\delta) + i_{\beta 3}\sin(12\delta) + \frac{1}{\sqrt{2}}i_z\right\} \\ i_F = \sqrt{\frac{2}{7}}\left\{i_{\alpha 1}\cos(5\delta) + i_{\beta 1}\sin(5\delta) + i_{\alpha 3}\cos(15\delta) + i_{\beta 3}\sin(15\delta) + \frac{1}{\sqrt{2}}i_z\right\} \\ i_G = \sqrt{\frac{2}{7}}\left\{i_{\alpha 1}\cos(6\delta) + i_{\beta 1}\sin(6\delta) + i_{\alpha 3}\cos(18\delta) + i_{\beta 3}\sin(18\delta) + \frac{1}{\sqrt{2}}i_z\right\} \end{cases} \tag{2.25}$$

Therefore, all new current references for the OC fault in phase *A* have been determined. It is noted that current i_z is time-variant, making the sum of all phase current references different from zero. Therefore, method (I)-1 can be applicable only when there is a neutral line connecting the neutral point of the wye-connected stator windings and the power source, or only when the stator windings are configured in an open-end topology. In addition, currents in the second fictitious machines (i_{d9}, i_{q9}) for control are always zero according to (2.22). Therefore, method (I)-1 have 6 constant d-q currents for control.

2.3.2.C. *Method (I)-2*

With ($i_{\beta 2}$=i_z=0), the current transformation in (2.20) becomes:

$$\begin{bmatrix} 0 \\ i_B \\ i_C \\ i_D \\ i_E \\ i_F \\ i_G \end{bmatrix} = \sqrt{\frac{2}{7}} \begin{bmatrix} 1 & 0 & 1 & 0 & 1 & 0 & 1/\sqrt{2} \\ \cos(\delta) & \sin(\delta) & \cos(2\delta) & \sin(2\delta) & \cos(3\delta) & \sin(3\delta) & 1/\sqrt{2} \\ \cos(2\delta) & \sin(2\delta) & \cos(4\delta) & \sin(4\delta) & \cos(6\delta) & \sin(6\delta) & 1/\sqrt{2} \\ \cos(3\delta) & \sin(3\delta) & \cos(6\delta) & \sin(6\delta) & \cos(9\delta) & \sin(9\delta) & 1/\sqrt{2} \\ \cos(4\delta) & \sin(4\delta) & \cos(8\delta) & \sin(8\delta) & \cos(12\delta) & \sin(12\delta) & 1/\sqrt{2} \\ \cos(5\delta) & \sin(5\delta) & \cos(10\delta) & \sin(10\delta) & \cos(15\delta) & \sin(15\delta) & 1/\sqrt{2} \\ \cos(6\delta) & \sin(6\delta) & \cos(12\delta) & \sin(12\delta) & \cos(18\delta) & \sin(18\delta) & 1/\sqrt{2} \end{bmatrix} \begin{bmatrix} i_{\alpha 1} \\ i_{\beta 1} \\ i_{\alpha 2} \\ 0 \\ i_{\alpha 3} \\ i_{\beta 3} \\ 0 \end{bmatrix} \tag{2.26}$$

Therefore, calculations of current $i_{\alpha 2}$ and phase currents (i_B, i_C, i_D, i_E, i_F, i_G) from four main currents ($i_{\alpha 1}$, $i_{\beta 1}$, $i_{\alpha 3}$, $i_{\beta 3}$) are described as follows:

$$\begin{cases} i_{\alpha 2} = -\{i_{\alpha 1} + i_{\alpha 3}\} \\ i_B = \sqrt{\frac{2}{7}} \{i_{\alpha 1}\cos(\delta) + i_{\beta 1}\sin(\delta) + i_{\alpha 2}\cos(2\delta) + i_{\alpha 3}\cos(3\delta) + i_{\beta 3}\sin(3\delta)\} \\ i_C = \sqrt{\frac{2}{7}} \{i_{\alpha 1}\cos(2\delta) + i_{\beta 1}\sin(2\delta) + i_{\alpha 2}\cos(4\delta) + i_{\alpha 3}\cos(6\delta) + i_{\beta 3}\sin(6\delta)\} \\ i_D = \sqrt{\frac{2}{7}} \{i_{\alpha 1}\cos(3\delta) + i_{\beta 1}\sin(3\delta) + i_{\alpha 2}\cos(6\delta) + i_{\alpha 3}\cos(9\delta) + i_{\beta 3}\sin(9\delta)\} \\ i_E = \sqrt{\frac{2}{7}} \{i_{\alpha 1}\cos(4\delta) + i_{\beta 1}\sin(4\delta) + i_{\alpha 2}\cos(8\delta) + i_{\alpha 3}\cos(12\delta) + i_{\beta 3}\sin(12\delta)\} \\ i_F = \sqrt{\frac{2}{7}} \{i_{\alpha 1}\cos(5\delta) + i_{\beta 1}\sin(5\delta) + i_{\alpha 2}\cos(10\delta) + i_{\alpha 3}\cos(15\delta) + i_{\beta 3}\sin(15\delta)\} \\ i_G = \sqrt{\frac{2}{7}} \{i_{\alpha 1}\cos(6\delta) + i_{\beta 1}\sin(6\delta) + i_{\alpha 2}\cos(12\delta) + i_{\alpha 3}\cos(18\delta) + i_{\beta 3}\sin(18\delta)\} \end{cases} \tag{2.27}$$

In this option, the wye-connected winding topology considered in heathy mode can be used in post-fault operations without additional hardware or changing the stator winding topology. Current $i_{\alpha 2}$ depends on currents in the first and third fictitious machines ($i_{\alpha 1}$, $i_{\alpha 3}$), resulting in time-variant currents (i_{d9}, i_{q9}) according to (2.22). Therefore, method (I)-2 have 5 constant d-q currents for control.

2.3.2.D. *Method (I)-3*

With ($i_B+i_D+i_F = i_C+i_E+i_G =0$) and ($i_z=0$), the current transformation in (2.20) becomes:

$$\begin{cases} \begin{bmatrix} 0 \\ i_B \\ i_C \\ i_D \\ i_E \\ i_F \\ i_G \end{bmatrix} = \sqrt{\frac{2}{7}} \begin{bmatrix} 1 & 0 & 1 & 0 & 1 & 0 & 1/\sqrt{2} \\ \cos(\delta) & \sin(\delta) & \cos(2\delta) & \sin(2\delta) & \cos(3\delta) & \sin(3\delta) & 1/\sqrt{2} \\ \cos(2\delta) & \sin(2\delta) & \cos(4\delta) & \sin(4\delta) & \cos(6\delta) & \sin(6\delta) & 1/\sqrt{2} \\ \cos(3\delta) & \sin(3\delta) & \cos(6\delta) & \sin(6\delta) & \cos(9\delta) & \sin(9\delta) & 1/\sqrt{2} \\ \cos(4\delta) & \sin(4\delta) & \cos(8\delta) & \sin(8\delta) & \cos(12\delta) & \sin(12\delta) & 1/\sqrt{2} \\ \cos(5\delta) & \sin(5\delta) & \cos(10\delta) & \sin(10\delta) & \cos(15\delta) & \sin(15\delta) & 1/\sqrt{2} \\ \cos(6\delta) & \sin(6\delta) & \cos(12\delta) & \sin(12\delta) & \cos(18\delta) & \sin(18\delta) & 1/\sqrt{2} \end{bmatrix} \begin{bmatrix} i_{\alpha 1} \\ i_{\beta 1} \\ i_{\alpha 2} \\ i_{\beta 2} \\ i_{\alpha 3} \\ i_{\beta 3} \\ 0 \end{bmatrix} \\ i_B + i_D + i_F = i_C + i_E + i_G = 0 \end{cases} \tag{2.28}$$

Therefore, currents ($i_{\alpha 2}$, $i_{\beta 2}$) and phase currents (i_B, i_C, i_D, i_E, i_F, i_G) are calculated from four main currents ($i_{\alpha 1}$, $i_{\beta 1}$, $i_{\alpha 3}$, $i_{\beta 3}$) as follows:

$$\begin{cases} i_{\alpha 2} = -\{i_{\alpha 1} + i_{\alpha 3}\} \\ i_{\beta 2} = \left\{ \dfrac{-\begin{pmatrix} i_{\alpha 1}[\cos(\delta) - \cos(2\delta) + \cos(3\delta) + \cos(5\delta) - \cos(6\delta) - \cos(10\delta)] + i_{\beta 1}[\sin(\delta) + \sin(3\delta) + \sin(5\delta)] + \\ i_{\alpha 3}[-\cos(2\delta) + \cos(3\delta) - \cos(6\delta) + \cos(9\delta) - \cos(10\delta) + \cos(15\delta)] + i_{\beta 3}[\sin(3\delta) + \sin(9\delta) + \sin(15\delta)] \end{pmatrix}}{\sin(2\delta) + \sin(6\delta) + \sin(10\delta)} \right\} \end{cases} \quad (2.29)$$

$$\begin{cases} i_B = \sqrt{\frac{2}{7}}\{i_{\alpha 1}\cos(\delta) + i_{\beta 1}\sin(\delta) + i_{\alpha 2}\cos(2\delta) + i_{\beta 2}\sin(2\delta) + i_{\alpha 3}\cos(3\delta) + i_{\beta 3}\sin(3\delta)\} \\ i_C = \sqrt{\frac{2}{7}}\{i_{\alpha 1}\cos(2\delta) + i_{\beta 1}\sin(2\delta) + i_{\alpha 2}\cos(4\delta) + i_{\beta 2}\sin(4\delta) + i_{\alpha 3}\cos(6\delta) + i_{\beta 3}\sin(6\delta)\} \\ i_D = \sqrt{\frac{2}{7}}\{i_{\alpha 1}\cos(3\delta) + i_{\beta 1}\sin(3\delta) + i_{\alpha 2}\cos(6\delta) + i_{\beta 2}\sin(6\delta) + i_{\alpha 3}\cos(9\delta) + i_{\beta 3}\sin(9\delta)\} \\ i_E = \sqrt{\frac{2}{7}}\{i_{\alpha 1}\cos(4\delta) + i_{\beta 1}\sin(4\delta) + i_{\alpha 2}\cos(8\delta) + i_{\beta 2}\sin(8\delta) + i_{\alpha 3}\cos(12\delta) + i_{\beta 3}\sin(12\delta)\} \\ i_F = \sqrt{\frac{2}{7}}\{i_{\alpha 1}\cos(5\delta) + i_{\beta 1}\sin(5\delta) + i_{\alpha 2}\cos(10\delta) + i_{\beta 2}\sin(10\delta) + i_{\alpha 3}\cos(15\delta) + i_{\beta 3}\sin(15\delta)\} \\ i_G = \sqrt{\frac{2}{7}}\{i_{\alpha 1}\cos(6\delta) + i_{\beta 1}\sin(6\delta) + i_{\alpha 2}\cos(12\delta) + i_{\beta 2}\sin(12\delta) + i_{\alpha 3}\cos(18\delta) + i_{\beta 3}\sin(18\delta)\} \end{cases} \quad (2.30)$$

In this option, like method (I)-2, the wye-connected winding topology can be used in post-fault operations without additional hardware or changing the stator winding topology. Currents ($i_{\alpha 2}$, $i_{\beta 2}$) are functions of currents in the first and third fictitious machines, resulting in time-variant currents (i_{d9}, i_{q9}) for control according to (2.22). Therefore, method (I)-3 have 5 constant d-q currents for control.

2.3.2.E. *Comparative analyses of calculated results by the proposed options of method (I)*

2.3.2.E.1. Preserving the torque as in healthy mode:

The post-fault torques, more precisely the average torques, are kept the same as in healthy mode when main current references ($i_{\alpha 1}$, $i_{\beta 1}$, $i_{\alpha 3}$, $i_{\beta 3}$) and (i_{d1}, i_{q1}, i_{d3}, i_{q3}) in the three options of method (I) are preserved as in Figs 2.22 and 2.23. Specifically, d-q currents are imposed with (i_{d1}=0 A, i_{q1}=12.7 A, i_{d3}=0 A, i_{q3}=4.1 A). Parameters of the experimental seven-phase drive described in Table 2.2 are used for calculations. If the first and third harmonics of the back-EMFs are considered, the torques with the three proposed options of method (I) are constant and equal to their average value of 33.3 Nm.

For clear comparative analyses of the three options of method (I), only currents ($i_{\alpha 2}$, $i_{\beta 2}$, i_z), (i_{d9}, i_{d9}, i_z), and phase currents (i_B, i_C, i_D, i_E, i_F, i_G) at 20 rad/s are presented in Figs 2.24-2.26. It is noted that current waveforms of the remaining healthy phases in each option of method (I) are no longer identical as in healthy mode. The zero-sequence current i_z in method (I)-1 is time-variant with a high amplitude (21.8 A) compared to the phase currents. This current generates torque ripples if the experimental back-EMFs contain the harmonics in the zero-sequence machine (7^{th}, 21^{st}, and so on). If method (I)-1 is chosen, it means that a constraint on machine design (no harmonics associated with the zero-sequence machine in back-EMFs, for example) is imposed. Meanwhile, currents (i_{d9}, i_{q9}) with methods (I)-2 and (I)-3 are time-variant, creating torque ripples if the back-EMFs contain the harmonics in the second machine (9^{th}, for example).

For control, the time-invariant property of the reference signals can facilitate the current control with conventional PI controllers. Method (I)-1 has 6 constant currents (i_{d1}, i_{q1}, i_{d9}, i_{q9}, i_{d3}, i_{q3}), only i_z is time-variant. Methods (I)-2 and (I)-3 have 5 constant currents (i_{d1}, i_{q1}, i_{d3}, i_{q3}, i_z) and 2 time-variant currents (i_{d9}, i_{q9}).

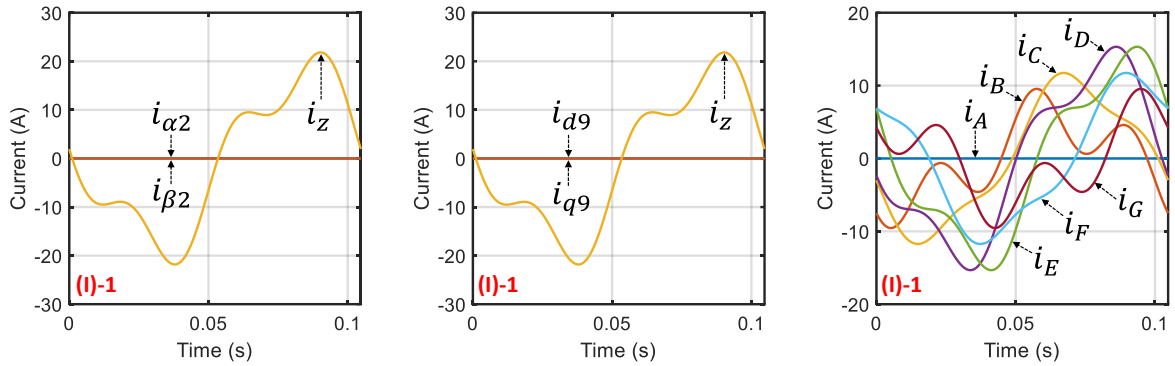

(a) (b) (c)

Fig. 2.24. Desired currents ($i_{\alpha 2}$, $i_{\beta 2}$, i_z) (a), currents (i_{d9}, i_{q9}, i_z) (b), and phase currents (c), at 20 rad/s with method (I)-1 for an OC fault in phase *A* to preserve the healthy-mode torque (i_{d1}=0 A, i_{q1}=12.7 A, i_{d3}=0 A, i_{q3}=4.1 A).

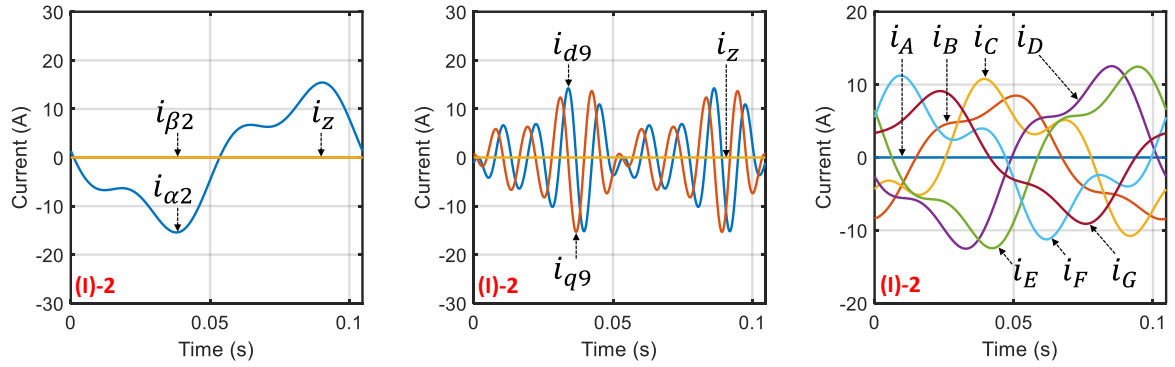

(a) (b) (c)

Fig. 2.25. Desired currents ($i_{\alpha 2}$, $i_{\beta 2}$, i_z) (a), currents (i_{d9}, i_{q9}, i_z) (b), and phase currents (c), at 20 rad/s with method (I)-2 for an OC fault in phase *A* to preserve the healthy-mode torque (i_{d1}=0 A, i_{q1}=12.7 A, i_{d3}=0 A, i_{q3}=4.1 A).

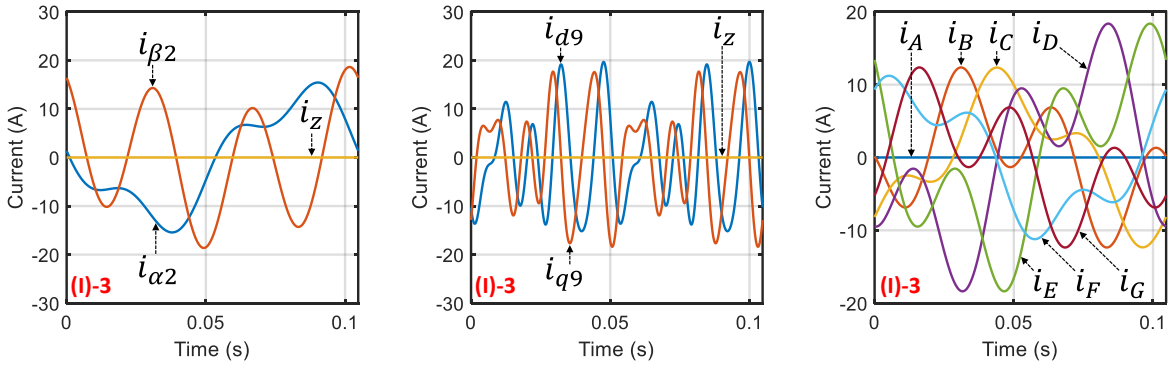

(a) (b) (c)

Fig. 2.26. Desired currents ($i_{\alpha 2}$, $i_{\beta 2}$, i_z) (a), currents (i_{d9}, i_{q9}, i_z) (b), and phase currents (c), at 20 rad/s with method (I)-3 for an OC fault in phase *A* to preserve the healthy-mode torque (i_{d1}=0 A, i_{q1}=12.7 A, i_{d3}=0 A, i_{q3}=4.1 A).

Calculated RMS values in all phase currents and the zero-sequence current of the three options are described in Table 2.7. It is noted that the RMS currents in the remaining healthy phases in each option of method (I) are different and higher than their rated value (5.1 A). In the three options, the highest RMS currents are often in phases *D* and *E*. In addition, method (I)-1 leads to the RMS zero-sequence current of 13.4 A, possibly causing the oversizing of the drive.

Table 2.7. Calculated RMS values of all phase currents and the zero-sequence current with methods (I)-1, (I)-2, and (I)-3 for an OC fault in phase *A* to preserve the healthy-mode torque at 20 rad/s.

Method	**RMS current (A)**							
	A	*B*	*C*	*D*	*E*	*F*	*G*	i_z
Method (I)-1	0	5.2	7.6	9.7	9.7	7.6	5.2	13.4
Method (I)-2	0	5.7	6.3	7.9	7.9	6.3	5.7	0
Method (I)-3	0	6.5	6.9	10	10	6.9	6.5	0

Table 2.8. Comparisons between calculated results with methods (I)-1, (I)-2, and (I)-3 for an OC fault in phase *A* to preserve the healthy-mode torque at 20 rad/s.

Method	**Torque T_{em} =T_{ave}**		**Highest RMS current I_{RMS}**		**Highest peak voltage V_{peak}**		**Total copper loss P_{loss}**	
	(Nm)	(pu)	(A)	(pu)	(V)	(pu)	(W)	(pu)
Healthy mode	33.3	1	5.1	1	45.9	1	255	1
Method (I)-1	33.3	1	9.7	1.90	51.4	1.12	500.5	1.96
Method (I)-2	33.3	1	7.9	1.55	47.1	1.03	375.5	1.47
Method (I)-3	33.3	1	10	1.96	57.9	1.26	536	2.1

pu: per unit where the base values are parameters of healthy mode.

Finally, comparisons between the three options of method (I) and healthy mode for the same torque at 20 rad/s are described in Table 2.8. Highest RMS current among all phases I_{RMS}, highest peak voltage among all phases V_{peak}, and the total copper loss P_{loss} are considered. It is noted that when the torque is preserved, I_{RMS} and P_{loss} in fault-tolerant operations can be doubled, dramatically exceeding its limit. Voltage V_{peak} is significantly higher than healthy mode (1.26 pu). Method (I)-2 provides the best results among the three options over all considered criteria. Indeed, method (I)-2 results in the lowest I_{RMS} (1.55 pu), the lowest V_{peak} (1.03 pu) and the lowest P_{loss} (1.47 pu). Meanwhile, method (I)-3 leads to the highest values of the considered parameters, especially the highest I_{RMS} (1.96 pu) and the highest P_{loss} (2.1 pu).

2.3.2.E.2. Optimal calculations under constraints on RMS current and peak voltage:

When the control scheme in Fig. 2.21 with the optimal control strategy in (2.16) is considered, the torques by the three options of method (I) will be reduced to respect constraints on current and voltage. Therefore, flux-weakening operations can be guaranteed. These constraints in faulty modes are the same as in healthy mode (in **section 2.1.4**) with I_{RMS_lim}=5.1 A and V_{lim_opt}=75 V to respect the experimental voltage limit V_{lim}=100 V. As previously assumed, only the first and third harmonic components of the back-EMFs are considered in the offline optimization.

In Figs. 2.27-2.29, main currents (i_{d1}, i_{q1}, i_{d3}, i_{q3}) or ($i_{\alpha 1}$, $i_{\beta 1}$, $i_{\alpha 3}$, $i_{\beta 3}$) at 20 rad/s are re-determined by *fmincon* to respect the considered constraints. It is worth noting that currents (i_{d1}, i_{q1}, i_{d3}, i_{q3}) in the three options of method (I) are no longer the same. These currents are also different from the currents preserving the heathy torque. The other currents (i_{d9}, i_{q9}, i_z) or ($i_{\alpha 2}$, $i_{\beta 2}$, i_z) are consequently calculated from the main currents. Consequently, the current waveforms of the remaining healthy phases in Figs. 2.27c-2.29c are changed compared to the previous case in Figs 2.24c-2.26c.

Calculated RMS values of all phase currents and the zero-sequence current under the constraints with method (I) at 20 rad/s are described in Table 2.9. In the three options, the highest RMS current appearing in phases *D* and *E* is equal to I_{RMS_lim} (5.1A). In addition, method (I)-1 results in the RMS zero-sequence current of 7.2 A.

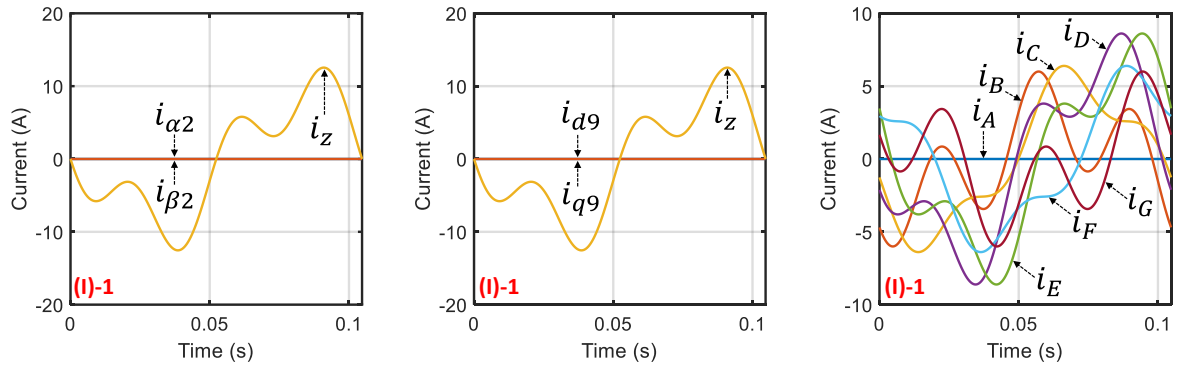

(a) (b) (c)

Fig. 2.27. Desired currents ($i_{\alpha 2}$, $i_{\beta 2}$, i_z) (a), currents (i_{d9}, i_{q9}, i_z) (b), and phase currents (c), at 20 rad/s with method (I)-1 for an OC fault in phase *A* under constraints on RMS current and peak voltage (i_{d1}=0 A, i_{q1}=6.4 A, i_{d3}=0 A, i_{q3}=3.2 A).

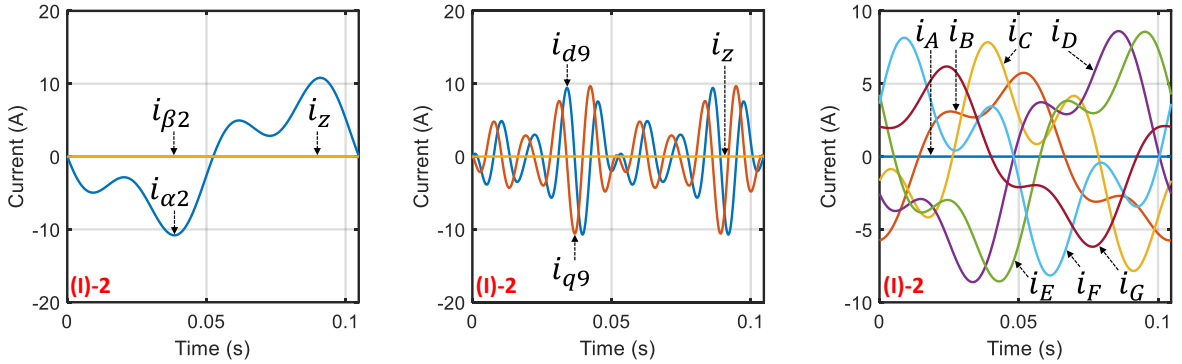

(a) (b) (c)

Fig. 2.28. Desired currents ($i_{\alpha 2}$, $i_{\beta 2}$, i_z) (a), currents (i_{d9}, i_{q9}, i_z) (b), and phase currents (c), at 20 rad/s with method (I)-2 for an OC fault in phase *A* under constraints on RMS current and peak voltage (i_{d1}=0 A, i_{q1}=7.9 A, i_{d3}=0 A, i_{q3}=3.8 A).

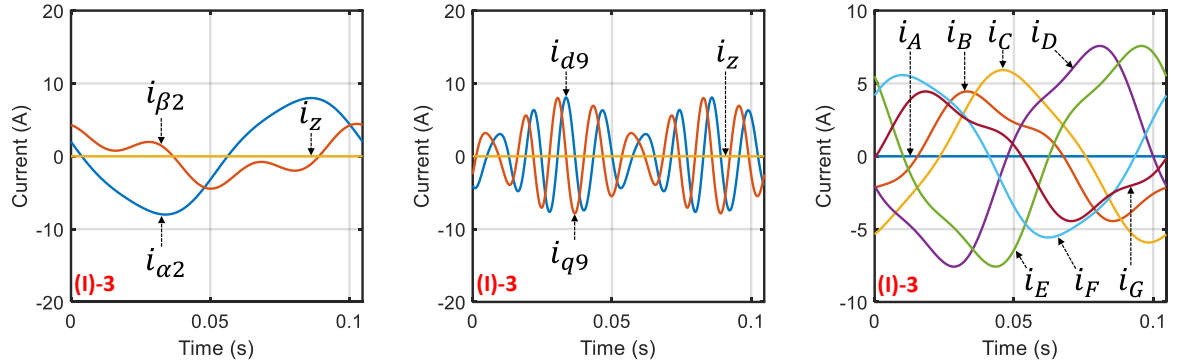

(a) (b) (c)

Fig. 2.29. Desired currents ($i_{\alpha 2}$, $i_{\beta 2}$, i_z) (a), currents (i_{d9}, i_{q9}, i_z) (b), and phase currents (c), at 20 rad/s with method (I)-3 for an OC fault in phase *A* under constraints on RMS current and peak voltage (i_{d1}=0 A, i_{q1}=7.9 A, i_{d3}=0 A, i_{q3}=0.5 A).

Table 2.9. Calculated RMS values of all phase currents and the zero-sequence current with methods (I)-1, (I)-2, and (I)-3 for an OC fault in phase *A* under constraints on RMS current and peak voltage at 20 rad/s.

Method	**RMS current (A)**							
	A	*B*	*C*	*D*	*E*	*F*	*G*	i_z
Method (I)-1	0	3.2	3.9	5.1	5.1	3.9	3.2	7.2
Method (I)-2	0	3.6	4.3	5.1	5.1	4.3	3.6	0
Method (I)-3	0	2.9	4	5.1	5.1	4	2.9	0

Table 2.10. Comparisons between calculated results with methods (I)-1, (I)-2, and (I)-3 for an OC fault in phase *A* under constraints on RMS current and peak voltage at 20 rad/s.

Method	Highest RMS current I_{RMS}		Torque T_{em}=T_{ave}		Highest peak voltage V_{peak}		Total copper loss P_{loss}	
	(A)	(pu)	(Nm)	(pu)	(V)	(pu)	(W)	(pu)
Healthy mode	5.1	1	33.3	1	45.9	1	255	1
Method (I)-1	5.1	1	17.7	0.53	42.8	0.93	144.4	0.57
Method (I)-2	5.1	1	21.7	0.65	42.3	0.92	162.6	0.64
Method (I)-3	5.1	1	19.1	0.57	39	0.85	140	0.55

pu: per unit where the base values are parameters of healthy mode.

Finally, comparisons between the post-fault operations using the three options of method (I) and healthy mode is described in Table 2.10. When I_{RMS_lim} is respected, method (I)-2 generates the highest T_{em} at 21.7 Nm (0.65 pu). Meanwhile, the torques with method (I)-1 and method (I)-3 are lower at 17.7 Nm (0.53 pu) and 19.1 Nm (0.57 pu), respectively. Additionally, compared to healthy mode and methods (I)-1 and (I)-2, the calculated V_{peak} with method (I)-3 is lowest (0.85 pu), leading to the highest base speed. Meanwhile, the calculated V_{peak} in healthy mode is lowest, resulting in the lowest base speed. Total copper losses P_{loss} in fault-tolerant operations are lower than that of healthy mode (0.55 to 0.64 pu) due to the current constraint. Indeed, in each method, the highest RMS current I_{RMS} appearing in phases *D* and *E* is equal to I_{RMS_lim}=5.1 A (1 pu) while RMS currents of the other phases are less than 5.1 A, resulting in lower P_{loss} than healthy mode. Especially, method (I)-2 having similar RMS currents (see Table 2.9) results in the highest P_{loss} among the three options.

When the operating speed varies, the optimal torque-speed characteristics, all RMS phase currents and all peak phase voltages by the three options of method (I) in terms of speed are expressed in Fig. 2.30. It is noted that method (I)-2 has the highest fault-tolerant torque-speed characteristic. In addition, all options of method (I) respect the constraints on RMS current and peak voltage, allowing flux-weakening operations.

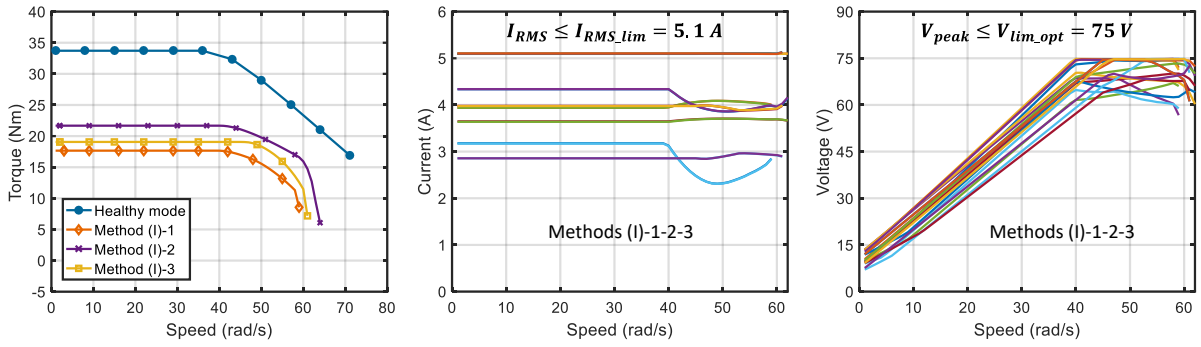

(a) (b) (c)

Fig. 2.30. (Calculated result) Optimal post-fault torque-speed characteristics (a), all RMS phase currents (b) and all peak phase voltages (c), in terms of speed under constraints on RMS current and peak voltage with methods (I)-1, (I)-2, and (I)-3 when phase *A* is open-circuited.

Table 2.11 describes the calculated base and maximum speeds of the healthy and faulty modes with the three options of method (I). The lowest base speed can be observed in healthy mode at 38 rad/s. The highest base speed is 46 rad/s (1.21 pu) with method (I)-3 while the base speeds with methods (I)-1 and (I)-2 are the same (1.08 pu). The lowest (healthy mode) and highest (method (I)-3) base speeds are consequences of the highest (healthy mode) and lowest (method (I)-3) values of V_{peak} in Table 2.10. The healthy mode has the highest maximum speed of 73

rad/s. Method (I)-2 results in the highest post-fault maximum speed (0.88 pu) while method (I)-1 has the lowest maximum speed (0.81 pu).

Table 2.11. Comparisons between the calculated base and maximum speeds with methods (I)-1, (I)-2, and (I)-3 for an OC fault in phase *A* under constraints on RMS current and peak voltage.

Method	Base speed Ω_{base}		Maximum speed Ω_{max}	
	(rad/s)	(pu)	(rad/s)	(pu)
Healthy mode	38	1	73	1
Method (I)-1	41	1.08	59	0.81
Method (I)-2	41	1.08	64	0.88
Method (I)-3	46	1.21	61	0.84

pu: per unit where the base values are parameters of healthy mode.

2.3.2.F. *Verification with experimental results for method (I)*

According to Fig. 2.30, Tables 2.10 and 2.11, method (I)-1, feasible in a system with a neutral line or in an open-end winding topology, generates the lowest torque and the shortest speed range among the three options of method (I). It is possible to physically change the existing wye-connected winding machine in the test bench (see Fig. 2.7) to a neutral line system an open-end winding system to facilitate method (I)-1. However, the high zero-sequence current with method (I)-1 (i_z in Fig. 2.27) will interact with the 7th and 21st harmonics of back-EMFs (9.4 and 3.2%, respectively) in the experimental machine to generate high torque ripples with low frequencies. In addition, the torques and phase currents will contain switching frequency components [90]. From the above reasons, in the scope of this doctoral thesis, method (I)-1 is not verified with the experimental test bench.

Only methods (I)-2 and (I)-3 with the control scheme in Fig. 2.21 are validated in the experimental test bench (see **section 2.1.4.A**). Although the torques with methods (I)-2 and (I)-3 are sensitive to the 9th harmonic (12.5%) of the experimental back-EMFs, these methods can be easily implemented in the test bench without any hardware modifications.

2.3.2.F.1. Current control performance:

To experimentally obtain the optimal torque-speed characteristics (see Fig. 2.30a), six d-q currents need to properly track their references (see Figs 2.28-2.29). At a speed, methods (I)-2 and (I)-3 have time-constant currents (i_{d1}, i_{q1}, i_{d3}, i_{q3}) and time-variant currents (i_{d9}, i_{q9}).

Currents in (d_1-q_1), creating most of the torque, are well controlled in speed ranges as described in Fig. 2.31. As in healthy mode (see **section 2.1.4**), currents in (d_3-q_3) and (d_9-q_9) frames have current harmonics caused by the unwanted back-EMF harmonics and the inverter nonlinearity. These types of disturbances can be eliminated by ADALINEs that will be presented in **Chapter 3**. Therefore, the control of currents in (d_3-q_3) in speed ranges is described in Fig. 2.32 with current harmonics. Similarly, the time-variant currents (i_{d9}, i_{q9}) are controlled at 20 rad/s with errors as shown in Fig. 2.33. However, these currents create a small proportion of the torque.

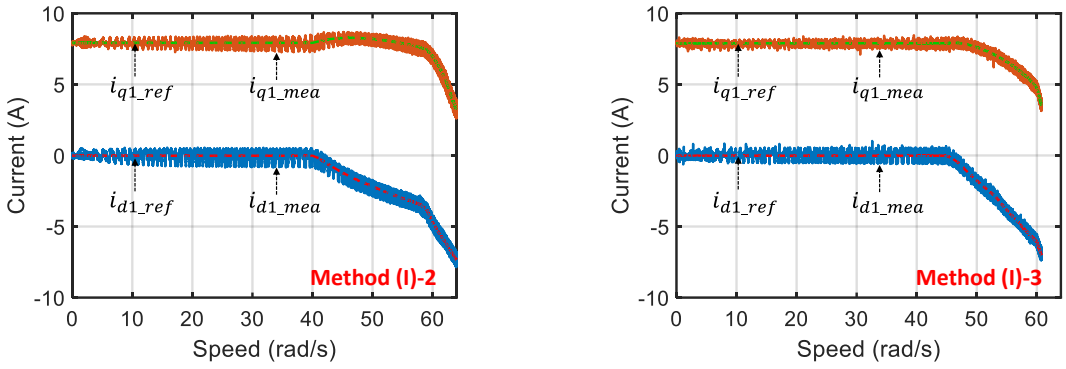

(a) (b)

Fig. 2.31. (Experimental result) Currents in (d_1-q_1) frame in terms of speed with method (I)-2 (a), and with method (I)-3 (b), when phase *A* is open-circuited.

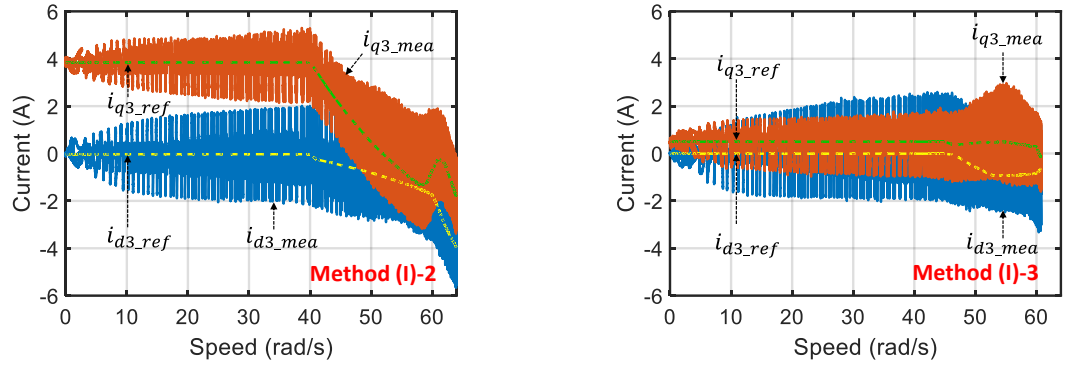

(a) (b)

Fig. 2.32. (Experimental result) Currents in (d_3-q_3) frame in terms of speed with method (I)-2 (a), and with method (I)-3 (b), when phase *A* is open-circuited.

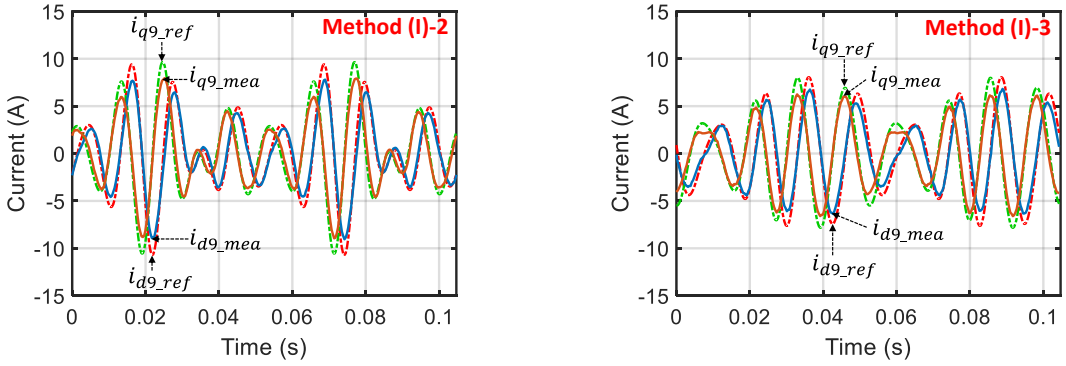

(a) (b)

Fig. 2.33. (Experimental results) Currents in (d_9-q_9) frame in terms of time at 20 rad/s with method (I)-2 (a), and with method (I)-3 (b), when phase *A* is open-circuited.

2.3.2.F.2. Torque performance:

An operation with three operating states at 20 rad/s as shown in Fig. 2.34 is investigated, including a healthy operation, an OC fault without reconfigurations, and a fault-tolerant operation with one of two methods (I)-2 and (I)-3. The first two operating states have been deeply investigated in **sections 2.1.4** and **2.2**. It is noted that the average torques in the third state with methods (I)-2 and methods (I)-3 are in good accordance with the optimal (calculated) values in Table 2.10. To respect the constraints on RMS current, the average torque is reduced from 33.5 Nm in healthy mode to 21.6 Nm (0.64 pu) with method (I)-2, and to 19 Nm (0.57 pu) with method (I)-3 in the post-fault operation. However, the experimental torques have ripples

of 31% with method (I)-2, and 32% with method (I)-3. The main reason is that the considered experimental back-EMFs have a significant proportion of the 9th harmonic (12.5%). This harmonic interacts with the time-variant currents (i_{d9}, i_{q9}) in methods (I)-2 and (I)-3 as described in Fig. 2.33, creating ripple torques. These torque ripples can be eliminated by an ADALINE that will be presented in **Chapter 3**. However, these torque ripples are much lower than the post-fault operation without reconfigurations with 50%.

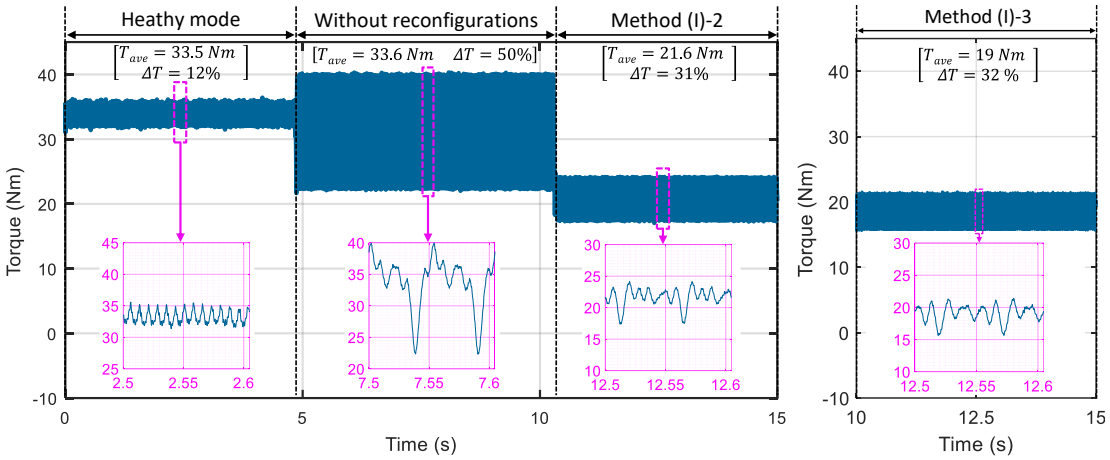

Fig. 2.34. (Experimental result) Torque in three operating states including healthy mode, an OC fault in phase *A* without reconfigurations, and when method (I)-2 (a) and method (I)-3 (b) are applied.

When the operating speed varies, the experimental torque-speed characteristics with methods (I)-2 and (I)-3 in comparison with healthy mode ($T_{em\_opt\_HM}$ and $T_{em\_exp\_HM}$) are described in Fig. 2.35. By using these methods, the experimental OC fault torques ($T_{em\_exp\_OC}$) are in good accordance with the optimal torques ($T_{em\_opt\_OC}$) (see Fig. 2.30). The experimental base and maximum speeds are the same as calculated results in Table 2.11.

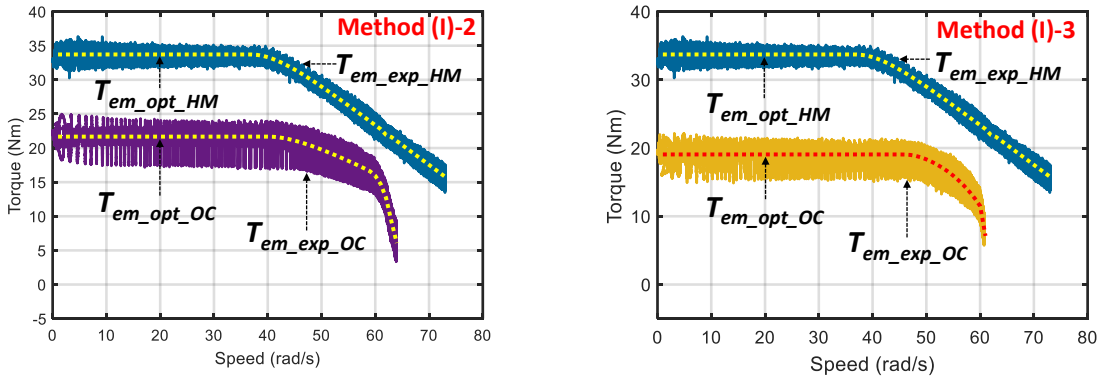

Fig. 2.35. (Experimental result) Post-fault torque-speed characteristics under an OC fault in phase *A* with method (I)-2 (a), and with method (I)-3 (b).

2.3.2.F.3. Constraints on RMS current and peak voltage:

Table 2.12 shows that experimental RMS currents in all phases at 20 rad/s are in good accordance with optimal values. The experimental highest RMS currents appear in phases *D* and *E* in the both options with (4.5 and 5.1 A) for method (I)-2, and (4.5 and 5 A) for method (I)-3.

Table 2.12. Experimental RMS currents in all phases with methods (I)-2 and (I)-3 for an OC fault in phase *A* under constraints on RMS current and peak voltage at 20 rad/s.

Method	RMS current (A)													
	A		*B*		*C*		*D*		*E*		*F*		*G*	
	opt	exp	opt	exp	opt	exp	opt	exp	opt	exp	opt	exp	opt	exp
Method (I)-2	0	0.1	3.6	3.8	4.3	3.9	5.1	4.5	5.1	5.1	4.3	4	3.6	3.8
Method (I)-3	0	0.1	2.9	3.3	4	3.5	5.1	4.5	5.1	5	4	3.6	2.9	3.2

opt: optimal calculated results; exp: experimental results.

When the operating speed varies, the constraints on RMS current and voltage are still respected in the experimental results with methods (I)-2 and (I)-3, including the flux-weakening regions. Measured phase currents by the two methods in terms of speed are described in Fig. 2.36 and Fig. 2.37. The waveforms of measured phase currents at 20 and 55 rad/s are also plotted. The waveforms of the remaining healthy phase currents are changed at high speed, but the highest RMS current is always less than or equal to its limit (I_{RMS_lim}=5.1 A).

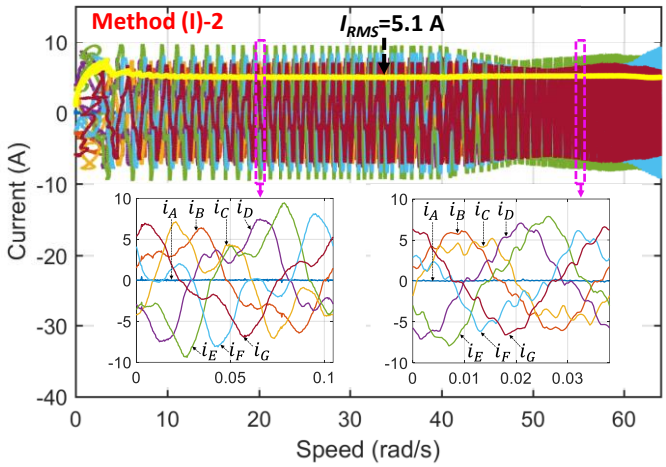

Fig. 2.36. (Experimental result) Phase currents in terms of speed, and current waveforms at 20 and 55 rad/s with method (I)-2 under an OC fault in phase *A*.

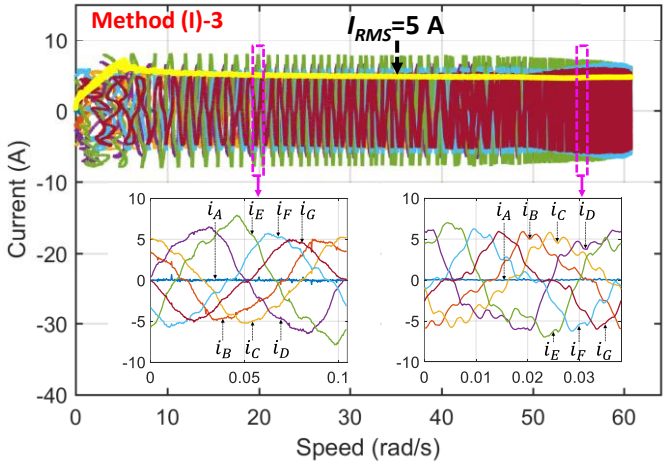

Fig. 2.37. (Experimental result) Phase currents in terms of speed, and current waveforms at 20 and 55 rad/s with method (I)-3 under an OC fault in phase *A*.

Similarly, phase voltage references with the two methods in terms of speed are presented in Fig. 2.38 and Fig. 2.39. Their waveforms in terms of time at 20 and 55 rad/s are also plotted. It is noted that the peak values of phase voltage references after the base speeds are relatively under their limit (V_{lim}=100 V).

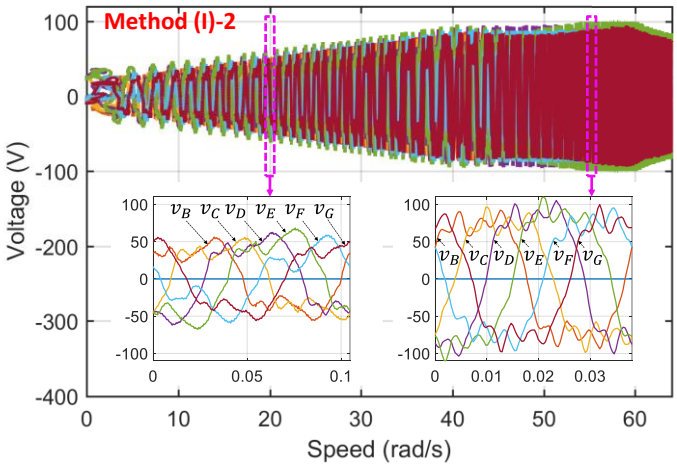

Fig. 2.38 (Experimental result) Phase voltage references in terms of speed, and current waveforms at 20 and 55 rad/s with method (I)-2 under an OC fault in phase *A*.

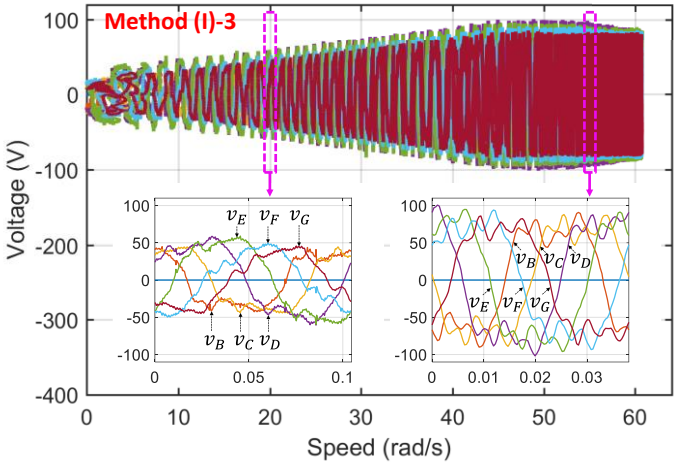

Fig. 2.39 (Experimental result) Phase voltage references in terms of speed, and current waveforms at 20 and 55 rad/s with method (I)-3 under an OC fault in phase *A*.

2.3.2.F.4. Comparative summary:

A comparative summary of experimental performances in a healthy operation, an OC fault without reconfigurations, and fault-tolerant operations with methods (I)-2 and (I)-3 is presented in Table 2.13. The highest RMS currents I_{RMS}, torques T_{em}, highest peak voltages V_{peak}, and total copper losses P_{loss} in the two methods are compared. The performances of current control, torque generations, and constraints have been analyzed in the previous subsections. In general, the calculated and experimental results in Table 2.10 and Table 2.13 are in good accordance.

However, the experimental voltage references in Table 2.13 are higher than the calculated values in Table 2.10. In addition, the experimental V_{peak} with healthy mode is no longer highest as shown in calculated results, related to the lowest base speed. The reason is that additional voltages caused by high-order harmonics of the experimental back-EMFs are added to the voltage references.

The experimental total copper losses P_{loss} with method (I)-2 (0.58 pu) and method (I)-3 (0.49 pu) are much lower than healthy mode (1 pu) and the OC fault without reconfigurations (1.27 pu). These copper losses are also slightly lower than calculated values due to the existing errors in current control.

Table 2.13. Comparisons between experimental results with methods (I)-2 and (I)-3 for an OC fault in phase *A* under constraints on RMS current and peak voltage at 20 rad/s.

Method	Highest RMS current I_{RMS}		Torque T_{em}			Highest peak voltage V_{peak}		Total copper loss P_{loss}	
	(A)	(pu)	T_{ave} (Nm)	T_{ave} (pu)	ΔT (%)	(V)	(pu)	(W)	(pu)
Healthy mode	5.1	1	33.5	1	12	60	1	255.2	1
OC fault without reconfigurations	7.9	1.55	33.6	1	50	104.1	1.74	323.7	1.27
Method (I)-2	5.1	1	21.6	0.64	31	68.2	1.14	149.1	0.58
Method (I)-3	5	0.98	19	0.57	32	59	0.98	124	0.49

pu: per unit where the base values are parameters of healthy mode.

2.3.3. Method (II): new current references determined from reduced-order transformation matrices

2.3.3.A. *Principle of method (II)*

The principle of methods using reduced-order transformation matrices is to design new current references for post-fault operations by modifying classical transformation matrices, especially matrix Clarke. An overview on this type of methods has been presented in [166]. Studies [126-129, 133] consider sinusoidal five-phase machines while methods in [134, 135, 149] are applied to non-sinusoidal five-phase machines. In general, for *n*-phase machine, when one phase is opened, this type of methods is to determine new current references by using new (*n*-1)-by-(*n*-1) transformation matrices. In other words, the post-fault *n*-phase machine can be considered as an asymmetrical (*n*-1)-phase machine with (*n*-1)-by-(*n*-1) transformation matrices. In this doctoral thesis, the case study with a 7-phase non-sinusoidal machine is considered. In addition, the constraints on RMS current and peak voltage are considered; hence, flux-weakening operations at high speed are guaranteed.

Like method (I), method (II) can generate constant post-fault torques when the back-EMFs consist of the first and third harmonics. Moreover, one option of method (II) can guarantee constant torques even when the back-EMFs consist of harmonic components in the second fictitious machines (9^{th}, for example). This feature can be considered as an advantage of method (II) over method (I).

To find new transformations as well as new current references for a 7-phase non-sinusoidal machine, two following steps are taken as follows:

1) When only new 6-by-6 Clarke matrix for the fundamental currents are determined, the generated sinusoidal currents can generate constant torques in a sinusoidal back-EMF machine. However, in a non-sinusoidal back-EMF machine, there are inevitable ripple torques due to the interactions between the fundamental currents and the higher-order harmonics of the back-EMFs (3^{rd}, for example).
2) The third harmonic currents are injected to eliminate the ripple torques by determining new 6-by-6 Clarke matrices for the third harmonic currents. Therefore, the non-sinusoidal currents interact with the non-sinusoidal back-EMFs to generate constant torques. There are two current design options that are considered as two options of method (II).

2.3.3.A.1. The use of fundamental currents:

When phase *A* is open-circuited, its phase current becomes zero. Therefore, the first column of the classical Clarke transformation matrix in (2.1), associated with phase *A*, should be removed. The transformation with the classical Clarke matrix in the post-fault condition for seven-phase machines can be written as follows:

$$\begin{bmatrix} i_{\alpha 1} \\ i_{\beta 1} \\ i_{\alpha 2} \\ i_{\beta 2} \\ i_{\alpha 3} \\ i_{\beta 3} \\ i_z \end{bmatrix} = \left[\boldsymbol{T}_{\boldsymbol{Clarke}}^{\boldsymbol{fault}}\right] \begin{bmatrix} i_B \\ i_C \\ i_D \\ i_E \\ i_F \\ i_G \end{bmatrix} \tag{2.31}$$

$$\left[\boldsymbol{T}_{\boldsymbol{Clarke}}^{\boldsymbol{fault}}\right] = \sqrt{\frac{2}{7}} \begin{bmatrix} \cos(\delta) & \cos(2\delta) & \cos(3\delta) & \cos(4\delta) & \cos(5\delta) & \cos(6\delta) \\ \sin(\delta) & \sin(2\delta) & \sin(3\delta) & \sin(4\delta) & \sin(5\delta) & \sin(6\delta) \\ \cos(2\delta) & \cos(4\delta) & \cos(6\delta) & \cos(8\delta) & \cos(10\delta) & \cos(12\delta) \\ \sin(2\delta) & \sin(4\delta) & \sin(6\delta) & \sin(8\delta) & \sin(10\delta) & \sin(12\delta) \\ \cos(3\delta) & \cos(6\delta) & \cos(9\delta) & \cos(12\delta) & \cos(15\delta) & \cos(18\delta) \\ \sin(3\delta) & \sin(6\delta) & \sin(9\delta) & \sin(12\delta) & \sin(15\delta) & \sin(18\delta) \\ 1/\sqrt{2} & 1/\sqrt{2} & 1/\sqrt{2} & 1/\sqrt{2} & 1/\sqrt{2} & 1/\sqrt{2} \end{bmatrix} \tag{2.32}$$

In $[\boldsymbol{T}_{\boldsymbol{Clarke}}^{\boldsymbol{fault}}]$, the first, third and fifth row vectors are no longer orthogonal to each other; hence, three fictitious machines associated with three reference frames which are decoupled in healthy mode are coupled in faulty mode. Consequently, currents cannot be properly controlled without any reconfigurations as analyzed in **section 2.2**.

According to the principle proposed in [134] for non-sinusoidal five-phase machines, new transformation matrices for non-sinusoidal seven-phase machines can be proposed according to the preservation of the fundamental MMF as in healthy mode. In other words, the post-fault seven-phase machine can be considered as an asymmetrical 6-phase machine with 6-by-6 transformation matrices. The relationship between new reference currents in natural frame (i_{B1}, i_{C1}, i_{D1}, i_{E1}, i_{F1}, i_{G1}) and currents in new d-q frames (i_{d11}, i_{q11}, i_{d91}, i_{q91}, i_{x1}, i_{z1}) is described as follows:

$$\begin{bmatrix} i_{B1} & i_{C1} & i_{D1} & i_{E1} & i_{F1} & i_{G1} \end{bmatrix}^T = \left[\boldsymbol{T}_{\boldsymbol{Clarke}}^{\boldsymbol{1}}\right]^{-1} \left[\boldsymbol{T}_{\boldsymbol{Park}}^{\boldsymbol{1}}\right]^{-1} \begin{bmatrix} i_{d11} & i_{q11} & i_{d91} & i_{q91} & i_{x1} & i_{z1} \end{bmatrix}^T \tag{2.33}$$

$$\left[\boldsymbol{T}_{\boldsymbol{Clarke}}^{\boldsymbol{1}}\right] = \sqrt{\frac{2}{7}} \begin{bmatrix} (\cos(\delta)-1) & (\cos(2\delta)-1) & (\cos(3\delta)-1) & (\cos(4\delta)-1) & (\cos(5\delta)-1) & (\cos(6\delta)-1) \\ \sin(\delta) & \sin(2\delta) & \sin(3\delta) & \sin(4\delta) & \sin(5\delta) & \sin(6\delta) \\ \cos(2\delta) & \cos(4\delta) & \cos(6\delta) & \cos(8\delta) & \cos(10\delta) & \cos(12\delta) \\ \sin(2\delta) & \sin(4\delta) & \sin(6\delta) & \sin(8\delta) & \sin(10\delta) & \sin(12\delta) \\ \sin(3\delta) & \sin(6\delta) & \sin(9\delta) & \sin(12\delta) & \sin(15\delta) & \sin(18\delta) \\ \sqrt{1/2} & \sqrt{1/2} & \sqrt{1/2} & \sqrt{1/2} & \sqrt{1/2} & \sqrt{1/2} \end{bmatrix} \tag{2.34}$$

$$\left[\boldsymbol{T}_{\boldsymbol{Park}}^{\boldsymbol{1}}\right] = \begin{bmatrix} \cos(\theta) & \sin(\theta) & 0 & 0 & 0 & 0 \\ -\sin(\theta) & \cos(\theta) & 0 & 0 & 0 & 0 \\ 0 & 0 & 1 & 0 & 0 & 0 \\ 0 & 0 & 0 & 1 & 0 & 0 \\ 0 & 0 & 0 & 0 & 1 & 0 \\ 0 & 0 & 0 & 0 & 0 & 1 \end{bmatrix} \tag{2.35}$$

where $[\boldsymbol{T}_{\boldsymbol{Clarke}}^{\boldsymbol{1}}]$ and $[\boldsymbol{T}_{\boldsymbol{Park}}^{\boldsymbol{1}}]$ are new 6-by-6 Clarke and Park matrices as presented in (2.34) and (2.35), respectively.

The index "1" in all elements in (2.33) means that the fundamental currents are considered. As previously discussed, the post-fault 7-phase machine can be considered as an asymmetrical 6-phase machine. Therefore, (d_{11}-q_{11}) and (d_{91}-q_{91}) are 2 reference frames associated with 2 two-phase fictitious machines while x_1 and z_1 are 2 reference frames associated with 2 zero-sequence machines, respectively. If the stator windings are wye-connected, the zero-sequence current i_{z1} is always zero.

New Clarke matrix $[\boldsymbol{T}^{\mathbf{1}}_{\boldsymbol{Clarke}}]$ is determined from $[\boldsymbol{T}^{\boldsymbol{fault}}_{\boldsymbol{Clarke}}]$ in (2.32) by:

1) Removing its fifth row because it is not orthogonal to the first and third row vectors, and frames (α_3-β_3) or (d_3-q_3) in healthy mode become x_1 in faulty mode.
2) Adding coefficient -1 to its first row to respect the orthogonal property between rows.

After the above modifications, the remaining row vectors of the new matrix $[\boldsymbol{T}^{\mathbf{1}}_{\boldsymbol{Clarke}}]$ in (2.34) are orthogonal to each other, allowing to control independently currents in new d-q frames.

To prove the robustness of method (II), the non-sinusoidal back-EMFs are assumed to consist of the 1st, 3rd, and 9th harmonics. The torque has ripples due to the interactions between the fundamental currents and these considered harmonics of the back-EMFs. Indeed, from (2.33)-(2.35), the machine torque T_{em1} with its average torque T_{ave1} and harmonics can be generally described as follows:

$$T_{em1} = \underline{e}_n^T \underline{i} = T_{ave1} + E_{n3} i_{q11} \{ f_1(2\theta) + f_2(4\theta) \} + \underline{e}_{nf}^T \left\{ [\boldsymbol{M_1}] \begin{bmatrix} i_{d91} & i_{q91} & i_{x1} \end{bmatrix}^T \right\} \tag{2.36}$$

$$[\boldsymbol{M_1}] = \begin{bmatrix} 0.363 & 0.521 & 0.232 \\ -0.815 & -0.232 & -0.418 \\ 0.452 & -0.418 & 0.521 \\ 0.452 & 0.418 & -0.521 \\ -0.815 & 0.232 & 0.418 \\ 0.363 & -0.521 & -0.232 \end{bmatrix} \tag{2.37}$$

where $\underline{e}_n$ and $\underline{i}$ are the 7-dimensional vectors of the speed-normalized back-EMFs and currents in natural frame; E_{n3} is the amplitude of the 3rd harmonic of $\underline{e}_n$; f_1 and f_2 are trigonometric functions of 2θ and 4θ, respectively; $\underline{e}_{nf}$ is a 6-dimensional vector of back-EMFs derived from $\underline{e}_n$ by removing the back-EMF of phase *A*; $\boldsymbol{[M_1]}$ is a constant 6-by-3 matrix described in (2.37) and obtained from the 3rd to 5th columns of $[\boldsymbol{T}^{\mathbf{1}}_{\boldsymbol{Clarke}}]^{-\mathbf{1}}$.

The generated torque is constant if a sinusoidal back-EMF machine is considered. In (2.36), currents (i_{d91}, i_{q91}, i_{x1}) can be used to eliminate the impact of the 1st, 3rd and 9th harmonics of $\underline{e}_{nf}$ on torque ripples by simply imposing currents (i_{d91}, i_{q91}, i_{x1}) to be zero. However, torques with frequencies of 2θ and 4θ in T_{em1} cannot be eliminated because of the presence of the 3rd harmonic of back-EMFs with amplitude E_{n3}. Therefore, the 3rd harmonic currents need to be injected to compensate the pulsating torques 2θ and 4θ.

2.3.3.A.2. The injection of the third harmonic currents:

The 3rd harmonic components of current in natural frame (i_{B3}, i_{C3}, i_{D3}, i_{E3}, i_{F3}, i_{G3}) are calculated from new d-q frame currents (i_{x3}, i_{d93}, i_{q93}, i_{d33}, i_{q33}, i_{z3}) as follows:

$$[i_{B3}\ i_{C3}\ i_{D3}\ i_{E3}\ i_{F3}\ i_{G3}]^T = [\boldsymbol{T}^{\mathbf{3}}_{\boldsymbol{Clarke}}]^{-1}[\boldsymbol{T}^{\mathbf{3}}_{\boldsymbol{Park}}]^{-1}[i_{x3}\ i_{d93}\ i_{q93}\ i_{d33}\ i_{q33}\ i_{z3}]^T \tag{2.38}$$

$$[\boldsymbol{T}^{\mathbf{3}}_{\boldsymbol{Clarke}}]=\sqrt{\frac{2}{7}}\begin{bmatrix} \sin(\delta) & \sin(2\delta) & \sin(3\delta) & \sin(4\delta) & \sin(5\delta) & \sin(6\delta) \\ \cos(2\delta) & \cos(4\delta) & \cos(6\delta) & \cos(8\delta) & \cos(10\delta) & \cos(12\delta) \\ \sin(2\delta) & \sin(4\delta) & \sin(6\delta) & \sin(8\delta) & \sin(10\delta) & \sin(12\delta) \\ (\cos(3\delta)-1) & (\cos(6\delta)-1) & (\cos(9\delta)-1) & (\cos(12\delta)-1) & (\cos(15\delta)-1) & (\cos(18\delta)-1) \\ \sin(3\delta) & \sin(6\delta) & \sin(9\delta) & \sin(12\delta) & \sin(15\delta) & \sin(18\delta) \\ \sqrt{1/2} & \sqrt{1/2} & \sqrt{1/2} & \sqrt{1/2} & \sqrt{1/2} & \sqrt{1/2} \end{bmatrix} \tag{2.39}$$

$$[\boldsymbol{T}^{\mathbf{3}}_{\boldsymbol{Park}}] = \begin{bmatrix} 1 & 0 & 0 & 0 & 0 & 0 \\ 0 & 1 & 0 & 0 & 0 & 0 \\ 0 & 0 & 1 & 0 & 0 & 0 \\ 0 & 0 & 0 & \cos(3\theta) & \sin(3\theta) & 0 \\ 0 & 0 & 0 & -\sin(3\theta) & \cos(3\theta) & 0 \\ 0 & 0 & 0 & 0 & 0 & 1 \end{bmatrix} \tag{2.40}$$

where $[\boldsymbol{T}^{\mathbf{3}}_{\boldsymbol{Clarke}}]$ and $[\boldsymbol{T}^{\mathbf{3}}_{\boldsymbol{Park}}]$ are new 6-by-6 Clarke and Park matrices as presented in (2.39) and (2.40), respectively.

Similarly, (d_{33}-q_{33}) and (d_{93}-q_{93}) are 2 reference frames associated with 2 two-phase fictitious machines while x_3 and z_3 are 2 reference frames associated with 2 zero-sequence machines. The zero-sequence current i_{z3} is always zero due to the wye connection of the stator windings.

As $[\boldsymbol{T}^{\mathbf{1}}_{\boldsymbol{Clarke}}]$, 6-by-6 matrix $[\boldsymbol{T}^{\mathbf{3}}_{\boldsymbol{Clarke}}]$ is defined from matrix $[\boldsymbol{T}^{\boldsymbol{fault}}_{\boldsymbol{Clarke}}]$ in (2.32) by:

1) Eliminating its first row and because it is not orthogonal to the third and fifth row vectors, and frames (α_1-β_1) or (d_1-q_1) in healthy mode become x_3 in faulty mode.
2) Adding coefficient -1 to its fifth row due to the requirement of orthogonality. As a result, the orthogonal property of the remaining row vectors in $[\boldsymbol{T}^{\mathbf{3}}_{\boldsymbol{Clarke}}]$ enables to independently control currents in the new d-q frames.

From (2.33)-(2.40), the machine torque T_{m13} including its average torque T_{ave13} and harmonics can be expressed by:

$$\begin{aligned} T_{m13} = T_{ave13} &+ \left\{E_{n3}i_{q11} + E_{n1}i_{q33}\right\}\left\{f_1(2\theta) + f_2(4\theta)\right\} \\ &+ \underline{e}_{nf}^T\left\{[\boldsymbol{M_1}]\begin{bmatrix} i_{d91} & i_{q91} & i_{x1}\end{bmatrix}^T + [\boldsymbol{M_3}]\begin{bmatrix} i_{x3} & i_{d93} & i_{q93}\end{bmatrix}^T\right\} \end{aligned} \tag{2.41}$$

$$[\boldsymbol{M_3}] = \begin{bmatrix} 0.418 & -0.452 & 0.521 \\ 0.521 & -0.363 & -0.232 \\ 0.232 & 0.815 & -0.418 \\ -0.232 & 0.815 & 0.418 \\ -0.521 & -0.363 & 0.232 \\ -0.418 & -0.452 & -0.521 \end{bmatrix} \tag{2.42}$$

where E_{n1} is the amplitude of the 1st harmonic of speed-normalized back-EMFs $\underline{e}_n$; $\boldsymbol{[M_3]}$ is a constant 6-by-3 matrix in (2.42) obtained from the 1st to 3rd columns of $[\boldsymbol{T}^{\mathbf{3}}_{\boldsymbol{Clarke}}]^{-\mathbf{1}}$.

In (2.41), it is noted that to eliminate torque ripples $f_1(2\theta)$ and $f_2(4\theta)$, the 3rd harmonic space current i_{q33} needs to be calculated as follows:

$$i_{q33} = -\frac{E_{n3}}{E_{n1}}i_{q11} \tag{2.43}$$

Therefore, the 1st and 3rd harmonic currents (i_{d11}, i_{q11}, i_{d33}, i_{q33}) must be determined either to preserve the healthy torque or to respect constraints on RMS current and peak voltage.

To reduce the impact of harmonics in $\underline{e}_{nf}$ on torque T_{m13}, the other currents (i_{d91}, i_{q91}, i_{x1}) and (i_{x3}, i_{d93}, i_{q93}) can be defined according to two current design options. Therefore, method (II) is proposed with two options as follows:

1) *Robust Control Approach (Method (II)-RCA)*: guarantees ripple-free torques even when the existing back-EMF harmonics in the second fictitious machines, for example, the 9th harmonic component.
2) *Similar Copper Losses (Method (II)-SCL)*: obtain similar copper losses in healthy phases, avoiding the overheated phase windings.

The details of the two options of method (II) are described in the following subsections.

2.3.3.B. *Method (II)-RCA (Robust Control Approach)*

In this option of method (II), 6 currents (i_{d91}, i_{q91}, i_{x1}) and (i_{x3}, i_{d93}, i_{q93}) are imposed to be zero. Therefore, besides the 1st and 3rd harmonics, if the back-EMFs contain other harmonics such as 9th in the second fictitious machine, the generated torque T_{m13} is still constant and equal to T_{ave13} according to (2.41). Thus, this option is called Robust Control Approach. As a result, the 1st harmonics of the 6 healthy phase currents in natural frame are calculated from (2.33) as follows:

$$i_{B1} = 0.9158 i_{q11} \sin(\theta + 152.8°) \tag{2.44}$$

$$i_{C1} = 0.6899 i_{q11} \sin(\theta + 49°) \tag{2.45}$$

$$i_{D1} = 0.4304 i_{q11} \sin(\theta + 32.6°) \tag{2.46}$$

$$i_{E1} = 0.4304 i_{q11} \sin(\theta - 32.6°) \tag{2.47}$$

$$i_{F1} = 0.6899 i_{q11} \sin(\theta - 49°) \tag{2.48}$$

$$i_{G1} = 0.9158 i_{q11} \sin(\theta - 152.8°) \tag{2.49}$$

These currents are illustrated in Fig. 2.40. It is noted that their amplitudes are different, probably causing overrated RMS currents in phase *B* and phase *G*.

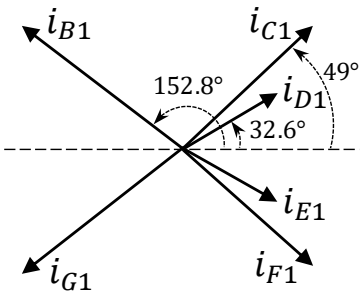

Fig. 2.40. The 1st harmonic components of the 6 remaining healthy phase currents determined with method (II)-RCA when phase *A* is open-circuited.

2.3.3.C. *Method (II)-SCL (Similar Copper Losses)*

In this option, the main idea is to distribute similar copper losses to all healthy phases; hence, the local thermal limit of each machine phase can be respected easily. Due to the back-EMF

harmonic property, the 3rd harmonic currents account for a small proportion compared to the 1st harmonic currents. Therefore, RMS currents as well as copper losses mainly depend on the 1st harmonic currents. Then, the 1st harmonics of the 6 healthy phase currents in natural frame can be determined according to [137] and illustrated in Fig. 2.41. It is noted that their amplitudes are designed to be identical. Expressions for these currents are presented as follows:

$$i_{B1} = 0.6591 i_{q11} \sin(\theta + 21.4°) \tag{2.50}$$

$$i_{C1} = 0.6591 i_{q11} \sin(\theta + 90°) \tag{2.51}$$

$$i_{D1} = 0.6591 i_{q11} \sin(\theta + 158.6°) \tag{2.52}$$

$$i_{E1} = 0.6591 i_{q11} \sin(\theta - 158.6°) \tag{2.53}$$

$$i_{F1} = 0.6591 i_{q11} \sin(\theta - 90°) \tag{2.54}$$

$$i_{G1} = 0.6591 i_{q11} \sin(\theta - 21.4°) \tag{2.55}$$

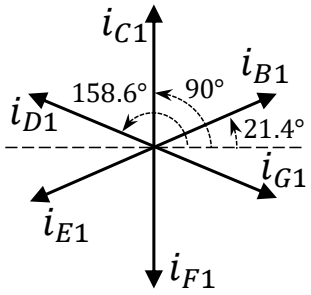

Fig. 2.41. The 1st harmonic components of the 6 remaining healthy phase currents determined with method (II)-SCL when phase *A* is open-circuited.

From (2.33), to obtain the currents as in (2.50)-(2.55), currents (i_{d91}, i_{q91}, i_{x1}) need to be calculated as follows:

$$i_{d91} = -\frac{\sin(6\pi/7)}{\sin(5\pi/7)}\left(i_{d11}\cos(\theta) - i_{q11}\sin(\theta)\right) \tag{2.56}$$

$$i_{q91} = \sqrt{8/7}\sin(6\pi/7)\left[\left(\frac{i_{d11}\sin(\theta) + i_{q11}\cos(\theta)}{\sqrt{8/7}\sin(3\pi/7)} - i_{C1}\right)\left(\frac{\cos(3\pi/7)}{\cos(2\pi/7)}\right) - i_{C1}\right] \tag{2.57}$$

$$i_{x1} = \sqrt{8/7}\sin(2\pi/7)\left[\left(\frac{i_{d11}\sin(\theta) + i_{q11}\cos(\theta)}{\sqrt{8/7}\sin(3\pi/7)} - i_{C1}\right)\left(\frac{\cos(\pi/7)}{\cos(2\pi/7)}\right) - i_{C1}\right] \tag{2.58}$$

However, from (2.41), as currents (i_{d91}, i_{q91}, i_{x1}) are time-variant, these currents interact with the 1st, 3rd and 9th harmonics of back-EMFs in $\underline{e}_{nf}$ to generate torque ripples. By using (2.43), currents (i_{x3}, i_{d93}, i_{q93}), eliminating the torque ripples caused by the 1st and 3rd harmonics of back-EMFs, can be expressed by:

$$i_{d93} = -\frac{\sin(6\pi/7)}{\sin(5\pi/7)}\left(i_{d33}\cos(3\theta) - i_{q33}\sin(3\theta)\right) \tag{2.59}$$

$$i_{q93} = \sqrt{8/7}\sin(6\pi/7)\left[\left(\frac{i_{d33}\sin(3\theta) + i_{q33}\cos(3\theta)}{\sqrt{8/7}\sin(3\pi/7)} - i_{C3}\right)\left(\frac{\cos(3\pi/7)}{\cos(2\pi/7)}\right) - i_{C3}\right] \tag{2.60}$$

$$i_{x3} = \sqrt{8/7}\sin(2\pi/7)\left[\left(\frac{i_{d33}\sin(3\theta) + i_{q33}\cos(3\theta)}{\sqrt{8/7}\sin(3\pi/7)} - i_{C3}\right)\left(\frac{\cos(\pi/7)}{\cos(2\pi/7)}\right) - i_{C3}\right] \tag{2.61}$$

with

$$i_{C3} = 0.6591 i_{q33} \sin(3\theta + 90°) \tag{2.62}$$

Then, the total torque T_{m13} with T_{ave13} and its harmonics can be expressed by:

$$T_{m13} = T_{ave13} + \underline{e}_{nf\_9}^{T} \left\{ [\boldsymbol{M_1}] \begin{bmatrix} i_{d91} & i_{q91} & i_{x1} \end{bmatrix}^T + [\boldsymbol{M_3}] \begin{bmatrix} i_{x3} & i_{d93} & i_{q93} \end{bmatrix}^T \right\} \tag{2.63}$$

where $\underline{e}_{nf\_9}$ is a 6-dimensional vector of the 9th harmonic of back-EMFs derived from $\underline{e}_{nf}$ by removing 1st and 3rd harmonics.

The torque ripples caused by the interaction between the 9th harmonic of back-EMFs $\underline{e}_{nf\_9}$ and 6 variable currents (i_{d91}, i_{q91}, i_{x1}) and (i_{x3}, i_{d93}, i_{q93}) make method (II)-SCL less robust than method (II)-RCA. However, for the optimal calculation in the control scheme (see Fig. 2.21), only the first and third harmonics of the back-EMFs are considered. Therefore, in this case, method (II)-SCL can generate time-constant torques.

2.3.3.D. *Summary of current design options in method (II)*

The summary of the two options of method (II) is described in Table 2.14. As previously discussed, 4 constant currents (i_{d11}, i_{q11}, i_{d33}, i_{q33}) while the other 6 currents can be zero or time-variant subject to different objectives.

Table 2.14. Description of the two options in method (II).

Option	Current design description						Objective
	i_{d91}	i_{q91}	i_{x1}	i_{x3}	i_{d93}	i_{q93}	
Method (II)-RCA	0	0	0	0	0	0	Torque is unaffected by the back-EMF harmonics of the second fictitious machine
Method (II)-SCL	time-variant	time-variant	time-variant	time-variant	time-variant	time-variant	Similar copper losses are distributed in the remaining healthy phases

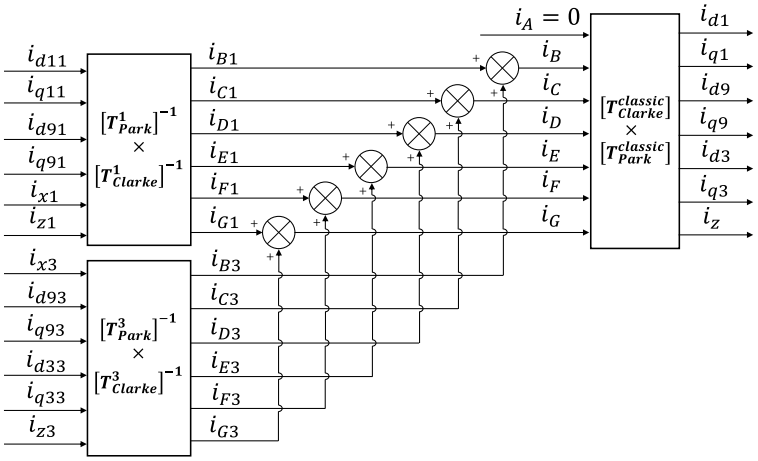

Fig. 2.42. Calculations of time-variant d-q current references by using new reduced-order and classical transformation matrices for the pre-fault control scheme when phase *A* is open-circuited.

After determining d-q currents (i_{d11}, i_{q11}, i_{d91}, i_{q91}, i_{x1}, i_{z1}) and (i_{x3}, i_{d93}, i_{q93}, i_{d33}, i_{q33}, i_{z3}) with either method (II)-RCA or method (II)-SCL, the total phase current reference of a remaining healthy phase is equal to the sum of its 1st and 3rd harmonic currents as shown in Fig. 2.42. If the pre-fault control scheme as described in Fig. 2.6 (or Fig. 2.21) with six current controllers is reused, six current references (i_{d1}, i_{q1}, i_{d9}, i_{q9}, i_{d3}, i_{q3}) need to be calculated. In this doctoral

thesis, the new total phase current references are transformed from natural frame into d-q frames by classical matrices, resulting in time-variant d-q current references for control. Time-variant d-q current references are also presented in [134] when reduced-order matrices for the 1st harmonic currents are reused. The reason for the use of these matrices is that a general transformation for the total currents, including the 1st and 3rd harmonics, has not been found.

2.3.3.E. *Comparative analyses of calculated results with methods (II)-RCA and (II)-SCL*

2.3.3.E.1. Preserving the same torque as in healthy mode:

With the considered drive (see Fig. 2.7), the average torque with the rated RMS current of 5.1 A is 33.3 Nm in healthy mode as discussed in **section 2.1.4**. According to Fig. 2.42, to preserve the pre-fault torque, currents (i_{d91}, i_{q91}, i_{x1}) and (i_{x3}, i_{d93}, i_{q93}), the remaining healthy phase currents, and d-q current references for control (i_{d1}, i_{q1}, i_{d9}, i_{q9}, i_{d3}, i_{q3}) with methods (II)-RCA and (II)-SCL are shown in Fig. 2.43 and Fig. 2.44. Notably, constant currents (i_{d11}=0 A, i_{q11}=15.7 A, i_{d33}=0 A, i_{q33}= -5 A) are not plotted in Fig. 2.43a and Fig. 2.44a for the sake of clarity. Six currents (i_{d91}, i_{q91}, i_{x1}) and (i_{x3}, i_{d93}, i_{q93}) are zero with method (II)-RCA and time-variant with method (II)-SCL. The waveforms of the remaining healthy phase currents with method (II)-RCA are very different to each other (see Fig. 2.43b) while these waveforms with method (II)-SCL are alike (see Fig. 2.44b). The highest peak phase current with method (II)-RCA (18.7 A) is higher than that of method (II)-SCL (14.3 A).

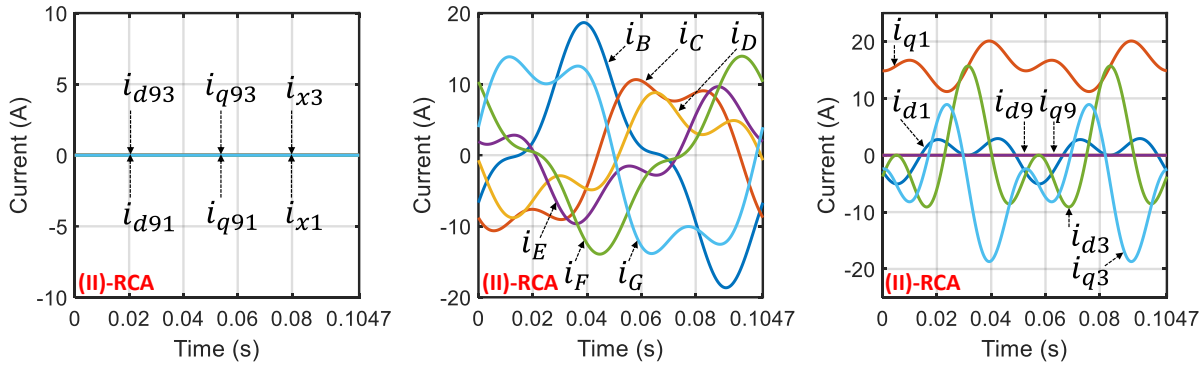

(a) (b) (c)

Fig. 2.43. Desired d-q currents (a), phase currents (b), d-q current references for control (c), with method (II)-RCA for an OC fault in phase *A* to preserve the healthy-mode torque at 20 rad/s with (i_{d11}=0 A, i_{q11}=15.7 A, i_{d33}=0 A, i_{q33}= -5 A).

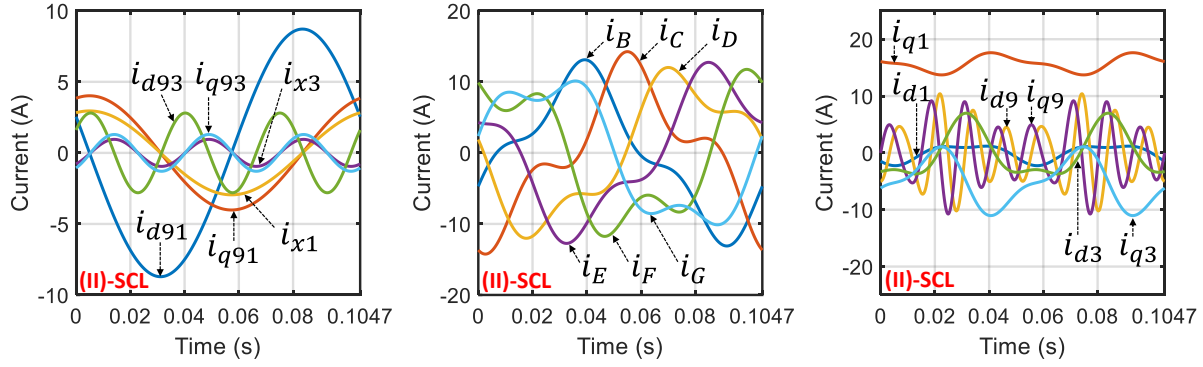

(a) (b) (c)

Fig. 2.44. Desired d-q currents (a), phase currents (b), d-q current references for control (c), with method (II)-SCL for an OC fault in phase *A* to preserve the healthy-mode torque at 20 rad/s with (i_{d11}=0 A, i_{q11}=15.7 A, i_{d33}=0 A, i_{q33}= -5 A).

In Fig. 2.43c, with method (II)-RCA, currents in (i_{d9}, i_{q9}) are zero while the other currents are time-variant. This point once again proves the robustness of method (II)-RCA when its torque is unaffected by the back-EMF harmonics in the second machine (9^{th}, for example). Meanwhile, method (II)-SCL has six time-variant d-q currents (see Fig. 2.44c). Therefore, the torque with method (II)-SCL is sensitive to the back-EMF harmonics in the second machine like methods (I)-2 and (I)-3.

Calculated RMS currents in all phases by the two options of method (II) are described in Table 2.15. It is noted that every calculated RMS current is higher than that of healthy mode (5.1 A). The RMS currents with method (II)-RCA vary from 5.3 to 10.6 A with the highest value in phase *B* and *G*. Meanwhile, these values with method (II)-SCL are similar from 7.6 to 7.9 A with the highest value in phases *C* and *F*. It is concluded that method (II)-RCA creates higher RMS currents than method (II)-SCL for the same torque.

Table 2.15. Calculated RMS currents in all phases with methods (II)-RCA and (II)-SCL for an OC fault in phase *A* when the healthy-mode torque is preserved at 20 rad/s.

Method	RMS current (A)						
	A	*B*	*C*	*D*	*E*	*F*	*G*
Method (II)-RCA	0	10.6	8	5.3	5.3	8	10.6
Method (II)-SCL	0	7.6	7.9	7.6	7.6	7.9	7.6

When only the first and third harmonics of the back-EMFs are considered, comparisons between the two methods and healthy mode are described in Table 2.16. It is noted that the torques by the two methods are constant in this case. In addition, method (II)-RCA generates a higher peak voltage (1.28 pu) and a higher total copper loss (2.25 pu) than method (II)-SCL does (0.99 pu and 1.95 pu, respectively).

Table 2.16. Comparisons between calculated results with methods (II)-RCA and (II)-SCL for an OC fault in phase *A* when the healthy-mode torque is preserved at 20 rad/s.

Method	Torque T_{em}=T_{ave}		Highest RMS current I_{RMS}		Highest peak voltage V_{peak}		Total copper loss P_{loss}	
	(Nm)	(pu)	(A)	(pu)	(V)	(pu)	(W)	(pu)
Healthy mode	33.3	1	5.1	1	45.9	1	255	1
Method (II)-RCA	33.3	1	10.6	2.08	58.9	1.28	572.5	2.25
Method (II)-SCL	33.3	1	7.9	1.55	45.5	0.99	496.4	1.95

pu: per unit where the base values are parameters of healthy mode.

When the back-EMFs have additional harmonics in the second machine, for instance, the 9^{th} harmonic with 12.5%, the torque with method (II)-RCA is still constant while method (II)-SCL generates a torque ripple of 17.6% as described in Fig. 2.45.

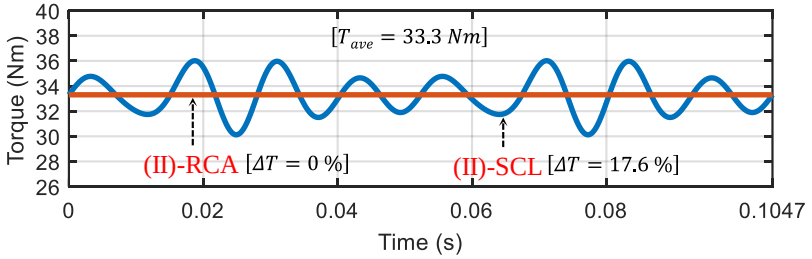

Fig. 2.45. (Calculated result) Torques under an OC fault in phase *A* generated with method (II)-RCA and method (II)-SCL at 20 rad/s when the 1^{st}, 3^{rd} and 9^{th} harmonics of the back-EMFs are considered.

2.3.3.E.2. Optimal calculations under constraints on RMS current and peak voltage:

If the control scheme in Fig. 2.21 with an optimal strategy in (2.16) is considered, the torques obtained by the two options of method (II) will be lower than the pre-fault torque (33.3 Nm). All currents are re-determined to respect the considered constraints. According to the considered drive, the RMS current limit is 5.1 A and the voltage limit for the offline optimization is 75 V. Different from method (I), currents i_{q11} and i_{q33} have a constraint as described in (2.43) to eliminate ripple torques. Therefore, only i_{q11} will be tuned by *fmincon*, then i_{q33} and the other currents will be derived from i_{q11}. As a result, the current waveforms in of all considered currents under constraints are the same as in Fig. 2.43 and Fig. 2.44 but with lower amplitudes generated by the lower d-q currents (i_{d11}=0 A, i_{q11}=7.6 A, i_{d33}=0 A, i_{q33}= -2.4 A).

RMS currents in all phases under the constraints with method (II) at 20 rad/s are described in Table 2.17. In the two options of method (II), the highest RMS currents are reduced to the RMS current limit of 5.1 A.

Table 2.17. Calculated RMS currents in all phases with methods (II)-RCA and (II)-SCL under constraints on RMS current and peak voltage at 20 rad/s when phase *A* is open-circuited.

Method	**RMS current (A)**						
	A	*B*	*C*	*D*	*E*	*F*	*G*
Method (II)-RCA	0	5.1	3.8	2.5	2.5	3.8	5.1
Method (II)-SCL	0	4.9	5.1	4.9	4.9	5.1	4.9

Finally, comparisons between the post-fault operations using the two options of method (II) and healthy mode at 20 rad/s are described in Table 2.18. When the RMS current limit of 5.1 A is respected, method (II)-SCL generates the higher torque at 21.6 Nm (0.65 pu), like method (I)-2. Meanwhile, the torque with method (II)-RCA is lower with 16 Nm (0.48 pu), less than all options of method (I). Additionally, the highest peak voltages V_{peak} by the two options of method (II) are less than that of healthy mode (0.77 and 0.78 pu), making their base speeds higher than that of healthy mode. Total copper losses in fault-tolerant operations are lower than that of healthy mode (0.52 pu for method (II)-RCA and 0.82 pu for method (II)-SCL) due to the current constraint.

Table 2.18. Comparisons between calculated results with methods (II)-RCA and (II)-SCL under constraints on RMS current and peak voltage at 20 rad/s when phase *A* is open-circuited.

Method	**Highest RMS current I_{RMS}**		**Torque T_{em}=T_{ave}**		**Highest peak voltage V_{peak}**		**Total copper loss P_{loss}**	
	(A)	(pu)	(Nm)	(pu)	(V)	(pu)	(W)	(pu)
Healthy mode	5.1	1	33.3	1	45.9	1	255	1
Method (II)-RCA	5.1	1	16	0.48	35.5	0.77	132.1	0.52
Method (II)-SCL	5.1	1	21.6	0.65	36	0.78	208.6	0.82

pu: per unit where the base values are parameters of healthy mode.

When the operating speed varies, the optimal torque-speed characteristics, all RMS phase currents and all peak phase voltages by the two options of method (II) in terms of speed are described in Fig. 2.46. It is noted that method (II)-SCL results in a higher fault-tolerant torque-speed characteristic than method (II)-RCA does. In addition, all options of method (II) respect the constraints on RMS current and peak voltage even in the flux-weakening region. Notably, in the flux-weakening region with method (II), all RMS currents are reduced because only i_{q11}

is tuned by *fmincon*, and the other currents are derived from i_{q11}. If i_{d11} and i_{d33} are varied to be nonzero, the high torque ripples will appear.

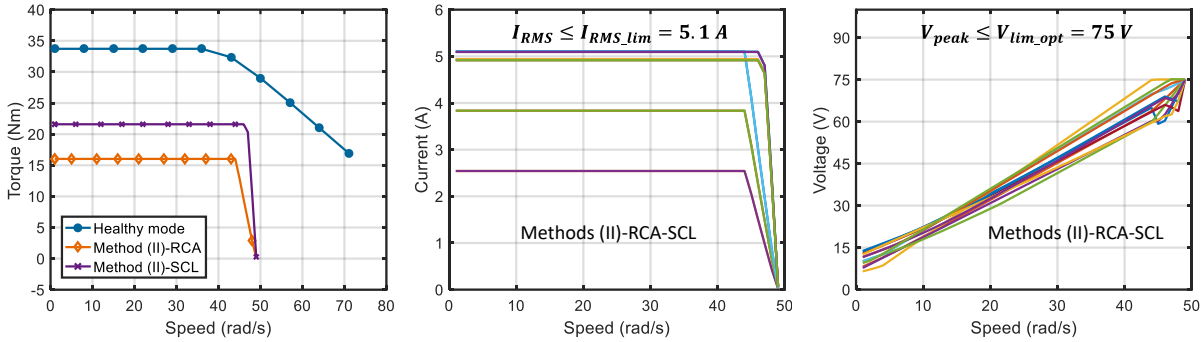

(a) (b) (c)

Fig. 2.46. (Calculated result) Optimal torque-speed characteristics (a), all RMS phase currents (b), and all peak phase voltages (c), in terms of speed under constraints on RMS current and peak voltage with methods (II)-RCA and (II)-SCL when phase *A* is open-circuited.

Table 2.19 describes the calculated base and maximum speeds of the healthy and faulty modes with the two proposed options of method (II). Method (II)-RCL has a base speed of 44 rad/s (1.16 pu) while method (II)-SCL has a base speed of 46 rad/s (1.21 pu). These base speeds are higher than that of healthy mode due to lower voltages V_{peak} (see Table 2.18). The post-fault operations with method (II) have the same maximum speed that is lower than that of healthy mode. In addition, the maximum speed with method (II) (0.67 pu) is shorter than with method (I) (0.88 pu) (see Table 2.11).

Table 2.19. Comparisons between the calculated base and maximum speeds with methods (II)-RCA and (II)-SCL for an OC fault in phase *A* under constraints on RMS current and peak voltage.

Method	Base speed Ω_{base}		Maximum speed Ω_{max}	
	(rad/s)	(pu)	(rad/s)	(pu)
Healthy mode	38	1	73	1
Method (II)-RCA	44	1.16	49	0.67
Method (II)-SCL	46	1.21	49	0.67

pu: per unit where the base values are parameters of healthy mode.

2.3.3.F. *Verification with experimental results for method (II)*

Methods (II)-RCA and (II)-SCL with the control scheme in Fig. 2.21 are validated in the experimental test bench (see **section 2.1.4.A**). As methods (I)-2 and (I)-3, methods (II)-RCA and (II)-SCL can be easily implemented in the test bench without any hardware modifications.

2.3.3.F.1. Current control performance:

To experimentally obtain the optimal torque-speed characteristics (see Fig. 2.46a), six d-q currents (i_{d1}, i_{q1}, i_{d9}, i_{q9}, i_{d3}, i_{q3}) need to properly track their references with waveforms as described in Fig. 2.43c and Fig. 2.44c. At a speed, method (II)-RCL has 4 time-variant current references (i_{d1}, i_{q1}, i_{d3}, i_{q3}) and 2 time-constant current references (i_{d9}, i_{q9}). Meanwhile, 6 current references with method (II)-SCL are time-variant. The current control performances at 20 rad/s are described in Figs 2.47-2.49. Because most current references are time-variant, the current control quality will be reduced at high speed when conventional PI controllers are applied. This phenomenon will be clearly observed in the torque-speed performance. The use of PIR controllers, as in [135, 167], can be a solution to deal with time-variant references at high speed

but several drawbacks have been discussed in **section 1.4** of **Chapter 1**. In this doctoral thesis, this problem can be solved by using ADALINEs in **Chapter 3**.

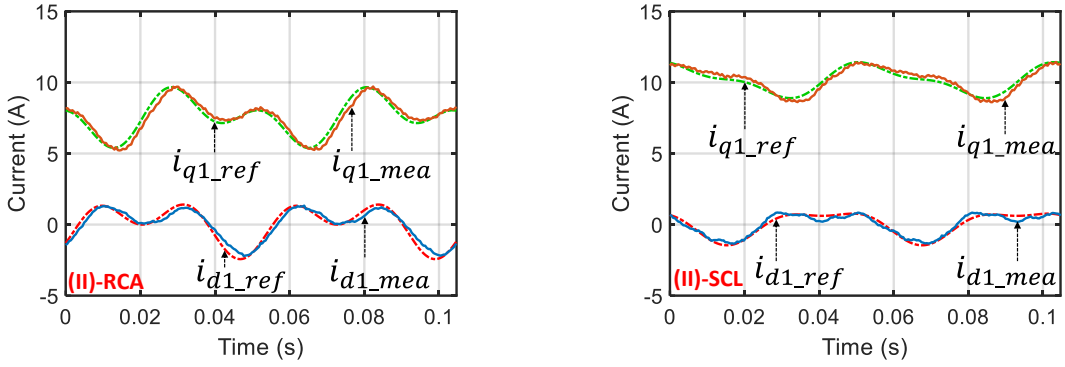

(a) (b)

Fig. 2.47. (Experimental result) Currents in (d_1-q_1) frame at 20 rad/s with method (II)-RCA (a), and with method (II)-SCL (b), when phase *A* is open-circuited.

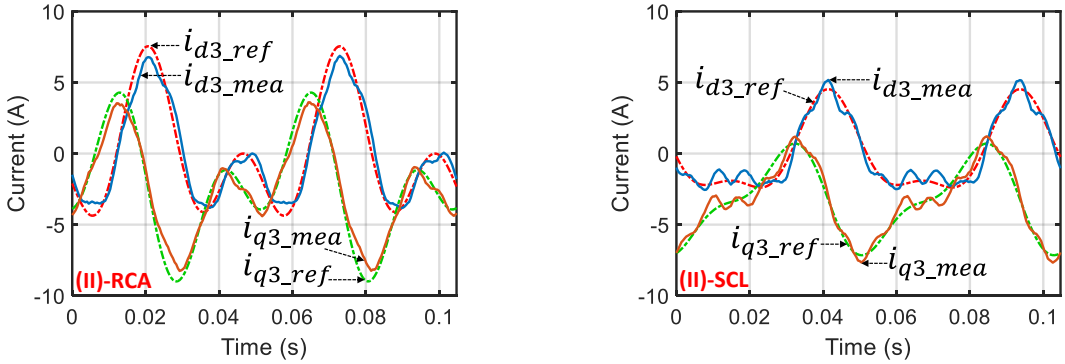

(a) (b)

Fig. 2.48. (Experimental result) Currents in (d_3-q_3) frame at 20 rad/s with method (II)-RCA (a), and with method (II)-SCL (b), when phase *A* is open-circuited.

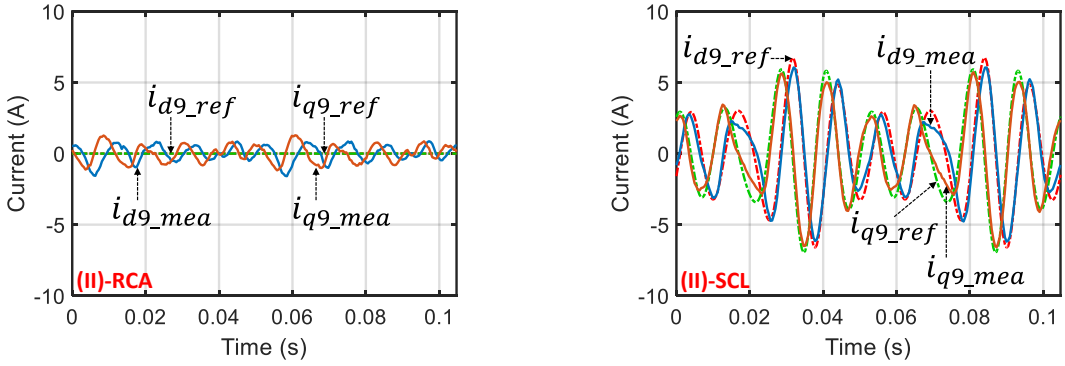

(a) (b)

Fig. 2.49. (Experimental results) Currents in (d_9-q_9) frame at 20 rad/s with method (II)-RCA (a), and with method (II)-SCL (b), when phase *A* is open-circuited.

2.3.3.F.2. Torque performance:

An operation with three operating states at 20 rad/s is shown in Fig. 2.50, including a healthy operation, an OC fault without reconfigurations, and a fault-tolerant operation with one of two methods (II)-RCA and (II)-SCL. The first two operating states have been deeply investigated in **sections 2.1.4** and **2.2**. It is noted that the average torques in the third state with methods (II)-RCA and (II)-SCL are in good accordance with the optimal (calculated) values in Table 2.18. To respect the constraints on RMS current, the average torque is reduced from 33.5 Nm in

healthy mode to 16 Nm (0.48 pu) with method (II)-RCA, and 21.6 Nm (0.64 pu) with method (II)-SCL in the post-fault operation. However, the experimental torques have ripples of 19% with method (II)-RCA and 24% with method (II)-SCL. The experimental back-EMFs with a significant proportion of the 9th harmonic (12.5%) interact with the time-variant currents (i_{d9}, i_{q9}) in methods (II)-SCL. Meanwhile, method (II)-RCA is unaffected by the 9th harmonic, verifying the robustness of method (II)-RCA.

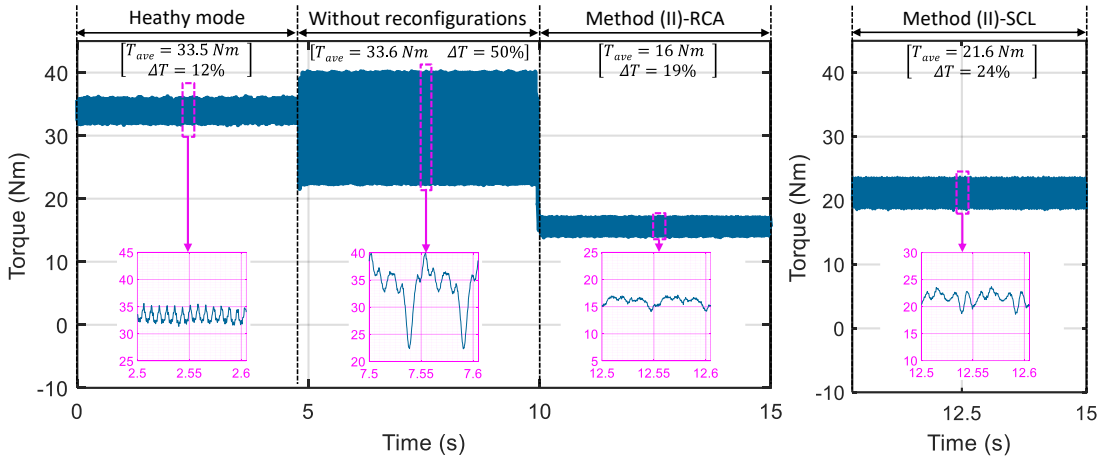

Fig. 2.50. (Experimental result) Torque in three operating states at 20 rad/s including healthy mode, an OC fault in phase *A* without reconfigurations, and when method (II)-RCA (a) and method (II)-SCL (b) are applied.

When the operating speed varies, the experimental torque-speed characteristics with methods (II)-RCA and (II)-SCL in comparison with healthy mode ($T_{em\_opt\_HM}$ and $T_{em\_exp\_HM}$) are described in Fig. 2.51. By using these methods, the experimental post-fault torques ($T_{em\_exp\_OC}$) are in good accordance with the optimal torques ($T_{em\_opt\_OC}$) from Fig. 2.46a. However, the torque ripples increase in both options of method (II) when the rotating speed increases. The reason is that most current references are time-variant, the current control quality is reduced at high speed when conventional PI controllers are applied. The experimental base and maximum speeds are the same as calculated results in Table 2.19.

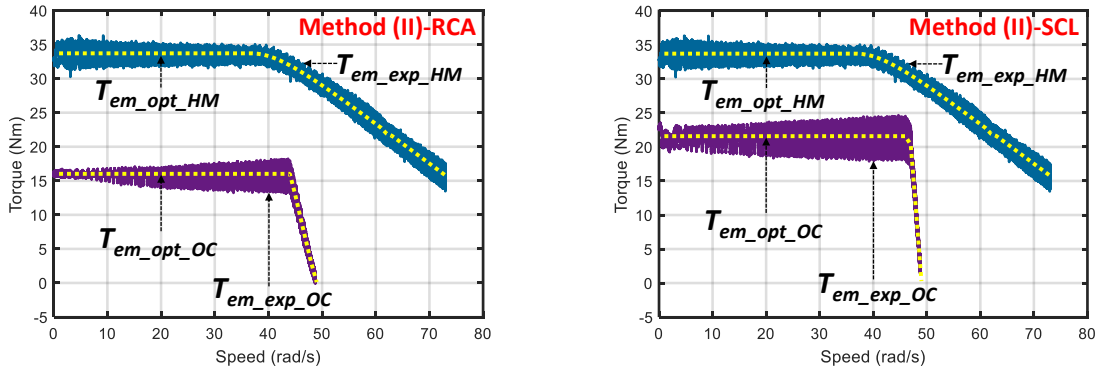

Fig. 2.51. (Experimental result) Post-fault torque-speed characteristics under an OC fault in phase *A* with method (II)-RCA (a), and with method (II)-SCL (b).

2.3.3.F.3. Constraints on RMS current and peak voltage:

Table 2.20 shows that experimental RMS currents in all phases at 20 rad/s are in good accordance with optimal values. The experimental highest RMS currents in both options of method (II) are within their limit 5.1 A. Notably, RMS phase currents with method (II)-SCL are similar in phases.

Table 2.20. Experimental RMS currents in all phases with methods (II)-RCA and (II)-SCL under constraints on RMS current and peak voltage at 20 rad/s.

Method	**RMS current (A)**													
	A		*B*		*C*		*D*		*E*		*F*		*G*	
	opt	exp	opt	exp	opt	exp	opt	exp	opt	exp	opt	exp	opt	exp
Method (II)-RCA	0	0.1	5.1	4.9	3.8	3.3	2.5	2.9	2.5	2.4	3.8	3.8	5.1	5
Method (II)-SCL	0	0.1	4.9	5	5.1	4.8	4.9	4.8	4.9	4.8	5.1	4.9	4.9	5.1

opt: optimal calculated results; exp: experimental results.

When the operating speed varies, the constraints on RMS current and voltage are still respected in the experimental results, including the flux-weakening regions. Measured phase currents obtained by the two methods in terms of speed are described in Figs. 2.52-2.53. The waveforms of measured phase currents at 20 and 47 rad/s are also plotted. The amplitudes of the remaining healthy phase currents are changed at high speed; hence, the highest RMS current is reduced at speeds over the base speed to respect the constraint on peak voltage.

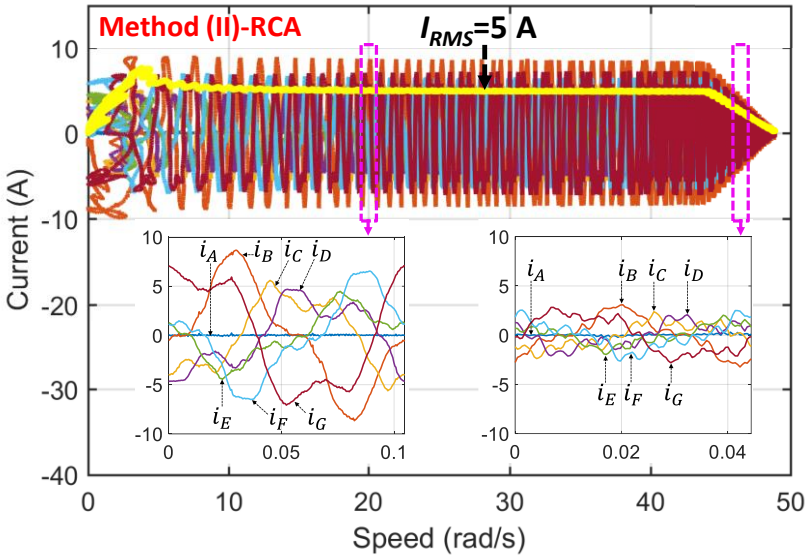

Fig. 2.52. (Experimental result) Phase currents in terms of speed, and current waveforms at 20 and 47 rad/s with method (II)-RCA under an OC fault in phase *A*.

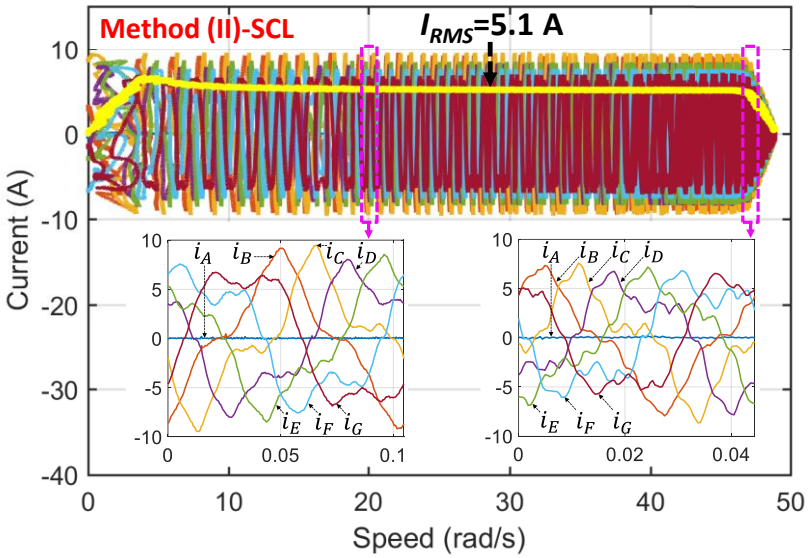

Fig. 2.53. (Experimental result) Phase currents in terms of speed, and current waveforms at 20 and 47 rad/s with method (II)-SCL under an OC fault in phase *A*.

Similarly, experimental phase voltage references with the two methods in terms of speed are presented in Figs. 2.54-2.55. Their waveforms in terms of time at 20 and 47 rad/s are also plotted. It is noted that the peak values of phase voltage references after the base speeds are maximal but relatively under their limit (V_{lim}=100 V).

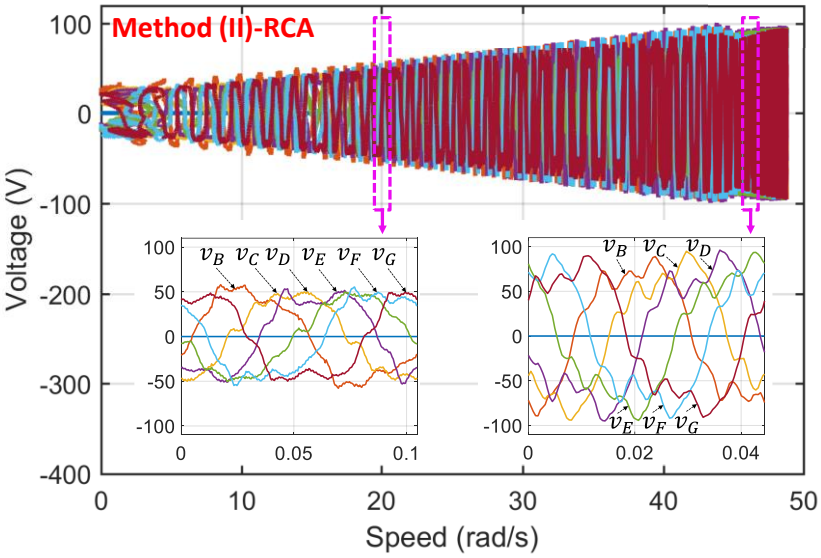

Fig. 2.54 (Experimental result) Phase voltage references in terms of speed, and current waveforms at 20 and 47 rad/s with method (II)-RCA under an OC fault in phase *A*.

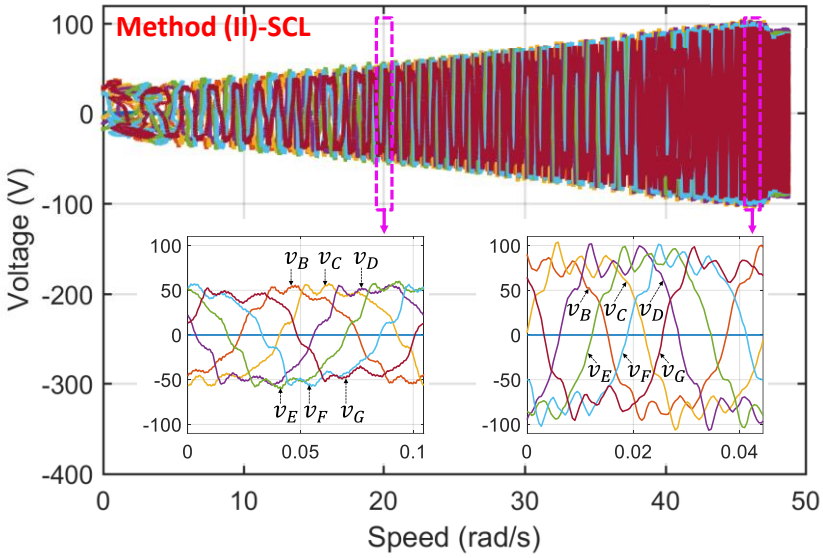

Fig. 2.55 (Experimental result) Phase voltage references in terms of speed, and current waveforms at 20 and 47 rad/s with method (II)-SCL under an OC fault in phase *A*.

2.3.3.F.4. Comparative summary:

A comparative summary of experimental performances in a healthy operation, an OC fault without reconfigurations, and fault-tolerant operations with methods (II)-RCA and (II)-SCL is presented in Table 2.21. The highest RMS currents, torques, highest peak voltages, and total copper losses in the two methods are compared. The performances of current control, torque generations, and constraints have been analyzed in the previous subsections. In general, the calculated and experimental results in Table 2.18 and Table 2.21 are in good accordance. However, the experimental voltage references are higher than the calculated values in Table 2.18 due to the additional voltages caused by high-order harmonics of the experimental back-EMFs.

Table 2.21. Comparisons between experimental results with methods (II)-RCL and (II)-SCL under constraints on RMS current and peak voltage at 20 rad/s.

Method	**Highest RMS current I_{RMS}**		**Torque T_{em}**			**Highest peak voltage V_{peak}**		**Total copper loss P_{loss}**	
	(A)	(pu)	T_{ave} (Nm)	T_{ave} (pu)	ΔT (%)	(V)	(pu)	(W)	(pu)
Healthy mode	5.1	1	33.5	1	12	60	1	255.2	1
OC fault without reconfigurations	7.9	1.55	33.6	1	50	104.1	1.74	323.7	1.27
Method (II)-RCA	5	0.98	16	0.48	19	64.4	1.07	123.4	0.48
Method (II)-SCL	5.1	1	21.6	0.64	24	59.9	1	203.3	0.8

pu: per unit where the base values are parameters of healthy mode.

2.3.4. Method (III): new current references determined from natural frame

2.3.4.A. *Principle of method (III)*

It is noted that new current references of the remaining healthy phases with unidentical waveforms in methods (I) and (II) can theoretically generate constant torques in a non-sinusoidal machine (with the 1st and 3rd harmonics of back-EMFs). However, under the constraints on RMS current, the highest post-fault average torque of the considered drive is equal to 65% of the healthy torque. This torque is relatively low in case only one of seven phases is open-circuited. Accordingly, method (III) is proposed with the aim of improving the average torque by using identical waveforms of the remaining healthy phase currents when one

phase is open-circuited [164, 165, 168-170]. The waveform uniformity of these phase currents allows to:

1) Distribute perfectly equal copper losses among healthy phases, avoiding overheated machine windings.
2) Maximize currents to produce more average torques when the constraint on current is considered. Indeed, under the constraint on RMS current, every remaining healthy phase current can reach their current limit, resulting in the maximum average torque.

In method (III) of this doctoral thesis, analytical torque expressions in natural frame will be used to determine parameters of new phase currents when one phase is open-circuited. Sinusoidal and non-sinusoidal waveforms of currents and back-EMFs are analyzed.

2.3.4.B. *Sinusoidal phase currents for sinusoidal back-EMFs*

In case of an OC fault in phase *A*, the speed-normalized sinusoidal back-EMFs of the remaining healthy phases can be described as follows:

$$\begin{cases} e_{nB} = E_{n1}\sin\left(\theta - \dfrac{2\pi}{7}\right) \\ e_{nC} = E_{n1}\sin\left(\theta - \dfrac{4\pi}{7}\right) \\ e_{nD} = E_{n1}\sin\left(\theta - \dfrac{6\pi}{7}\right) \\ e_{nE} = E_{n1}\sin\left(\theta - \dfrac{8\pi}{7}\right) \\ e_{nF} = E_{n1}\sin\left(\theta - \dfrac{10\pi}{7}\right) \\ e_{nG} = E_{n1}\sin\left(\theta - \dfrac{12\pi}{7}\right) \end{cases} \tag{2.64}$$

where E_{n1} is the amplitude of the speed-normalized sinusoidal back-EMFs; θ is the electrical position. According to [137], the fundamental magnetomotive force in faulty modes needs to be preserved to generate the same constant torque as in healthy mode. In this doctoral thesis, current references in natural frame are generally determined to have the same amplitude with different initial phase angles as follows:

$$\begin{cases} i_B = I_{m1}\sin(\theta + \varphi_B) \\ i_C = I_{m1}\sin(\theta + \varphi_C) \\ i_D = I_{m1}\sin(\theta + \varphi_D) \\ i_E = -i_B \\ i_F = -i_C \\ i_G = -i_D \end{cases} \tag{2.65}$$

where I_{m1} is the amplitude of all healthy phase currents; φ_B, φ_C, and φ_D are initial phase angles of currents in phase *B*, *C* and *D*, respectively. Then, analytical torque expressions in natural

frame can be used to determine parameters of the current references. The electromagnetic torque is analytically expressed by:

$$T_{em} = T_{ave} + T_{2\theta} \tag{2.66}$$

with

$$\begin{cases} T_{ave} = I_{m1}E_{n1}\sin\left(\frac{3\pi}{7}\right)\left\{-2\cos\left(\frac{\varphi_B-\varphi_D}{2}-\frac{2\pi}{7}\right)\sin\left(\frac{\varphi_B+\varphi_D}{2}\right)-\sin(\varphi_C)\right\} \\ T_{2\theta} = I_{m1}E_{n1}\sin\left(\frac{3\pi}{7}\right)\left\{-2\cos\left(\frac{\varphi_B-\varphi_D}{2}+\frac{2\pi}{7}\right)\sin\left(2\theta+\frac{\varphi_B+\varphi_D}{2}\right)-\sin(2\theta+\varphi_C)\right\} \end{cases}$$

where T_{ave} is the average torque; $T_{2\theta}$ is the ripple torque at a frequency of 2θ. To eliminate the ripple torque $T_{2\theta}$ in (2.66), the initial phase angles of the phase currents in (2.65) are simply determined based on trigonometric calculations as follows:

$$\begin{cases} \frac{\varphi_B+\varphi_D}{2} = \varphi_C + 2k_1\pi \\ \frac{\varphi_B-\varphi_D}{2} + \frac{2\pi}{7} = \arccos\left(-\frac{1}{2}\right) = \pm\frac{2\pi}{3} + 2k_2\pi \end{cases} \quad \text{with } k_1 \text{ and } k_2 \in \mathbb{Z} \tag{2.67}$$

As a result, the electromagnetic torque of the machine is perfectly constant. According to (2.67), the initial phase angles and their corresponding torques are calculated with the two following possibilities:

$$\begin{cases} \frac{\varphi_B+\varphi_D}{2} = \varphi_C \\ \frac{\varphi_B-\varphi_D}{2} = \frac{8\pi}{21} \\ T_{em} = T_{ave} = -2.84 I_{m1}E_{n1}\sin(\varphi_C) \end{cases} \tag{2.68}$$

$$\begin{cases} \frac{\varphi_B+\varphi_D}{2} = \varphi_C \\ \frac{\varphi_B-\varphi_D}{2} = -\frac{20\pi}{21} \\ T_{em} = T_{ave} = 0.45 I_{m1}E_{n1}\sin(\varphi_C) \end{cases} \tag{2.69}$$

In (2.68) and (2.69), the torque values are proportional to the amplitudes of the fundamental components of currents and back-EMFs. In addition, the torques T_{em} also depend on the sine function of φ_C.

It is noted that the torque in (2.68) is much higher than (2.69). Thus, the maximal torque and the corresponding initial phase angles are given by:

$$\begin{cases} \varphi_C = -\dfrac{\pi}{2} \\ \varphi_B = -\dfrac{5\pi}{42} \\ \varphi_D = -\dfrac{37\pi}{42} \\ T_{em} = T_{ave} = 2.84 I_{m1} E_{n1} \end{cases} \tag{2.70}$$

These obtained results are similar to the study in [137] for seven-phase induction machines.

2.3.4.C. *Sinusoidal phase currents for non-sinusoidal back-EMFs*

The back-EMFs with the first and third harmonic components in the remaining healthy phases are given by:

$$\begin{cases} e_{nB} = E_{n1}\left\{\sin\left(\theta - \dfrac{2\pi}{7}\right) + k_e \sin\left[3\left(\theta - \dfrac{2\pi}{7}\right) + \varphi_e\right]\right\} \\ e_{nC} = E_{n1}\left\{\sin\left(\theta - \dfrac{4\pi}{7}\right) + k_e \sin\left[3\left(\theta - \dfrac{4\pi}{7}\right) + \varphi_e\right]\right\} \\ e_{nD} = E_{n1}\left\{\sin\left(\theta - \dfrac{6\pi}{7}\right) + k_e \sin\left[3\left(\theta - \dfrac{6\pi}{7}\right) + \varphi_e\right]\right\} \\ e_{nE} = E_{n1}\left\{\sin\left(\theta - \dfrac{8\pi}{7}\right) + k_e \sin\left[3\left(\theta - \dfrac{8\pi}{7}\right) + \varphi_e\right]\right\} \\ e_{nF} = E_{n1}\left\{\sin\left(\theta - \dfrac{10\pi}{7}\right) + k_e \sin\left[3\left(\theta - \dfrac{10\pi}{7}\right) + \varphi_e\right]\right\} \\ e_{nG} = E_{n1}\left\{\sin\left(\theta - \dfrac{12\pi}{7}\right) + k_e \sin\left[3\left(\theta - \dfrac{12\pi}{7}\right) + \varphi_e\right]\right\} \end{cases} \tag{2.71}$$

where k_e is the amplitude ratio of the third harmonic to the first harmonic of the back-EMFs; φ_e is the phase shift angle between the third and first harmonic components of the back-EMFs. If the sinusoidal currents in (2.65) are imposed, the electromagnetic torque is expressed by:

$$T_{em} = T_{ave} + T_{2\theta} + T_{4\theta} \tag{2.72}$$

with

$$\begin{cases} T_{ave} = I_{m1} E_{n1} \sin\left(\dfrac{3\pi}{7}\right)\left\{-2\cos\left(\dfrac{\varphi_B - \varphi_D}{2} - \dfrac{2\pi}{7}\right)\sin\left(\dfrac{\varphi_B + \varphi_D}{2}\right) - \sin(\varphi_C)\right\} \\ T_{2\theta} = I_{m1} E_{n1} \left\{\begin{array}{l} \sin\left(\dfrac{3\pi}{7}\right)\left\{-2\cos\left(\dfrac{\varphi_B - \varphi_D}{2} + \dfrac{2\pi}{7}\right)\sin\left(2\theta + \dfrac{\varphi_B + \varphi_D}{2}\right) - \sin(2\theta + \varphi_C)\right\} \\ + k_e \sin\left(\dfrac{9\pi}{7}\right)\left\{2\cos\left(\dfrac{\varphi_B - \varphi_D}{2} - \dfrac{6\pi}{7}\right)\sin\left(2\theta - \dfrac{\varphi_B + \varphi_D}{2} + \varphi_e\right) + \sin(2\theta - \varphi_C + \varphi_e)\right\} \end{array}\right\} \\ T_{4\theta} = I_{m1} E_{n1} k_e \sin\left(\dfrac{9\pi}{7}\right)\left\{-2\cos\left(\dfrac{\varphi_B - \varphi_D}{2} + \dfrac{6\pi}{7}\right)\sin\left(4\theta + \dfrac{\varphi_B + \varphi_D}{2} + \varphi_e\right) - \sin(4\theta + \varphi_C + \varphi_e)\right\} \end{cases}$$

where T_{ave} is the average torque; $T_{2\theta}$ and $T_{4\theta}$ are the ripple torques at frequencies of 2θ and 4θ, respectively. Compared to (2.66), the torque in (2.72) has additional components associated with k_e including an extra term of $T_{2\theta}$ and the ripple torque $T_{4\theta}$.

2.3.4.C.1. An attempt to eliminate all ripple torques:

To eliminate $T_{4\theta}$ in (2.72), the initial phase angles of the currents need to respect:

$$\begin{cases} \dfrac{\varphi_B+\varphi_D}{2} = \varphi_C + 2k_1\pi \\ \dfrac{\varphi_B-\varphi_D}{2} + \dfrac{6\pi}{7} = \arccos\left(-\dfrac{1}{2}\right) = \pm\dfrac{2\pi}{3} + 2k_2\pi \end{cases} \quad \text{with } k_1 \text{ and } k_2 \in \mathbb{Z} \tag{2.73}$$

After eliminating $T_{4\theta}$, the remaining torques including T_{ave} and $T_{2\theta}$ with corresponding initial phase angles of the currents can be calculated as follows:

$$\begin{cases} \dfrac{\varphi_B+\varphi_D}{2} = \varphi_C \\ \dfrac{\varphi_B-\varphi_D}{2} = -\dfrac{4\pi}{21} \\ T_{ave} = -1.12 I_{m1} E_{n1} \sin(\varphi_C) \\ T_{2\theta} = I_{m1} E_{n1} \{-2.84\sin(2\theta+\varphi_C) + k_e 0.76\sin(2\theta-\varphi_C+\varphi_e)\} \end{cases} \tag{2.74}$$

or

$$\begin{cases} \dfrac{\varphi_B+\varphi_D}{2} = \varphi_C \\ \dfrac{\varphi_B-\varphi_D}{2} = -\dfrac{32\pi}{21} \\ T_{ave} = -2.59 I_{m1} E_{n1} \sin(\varphi_C) \\ T_{2\theta} = I_{m1} E_{n1} \{0.45\sin(2\theta+\varphi_C) - k_e 1.35\sin(2\theta-\varphi_C+\varphi_e)\} \end{cases} \tag{2.75}$$

Remarks:

1) With arbitrary values of k_e and φ_C, the ripple torques $T_{2\theta}$ in (2.74)-(2.75) cannot be nullified. It means that the attempt to eliminate all ripple torques is unfeasible due to the waveform uniformity of the remaining phase currents in (2.65).
2) In only two special values of k_e, ripple torques $T_{2\theta}$ in (2.74)-(2.75) can be nullified to obtain constant torques. Specifically, k_e must be 3.74 in (2.74) and 0.33 in (2.75). At the same time, φ_C must be $0.5\varphi_e$. However, if the first and third harmonic back-EMFs are in phase (φ_e=0), the average torques T_{ave} in both cases become zero due to (φ_C=0.5φ_e=0).
3) In (2.74) and (2.75), the average torques are proportional to the amplitudes of the fundamental components of currents (I_{m1}) and back-EMFs (E_{n1}). In addition, the torque values also depend on the sine function of φ_C. The maximum average torque in (2.75) is higher than (2.74) but less than in (2.70).
4) From the above analyses, current parameters in (2.74)-(2.75) will not be used in method (III).

2.3.4.C.2. An attempt to increase the average torque:

Accordingly, if the initial current angles in (2.70) are applied in (2.72), the average torque T_{ave} is significantly increased 10% compared to (2.75). In this case, only one part of $T_{2\theta}$ is eliminated, and the remaining torques become:

$$\begin{cases} \varphi_C = -\dfrac{\pi}{2} \\ \varphi_B = -\dfrac{5\pi}{42} \\ \varphi_D = -\dfrac{37\pi}{42} \\ T_{ave} = 2.84 I_{m1} E_{n1} \\ T_{2\theta} = -0.9 I_{m1} E_{n1} k_e \cos(2\theta + \varphi_e) \\ T_{4\theta} = 0.36 I_{m1} E_{n1} k_e \cos(4\theta + \varphi_e) \end{cases} \tag{2.76}$$

It is noted that the amplitudes of the torque ripples depend on the amplitude ($E_{n1}k_e$) and the phase shift angle (φ_e) of the third harmonic in the back-EMFs.

2.3.4.D. *Non-sinusoidal phase currents for non-sinusoidal back-EMFs*

The injection of the third harmonic component aims at improving the average torque with reasonable existing ripples. The phase currents considering the additional third harmonic components are expressed by:

$$\begin{cases} i_B = I_{m1}\{\sin(\theta + \varphi_B) + k_i \sin[3(\theta + \varphi_B) + \varphi_i]\} \\ i_C = I_{m1}\{\sin(\theta + \varphi_C) + k_i \sin[3(\theta + \varphi_C) + \varphi_i]\} \\ i_D = I_{m1}\{\sin(\theta + \varphi_D) + k_i \sin[3(\theta + \varphi_D) + \varphi_i]\} \\ i_E = -i_B \\ i_F = -i_C \\ i_G = -i_D \end{cases} \tag{2.77}$$

where k_i is the amplitude ratio of the third harmonic to the first harmonic of the currents; φ_i is the phase shift angle between the third and first harmonic components of the currents. As a result, the electromagnetic torque consists of a constant torque, ripple torques with frequencies of 2θ, 4θ, and 6θ as follows:

$$T_{em} = T_{ave} + T_{2\theta} + T_{4\theta} + T_{6\theta} \tag{2.78}$$

with

$$\begin{cases} T_{ave} = I_{m1}E_{n1}\begin{Bmatrix} \sin\left(\frac{3\pi}{7}\right)\left\{-2\cos\left(\frac{\varphi_B-\varphi_D}{2}-\frac{2\pi}{7}\right)\sin\left(\frac{\varphi_B+\varphi_D}{2}\right)-\sin(\varphi_C)\right\} \\ +k_ek_i\sin\left(\frac{9\pi}{7}\right)\left\{-2\cos\left(3\left(\frac{\varphi_B-\varphi_D}{2}\right)-\frac{6\pi}{7}\right)\sin\left(3\left(\frac{\varphi_B+\varphi_D}{2}\right)+\varphi_i-\varphi_e\right)-\sin(3\varphi_C+\varphi_i-\varphi_e)\right\} \end{Bmatrix} \\ T_{2\theta} = I_{m1}E_{n1}\begin{Bmatrix} \sin\left(\frac{3\pi}{7}\right)\left\{-2\cos\left(\frac{\varphi_B-\varphi_D}{2}+\frac{2\pi}{7}\right)\sin\left(2\theta+\frac{\varphi_B+\varphi_D}{2}\right)-\sin(2\theta+\varphi_C)\right\} \\ +k_e\sin\left(\frac{9\pi}{7}\right)\left\{2\cos\left(-\left(\frac{\varphi_B-\varphi_D}{2}\right)+\frac{6\pi}{7}\right)\sin\left(2\theta-\frac{\varphi_B+\varphi_D}{2}+\varphi_e\right)+\sin(2\theta-\varphi_C+\varphi_e)\right\} \\ +k_i\sin\left(\frac{3\pi}{7}\right)\left\{-2\cos\left(3\left(\frac{\varphi_B-\varphi_D}{2}\right)-\frac{2\pi}{7}\right)\sin\left(2\theta+3\left(\frac{\varphi_B+\varphi_D}{2}\right)+\varphi_i\right)-\sin(2\theta+3\varphi_C+\varphi_i)\right\} \end{Bmatrix} \\ T_{4\theta} = I_{m1}E_{n1}\begin{Bmatrix} k_e\sin\left(\frac{9\pi}{7}\right)\left\{-2\cos\left(\frac{\varphi_B-\varphi_D}{2}+\frac{6\pi}{7}\right)\sin\left(4\theta+\frac{\varphi_B+\varphi_D}{2}+\varphi_e\right)-\sin(4\theta+\varphi_C+\varphi_e)\right\} \\ +k_i\sin\left(\frac{3\pi}{7}\right)\left\{-2\cos\left(3\left(\frac{\varphi_B-\varphi_D}{2}\right)+\frac{2\pi}{7}\right)\sin\left(4\theta+3\left(\frac{\varphi_B+\varphi_D}{2}\right)+\varphi_i\right)-\sin(4\theta+3\varphi_C+\varphi_i)\right\} \end{Bmatrix} \\ T_{6\theta} = I_{m1}E_{n1}k_ek_i\sin\left(\frac{9\pi}{7}\right)\left\{-2\cos\left(3\left(\frac{\varphi_B-\varphi_D}{2}\right)+\frac{6\pi}{7}\right)\sin\left(6\theta+3\left(\frac{\varphi_B+\varphi_D}{2}\right)+\varphi_i+\varphi_e\right)-\sin(6\theta+3\varphi_C+\varphi_i+\varphi_e)\right\} \end{cases}$$

Compared to (2.72), T_{ave}, $T_{2\theta}$ and $T_{4\theta}$ in (2.78) have extra terms associated with k_i. In addition, the torque also contains a ripple with frequency 6θ associated with both k_i and k_e.

2.3.4.D.1. An attempt to eliminate all ripple torques:

To eliminate $T_{6\theta}$ in (2.78), the initial phase angles of the currents need to respect:

$$\begin{cases} \frac{\varphi_B+\varphi_D}{2} = \varphi_C + 2k_1\pi \\ 3\left(\frac{\varphi_B-\varphi_D}{2}\right)+\frac{6\pi}{7} = \arccos\left(-\frac{1}{2}\right) = \pm\frac{2\pi}{3}+2k_2\pi \end{cases} \quad \text{with } k_1 \text{ and } k_2 \in \mathbb{Z} \tag{2.79}$$

After eliminating $T_{6\theta}$, the remaining torques including T_{ave}, $T_{2\theta}$ and $T_{4\theta}$ with corresponding initial phase angles of the currents are expressed by:

$$\begin{cases} \frac{\varphi_B+\varphi_D}{2} = \varphi_C \\ 3\left(\frac{\varphi_B-\varphi_D}{2}\right) = -\frac{4\pi}{21} \\ T_{ave} = I_{m1}E_{n1}\left\{-1.86\sin(\varphi_C)-0.76k_ek_i\sin(3\varphi_C+\varphi_i-\varphi_e)\right\} \\ T_{2\theta} = I_{m1}E_{n1}\left\{-2.47\sin(2\theta+\varphi_C)+0.73k_e\sin(2\theta-\varphi_C+\varphi_e)-1.12k_i\sin(2\theta+3\varphi_C+\varphi_i)\right\} \\ T_{4\theta} = I_{m1}E_{n1}\left\{-0.46k_e\sin(4\theta+\varphi_C+\varphi_e)-2.84k_i\sin(4\theta+3\varphi_C+\varphi_i)\right\} \end{cases} \tag{2.80}$$

or

$$\begin{cases} \dfrac{\varphi_B+\varphi_D}{2}=\varphi_C \\ 3\left(\dfrac{\varphi_B-\varphi_D}{2}\right)=-\dfrac{32\pi}{21} \\ T_{ave}=I_{m1}E_{n1}\{0.58\sin(\varphi_C)+1.35k_ek_i\sin(3\varphi_C+\varphi_i-\varphi_e)\} \\ T_{2\theta}=I_{m1}E_{n1}\{-2.47\sin(2\theta+\varphi_C)-0.14k_e\sin(2\theta-\varphi_C+\varphi_e)-2.59k_i\sin(2\theta+3\varphi_C+\varphi_i)\} \\ T_{4\theta}=I_{m1}E_{n1}\{1.5k_e\sin(4\theta+\varphi_C+\varphi_e)+0.45k_i\sin(4\theta+3\varphi_C+\varphi_i)\} \end{cases} \quad (2.81)$$

After nullifying $T_{6\theta}$, to continue eliminating $T_{4\theta}$ in (2.80), the initial phase angles of the currents need to respect:

$$\begin{cases} \dfrac{\varphi_B+\varphi_D}{2}=\varphi_C \\ 3\left(\dfrac{\varphi_B-\varphi_D}{2}\right)=-\dfrac{4\pi}{21} \\ k_i=-\dfrac{0.46k_e}{2.84}=-0.16k_e \\ \varphi_i=\varphi_e-2\varphi_C \\ T_{ave}=I_{m1}E_{n1}\{-1.86-0.76k_ek_i\}\sin(\varphi_C) \\ T_{2\theta}=I_{m1}E_{n1}\{-2.47\sin(2\theta+\varphi_C)+0.73k_e\sin(2\theta-\varphi_C+\varphi_e)+0.16k_e\sin(2\theta+\varphi_C+\varphi_e)\} \end{cases} \quad (2.82)$$

Meanwhile, to eliminate $T_{4\theta}$ in (2.81), the initial phase angles of the currents need to respect:

$$\begin{cases} \dfrac{\varphi_B+\varphi_D}{2}=\varphi_C \\ 3\left(\dfrac{\varphi_B-\varphi_D}{2}\right)=-\dfrac{32\pi}{21} \\ k_i=-\dfrac{1.5k_e}{0.45}=-3.33k_e \\ \varphi_i=\varphi_e-2\varphi_C \\ T_{ave}=I_{m1}E_{n1}\{0.58+1.35k_ek_i\}\sin(\varphi_C) \\ T_{2\theta}=I_{m1}E_{n1}\{-2.47\sin(2\theta+\varphi_C)-0.14k_e\sin(2\theta-\varphi_C+\varphi_e)+8.63k_e\sin(2\theta+\varphi_C+\varphi_e)\} \end{cases} \quad (2.83)$$

Remarks:

1) From (2.82) and (2.83), it is concluded that all ripple torques cannot be eliminated.
2) Compared to (2.70) and (2.76), the average torques in (2.82) and (2.83) are lower.
3) From the above remarks, the current parameters in (2.82) and (2.83) will not be used in method (III).

2.3.4.D.2. An attempt to increase the average torque:

From the above remarks, if the initial current angles in (2.70) are applied in (2.78), the average torque T_{ave} is significantly increased compared to (2.82) and (2.83). In this case, only one part of $T_{2\theta}$ is eliminated, and the remaining torques are described as follows:

$$\begin{cases} \varphi_C = -\dfrac{\pi}{2} \\ \varphi_B = -\dfrac{5\pi}{42} \\ \varphi_D = -\dfrac{37\pi}{42} \\ T_{ave} = I_{m1}E_{n1}\{2.84 + 1.76k_e k_i \cos(\varphi_i - \varphi_e)\} \\ T_{2\theta} = I_{m1}E_{n1}\{-0.9k_e \cos(2\theta + \varphi_e) + 0.78k_i \cos(2\theta + \varphi_i)\} \\ T_{4\theta} = I_{m1}E_{n1}\{0.36k_e \cos(4\theta + \varphi_e) - 0.54k_i \cos(4\theta + \varphi_i)\} \\ T_{6\theta} = 2.35I_{m1}E_{n1}k_e k_i \cos(6\theta + \varphi_e + \varphi_i) \end{cases} \quad (2.84)$$

Remarks:

1) It is noted that the average torque in (2.84) can be higher than (2.70) and (2.76), especially when φ_i is equal to φ_e. Accordingly, non-sinusoidal currents in (2.77) with parameters in (2.84) can meet the general requirement of method (III) to generate a high average torque.
2) The amplitudes of the torque harmonics depend on not only the amplitude ($E_{n1}k_e$) and the phase shift angle (φ_e) of the third harmonic in the back-EMFs but also the amplitude ($I_{m1}k_i$) and the phase shift angle (φ_i) of the third harmonic of the phase currents.
3) All torques including T_{ave} and torque harmonics are proportional to the current amplitude I_{m1}. Therefore, the total torque ripple ΔT calculated in (2.17) is unaffected by I_{m1}.
4) Phase angle φ_i equal to φ_e enables to not only maximize the average torque T_{ave} but also reduce torque ripples $T_{2\theta}$ and $T_{4\theta}$. Indeed, in this case, two terms have the same cosine functions with frequency 2θ in $T_{2\theta}$ (and 4θ in $T_{4\theta}$) but opposite signs.

To simply illustrate the impact of current parameters in (2.84) on torque generations, parameters of the machine drive in **section 2.1.4.A** with k_e=0.32 and φ_e=0.9 are considered.

Fig. 2.56a shows the impact of φ_i on the torque generations when k_i is supposed to be k_e. It is noted that when φ_i is equal φ_e, the average torque T_{ave} is highest and the torque ripple ΔT is lowest. In addition, when φ_i varies, the torque ripple rapidly increases.

Meanwhile, the impact of k_i on the torque generation is described in Fig. 2.56b when φ_i is supposed to be φ_e. The value of k_i equal to k_e gives the best values of the torque ripple and average torque, and the torque ripple rapidly increases when k_i exceeds k_e.

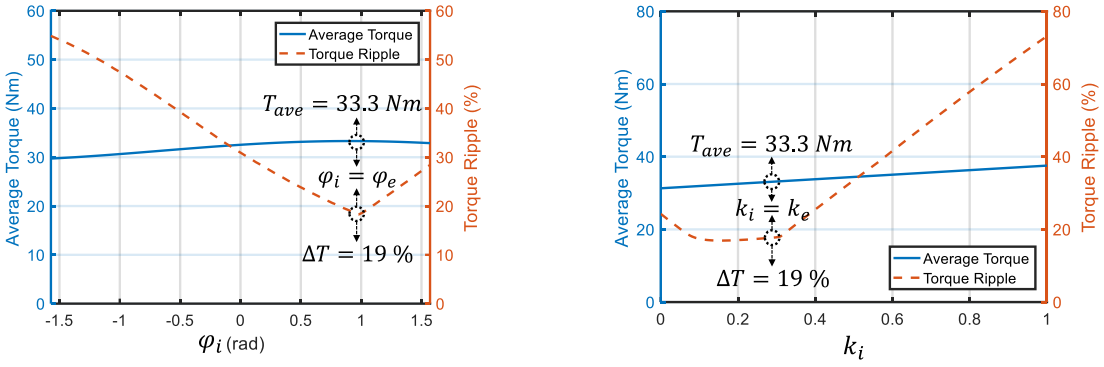

Fig. 2.56. Impacts of φ_i (a) and k_i (b) on the average torque and the ripple torque when new phase current references are determined in (2.77) and (2.84) for an OC fault in phase *A*.

In conclusion, the remaining healthy phase currents with waveforms like the back-EMF waveform, such as in Fig. 2.57, can generate the highest average torque and lowest torque ripple in the case of the uniformity of current waveforms.

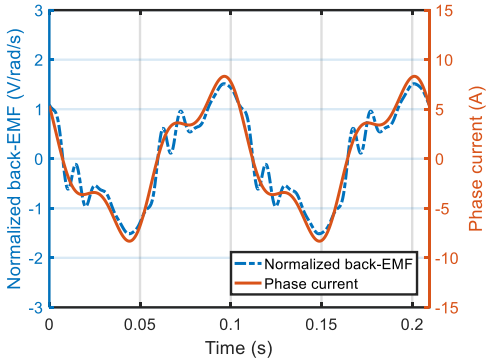

Fig. 2.57. The current reference of a remaining phase determined in (2.77) and (2.84), and the considered experimental speed-normalized back-EMF at 20 rad/s for an OC fault in phase *A*.

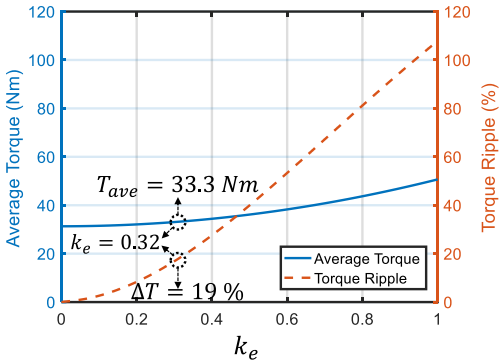

Fig. 2.58. Impacts of k_e on the average torque and the ripple torque when new phase current references are determined in (2.77) and (2.84) for an OC fault in phase *A*.

Notably, this approach cannot guarantee a smooth torque with a machine having a high proportion of the third harmonic in its back-EMFs. Indeed, Fig. 2.58 shows that the torque ripple and average torque are proportional to k_e. However, with an increase in k_e, the improvement of the average torque is not significant while the torque ripple dramatically rises.

2.3.4.E. *Summary of current design options in method (III)*

The possible average torque in (2.84) is highest among the above considerations, followed by the torque in (2.76). It is noted that (2.76) is a special case of (2.84) when sinusoidal currents are considered (k_i=0). Therefore, method (III) can be divided into two design options denoted by method (III)-1 and method (III)-2. These options are described in Table 2.22 with phase current expressions in (2.77).

Table 2.22. Description of the two options in method (III).

Option	Current design description					Objective
	φ_B	φ_C	φ_D	k_i	φ_i	
Method (III)-1	$-\frac{5\pi}{42}$	$-\frac{\pi}{2}$	$-\frac{37\pi}{42}$	0	0	Enhance the average torque by using only sinusoidal currents $T_{ave} = 2.84 I_{m1} E_{n1}$
Method (III)-2	$-\frac{5\pi}{42}$	$-\frac{\pi}{2}$	$-\frac{37\pi}{42}$	k_e	φ_e	Enhance the average torque by using non-sinusoidal currents with the waveform of back-EMFs $T_{ave} = I_{m1} E_{n1} \{2.84 + 1.76 k_e^2\}$

2.3.4.F. *Comparative analyses of calculated results with methods (III)-1 and (III)-2*

2.3.4.F.1. Preserving the same torque as in healthy mode:

In the considered drive, the average torque, with the rated RMS current of 5.1 A, is 33.3 Nm in healthy mode as discussed in **section 2.1.4**.

The remaining healthy phase currents and d-q current references, determined with methods (III)-1 and (III)-2, are shown in Fig. 2.59 and Fig. 2.60. In each option of method (III), the waveforms of the remaining healthy phase currents are the same as shown in Fig. 2.59a and Fig. 2.60a. Method (III)-1 has two constant currents (i_{d1}, i_{q1}) and four time-variant currents (i_{d9}, i_{q9}, i_{d3}, i_{q3}) for control. Meanwhile, all currents for control with method (III)-2 are time-variant. However, it is noted that the main d-q currents (i_{d1}, i_{q1}), generating most of the torque, are constant in method (III)-1 and slightly fluctuate in method (III)-2.

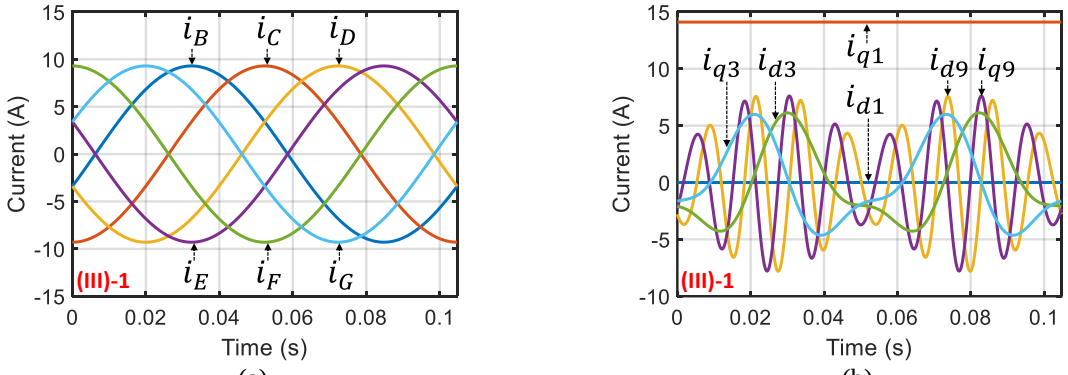

(a) (b)

Fig. 2.59. Desired phase currents (a), and d-q currents (b), with method (III)-1 for an OC fault in phase *A* to preserve the healthy-mode torque at 20 rad/s (I_{m1}=9.3 A).

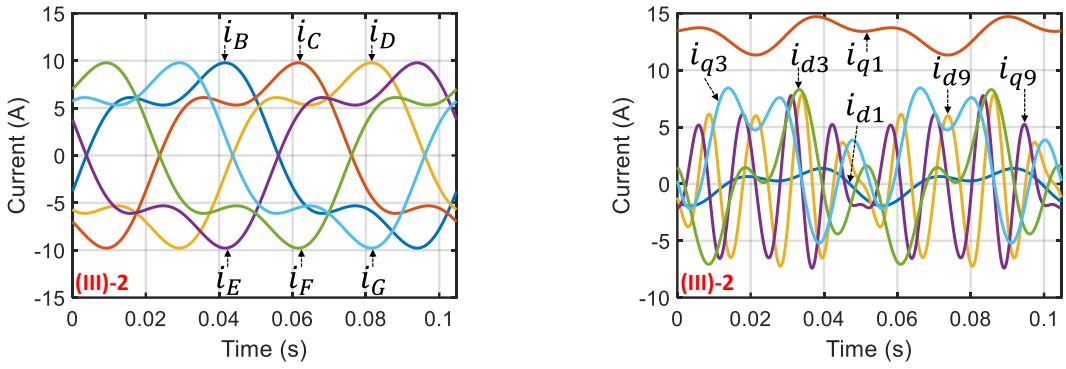

(a) (b)

Fig. 2.60. Desired phase currents (a), and d-q currents (b), with method (III)-2 for an OC fault in phase *A* to preserve the healthy-mode torque at 20 rad/s (I_{m1}=8.7 A).

Calculated RMS currents in all phases by the two options of method (III) are described in Table 2.23. It is noted that all calculated RMS currents in each option of method (III) are the same and slightly higher than healthy mode (5.1 A).

Table 2.23. Calculated RMS currents in all phases with methods (III)-1 and (III)-2 for an OC fault in phase *A* when the healthy-mode torque is preserved at 20 rad/s.

Method	**RMS current (A)**						
	A	*B*	*C*	*D*	*E*	*F*	*G*
Method (III)-1	0	6.6	6.6	6.6	6.6	6.6	6.6
Method (III)-2	0	6.5	6.5	6.5	6.5	6.5	6.5

When only the first and third harmonics of the back-EMFs are considered, comparisons between the two options of method (III) and healthy mode are described in Table 2.24. The torques generated with method (III) are not constant as in methods (I) and (II). Specifically, method (III)-1 generates a higher torque ripple (24%) than method (III)-2 does (19%). Compared to methods (I) and (II) (see Table 2.8 and Table 2.16), method (III) has lower RMS currents I_{RMS} and total copper losses P_{loss} for the same torque.

Table 2.24. Comparisons between calculated results with methods (III)-1 and (III)-2 for an OC fault in phase *A* when the healthy-mode torque is preserved at 20 rad/s.

Method	**Torque T_{em}**			**Highest RMS current I_{RMS}**		**Highest peak voltage V_{peak}**		**Total copper loss P_{loss}**	
	T_{ave} (Nm)	(pu)	ΔT (%)	(A)	(pu)	(V)	(pu)	(W)	(pu)
Healthy mode	33.3	1	0	5.1	1	45.9	1	255	1
Method (III)-1	33.3	1	24	6.6	1.29	40	0.87	363.1	1.42
Method (III)-2	33.3	1	19	6.5	1.27	37.6	0.82	352.3	1.38

pu: per unit where the base values are parameters of healthy mode.

2.3.4.F.2. Optimal calculations under constraints on RMS current and peak voltage:

Similar to methods (I) and (II), if the control scheme in Fig. 2.21 with an optimal strategy in (2.16) is considered, the torques obtained by the two options of method (III) become lower than the pre-fault torque (33.3 Nm). All currents are re-determined to respect constraints on RMS current and peak voltage. According to the considered drive, the RMS current limit is 5.1 A and the voltage limit for the offline optimization is 75 V. Different from method (I), only I_{m1} in method (III) will be tuned by *fmincon* to respect the current constraint, including flux-weakening region. The reason is that the torque ripple is unaffected by I_{m1} but it is sensitive to the other parameters of phase currents (k_i and φ_i) as described in Fig. 2.56. After considering the RMS current constraint, the RMS currents of all phases with method (III) at 20 rad/s are equal to the RMS current limit of 5.1 A.

Comparisons between the post-fault operations using the two options of method (III) and healthy mode are described in Table 2.25. When the RMS current limit of 5.1 A is respected, method (III)-2 generates the higher torque at 26.2 Nm (0.79 pu) while the torque with method (III)-1 is slightly lower with 25.9 Nm (0.78 pu). It is noted that method (III) generates higher average torques than both methods (I) and (II) (only 0.65 pu). Additionally, the highest peak voltages V_{peak} by the two options of method (III) (0.84 and 0.97 pu) are less than that of healthy mode, making their base speeds higher than that of healthy mode. Total copper losses in fault-tolerant operations with both options of method (III) are 0.86 pu, higher than those of method (I) (0.55 to 0.64 pu) and method (II) (0.52 to 0.82 pu) (see Table 2.10 and Table 2.18).

Table 2.25. Comparisons between calculated results with methods (III)-1 and (III)-2 under constraints on RMS current and peak voltage at 20 rad/s.

Method	Highest RMS current I_{RMS}		Torque T_{em}			Highest peak voltage V_{peak}		Total copper loss P_{loss}	
	(A)	(pu)	T_{ave} (Nm)	(pu)	ΔT (%)	(V)	(pu)	(W)	(pu)
Healthy mode	5.1	1	33.3	1	0	45.9	1	255	1
Method (III)-1	5.1	1	25.9	0.78	24	38.6	0.84	218.1	0.86
Method (III)-2	5.1	1	26.2	0.79	19	44.3	0.97	218.3	0.86

pu: per unit where the base values are parameters of healthy mode.

When the operating speed varies, the optimal torque-speed characteristics, all RMS phase currents and all peak phase voltages by the two options of method (III) in terms of speed are described in Fig. 2.61. It is noted that method (III)-2 has a higher fault-tolerant torque-speed characteristic as shown in Fig. 2.61a. In Fig. 2.61b, the two options of method (III) respect the constraints on RMS current when RMS currents of all remaining healthy phases are equal to 5.1 A at low speed. Notably, in the flux-weakening region with method (III), all RMS currents are reduced because only i_{m1} is tuned by *fmincon*, and the other parameters of phase currents are fixed to avoid any increases in the torque ripples. The maximum peak voltages are within their limit along the speed range as described in Fig. 2.61c.

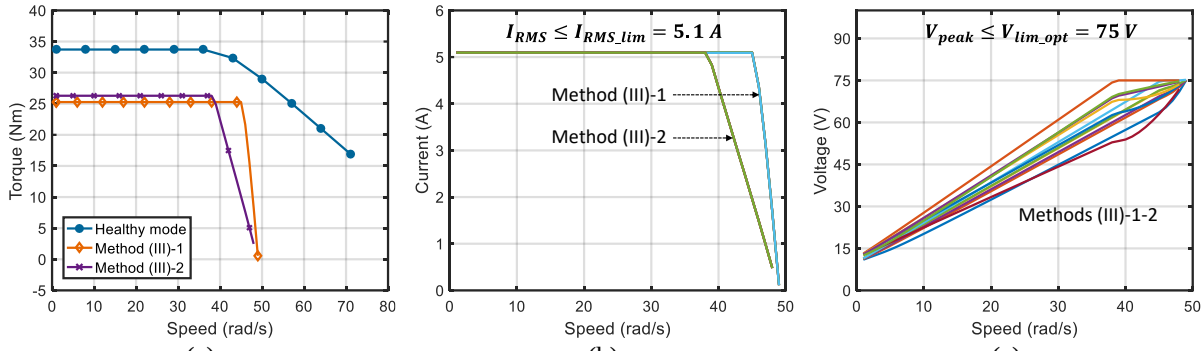

(a) (b) (c)

Fig. 2.61. (Calculated result) Optimal torque-speed characteristic (a), all RMS phase currents (b), all peak phase voltages (c), in terms of speed under constraints on RMS current and peak voltage with methods (III)-1 and (III)-2 when phase *A* is open-circuited.

Table 2.26 describes the calculated base and maximum speeds of the healthy and faulty modes with the two proposed options of method (III). Like methods (I) and (II), the post-fault operation with method (III) has shorter speed ranges than the healthy operation. The two proposed options of method (III) have similar post-fault maximum speeds (0.66 and 0.67 pu). These maximum speeds are like those of method (II) (0.67 pu) but lower than those of method (I) (0.81 to 0.88

pu). The base speed with method (III)-2 is 38 rad/s (1 pu) while that of method (III)-1 is 45 rad/s (1.18 pu).

Table 2.26. Comparisons between the calculated base and maximum speeds with methods (III)-1 and (III)-2 for an OC fault in phase *A* under constraints on RMS current and peak voltage.

Method	Base speed Ω_{base}		Maximum speed Ω_{max}	
	(rad/s)	(pu)	(rad/s)	(pu)
Healthy mode	38	1	73	1
Method (III)-1	45	1.18	49	0.67
Method (III)-2	38	1	48	0.66

pu: per unit where the base values are parameters of healthy mode.

2.3.4.G. *Verification with experimental results for method (III)*

Methods (III)-1 and (III)-2 with the control scheme in Fig. 2.21 are validated in the experimental test bench (see **section 2.1.4.A**). As methods (I)-2, (I)-3, and (II), method (III) can be easily implemented in the test bench without any hardware modifications.

2.3.4.G.1. Current control performance:

To experimentally obtain the optimal torque-speed characteristics (see Fig. 2.61), six d-q currents (i_{d1}, i_{q1}, i_{d9}, i_{q9}, i_{d3}, i_{q3}) need to properly track their references as presented in Fig. 2.59b and Fig. 2.60b. At a speed, method (III)-1 has 2 time-constant current references (i_{d1}, i_{q1}) and 4 time-variant current references (i_{d3}, i_{q3}, i_{d9}, i_{q9}). Meanwhile, 6 current references in method (III)-2 are time-variant with small fluctuations in main currents (i_{d1}, i_{q1}).

The current control performances at 20 rad/s are described in Figs. 2.62-2.64. Because most current references are time-variant, the control quality may be reduced at high speed when conventional PI controllers are applied. This phenomenon will be clearly observed in the torque-speed performance.

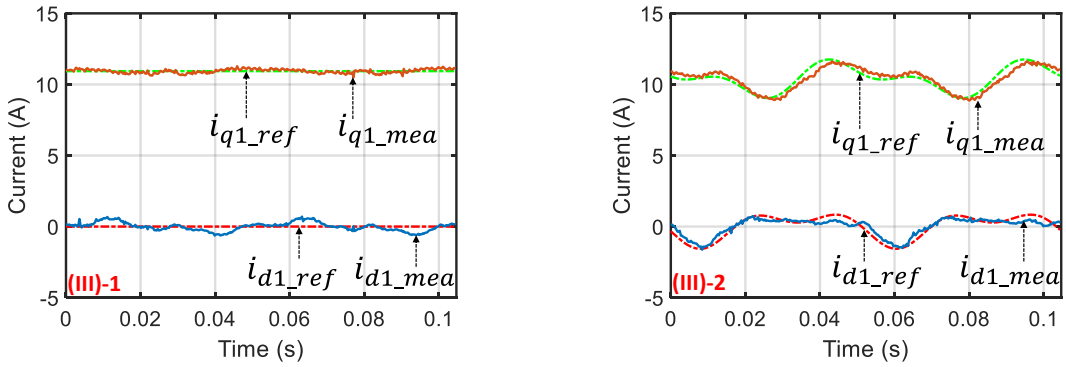

Fig. 2.62. (Experimental result) Currents in (d_1-q_1) frame at 20 rad/s with method (III)-1 (a), and with method (III)-2 (b), when phase *A* is open-circuited.

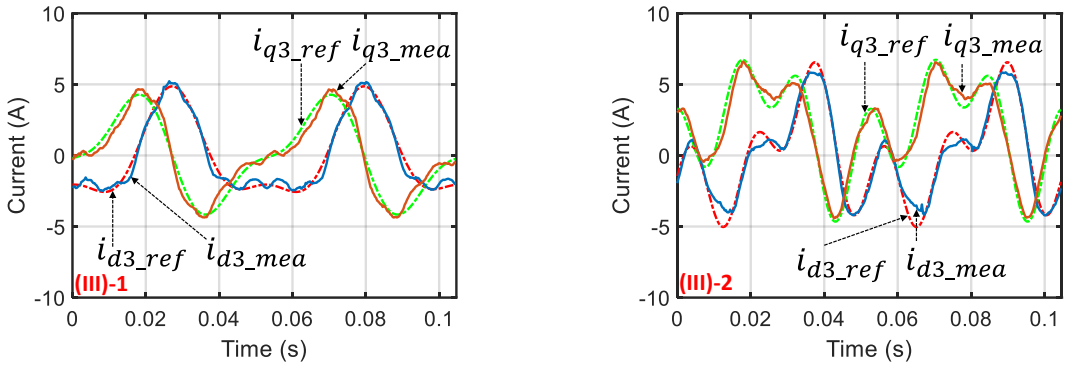

(a) (b)

Fig. 2.63. (Experimental result) Currents in (d_3-q_3) frame at 20 rad/s with method (III)-1 (a), and with method (III)-2 (b), when phase *A* is open-circuited.

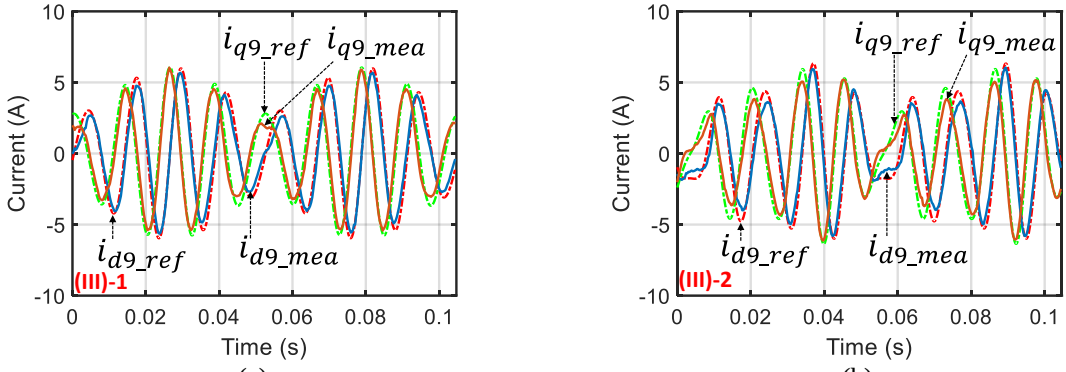

(a) (b)

Fig. 2.64. (Experimental results) Currents in (d_9-q_9) frame at 20 rad/s with method (III)-1 (a), and with method (III)-2 (b), when phase *A* is open-circuited.

2.3.4.G.2. Torque performance:

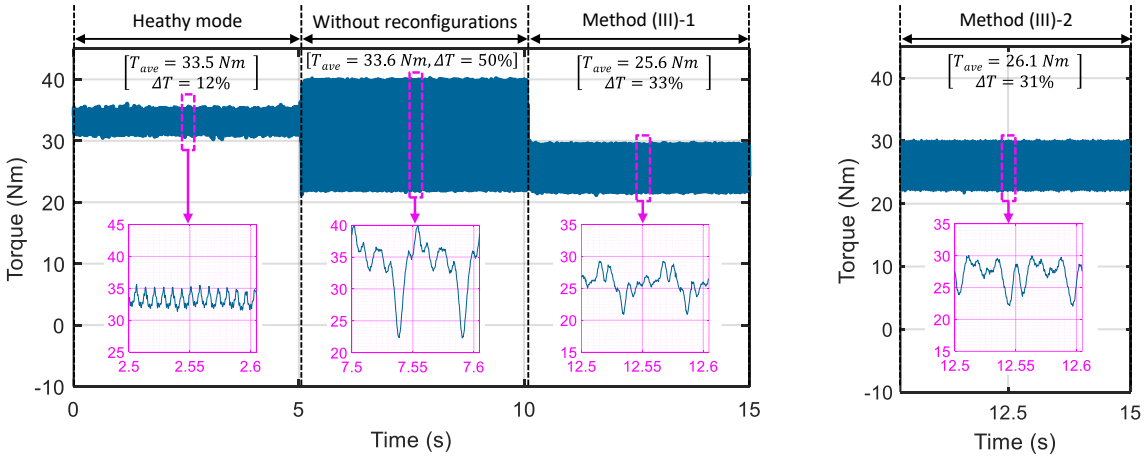

(a) (b)

Fig. 2.65. (Experimental result) Torque in three operating states including healthy mode, an OC fault in phase *A* without reconfigurations, and when method (III)-1 (a) and method (III)-2 (b) are applied.

To see the effectiveness of methods (III)-1 and (III)-2, an operation with three operating states at 20 rad/s as shown in Fig. 2.65 is investigated, including a healthy operation, a post-fault operation without reconfigurations, and a fault-tolerant operation with one of two methods (III)-1 and (III)-2. The first two operating states have been deeply investigated in **sections 2.1.4** and **2.2**. It is noted that the average torques in the third state with methods (III)-1 and (III)-2 are in good accordance with the optimal (calculated) values in Fig. 2.61a. To respect the constraints

on RMS current, the average torque is reduced from 33.5 Nm in healthy mode to 25.6 Nm (0.76 pu) with method (III)-1 and 26.1 Nm (0.78 pu) with method (III)-2 in the post-fault operation. However, the experimental torques have ripples of 33% with method (III)-1, and 31% with method (III)-2. Especially, the differences between the maximum and minimum torques are about 8 Nm, relatively high compared to the previous methods.

When the operating speed varies, the experimental torque-speed characteristics with methods (III)-1 and (III)-2 in comparison with healthy mode ($T_{em\_opt\_HM}$ and $T_{em\_exp\_HM}$) are described in Fig. 2.66. By using these methods, the experimental post-fault torques ($T_{em\_exp\_OC}$) are in good accordance with the optimal torques ($T_{em\_opt\_OC}$) from Fig. 2.61. However, the torque ripple increases in method (III)-2 when the rotating speed increases. The reason is that all current references in method (III)-2, especially (i_{d1}, i_{q1}), are time-variant; hence, the current control quality will be reduced at high speed with conventional PI controllers. Meanwhile, method (III)-1 does not have this phenomenon because its current references (i_{d1}, i_{q1}) are time-constant. The high fluctuations of torques in method (III) will be solved in **Chapter 3** by using ADALINEs. The experimental base and maximum speeds in Fig. 2.66 are the same as calculated results in Table 2.26.

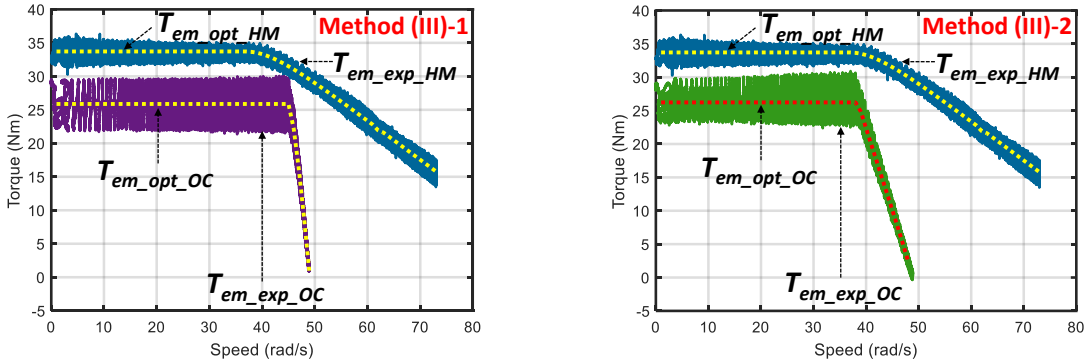

(a) (b)

Fig. 2.66. (Experimental result) Post-fault torque-speed characteristics under an OC fault in phase *A* with method (III)-1 (a), and with method (III)-2 (b).

2.3.4.G.3. Constraints on RMS current and peak voltage:

Table 2.27 shows that experimental RMS currents in the remaining healthy phases at 20 rad/s are similar and around the RMS current limit (5.1 A). The experimental highest RMS currents in both options of method (III) are 5.3 A due to the imperfection of current control.

Table 2.27. Experimental RMS currents in all phases with methods (III)-1 and (III)-2 under constraints on RMS current and peak voltage at 20 rad/s when phase *A* is opened.

Method	RMS current (A)						
	A	*B*	*C*	*D*	*E*	*F*	*G*
Method (III)-1	0.1	5.3	4.8	4.9	5	4.9	5.3
Method (III)-2	0.1	5.3	4.8	4.9	5	4.8	5.1

When the operating speed varies, the constraints on RMS current and voltage are still respected in the experimental results, guaranteeing flux-weakening operations. Measured phase currents by the two methods in terms of speed are described in Figs. 2.67-2.68. The waveforms of measured phase currents at 20 and 47 rad/s are also plotted. The waveforms of the remaining

healthy phase currents are changed at high speed and the highest RMS currents reduce at speeds over the base speeds to respect the constraint on peak voltage.

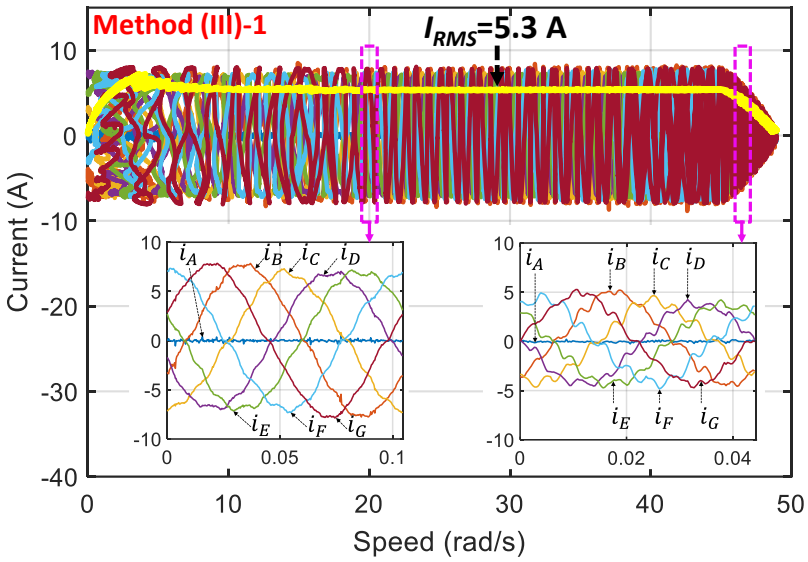

Fig. 2.67. (Experimental result) Phase currents in terms of speed, and current waveforms at 20 and 47 rad/s with method (III)-1 under an OC fault in phase *A*.

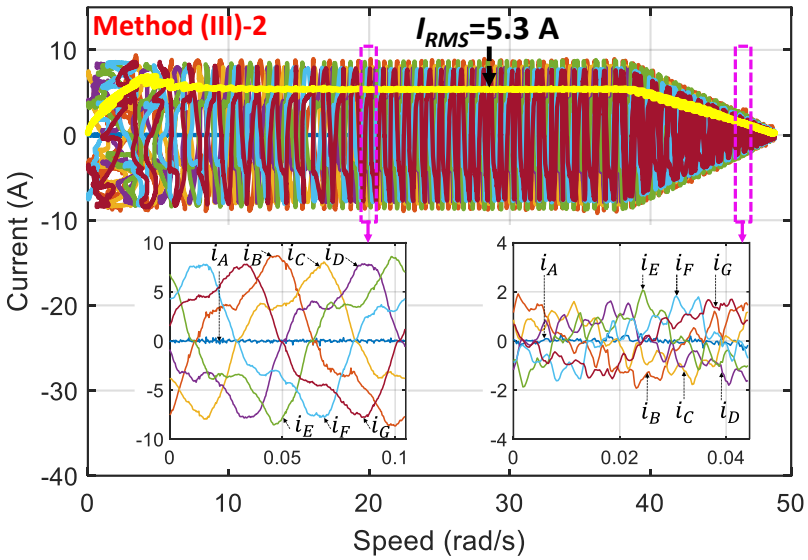

Fig. 2.68. (Experimental result) Phase currents in terms of speed, and current waveforms at 20 and 47 rad/s with method (III)-2 under an OC fault in phase *A*.

Similarly, phase voltage references with the two options of method (III) in terms of speed are presented in Fig. 2.69 and Fig. 2.70. Their waveforms in terms of time at 20 and 47 rad/s are also plotted. It is noted that the peak values of phase voltage references after the base speeds are maximal but relatively under their limit (V_{lim}=100 V).

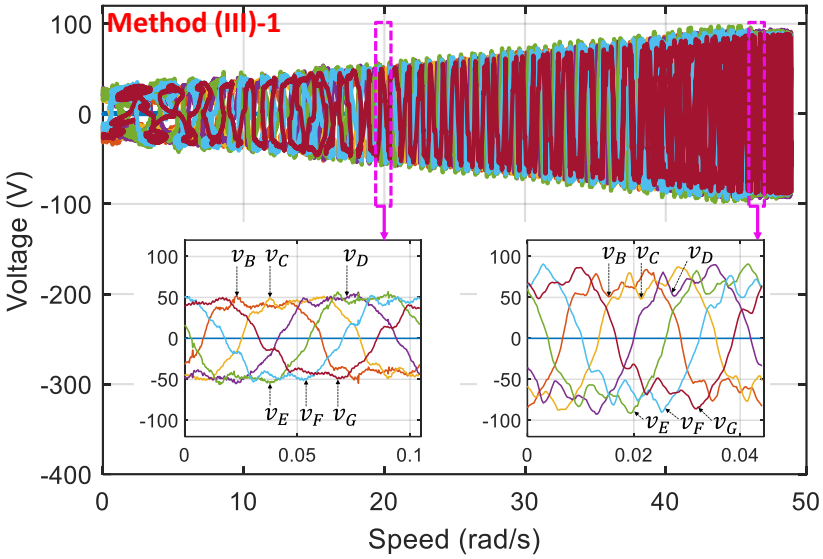

Fig. 2.69. (Experimental result) Phase voltage references in terms of speed, and current waveforms at 20 and 47 rad/s with method (III)-1 under an OC fault in phase *A*.

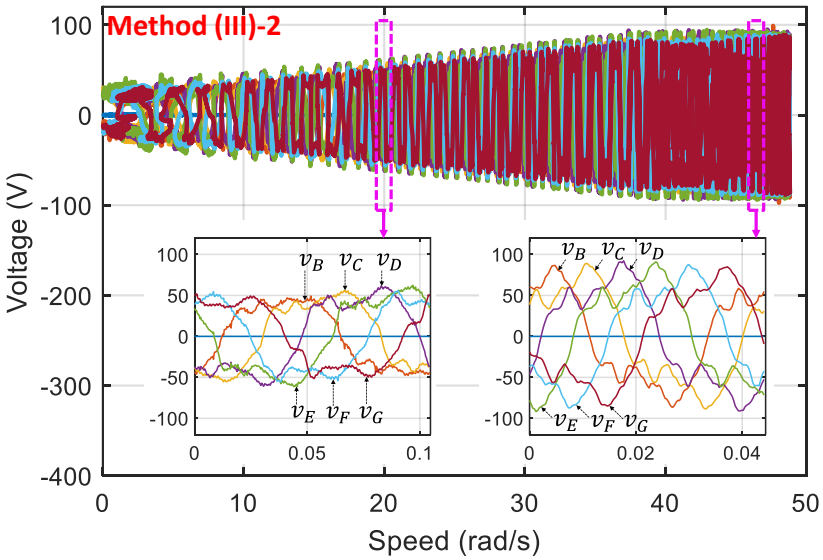

Fig. 2.70. (Experimental result) Phase voltage references in terms of speed, and current waveforms at 20 and 47 rad/s with method (III)-2 under an OC fault in phase *A*.

2.3.4.G.4. Comparative summary:

A comparative summary of experimental performances in a healthy operation, an OC fault without reconfigurations, and fault-tolerant operations with methods (III)-1 and (III)-2 is presented in Table 2.28. Especially, the highest RMS currents, torques, highest peak voltages, and total copper losses are compared. In general, the calculated and experimental results in Table 2.25 and Table 2.28 are in good accordance. However, the experimental voltage references are higher than the calculated values due to the additional voltages caused by high-order harmonics of the experimental back-EMFs.

Table 2.28. Comparisons between experimental results with methods (III)-1 and (III)-2 under constraints on RMS current and peak voltage at 20 rad/s.

Method	Highest RMS current I_{RMS}		Torque T_{em}			Highest peak voltage V_{peak}		Total copper loss P_{loss}	
	(A)	(pu)	T_{ave} (Nm)	T_{ave} (pu)	ΔT (%)	(V)	(pu)	(W)	(pu)
Healthy mode	5.1	1	33.5	1	12	60	1	255.2	1
OC fault without reconfigurations	7.9	1.55	33.6	1	50	104.1	1.74	323.7	1.27
Method (III)-1	5.3	1.04	25.6	0.76	33	56.5	0.94	212.5	0.83
Method (III)-2	5.3	1.04	26.1	0.78	31	62.4	1.04	208.6	0.82

pu: per unit where the base values are parameters of healthy mode.

2.3.5. Comparative analyses of fault-tolerant control methods (I), (II) and (III)

In this chapter, the seven fault-tolerant methods have been presented and classified into three main control methods (I), (II), and (III). Each method has its own advantages and disadvantages.

2.3.5.A. *Comparisons in terms of control facilitation*

Regarding the current control, if FOC technique and classical PI controllers are applied, time-constant current references can guarantee the control quality, resulting in smooth torques.

Table 2.29. Current references in d-q frames for control generated in healthy mode and in a post-fault operation with methods (I), (II), and (III).

Method	i_{d1_ref}	i_{q1_ref}	i_{d9_ref}	i_{q9_ref}	i_{d3_ref}	i_{q3_ref}	i_{z_ref}
Healthy mode	constant	constant	constant	constant	constant	constant	0
Method (I)-1	constant	constant	constant	constant	constant	constant	variant
Method (I)-2	constant	constant	variant	variant	constant	constant	0
Method (I)-3	constant	constant	variant	variant	constant	constant	0
Method (II)-RCA	variant	variant	0	0	variant	variant	0
Method (II)-SCL	variant	variant	variant	variant	variant	variant	0
Method (III)-1	constant	constant	variant	variant	variant	variant	0
Method (III)-2	variant	variant	variant	variant	variant	variant	0

constant: time-constant; variant: time-variant.

From Table 2.29, all d-q currents in healthy mode are constant and the zero-sequence current is zero. In fault-tolerant methods, method (I)-1 has the highest number of constant d-q currents (6 currents) while methods (I)-2 and (I)-3 have only 4 constant d-q currents for control. However, method (I)-1 is the only option that requires hardware modifications with a high zero-sequence current. This current not only results in high-frequency components in torques and phase currents but also high torque ripples related to back-EMF harmonics associated with the zero-sequence machine (7^{th} and its multiples). Methods (I)-2 and (I)-3 deal with time-variant currents in the second fictitious machine (sensitive to the 9^{th} harmonic of back-EMFs). Method (III)-1 has 2 constant d-q currents in the first (main) fictitious machine, making its torque ripple less dependent on the rotating speed. Method (II)-RCA also has 2 constant d-q currents in the second fictitious machine, leading to its robustness (unaffected by back-EMF harmonics associated with the second fictitious machine). The other methods including (II)-SCL and (III)-2 have 6 time-variant d-q currents for control. Therefore, in their torque-speed characteristics, significant increases of torque ripples can be witnessed when the rotating speed increases. However, this problem can be solved in **Chapter 3** by using ADALINEs.

2.3.5.B. *Comparisons in terms of torque, copper loss, and speed range*

The optimal torque-speed characteristics in healthy and under an OC fault in phase *A* with the seven proposed control options are plotted in Fig. 2.71. These characteristics also represent the

comparison between average torques generated with the proposed methods. It is noted that a combination of these proposed methods can improve the operating performances of the drive under the faulty condition. In this case, the highest post-fault average torque for the starting period and a longer speed range are obtained while RMS phase currents and peak phase voltages are within their limits.

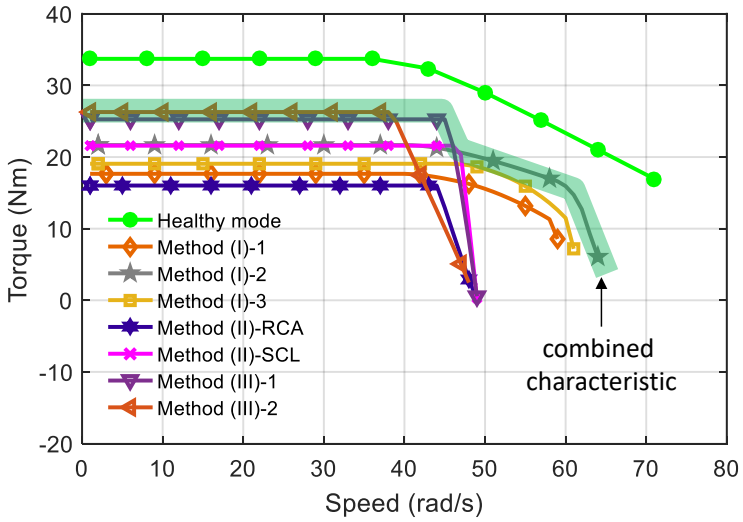

Fig. 2.71. (Calculated result) Torque-speed characteristics in healthy mode and under an OC fault in phase *A* applying the seven proposed control methods.

Table 2.30 compares healthy mode, an OC fault without reconfigurations, and post-fault operations using the seven proposed fault-tolerant methods in this chapter. Torque performances, total copper losses, base speeds, and maximum speeds are considered in these comparisons. Due to a high torque ripple (46% or 50%) and a high total copper loss (1.4 pu or 1.27 pu) under the OC fault without reconfigurations, the use of fault-tolerant control strategies for the electric drive is necessary. It is noted that calculated results for an OC fault without reconfigurations are obtained from MATLAB Simulink while results with proposed methods are obtained from the offline optimization.

Table 2.30. Comparisons between healthy mode, an OC fault in phase *A* without reconfigurations, and post-fault operations with methods (I), (II), and (III) under constraints on RMS current and peak voltage at 20 rad/s.

Method	T_{ave}				ΔT		P_{loss}				Ω_{base}*		Ω_{max}*	
	opt		exp		opt	exp	opt		exp					
	(Nm)	(pu)	(Nm)	(pu)	(%)	(%)	(W)	(pu)	(W)	(pu)	(rad/s)	(pu)	(rad/s)	(pu)
Healthy mode	33.3	1	33.5	1	0	12	255	1	255.2	1	38	1	73	1
OC fault without reconfigurations	**33**	**0.99**	**33.6**	**1**	**46**	**50**	**366.5**	**1.4**	**323.7**	**1.27**	**36**	**0.95**	**36**	**0.49**
Method (I)-1	17.7	0.53	-	-	0	-	144.4	0.57	-	-	41	1.08	59	0.81
Method (I)-2	21.7	0.65	21.6	0.64	0	31	162.6	0.64	149.1	0.58	41	1.08	64	0.88
Method (I)-3	19.1	0.57	19	0.57	0	32	140	0.55	124	0.49	46	1.21	61	0.84
Method (II)-RCA	16	0.48	16	0.48	0	19	132.1	0.52	123.4	0.48	44	1.16	49	0.67
Method (II)-SCL	21.6	0.65	21.6	0.64	0	24	208.6	0.82	203.3	0.8	46	1.21	49	0.67
Method (III)-1	25.9	0.78	25.6	0.76	24	33	218.1	0.86	212.5	0.83	45	1.18	49	0.67
Method (III)-2	26.2	0.79	26.1	0.78	19	31	218.3	0.86	208.6	0.82	38	1	48	0.66

opt: optimal calculated results; exp: experimental results.
pu: per unit where the base values are parameters of healthy mode.
* Ω_{base} and Ω_{max} in offline optimizations and experiments are the same.

In general, the optimal (calculated) and experimental results, as summarized in Table 2.30, are in good accordance. However, the experimental machine contains unwanted harmonics of the back-EMFs, resulting in higher torque ripples than optimal results in all operating modes, including healthy mode. In healthy mode as well as in a post-fault operation with each proposed

method, the base speed and the maximum speed obtained in the offline optimization and experiments are the same.

For the torque performance, the highest average torque is generated with method (III)-2 at 0.79 pu in the offline optimization (opt=0.79 pu), and at 0.78 pu in experiments (exp=0.78 pu) thanks to the uniformity of remaining phase current waveforms. However, its torque fluctuation is relatively high compared to the other methods (opt=19% and exp=31%). Method (II)-RCA shows its robustness when its torque is unaffected by the harmonics of the second machine in the experimental machine. Therefore, its experimental torque ripple is lowest with 19%. However, under the constraint on RMS current, its average torque is lowest (opt=exp=0.48 pu). Method (I)-2 has the highest average torque among the three options of method (I) (opt=0.65 pu and exp=0.64 pu).

The total copper loss dramatically increases to 1.27 pu in the OC fault without reconfigurations. This value reduces to the lowest value in method (II)-RCA (opt=0.52 pu and exp=0.48 pu). Meanwhile, the highest total copper loss is generated in method (III) (opt=0.86 pu and exp=0.83 pu). Among the three options of method (I), method (I)-2 generates the highest total copper loss (opt=0.64 pu and exp=0.58 pu).

Regarding the base and maximum speeds, it is noted that post-fault speed ranges are always shorter than that of healthy mode. Among the proposed methods, method (I) results in largest speed ranges while methods (II) and (III) have shorter speed ranges. Method (I)-2 enables the drive to reach the highest speed (0.88 pu) while the shortest speed range is created with method (III)-2 (0.66 pu). Basically, these speed range reductions are caused by putting more constraints on currents in either d-q or natural frames to respect limits of currents and voltages or to obtain smooth torques. For example, in method (III), at high speed, the amplitude of phase currents needs to be immediately reduced instead of alternating current phase angles to guarantee smooth torques. Therefore, in this case, torques decline rapidly when the rotating speeds exceed the base speeds.

2.3.5.C. *Comparisons of three remarkable methods using radar charts*

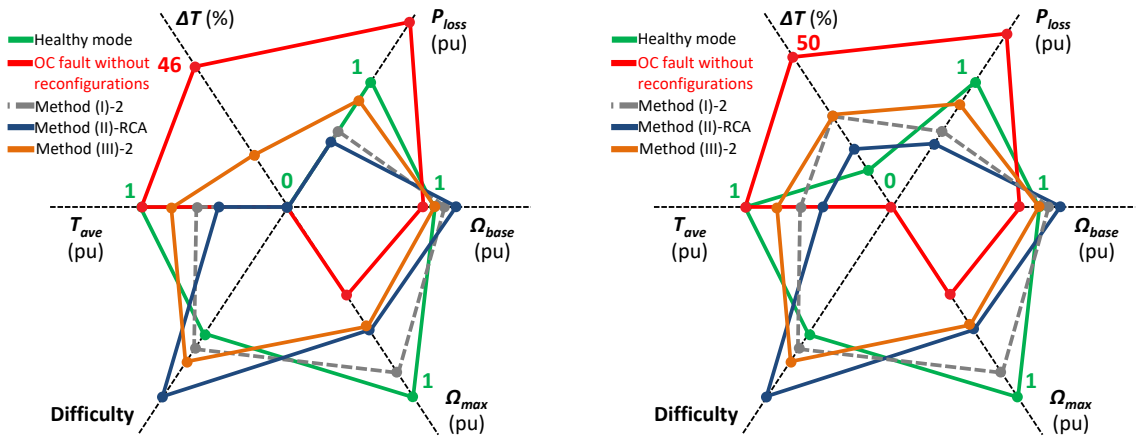

(a) (b)

Fig. 2.72. (Experimental result) Comparisons using radar charts: optimal calculated results (a), experimental results (b), with T_{ave}, ΔT, and P_{loss} at 20 rad/s.

To compare methods (I), (II), and (III) more clearly, three remarkable options are selected from the seven proposed options to plot radar charts in Fig. 2.72. In addition, healthy mode and the OC fault without reconfigurations are considered. Torque performances (T_{ave}, ΔT), total copper losses (P_{loss}), base speeds (Ω_{base}), maximum speeds (Ω_{max}), and difficulty are considered in these comparisons. The difficulty is a heuristic assessment according to hardship in calculations and implementations of the considered methods. Method (III)-RCA is the most difficult one because of its calculation burden for all cases of faults.

It is noted that experimental results in all operating modes are in good accordance with calculated results. Only experimental torque ripples are significantly higher than calculated results. Healthy mode is considered as the ideal operating mode with the best performances. Meanwhile the OC fault without reconfigurations generates the worst parameters such as the highest torque ripple (opt=46% and exp=50%) and the highest total copper loss (opt=1.4 pu and exp=1.27 pu). Therefore, fault-tolerant control methods are required for post-fault operations. In these radar charts, method (I)-2 is chosen because it has the highest maximum speed (0.88 pu). Meanwhile, method (II)-RCA is selected because of its robustness with the lowest experimental torque ripple (exp=19%). Method (III)-2 is added to the radar charts because it generates the highest average torque (opt=0.79 pu).

2.3.5.D. *Comparisons with recent studies*

Compared to existing studies, for example studies in [87, 120, 126-129, 133-135, 137, 149], the proposed methods in this doctoral thesis can be applied to non-sinusoidal machines with different choices in terms of torque performance (average torque and torque ripple). Especially, the proposed methods in this doctoral thesis take into account the thermal limit (RMS current) and flux-weakening operations by imposing constraints on RMS current and peak voltage. Besides the methods with several constant d-q currents, two proposed methods in this doctoral thesis using 6 time-variant current references for control (methods (II)-SCL and (III)-2) can be compared with the vectorial approach in [121]. Indeed, the existing approach in [121] can generate ripple-free torques regardless of one or two open-circuited phases or the type of back-EMFs. However, d-q current references usually fluctuate with very high amplitudes. Therefore, hysteresis controllers are applied in [121] to directly control currents in natural frame, resulting in variable switching frequencies, increases in switching losses, high-frequency currents and electromagnetic compatibility (EMC) problems. In addition, if a current limit is considered, unidentical waveforms of healthy phase currents in [121] will generate low average torques. Meanwhile, methods (II)-SCL and (III)-2 in this doctoral thesis have low fluctuations of currents in frame (d_1-q_1) which generates most of the torque. Therefore, the pre-fault control scheme with conventional PI controllers can be used in faulty mode. Moreover, the uniformity of phase currents in these methods results in higher average torques if a current constraint is considered.

2.4. Conclusions

This chapter has presented the modeling and control the multiphase PMSM drive with non-sinusoidal back-EMFs under heathy and faulty modes. Constraints on RMS current and peak

voltage have been always considered. A case study with a seven-phase non-sinusoidal machine and a single-phase OC fault has been chosen to illustrate theories in this chapter. In case of two-phase OC faults, fault-tolerant control strategies and experimental results are presented in **Appendix B** of this doctoral thesis.

Specifically, the modeling and control of the drive in healthy mode have been introduced in **section 2.1**. In **section 2.2**, an investigation into the multiphase drive performances in a post-fault operation has shown serious deteriorations with a high-ripple torque, a significant increase in RMS currents as well as in the total copper loss. The reason is that the coupling issue prevents the post-fault drive from continuing to use the current references of healthy mode. Therefore, a reconfiguration with fault-tolerant control strategies is required to guarantee a smooth torque and a safe post-fault operation for the drive as well as for EVs.

In **section 2.3**, three main proposed fault-tolerant control strategies with seven options have been introduced by exploiting the mathematical model of the multiphase drive. Specifically, new current references have been determined in decoupled frames (methods (I)-1-2-3), in natural frame (methods (III)-1-2), or by using new transformation matrices (methods (II)-RCA-SCL). Methods (I) and (II) have theoretically obtained constant torques when the first and third harmonics of back-EMFs are considered. However, their average torques have been relatively low if the RMS phase currents are limited. Therefore, method (III) has been proposed to obtain higher average torques by using identical phase currents. Under the current constraint, these currents with an identical waveform have been effectively exploited to produce more torques. However, torque ripples have been inevitable in method (III). Therefore, there is theoretically a compromise between a high average torque with a high ripple and a smooth torque with a low average value. Therefore, a combination of more than one strategy according to the payload of EVs can take advantage of each method.

The quality of the drive control will be improved by applying ADALINEs in **Chapter 3** of this doctoral thesis. Indeed, negative effects of unwanted back-EMF harmonics and other uncertainties in the drive on currents and torques will be eliminated.

Chapter 3. Enhancements of Multiphase Drive Performances with Adaptive Linear Neurons

This chapter is to present improvements of the quality of current control and torque discussed in **Chapter 2**, including healthy and faulty operations. Specifically, **section 3.1** will present basic knowledge about ADALINE (ADAptive LInear NEuron). This choice has been justified in **section 1.4** of **Chapter 1**. Then, **section 3.2** will describe how unwanted back-EMF harmonics and the nonlinearity of the inverter deteriorate the quality of current control and torques in healthy mode. These problems will be tackled by using six ADALINEs for current harmonics and one ADALINE for torque ripples with appropriate harmonic injections. Determinations of harmonic components existing in currents and torques allow a fast response of control (fast convergence) and reduce the calculation burden. The improvements of current control and torque performances under a post-fault operation will be described in **section 3.3**. Indeed, method (III) in **Chapter 2**, producing the highest average torque with high ripples, will be improved by a single ADALINE like the one for torque ripple eliminations in healthy mode. When harmonic components of the post-fault torque are identified, the ADALINE can directly eliminate torque ripples without the calculation burden. Another application of ADALINEs is to improve current control quality in faulty modes, indirectly enhancing the torque quality. Specifically, time-variant d-q current references with method (II) in **Chapter 2** have deteriorated the current tracking performance at high speed, resulting in more torque ripples. A new control scheme with one ADALINE will replace time-variant current references by time-constant references for control. This chapter will be concluded in **section 3.4**.

3.1. Introduction to adaptive linear neurons

3.1.1. Artificial neural networks and adaptive linear neurons

Artificial Neural Network (ANN), as a part of Artificial Intelligence (AI), was introduced in 1940s when the modeling of biological neurons was conducted [171]. The main idea of ANNs is to implant humanoid neurons in a machine, enabling the machine to learn from the past data and intelligently react to unprecedented problems during its operation. Thanks to the technological evolution in the domain of numerical calculations, applications of ANNs became more popular in 1990s. ADALINE is an early single-layer artificial neuron that was developed in 1960 [172, 173]. Its outputs are a linear combination of its inputs. A general structure of an ADALINE is described in Fig. 3.1. An ADALINE includes m inputs represented by a m-dimensional vector $\underline{x}_{in}$, and m corresponding weights with a m-dimensional vector $\underline{w}$ while its output y is equal to the weighted sum of the inputs. Therefore, the output can be expressed as a dot product of the input vector and the weight vector as follows:

$$y = \underline{w} \bullet \underline{x}_{in} = \sum_{k=1}^{m} w_k x_{ink}(t) \tag{3.1}$$

where $\underline{x}_{in} = \left[x_{in1}(t) \quad x_{in2}(t) \quad \cdots \quad x_{inm}(t)\right]^T$ and $\underline{w} = \left[w_1 \quad w_2 \quad \cdots \quad w_m\right]^T$.

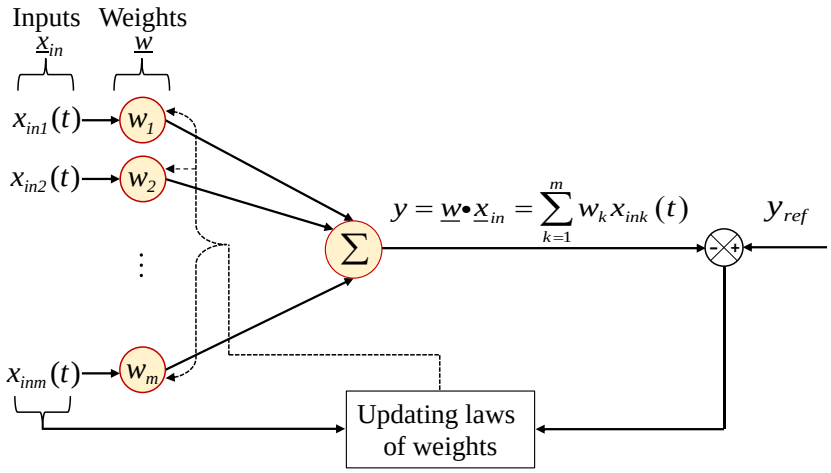

Fig. 3.1. A general structure of an ADALINE.

The Least Mean Square (LMS) or Widrow-Hoff learning rule can be used to update the weights. This learning rule aims at minimizing the squared error between the reference output y_{ref} and the output of the ADALINE y as given by:

$$E_y = \left[y_{ref}(j) - y(j)\right]^2 \tag{3.2}$$

In fact, this rule is the stochastic gradient descent for linear regression as expressed by:

$$\frac{\partial E_y}{\partial \underline{w}} = 2\left[y_{ref}(j) - y(j)\right]\frac{\partial\left[y_{ref}(j) - y(j)\right]}{\partial \underline{w}} = -2\left[y_{ref}(j) - y(j)\right]\frac{\partial\left[\underline{w} \bullet \underline{x}_{in}\right]}{\partial \underline{w}} = -2\left[y_{ref}(j) - y(j)\right]\underline{x}_{in} \tag{3.3}$$

where j is the order of iteration. Therefore, the updating rule with learning rate η at the $(j+1)^{th}$ iteration becomes:

$$\underline{w}(j+1) = \underline{w}(j) + \eta\left[y_{ref}(j) - y(j)\right]\underline{x}_{in}(j) \tag{3.4}$$

According to [38], the LMS algorithm can be applied with unknown inputs. The initial values of the weights can be chosen or set to zero. After several iterations, the weights will converge to their optimal values when the output y reaches its reference value y_{ref}.

To guarantee the stability of an applied system, the learning rate with LMS algorithm should be a value between 0 and 1 [173]. The learning rate depends on parameters of the applied system such as: values of the inputs, the output error, and the sampling time in calculations. Specifically, if the values of the inputs are relatively big compared to the maximum value of the learning rate, the learning rate should be divided by the norm of the inputs to guarantee the stability. When the output error is relatively big compared to the output reference value, the learning rate must be high to quickly reduce the output error. If the output error becomes small, the learning rate must be decreased or even equal to zero to guarantee the stability. In addition, the learning rate is proportional to the sampling time in calculations. With a small value of the sampling time, the learning rate is required to be small. The selection of the learning rate has not been specified for all applications. Therefore, the learning rate must be chosen according to analyses of the above parameters of the applied system. Fig. 3.2 illustrates how the learning rate affects the learning process of the weights. If the learning rate is set too low as in Fig. 3.2a,

the training process of weights will be very slow, fast responses of the applied system cannot be guaranteed. However, if the learning rate is set too high as in Fig. 3.2b, the divergence can happen, leading to instability of the applied system. The relatively suitable one is presented in Fig. 3.2c.

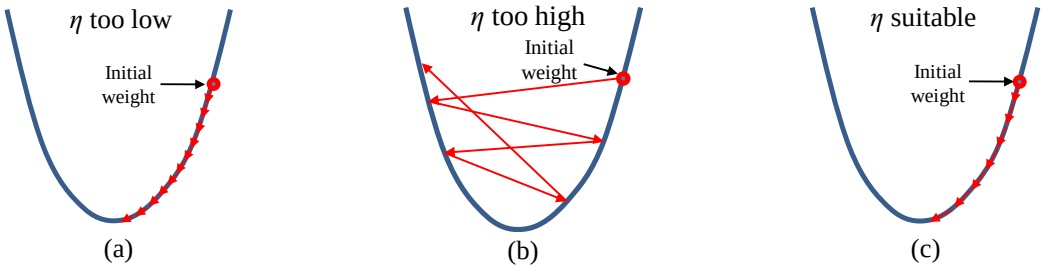

Fig. 3.2. The effect of learning rate η on the convergence of weights: η is too low (a), η is too high (b), η is suitable (c).

3.1.2. Possible applications of ADALINEs in the electric drive

ADALINEs have been applied to various domains such as telecommunication [172], electrical engineering [38, 86, 174, 175]. This doctoral is to apply ADALINEs in several cases with the aim of refining the considered electric drive as discussed in **Chapter 2**. Indeed, their applications categorized into healthy and faulty modes are presented in next sections. Besides several advantages such as self-learning and simplicity, ADALINEs have some drawbacks such as: the risk of instability due to an inappropriate learning rate η; and the calculation burden when the number of inputs and weights increases. Therefore, the structures and parameters of ADALINEs need to be properly designed based on properties of specific applications, minimizing these drawbacks.

3.2. Control quality in healthy mode

ADALINEs are applied to tackle the existing problems in healthy mode presented in **Chapter 2** for a seven-phase machine. Specifically, torque ripples in healthy mode are caused by unwanted harmonics of currents and the back-EMFs of the considered machine as follows:

1) Current harmonics exist in d-q frames although the current references for control are time-constant, especially in (d_3-q_3) and (d_9-q_9) frames with a main frequency of 14θ as discussed in **Chapter 2**. This problem can happen in all electric drives with imperfect back-EMF machines and the inverter nonlinearity. In this case, PI controllers cannot properly filter these current harmonics; hence, PI controllers combined with ADALINEs can be a suitable solution.
2) However, the above combination of PI controllers and ADALINEs for current harmonic eliminations cannot nullify the existing torque ripples in **Chapter 2**. These torque ripples are also caused by the unwanted harmonic components in the imperfect back-EMFs of the considered machine. In a seven-phase machine, these torque ripples have a main frequency of 14θ. Therefore, these torque ripples need to be eliminated by another ADALINE.

The origins of the current harmonics in d-q frames and torque ripples will be analyzed to effectively define the structure of the ADALINEs, avoiding the calculation burden. In general, these eliminations using ADALINEs can be applied to other electric machines with a different number of phases and various back-EMF waveforms.

3.2.1. Impacts of unwanted back-EMF harmonics and the inverter nonlinearity

3.2.1.A. *Impacts of unwanted back-EMF harmonics*

According to the multi-reference frame theory [35], control of a wye-connected electrical machine is ideal when only one harmonic is associated with each d-q frame. For example, the back-EMFs of a seven-phase machine should have only 3 harmonics distributed among 3 fictitious machines (reference frames). In this case, a constant torque can be generated by constant d-q currents. Due to wye-connected stator windings with a nullified zero-sequence current, impacts of the time-variant zero-sequence back-EMFs on phase currents and torques are automatically eliminated. However, the back-EMFs may contain more than one back-EMF harmonic in each fictitious machine, called unwanted back-EMF harmonics. For example, more than one harmonic associated with each reference frame are generally described in Table 3.1 for a seven-phase machine. If the back-EMFs contain only the 1st, 3rd, and 9th harmonics, the values of the back-EMFs in (d_1-q_1), (d_3-q_3), and (d_9-q_9) frames are constant.

Table 3.1. Fictitious machines, d-q reference frames, and several associated odd harmonics in natural frame of a seven-phase machine.

Fictitious machine	Reference frame	Associated harmonic
The first machine (FM1)	d_1-q_1	1, 13, 15
The second machine (FM2)	d_9-q_9	5, 9, 19
The third machine (FM3)	d_3-q_3	3, 11, 17

Without loss of generality, to see impacts of unwanted back-EMF harmonics on current control, it is assumed that there are two associated harmonics per reference frame as follows:

1) The 1st and 13th harmonics associated with (d_1-q_1).
2) The 9th and 19th harmonics associated with (d_9-q_9)[2].
3) The 3rd and 11th harmonics associated with (d_3-q_3).

Therefore, the unwanted back-EMFs are the 11th, 13th, and 19th harmonics. In this case, the back-EMF of a phase in natural frame is generally given by:

$$e_j = \begin{Bmatrix} E_1 \sin\left[\theta-(j-1)\frac{2\pi}{7}\right] + E_3 \sin\left[3\left(\theta-(j-1)\frac{2\pi}{7}\right)+\varphi_3\right] + E_9 \sin\left[9\left(\theta-(j-1)\frac{2\pi}{7}\right)+\varphi_9\right] + \\ E_{11} \sin\left[11\left(\theta-(j-1)\frac{2\pi}{7}\right)+\varphi_{11}\right] + E_{13} \sin\left[13\left(\theta-(j-1)\frac{2\pi}{7}\right)+\varphi_{13}\right] + E_{19} \sin\left[19\left(\theta-(j-1)\frac{2\pi}{7}\right)+\varphi_{19}\right] \end{Bmatrix} \quad (3.5)$$

where e_j is the back-EMF of phase j (from 1 to 7, representing phases A to G, respectively); (E_1, E_3, E_9, E_{11}, E_{13}, E_{19}) and (0, φ_3, φ_9, φ_{11}, φ_{13}, φ_{19}) are the amplitudes and phase shift angles of the 1st, 3rd, 9th, 11th, 13th, and 19th harmonics of the back-EMF, respectively.

[2] Without loss of generality, the selection of the 9th harmonic comes from the back-EMF harmonic spectrum of the considered machine (see **section 2.1.4.A** of **Chapter 2**). If the 5th harmonic of the back-EMF is considered, analyses and solutions are similar.

By applying the classical Clarke and Park transformation matrices in **section 2.1** of **Chapter 2**, the back-EMFs in d-q reference frames become:

$$\begin{cases} e_{d1} = \left(\sqrt{7/2}\right) E_{13} \sin\left(14\theta + \varphi_{13}\right) \\ e_{q1} = \left(\sqrt{7/2}\right) E_{1} + \left(\sqrt{7/2}\right) E_{13} \cos\left(14\theta + \varphi_{13}\right) \\ e_{d9} = \left(\sqrt{7/2}\right) E_{19} \sin\left(28\theta + \varphi_{19}\right) \\ e_{q9} = \left(\sqrt{7/2}\right) E_{9} + \left(\sqrt{7/2}\right) E_{19} \cos\left(28\theta + \varphi_{19}\right) \\ e_{d3} = \left(\sqrt{7/2}\right) E_{11} \sin\left(14\theta + \varphi_{11}\right) \\ e_{q3} = \left(\sqrt{7/2}\right) E_{3} + \left(\sqrt{7/2}\right) E_{11} \cos\left(14\theta + \varphi_{11}\right) \end{cases} \tag{3.6}$$

In (3.6), it is worth noting that the back-EMFs in d-q reference frames are constant if there are only the 1st harmonic (E_1), the 9th harmonic (E_9), and the 3rd harmonic (E_3). However, the presence of the unwanted back-EMF harmonics results in harmonics in d-q frames. The back-EMFs have frequencies: 14θ in (d_1-q_1), 28θ in (d_9-q_9), and 14θ in (d_3-q_3). Especially, these back-EMF harmonics generate corresponding current harmonics in d-q frames. The current harmonic amplitudes in d-q frames depend on the harmonic distribution in the back-EMFs, and especially on the rotating speed.

3.2.1.B. *Impacts of the inverter nonlinearity*

Besides the current harmonics caused by the unwanted back-EMF harmonics, the nonlinearity of the inverters also creates extra current harmonics in d-q frames. The dead time, the time interval in which both of switches of one inverter leg are off, can mainly cause the nonlinearity of inverters. To represent this nonlinearity, according to [176], a "dead-time" voltage in a phase of a 7-phase VSI can be generally expressed by:

$$v_{j\_dead} = -V_{dead} \frac{4}{\pi} \begin{Bmatrix} \sin\left[\theta - (j-1)\frac{2\pi}{7}\right] + \frac{1}{3}\sin\left[3\left(\theta - (j-1)\frac{2\pi}{7}\right)\right] + \frac{1}{5}\sin\left[5\left(\theta - (j-1)\frac{2\pi}{7}\right)\right] + \\ \frac{1}{9}\sin\left[9\left(\theta - (j-1)\frac{2\pi}{7}\right)\right] + \frac{1}{11}\sin\left[11\left(\theta - (j-1)\frac{2\pi}{7}\right)\right] + \frac{1}{13}\sin\left[13\left(\theta - (j-1)\frac{2\pi}{7}\right)\right] + \\ \frac{1}{15}\sin\left[15\left(\theta - (j-1)\frac{2\pi}{7}\right)\right] + \frac{1}{17}\sin\left[17\left(\theta - (j-1)\frac{2\pi}{7}\right)\right] + \frac{1}{19}\sin\left[19\left(\theta - (j-1)\frac{2\pi}{7}\right)\right] + \ldots \end{Bmatrix} \tag{3.7}$$

with $V_{dead} = \frac{T_{dead}}{T_{PWM}} V_{DC}$

where v_{j_dead} is the "dead-time" voltage of phase j; V_{dead} is a constant voltage; T_{dead} is the inverter dead time; T_{PWM} is the switching period of the inverter; V_{DC} is the DC-bus voltage.

Indeed, using the Fourier analysis, the "dead-time" voltage is expressed by an average signal composed of odd harmonics in (3.7). The harmonic amplitudes are inversely proportional to their orders. Therefore, without loss of generality, the considered harmonics can be up to 19θ. In addition, harmonics with frequencies equal to multiples of the number of phases (7 phases in this doctoral thesis) are null.

The "dead-time" voltages of all phases are transformed into d-q reference frames as follows:

$$\begin{cases} v_{d1\_dead} = -\left(\sqrt{7/2}\right)\left[4V_{dead}/\pi\right]\left[1/13+1/15\right]\sin\left(14\theta\right) \\ v_{q1\_dead} = -\left(\sqrt{7/2}\right)\left[4V_{dead}/\pi\right]\left\{1+\left[1/13+1/15\right]\cos\left(14\theta\right)\right\} \\ v_{d9\_dead} = -\left(\sqrt{7/2}\right)\left[4V_{dead}/\pi\right]\left[1/5\sin\left(14\theta\right)+1/19\sin\left(28\theta\right)\right] \\ v_{q9\_dead} = -\left(\sqrt{7/2}\right)\left[4V_{dead}/\pi\right]\left\{1/9+\left[1/5\cos\left(14\theta\right)+1/19\cos\left(28\theta\right)\right]\right\} \\ v_{d3\_dead} = -\left(\sqrt{7/2}\right)\left[4V_{dead}/\pi\right]\left[1/11+1/17\right]\sin\left(14\theta\right) \\ v_{q3\_dead} = -\left(\sqrt{7/2}\right)\left[4V_{dead}/\pi\right]\left\{1/3+\left[1/11+1/17\right]\cos\left(14\theta\right)\right\} \end{cases} \quad (3.8)$$

In (3.8), it is noted that the "dead-time" voltages in rotating frames (d_1-q_1) and (d_3-q_3) have a frequency of 14θ while these voltages in (d_9-q_9) have frequencies of 14θ and 28θ. There are no "dead-time" voltage harmonics in the zero-sequence frame because there are no frequencies equal to multiples of the number of phases as shown in (3.7). Therefore, current harmonics in d-q reference frames are also caused by the inverter nonlinearity with the "dead-time" voltages. The harmonic amplitudes do not depend on the rotating speed but V_{dead} that is related to T_{dead}, T_{PWM}, and V_{DC}.

3.2.1.C. *Summary of the impacts of unwanted back-EMF harmonics and the inverter nonlinearity*

From the previous subsections, the current harmonics in rotating reference frames caused by the unwanted back-EMF harmonics in (3.6) and the "dead-time" voltages in (3.8) are summarized in Table 3.2. Based on the previous analyses, in a specific drive, the amplitudes of the total current harmonics mostly depend on the rotating speed, harmonic spectrum, and V_{dead} but not the current reference values.

Table 3.2. Current harmonics in d-q frames caused by unwanted back-EMF harmonics and the inverter nonlinearity with "dead-time" voltages in a seven-phase machine.

Frame	Current harmonics by unwanted back-EMF harmonics	Current harmonics by "dead-time" voltages
d_1-q_1	14θ	14θ
d_9-q_9	28θ	14θ, 28θ
d_3-q_3	14θ	14θ

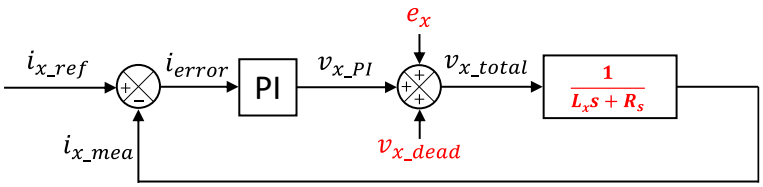

Fig. 3.3. The control scheme of current i_x under the impacts of the unwanted back-EMF harmonic e_x and the inverter nonlinearity with "dead-time" voltage v_{x_dead} without any compensations (x can be d_1, q_1, d_9, q_9, d_3, or q_3).

There are six d-q currents to be controlled as described in Fig. 2.6 in **section 2.1** of **Chapter 2** for a wye-connected winding topology. Current i_x (x can be d_1, q_1, d_9, q_9, d_3, q_3) is controlled in the scheme as described in Fig. 3.3 where a conventional PI controller is applied. Transfer function ($1/(L_x s+R_s)$) represents the fictitious machine model with their inductance and resistance in the corresponding d-q reference frame. This control scheme under the impacts of the unwanted back-EMF harmonic e_x and the "dead-time" voltage v_{x_dead} without any

compensations. In Fig. 3.3, parameters in red represent unchangeable internal properties of the drive.

3.2.2. Eliminations of current harmonics in rotating frames

3.2.2.A. *The conventional control scheme with the back-EMF compensation*

Theoretically, the current harmonics in d-q frames, generated by the unwanted back-EMF harmonics, can be eliminated by imposing corresponding estimated back-EMF harmonics as calculated in (3.6), called the back-EMF compensation. The conventional control scheme using the back-EMF compensation (e_{x_com}) for a current (i_{d1}, i_{q1}, i_{d9}, i_{q9}, i_{d3}, or i_{q3}) is described in Fig. 3.4.

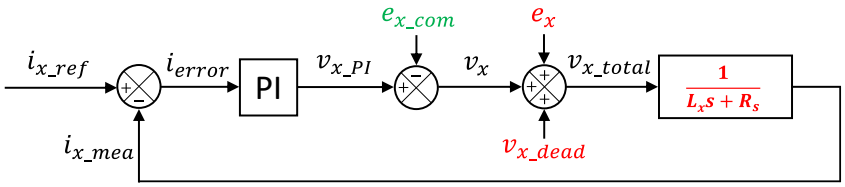

Fig. 3.4. The conventional control scheme of current i_x under the impacts of the unwanted back-EMF harmonic e_x and the "dead-time" voltage v_{x_dead} with the back-EMF compensation e_{x_com} (x can be d_1, q_1, d_9, q_9, d_3, or q_3).

However, the accuracy of the back-EMF compensation depends on the parasitic time constant of the drive, resulting in phase angle differences between the estimated back-EMFs and the experimental back-EMFs. In addition, the estimated back-EMFs based on the no-load operation are different from the experimental back-EMFs under loads. Therefore, the back-EMF compensation may increase, instead of decreasing, the amplitudes of current harmonics. In addition, current harmonics in d-q reference frames are also caused by the inverter nonlinearity with the "dead-time" voltages. Obviously, these current harmonics cannot be eliminated by the back-EMF compensation.

3.2.2.B. *The proposed control scheme to eliminate current harmonics in rotating frames*

As described in Table 3.2, the current harmonics have frequencies of 14θ and 28θ in d-q reference frames. Their amplitudes depend on the back-EMF harmonic distribution, rotating speed, inverter dead time, switching period, and DC-bus voltage. Due to the complexity of the real drive, these values need to be automatically learned in real time to correctly eliminate the current harmonics. With the knowledge of the existing harmonics, the use of ADALINEs is suitable because a fast response of control is guaranteed, and the calculation burden is avoided. Studies in [38, 86] have proved the effectiveness of ANNs as well as ADALINEs thanks to their self-learning, simplicity, and fast convergence. Recently, an ADALINE has been used to eliminate parasitic current harmonics caused by unwanted back-EMFs at high speed in healthy operation for a 3-phase machine as proposed in [174].

Therefore, based on the control structure in Fig. 2.6 in **section 2.1** of **Chapter 2**, a new current control scheme is a combination of a PI controller and an ADALINE as proposed in Fig. 3.5. Current i_x (x can be d_1, q_1, d_9, q_9, d_3, or q_3) is controlled by a PI controller with an adaptive compensating voltage (v_{x_com}) generated by an ADALINE. By using the compensating voltage (v_{x_com}), all current harmonics in d-q frames generated by either the unwanted back-EMF

harmonics or the "dead-time" voltages (inverter nonlinearity) can be eliminated. This compensation is called the ADALINE compensation.

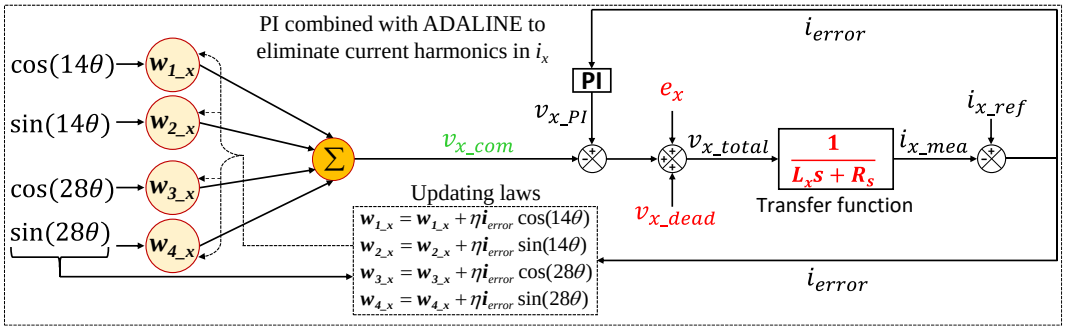

Fig. 3.5. The proposed control scheme of current i_x with current harmonic eliminations by using the ADALINE compensation (v_{x_com}) (x can be d_1, q_1, d_9, q_9, d_3, or q_3).

The inputs of the ADALINE are based on current harmonics as described in Table 3.2. The output of the ADALINE is the compensating voltage v_{x_com} that is generally calculated from harmonics 14θ and 28θ as follows:

$$v_{x\_com} = \left[w_{1\_x}\cos(14\theta) + w_{2\_x}\sin(14\theta)\right] + \left[w_{3\_x}\cos(28\theta) + w_{4\_x}\sin(28\theta)\right] \tag{3.9}$$

where (w_{1_x}, w_{2_x}) are weights associated with harmonic 14θ; (w_{3_x}, w_{4_x}) are weights associated with harmonic 28θ.

To online update these weights, the error $v_{x\_com\_error}$ that is the difference between the output v_{x_com} and its desired value $v_{x\_com\_ref}$ needs to be found. Because v_{x_com} is designed to compensate the unwanted back-EMF harmonics and "dead-time" voltages, the desired output $v_{x\_com\_ref}$ is the sum of the back-EMF (e_x) and "dead-time" voltages (v_{x_dead}). Therefore, the error $v_{x\_com\_error}$ can be calculated as follows:

$$v_{x\_com\_error} = v_{x\_com\_ref} - v_{x\_com} = \left(e_x + v_{x\_dead}\right) - v_{x\_com} \tag{3.10}$$

As previously discussed, the back-EMF (e_x) and "dead-time" voltages (v_{x_dead}) cannot be measured during the operation of the experimental drive. Therefore, $v_{x\_com\_ref}$ is difficult to be determined, leading to the difficulty in determining the error $v_{x\_com\_error}$ for the updating laws. However, it is noted that the compensating voltage error $v_{x\_com\_error}$ is proportional to the current error i_{error} between i_{x_mea} and i_{x_ref}. Indeed, when $v_{x\_com\_error}$ is small, the proper compensating voltage is injected to reduce the impacts of the unwanted back-EMF harmonics and the inverter nonlinearity. Therefore, i_{error} becomes small or even zero if the PI controller is well designed. In addition, current i_{x_mea} can be measured from the drive; hence, the updating laws of harmonic weights can be expressed in Fig. 3.5 with current error i_{error}. Weights of a harmonic are estimated by a learning process with learning rate η, current error i_{error}, and corresponding inputs (harmonics).

It is noted that there are six ADALINEs combined with six PI controllers for six d-q currents (i_{d1}, i_{q1}, i_{d9}, i_{q9}, i_{d3}, and i_{q3}) in a wye-connected winding seven-phase machine. The presence of harmonics (14θ and 28θ) in voltage v_{x_com} in one ADALINE depends on the reference frame of the controlled current according to Table 3.2. Specifically, if x is d_1, q_1, d_3 or q_3, the

ADALINE structure has only 2 weights (w_{1_x}, w_{2_x}) for harmonic 14θ. Meanwhile, if x is d_9 or q_9, 4 weights (w_{1_x}, w_{2_x}, w_{3_x}, w_{4_x}) are used for 2 harmonics 14θ and 28θ. Therefore, the number of weights is optimized to avoid the calculation burden.

The proposed control scheme, eliminating current harmonics caused by unwanted back-EMF harmonics and the inverter nonlinearity, can be generally applied to different electric machines with different back-EMF characteristics and a different number of phases. In a specific case, the harmonic components of currents in d-q frames need to be determined to avoid the calculation burden. Generally, the proposed control scheme can improve the current control quality even when current references in d-q frames are time-variant.

3.2.2.C. *Verification with experimental results*

The considered experimental drive (see **section 2.1.4.A** of **Chapter 2**) is applied to verify effectiveness in eliminating current harmonics in rotating frames of the proposed control scheme in Fig. 3.5 over the back-EMF compensation in Fig. 3.4.

3.2.2.C.1. The back-EMF compensation:

The conventional current control scheme in Fig. 3.3 is applied to the experimental drive (see **section 2.1.4.A**). It is noted that the back-EMF compensation results in high amplitudes of current harmonics in all d-q frames as described in Fig. 3.6. This current control performance is worse than the case without any compensations in **section 2.1.4** of **Chapter 2**.

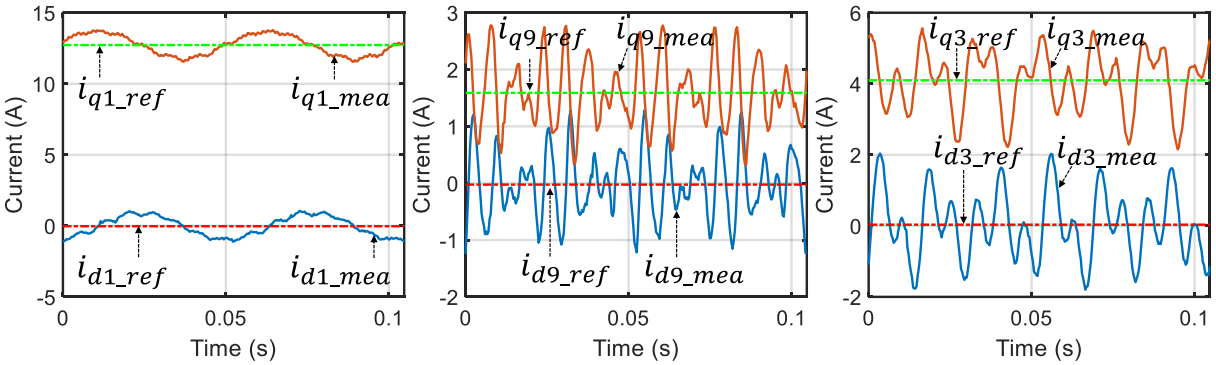

Fig. 3.6. (Experimental result) Currents in (d_1-q_1) frame (a), (d_9-q_9) frame (b), and (d_3-q_3) frame (c) with the back-EMF compensation for current harmonics in rotating frames at 20 rad/s in healthy mode.

As previously discussed, the reason of these distortions is that the compensating back-EMFs are not the same as experimental back-EMFs in terms of phase shift angles even amplitudes. Indeed, the experimental drive contains the parasitic time delay, uncertainties of back-EMFs, inverter "dead-time" impacts, and delays caused by calculations. In conclusion, a self-learning compensation instead of the back-EMF compensation needs to be implemented in the real-time experimental drive. Therefore, the ADALINE compensation is a suitable solution.

3.2.2.C.2. The ADALINE compensation:

The effectiveness of the ADALINE compensation in current harmonic eliminations is shown in Fig. 2.9. The current control performances are significantly improved, especially in (d_9-q_9) and (d_3-q_3) frames. Fig. 3.8a and Fig. 3.9a show the convergence of harmonic weights within

20 s when the learning rate η is 0.0001. According to the LMS rule, η is between 0 and 1. In this doctoral thesis, the value of η has been determined through simulations before applying to the experimental drive. It is noted that this value is proportional to the calculating step (sampling time) of the simulating and experimental systems. In addition, with more powerful processors of the computer and dSPACE, the sampling time is smaller; hence, the response time is shorter.

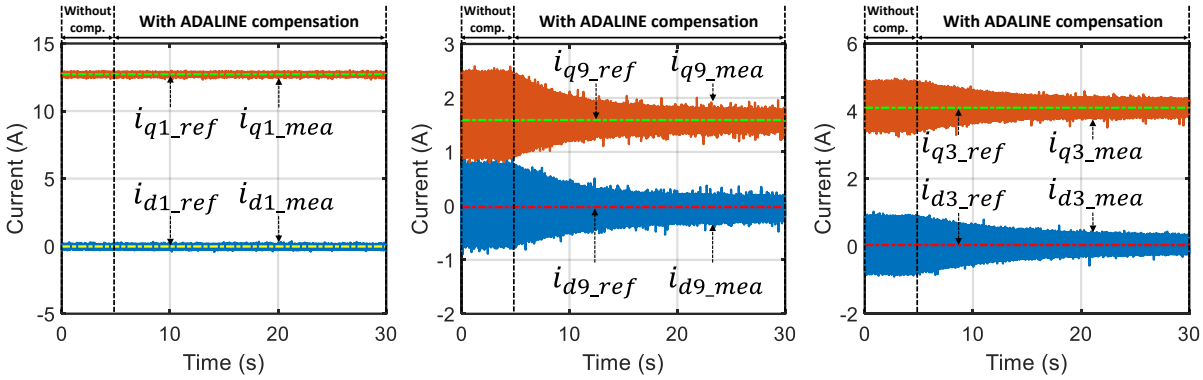

(a) (b) (c)

Fig. 3.7. (Experimental result) Currents in (d_1-q_1) (a), currents in (d_9-q_9) (b), currents in (d_3-q_3) (c) without and with the ADALINE compensation for current harmonics in rotating frames at 20 rad/s in healthy mode.

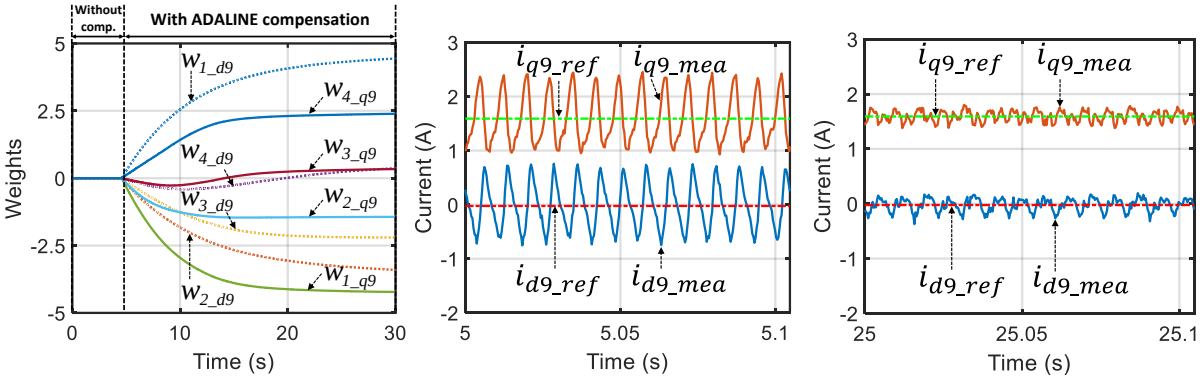

(a) (b) (c)

Fig. 3.8. (Experimental result) Harmonic weights for currents in (d_9-q_9) (a), currents in (d_9-q_9) frame without (b) and with (c) the ADALINE compensation for current harmonics in rotating frames at 20 rad/s in healthy mode.

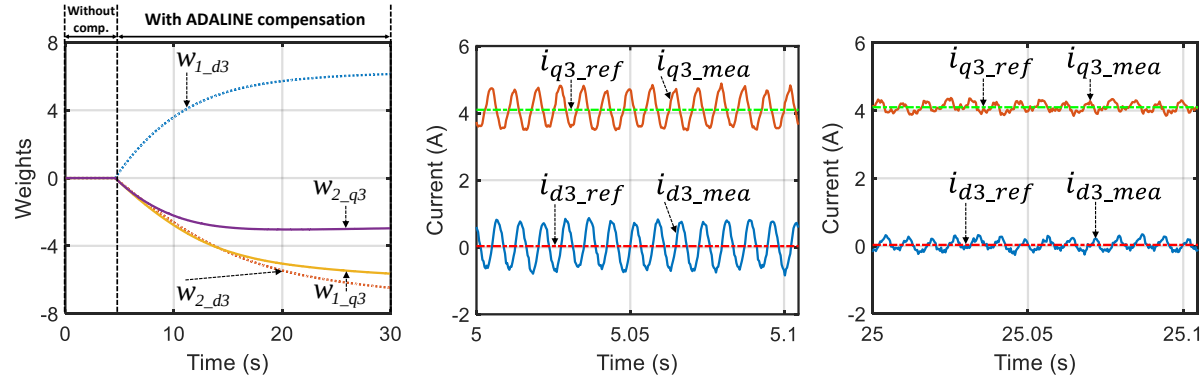

(a) (b) (c)

Fig. 3.9. (Experimental result) Harmonic weights for currents in (d_3-q_3) (a), currents in (d_3-q_3) frame without (b), and with (c) the ADALINE compensation for current harmonics in rotating frames at 20 rad/s in healthy mode.

Current control performances without and with the ADALINE compensation in frames (d_9-q_9) are described in Fig. 3.8b and Fig. 3.8c, respectively. Similarly, Fig. 3.9b and Fig. 3.9c are for currents in (d_3-q_3) frame. The current of phase *A* without and with the ADALINE compensation is shown in Fig. 3.10a. The current waveforms in the two cases are slightly different but the

constraint on RMS current is always respected ($I_{RMS\_A\_com} \leq 5.1$ A). The current harmonics in natural frame generated by the unwanted back-EMFs are mostly eliminated as shown in Fig. 3.10c compared to Fig. 3.10b, especially the 11th harmonic (5.8 to 0.9%). Relatively, only the 1st, 3rd, and 9th harmonics exist in the phase current.

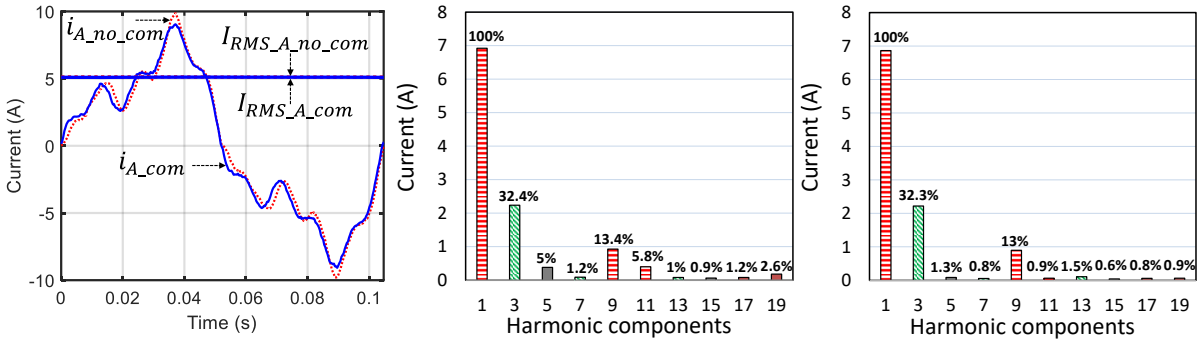

(a) (b) (c)

Fig. 3.10. (Experimental result) Phase-*A* current without ($i_{A\_no\_com}$) and with the ADALINE compensation for current harmonics in rotating frames (i_{A_com}) (a), harmonic spectrums of phase-*A* current without (b) and with (c) the ADALINE compensation at 20 rad/s in healthy mode.

The dynamic performances of the proposed current control structure with ADALINEs are verified with variable speeds and variable current references. The changes of the rotating speed (from 20 to 10 and 30 rad/s) slightly reduce the current control quality as shown in Fig. 3.11.

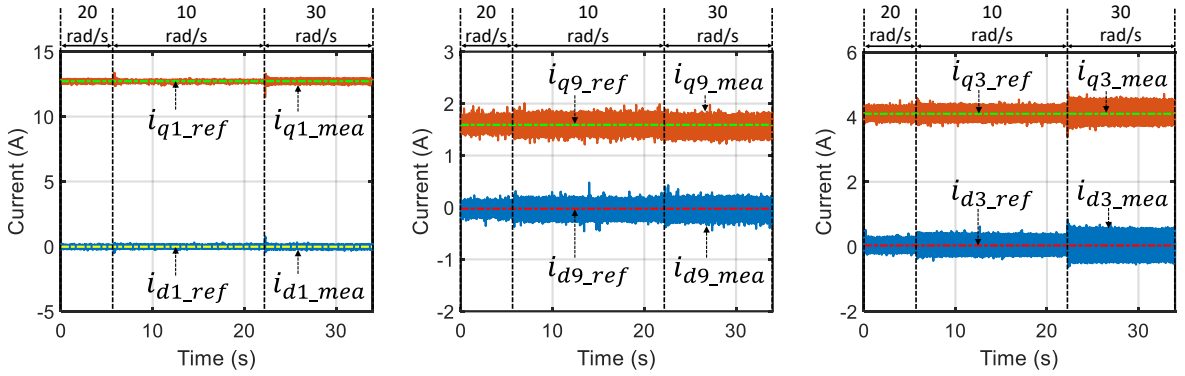

(a) (b) (c)

Fig. 3.11. (Experimental result) Currents with variable speeds in (d_1-q_1) frame (a), in (d_9-q_9) frame (b), and in (d_3-q_3) frame (c) with the ADALINE compensation in healthy mode.

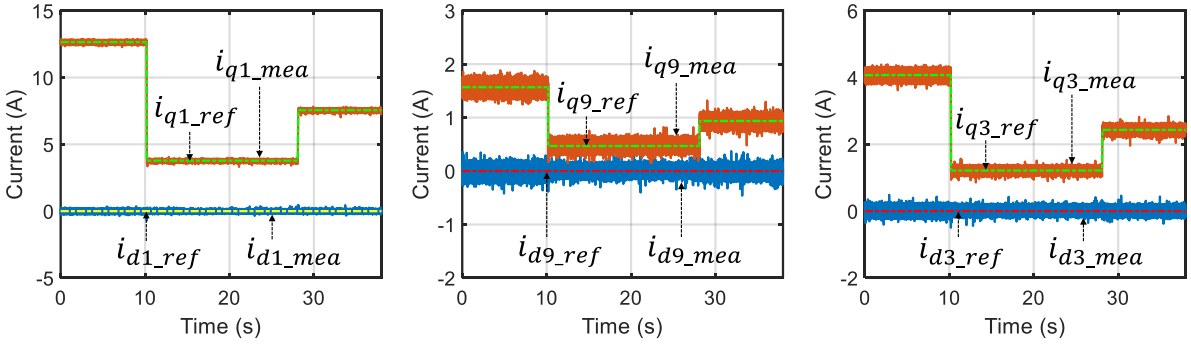

(a) (b) (c)

Fig. 3.12. (Experimental result) Currents with variable current references in (d_1-q_1) frame (a), in (d_9-q_9) frame (b), and in (d_3-q_3) frame (c) with the ADALINE compensation in healthy mode at 20 rad/s.

Meanwhile the variations of current references (torque references) at 20 rad/s do not affect the current control quality as described in Fig. 3.12. As previously discussed, the reason is that the

current harmonics in rotating frames significantly depend on the rotating speed but not on the d-q current references. To see demonstration videos, please click on this link: https://youtu.be/jJcokkMIusI or scan the nearest QR code in this page.

3.2.2.D. *Torque performance after eliminating current harmonics in rotating frames*

When the current harmonics in d-q frames are previously eliminated by the ADALINE compensation, all d-q currents are well controlled. In other words, phase currents only contain the imposed harmonics, for example 1st, 3rd, and 9th in the considered drive. However, the torque ripple still exists at 11% as shown in Fig. 3.13, like the torque ripple of 12% without current harmonic eliminations (see **section 2.1.4** of **Chapter 2**). The reason is that the remaining current harmonics (1st, 9th, and 3rd) interact with unwanted back-EMF harmonics (13th, 19th, and 11th) to generate torque ripples with frequencies of 14θ and 28θ as described in Table 3.3. For example, the torque in the first fictitious machine T_{1_exp} has a frequency of 14θ because the 1st harmonic component of currents interacts with the 13th harmonic of back-EMFs. Similarly, torques in the second and third fictitious machines (T_{2_exp} and T_{3_exp}) have frequencies of 28θ and 14θ, respectively. Finally, the experimental torque of the considered machine T_{em_exp} that is the sum of the three torques generated by the three fictitious machines has frequencies of 14θ and 28θ.

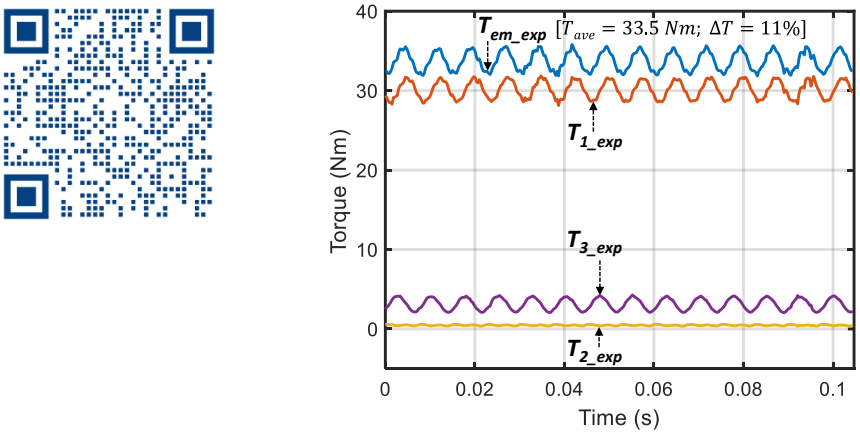

Fig. 3.13. (Experimental result) Torques in one period at 20 rad/s in healthy mode after the eliminations of current harmonics in rotating frames.

Table 3.3. Torque ripples generated by unwanted back-EMF harmonics in fictitious machines of a seven-phase machine.

Fictitious machine	Current harmonics	Unwanted back-EMF harmonics	Torque ripples
The first machine (FM1) with torque T_{1_exp}	1	13	14θ
The second machine (FM2) with torque T_{2_exp}	9	19	28θ
The third machine (FM3) with torque T_{3_exp}	3	11	14θ

Eventually, the current harmonic eliminations can improve current control quality but cannot guarantee a smooth torque. In the next subsection, the above torque ripples will be nullified by another single ADALINE.

3.2.3. Direct eliminations of torque ripples in healthy mode

3.2.3.A. *The proposed control scheme to directly eliminate torque ripples in healthy mode*

The principle of the proposed control scheme is to add compensating currents to the existing constant current references of the offline optimization. These compensating currents are directly determined from harmonic components of the electromagnetic torque. In other words, an additional torque, called compensating torque T_{em_com}, needs to be added. This torque is expected to be equal to the difference between the constant torque reference T_{em_ref} and the experimental torque T_{em_exp} with ripples in Fig. 3.13. The torque reference T_{em_ref} is a constant torque in the optimal torque-speed characteristic, as described in Fig. 2.9a of **Chapter 2**, to respect the constraints on current and voltage. Therefore, the desired value of the compensating torque is described as follows:

$$T_{em\_com\_ref} = T_{em\_ref} - T_{em\_exp} \tag{3.11}$$

To determine the compensating torque, the control structure with only one ADALINE is proposed in Fig. 3.14.

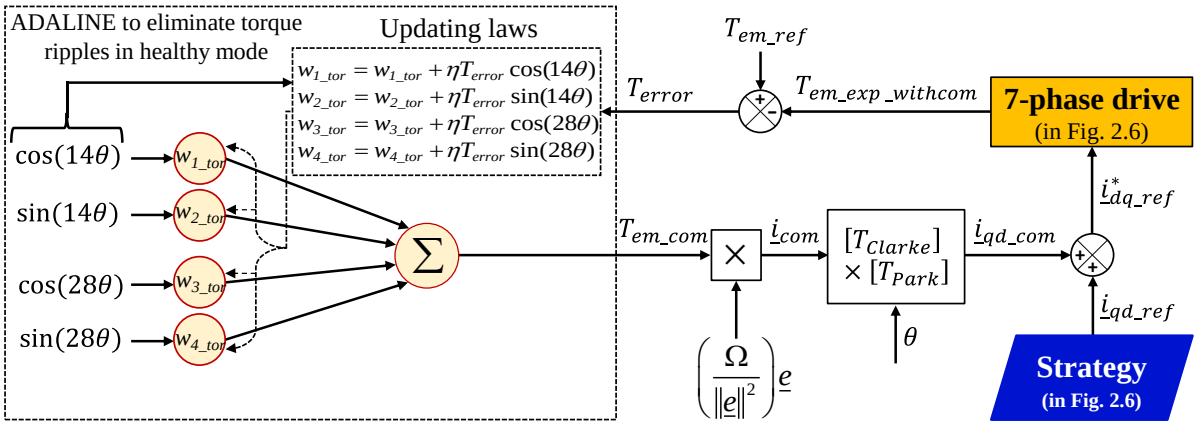

Fig. 3.14. The proposed structure using an ADALINE to directly eliminate torque ripples in healthy mode.

The inputs are harmonic components presenting in the experimental torque in Table 3.3. The output of the ADALINE is the compensating torque T_{em_com} that is the weighted sum of the inputs as follows:

$$T_{em\_com} = \left[w_{1\_tor} \cos(14\theta) + w_{2\_tor} \sin(14\theta) \right] + \left[w_{3\_tor} \cos(28\theta) + w_{4\_tor} \sin(28\theta) \right] \tag{3.12}$$

where (w_{1_tor}, w_{2_tor}) and (w_{3_tor}, w_{4_tor}) are weights of two harmonics 14θ and 28θ, respectively.

According to the ADALINE principle, the error $T_{em\_com\_error}$, the difference between the desired compensating torque $T_{em\_com\_ref}$ and the output of the ADALINE T_{em_com}, needs to be determined for weight updating laws. Meanwhile, as previously mentioned, the desired compensating torque is calculated as in (3.11). Therefore, the error can be calculated as follows:

$$\begin{aligned} T_{em\_com\_error} &= T_{em\_com\_ref} - T_{em\_com} = \left(T_{em\_ref} - T_{em\_exp}\right) - T_{em\_com} \\ &= T_{em\_ref} - \left(T_{em\_exp} + T_{em\_com}\right) \end{aligned} \tag{3.13}$$

$$T_{em\_com\_error} = T_{em\_ref} - T_{em\_exp\_withcom} = T_{error} \tag{3.14}$$

From (3.13), the error of the compensating torque for updating laws can be described in (3.14) where $T_{em\_exp\_withcom}$ is the experimental torque with the compensating torque. The details of the updating laws are shown in Fig. 3.14. Therefore, the weights of harmonic components are updated by the learning rate η, torque error T_{error}, and corresponding harmonics.

Thereafter, as introduced in [121], compensating currents in natural frame $\underline{i}_{com}$, calculated from compensating torque T_{em_com} and back-EMFs $\underline{e}$, are expressed by:

$$\underline{i}_{com} = \frac{T_{em\_com}\Omega}{\|\underline{e}\|^2}\underline{e} \tag{3.15}$$

Then, these currents are transformed into d-q frames $\underline{i}_{dq\_com}$ and added to constant current references $\underline{i}_{dq\_ref}$ generated by the offline optimization in Fig. 2.6 of **Chapter 2**. Eventually, the total current references $\underline{i}^*_{dq\_ref}$ are used to create the electromagnetic torque $T_{em\_exp\_withcom}$ in the seven-phase drive. The total current references in d-q frames are no longer constant due to the compensating currents.

It is worth noting that the approach in Fig. 3.14 only aims at learning only pulsating components of the torque. Therefore, d-axis current references that do not generate torques are almost zero, facilitating current control with conventional PI controllers. Meanwhile, the approach in [86] considers the entire torque in the learning process, resulting in all time-variant current references, similar to [121]. For the sake of simplicity, in the next subsection, study [121] will be used to compared with the proposed structure in Fig. 3.14 of this doctoral thesis.

This proposed structure in Fig. 3.14 to eliminate torque ripples caused by unwanted back-EMF harmonics can be generally applied to different electric machines with different back-EMF characteristics and a different number of phases. In those cases, the harmonic components of the electromagnetic torque need to be determined to reduce the number of weights, avoiding the calculation burden. Theoretically, these harmonics are multiples of the number of phases.

3.2.3.B. *Comparisons with the vectorial approach by real-time simulation results*

With the vectorial approach in [121], a constant torque can always be obtained regardless of operating modes by using current references as generally calculated in (2.8)-(2.9) in **Chapter 2**. The performances of the vectorial approach are compared with the proposed structure using an ADALINE in Fig. 3.14. The comparisons are based on real-time simulations by Simulink in MATLAB and the considered drive from **section 2.1.4** of **Chapter 2** with the unwanted back-EMF harmonics (11^{th}, 13^{th}, and 19^{th}). The learning rate η in all ADALINEs is chosen to be 0.0001. The average torque is expected to be unchanged regardless of control strategies. It is noted that, the case using only ADALINEs for current harmonic eliminations in rotating frames has been previously discussed in **section 3.2.2.D**. These eliminations of current harmonics cannot eliminate torque ripples. Therefore, for the sake of simplicity, an operation of the drive consists of 4 stages as follows:

1) *Stage 1:* Use original constant d-q current references $\underline{i}_{dq\_ref}$ from the offline optimization in Fig. 2.6 of **Chapter 2** with inevitable torque ripples.
2) *Stage 2:* Apply the vectorial approach in [121] to define new current references (time-variant), as calculated in (2.8)-(2.9) in **Chapter 2**, to generate a theoretically constant torque.
3) *Stage 3:* Apply the proposed structure in Fig. 3.14 using the ADALINE for torque ripple eliminations.
4) *Stage 4:* Combine the ADALINE for torque ripple eliminations in Fig. 3.14 and the six ADALINEs for current harmonic eliminations[3] in Fig. 3.5.

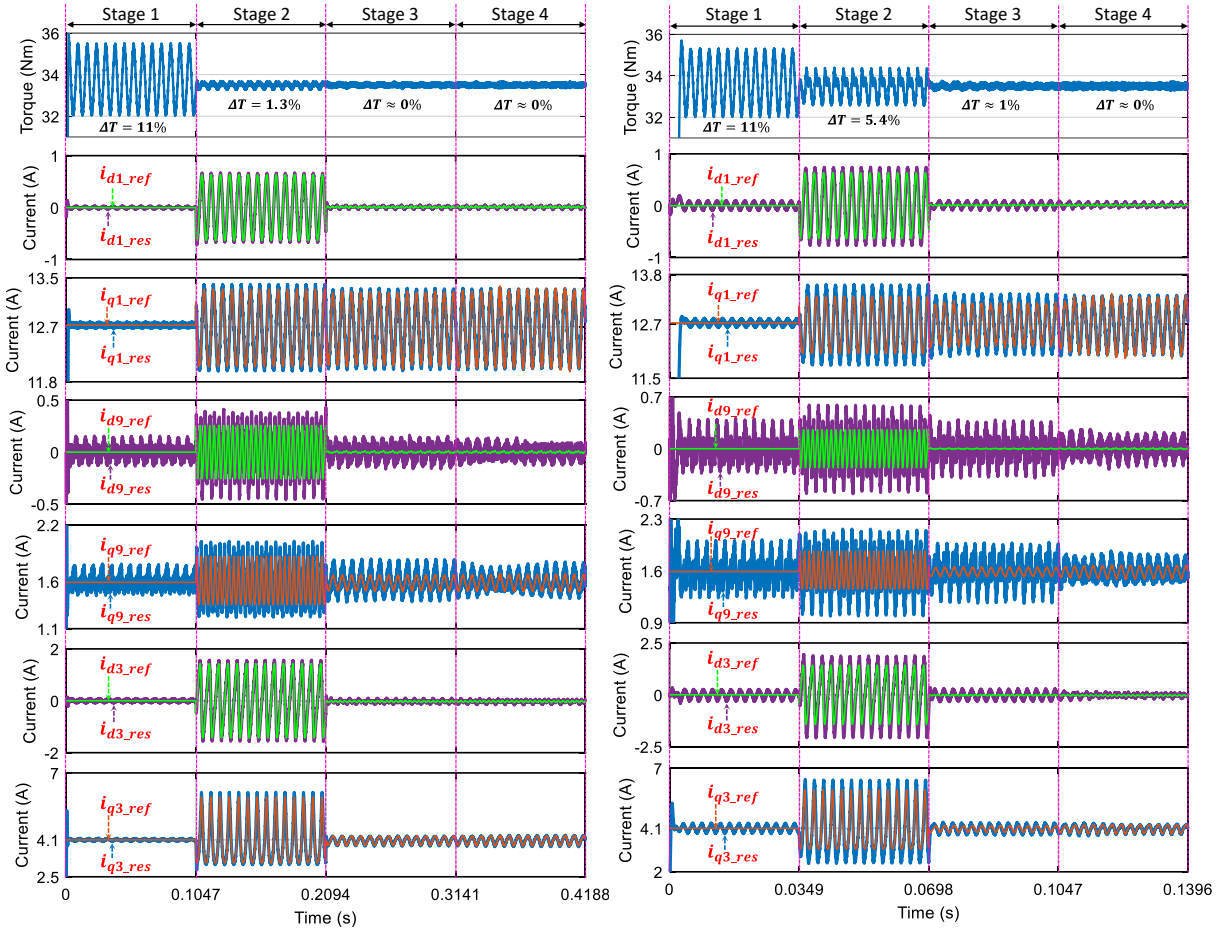

Fig. 3.15. (Real-time simulation result) Torque and current control performances at 20 rad/s (a), and at 60 rad/s (b) in healthy mode with 4 operating stages (η=0.0001 for torque eliminations in stages 3 and 4).

At a speed of 20 rad/s, as described in Fig. 3.15a, torques in stages 3 and 4 are almost constant, much better than stage 1 with a ripple of 11%, and slightly better than stage 2 with a ripple of 1.3%. Therefore, the effectiveness of the single ADALINE for torque ripple eliminations (stage 3) and its combination (stage 4) with the six ADALINEs for current harmonic eliminations is not clear at low speed. It is worth noting that current references in stages 2, 3, and 4 are not constant. The current references in stage 2, generated by the vectorial approach in [121], are

[3] The use of the six ADALINEs for current harmonic eliminations in Fig. 3.5 aims at eliminating the impacts of the unwanted back-EMF harmonics and the inverter nonlinearity with "dead-time" voltages, improving current control quality even when current references are not constant.

time-variant with high amplitudes. Meanwhile, these currents of the proposed structure with ADALINEs in stages 3 and 4 have lower amplitudes, especially the d-axis currents. This important characteristic affects current control quality at higher speeds.

Indeed, at a speed of 60 rad/s, as shown in Fig. 3.15b, the torque in stage 4 is still constant while stage 2 with the vectorial approach has a ripple of 5.4%. The torque in stage 3 is no longer constant with a ripple of about 1%. It is noted that the ADALINE for torque ripple eliminations combined with the six ADALINEs for current harmonic eliminations in stage 4 results in the highest control and torque quality. Thanks to the six ADALINEs for current harmonic eliminations as presented in the previous subsection, the currents are better controlled.

Eventually, from now on in this chapter, the torque ripple elimination in Fig. 3.14 is always combined with the current harmonic elimination in Fig. 3.5, generally called the torque ripple elimination. However, for the sake of simplicity, only the learning process to eliminate torque ripples will be discussed in the next subsections.

3.2.3.C. *Verification with experimental results*

If the optimal torque speed-characteristic for the torque ripple elimination is the same as the original characteristic as described in Fig. 2.9a of **Chapter 2**, the constraint on RMS current is mostly respected but the peak phase voltage references will exceed its limit 100 V. Therefore, the offline optimization in Fig. 2.6 of **Chapter 2** needs to be recalculated with a smaller value of V_{lim_opt} instead of 75 V. In Fig. 3.16a, according to simulation assessments, a new optimal torque-speed characteristic for the torque ripple elimination is calculated with V_{lim_opt}=55 V, called the reduced characteristic. The base speed is reduced from 38 to 25 rad/s. Calculated torque values at speeds over the new base speed are smaller than those in the original characteristic, leading to a smaller speed range.

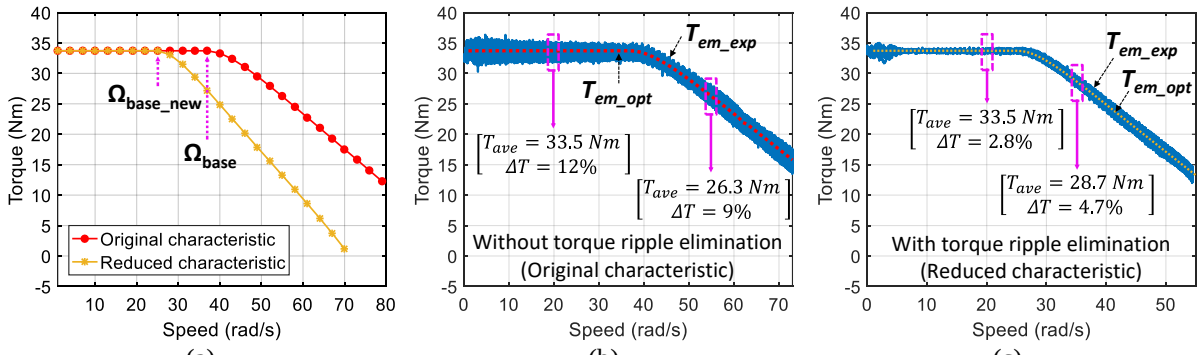

(a) (b) (c)

Fig. 3.16. (Experimental result) The optimal calculated torque-speed characteristics (a), experimental torque-speed characteristics without (b) and with (c) the torque ripple elimination in healthy mode.

The experimental torque-speed characteristics without and with the torque ripple elimination are described in Fig. 3.16b and Fig. 3.16c. It is noted that the torque ripple at 20 rad/s, before the base speed, is significantly reduced from about 12 to 2.8% after the torque ripple elimination. In the flux-weakening regions, the ripple of the original characteristic at 55 rad/s is 9% while the torque ripple of the new characteristic at 35 rad/s is 4.7%. In the flux-weakening

region of the reduced characteristic, torque ripples are slightly higher than the low-speed region because ADALINEs respond to fast coincident variations in speed and current references.

The measured phase currents are described in Fig. 3.17a with a slight increase in the RMS current from 5.1 to 5.3 A. The reason is that the compensating currents with harmonics are imposed to eliminate torque ripples. Meanwhile, the phase voltage references almost respect the peak voltage limit of 100 V as described in Fig. 3.17b. Indeed, as previously discussed, the voltage limit for the offline optimization V_{lim_opt} is reduced from 75 V to 55 V to respect the voltage constraint in the experimental drive.

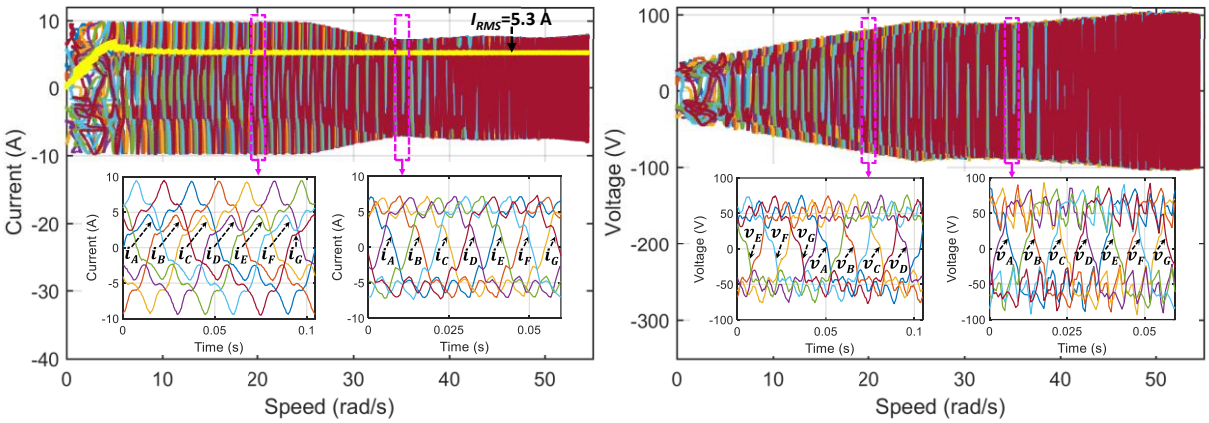

Fig. 3.17. (Experimental result) Phase currents (a), and phase voltage references (b) in terms of speed and time with the torque ripple elimination in healthy mode.

The ADALINE learning process to eliminate torque ripples at 20 rad/s are described in Fig. 3.18a. With a learning rate η of 0.001, harmonic weights (w_{1_tor}, w_{2_tor}, w_{3_tor}, w_{4_tor}) converge within 7 s. An increase in the learning rate η can make the convergence of the harmonic weights faster, but the instability of the control system may happen. With more powerful processors of the computer and dSPACE, the convergence time could be reduced. After the learning process, the torque ripples are significantly reduced from 12 to 2.8%. More clearly, torque and current control performances in one period from the 40th second after the learning process are shown in Fig. 3.18b. The time-variant d-q currents are properly controlled, especially currents (i_{d1}, i_{q1}), generating most of the torque. Like the simulation results in Fig. 3.15, the d-axis currents (i_{d1}, i_{d9}, i_{d3}) are almost zero, facilitating current control with conventional PI controllers.

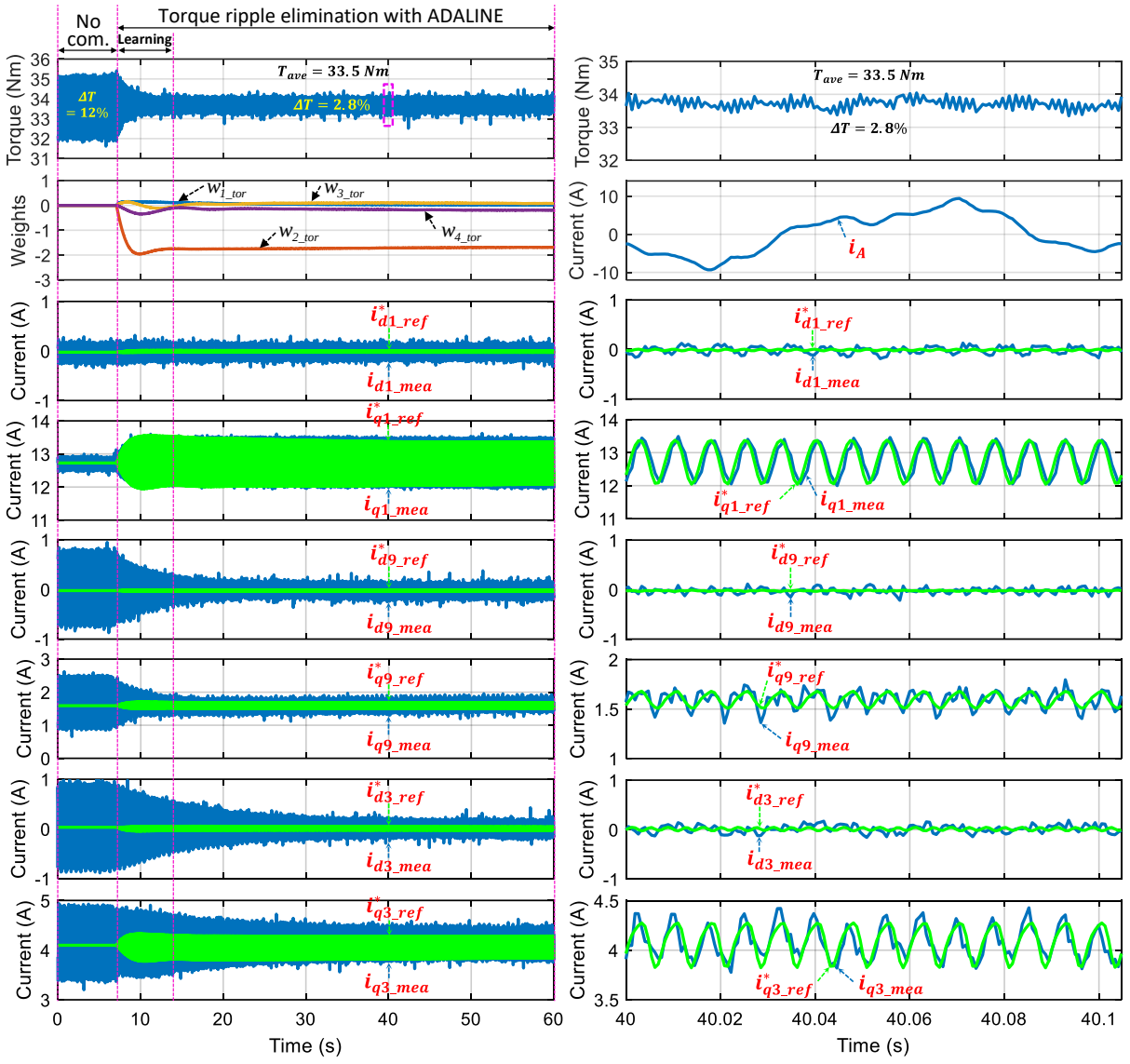

Fig. 3.18. (Experimental result) Torque, torque harmonic weights, and current control performances with the ADALINE learning process (η=0.001) (a), and in one period from the 40th second at 20 rad/s (b) in healthy mode.

The dynamic performances of the proposed control structure to eliminate torque ripples are validated when the operating speed suddenly changes from 20 to 35 rad/s, over the base speed, and return to 20 rad/s. According to the torque-speed characteristic in Fig. 3.16c, this speed variation also leads to changes of the torque as well as current references to respect the constraint on peak phase voltage references. Fig. 3.19 shows adaptations of the torque, torque harmonic weights, and current control performances in response to the changes of the rotating speed and current references. An increase in the rotating speed from 20 to 35 rad/s results in a decrease in the average torque from 33.5 to 28.7 Nm. In addition, the corresponding torque ripple increases from 2.8 to 4.7%. However, this increase in the torque ripple is mainly due to the decrease in the average torque but not due to the ADALINE performance. To see demonstration videos, please click on this link: https://youtu.be/ylb0cc0_n7U or scan the nearest QR code in this page.

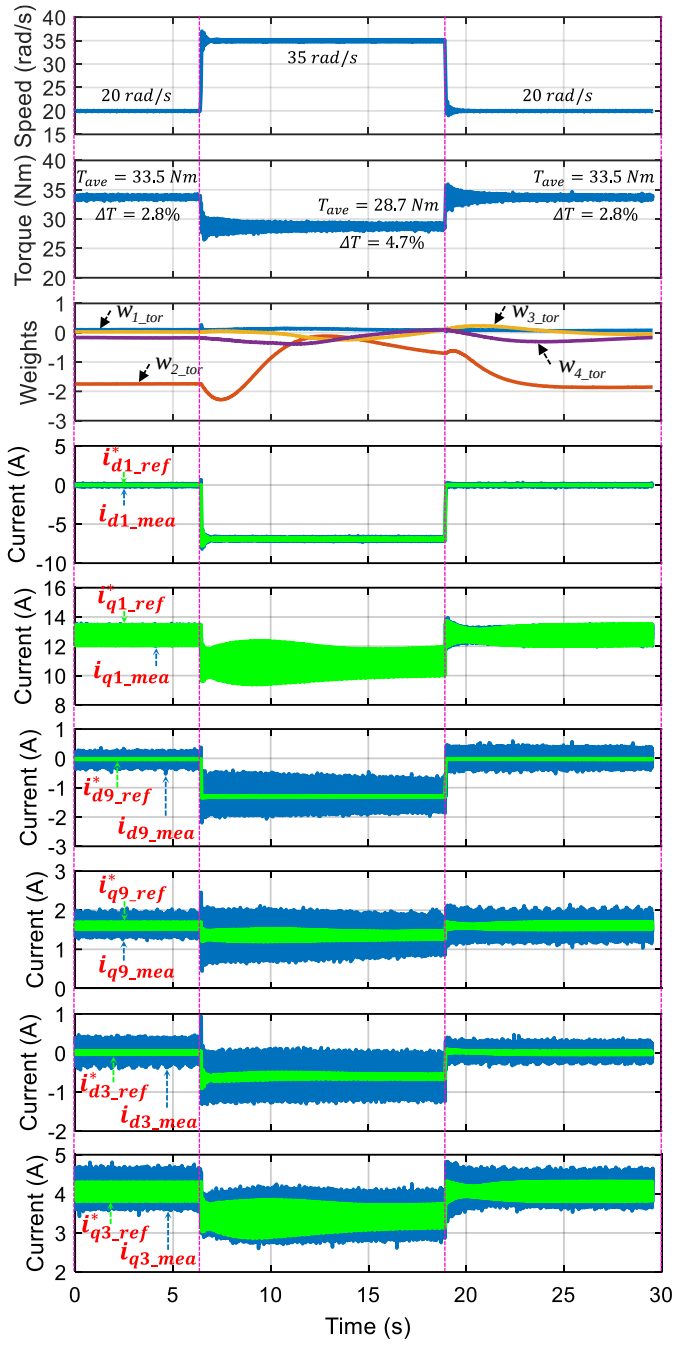

Fig. 3.19. (Experimental result) Torque, torque harmonic weights (η=0.001), and current control performances in response to the rotating speed from 20 to 35 rad/s, then to 20 rad/s, including current reference variations in healthy mode.

3.3. Control quality in faulty mode

Among the fault-tolerant control methods proposed in **Chapter 2**, method (III)-2 results in the highest average torque but high torque ripples (see **section 2.3.4.G** of **Chapter 2**). Meanwhile, method (II)-RCA with robustness, unaffected by the back-EMF harmonics in the second fictitious machine (5^{th} and 9^{th}, for example), suffers from the time-variant d-q current references. Consequently, at high speed, the current control quality with conventional PI controllers is reduced, leading to higher torque ripples (see **section 2.3.3.F** of **Chapter 2**).

Therefore, this section provides various solutions to improve the torque performance with ADALINEs in faulty mode as follows:

1) An ADALINE is used to directly eliminate torque ripples in method (III)-2. Its structure is like the one in healthy mode, but harmonic components of the torque are redefined to avoid the calculation burden.
2) An ADALINE is applied to method (II)-RCA to improve current control quality, resulting in higher-quality torques. Indeed, the ADALINE is to separate harmonics of measured phase currents in natural frame, enabling current control with time-constant references. Therefore, the torque quality can be improved at high speed.

3.3.1. Direct eliminations of torque ripples in faulty mode with method (III)-2

3.3.1.A. *Harmonic components of torque and the proposed control structure*

In method (III)-2, new current references are designed in natural frame with identical waveforms, including the first and third harmonic components. As discussed in **Chapter 2**, when only the first and third harmonic components of the back-EMFs are considered, the torque consists of ripples with frequencies of 2θ, 4θ, and 6θ and the total calculated ripple of 19%.

More generally, when the 9^{th}, 11^{th}, and 13^{th} harmonics are considered in the back-EMFs besides the 1^{st} and 3^{rd} harmonics, possible harmonic components of the torque can be up to 22θ as presented in Table 3.4.

Table 3.4. Possible harmonic components of the torque generated with method (III)-2.

Back-EMF harmonic / Current harmonic	**1st**	**3rd**	**9th**	**11th**	**13th**	**19th**
1st	2θ	2θ, 4θ	8θ, 10θ	10θ, 12θ	12θ, 14θ	18θ, 20θ
3rd	2θ, 4θ	6θ	6θ, 12θ	10θ, 12θ	10θ, 16θ	16θ, 22θ

Therefore, the structure of an ADALINE for method (III)-2 is described in Fig. 3.20 with the updating laws as in healthy mode. The compensating torque (ADALINE output) T_{em_com} is directly determined from harmonic components of the torque (ADALINE inputs) as follows:

$$\begin{aligned} T_{em\_com} = &\left[w_{1\_tor}\cos(2\theta) + w_{2\_tor}\sin(2\theta) \right] + \left[w_{3\_tor}\cos(4\theta) + w_{4\_tor}\sin(4\theta) \right] + \cdots \\ &+ \left[w_{21\_tor}\cos(22\theta) + w_{22\_tor}\sin(22\theta) \right] \end{aligned} \tag{3.16}$$

where 22 weights from w_{1_tor} to w_{22_tor} are used for 11 corresponding even harmonics.

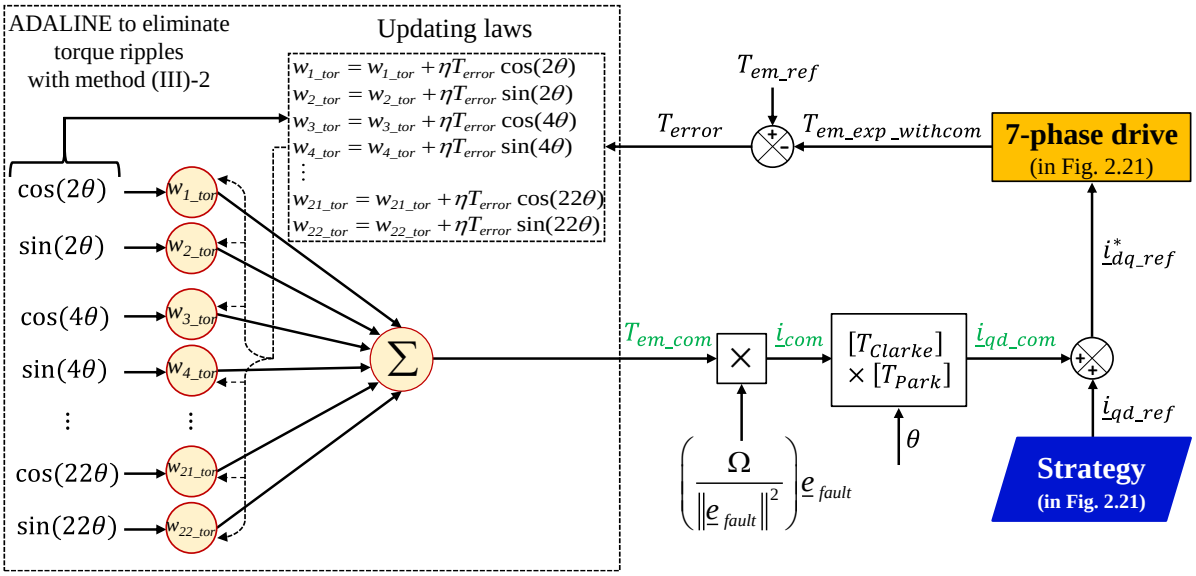

Fig. 3.20. The proposed structure using an ADALINE to directly eliminate torque ripples in faulty mode with method (III)-2.

After obtaining the compensating torque T_{em_com}, as in [121], the compensating currents are calculated as follows:

$$i_{com} = \frac{T_{em\_com}\Omega}{\|e_{fault}\|^2} e_{fault} \quad \text{with } e_{fault} = [0 \quad e_B \quad e_C \quad e_D \quad e_E \quad e_F \quad e_G] \tag{3.17}$$

where the back-EMF of phase *A* is zero in e_{fault}. However, in real-time calculations, only main harmonics of the torque, determined from the back-EMF or torque harmonic spectrum, can be selected instead of all possible harmonics to reduce the number of weights, avoiding the calculation burden.

3.3.1.B. *Verification with experimental results*

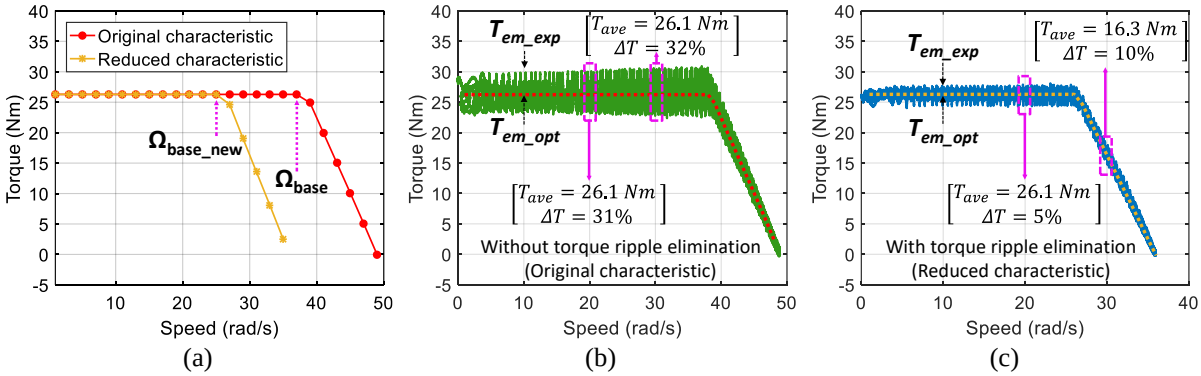

(a) (b) (c)

Fig. 3.21. (Experimental result) The optimal calculated torque-speed characteristics (a), the experimental torque-speed characteristics without (b) and with (c) the torque ripple elimination when phase *A* is open-circuited.

A reduced optimal torque-speed characteristic is defined to respect the constraints on peak voltage as described in Fig. 3.21a. Like healthy mode, the base speed reduces from 38 to 25 rad/s. The experimental characteristics without and with the torque ripple elimination are shown in Fig. 3.21b and Fig. 3.21c, respectively. At 20 rad/s, before the base speed, the torque ripple is significantly reduced from 31 to 5% after the torque ripple elimination with the same average

torque of 26.1 Nm. At 30 rad/s, the average torque decreases to 16.3 Nm in the reduced characteristic due to the peak voltage limit. It is worth noting that the torque ripple reduces from 32% to 10% after the ripple elimination.

The measured phase currents are described in Fig. 3.22a with a slight increase in the highest RMS current from 5.1 to 5.4 A. The reason is that the compensating currents with harmonics are imposed to eliminate torque ripples. Meanwhile, the phase voltage references almost respect the peak voltage limit of 100 V as described in Fig. 3.22b. Indeed, as previously discussed, the voltage limit for the offline optimization V_{lim_opt} is reduced from 75 to 55 V to respect the voltage constraint in the experimental drive.

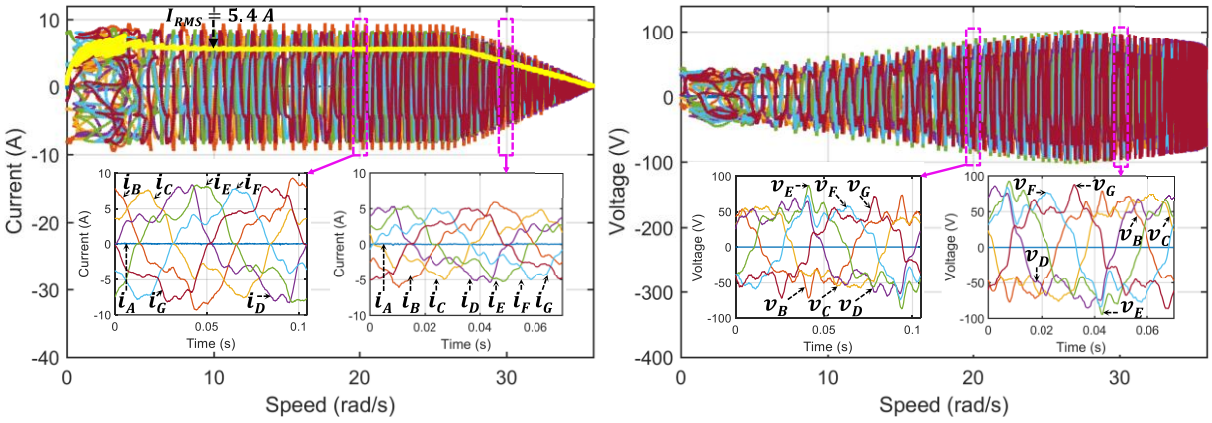

Fig. 3.22. (Experimental result) Phase currents (a), and phase voltage references (b) in terms of speed and time with the torque ripple elimination when phase *A* is open-circuited.

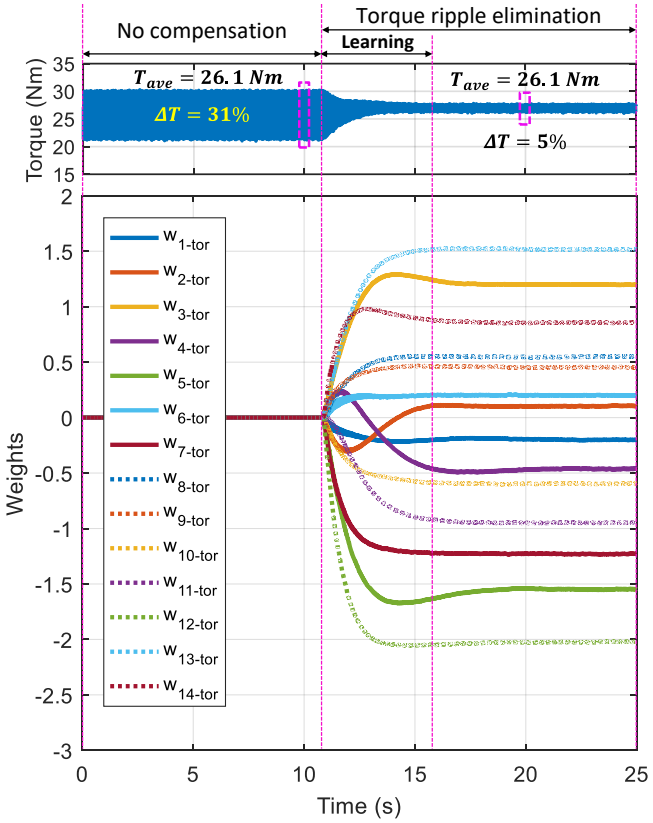

Fig. 3.23. (Experimental result) Torque, torque harmonic weights with the learning process at 20 rad/s to eliminate torque ripples when phase *A* is open-circuited with method (III)-2 and η=0.001.

The ADALINE learning process to eliminate torque ripples at 20 rad/s are described in Fig. 3.23. According to the experimental seven-phase machine in this doctoral thesis, the harmonic components for the ADALINE to eliminate torque ripples can be down to 14θ with 7 even harmonics. Therefore, there are 14 harmonic weights that converge within 5 s with the learning rate η of 0.001. An increase in the learning rate η can make the convergence of the harmonic weights faster, but the instability of the control system may happen. With more powerful processors of the computer and dSPACE, the convergence time could be reduced. After the learning process, the torque ripples are significantly reduced from 31 to 5%. More clearly, torque and current control performances in one period from the 10th and 20th second, equivalent to without and with the torque ripple elimination, are respectively shown in Fig. 3.24a and Fig. 3.24b. The current control quality in these figures is similar. However, because of generating most of the torque, new current references in (d_1-q_1) frame in Fig. 3.24b are significantly modified by the ADALINE with additional compensating currents to eliminate torque ripples.

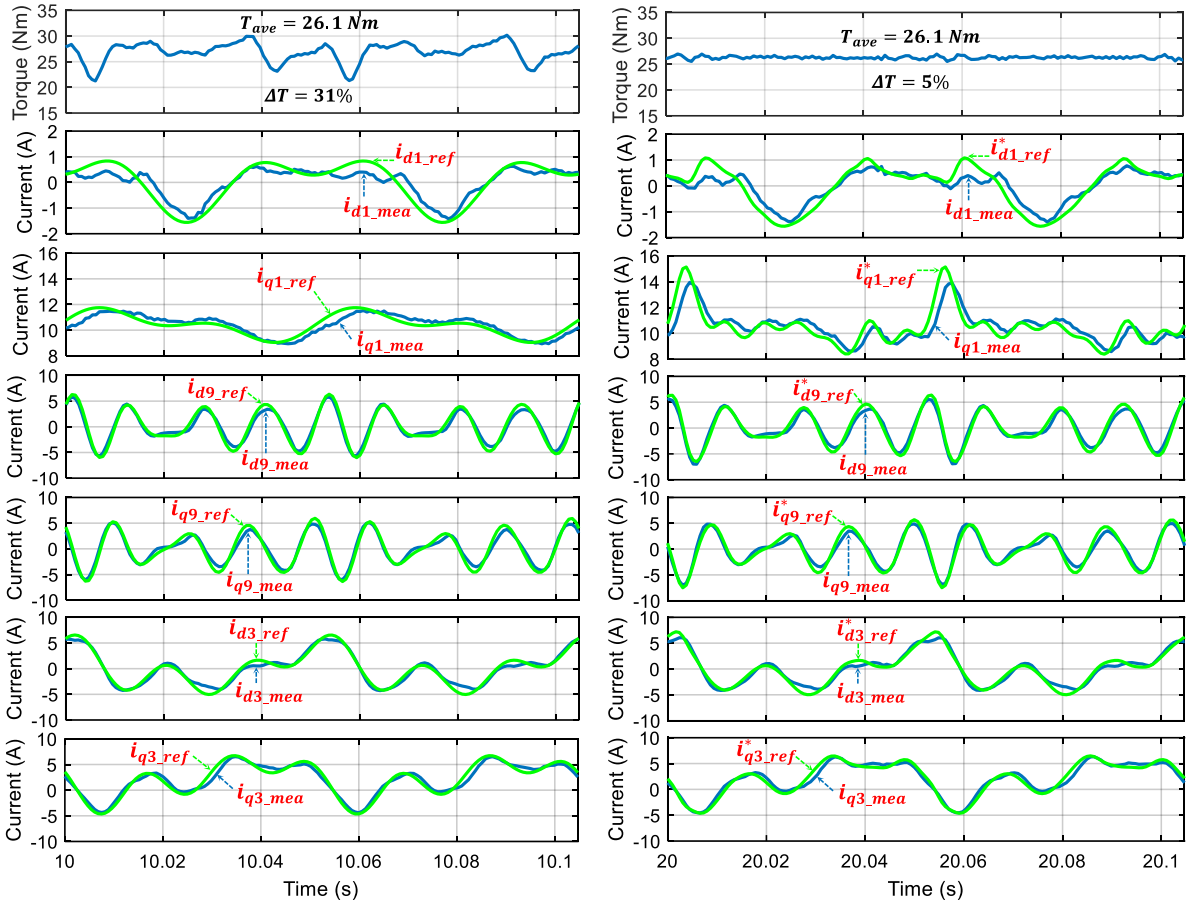

Fig. 3.24. (Experimental result) Torque and current control performances in one period from the 10th second (without the torque ripple elimination) (a), and from the 20th second (with the torque ripple elimination and η=0.001) (b) when phase *A* is open-circuited with method (III)-2.

The dynamic performances of the proposed control structure to eliminate torque ripples are validated when the operating speed changes from 20 to 30 rad/s, over the base speed, and then returns to 20 rad/s. According to the torque-speed characteristic in Fig. 3.21c, these speed variations also lead to changes in the torque reference as well as current references to respect the constraint on peak voltage. Fig. 3.25 shows adaptations of the torque and harmonic weights

in response to the changes of the rotating speed and current references. An increase in the rotating speed from 20 to 30 rad/s results in a decrease in the average torque from 26.1 to 16.3 Nm. In addition, the corresponding torque ripple increases from 5 to 10%. However, this increase in the torque ripple is due to the decrease in the average torque but not due to the ADALINE performance. To see demonstration videos, please click on this link: https://youtu.be/pqxElkrpU0Y or scan the nearest QR code in this page.

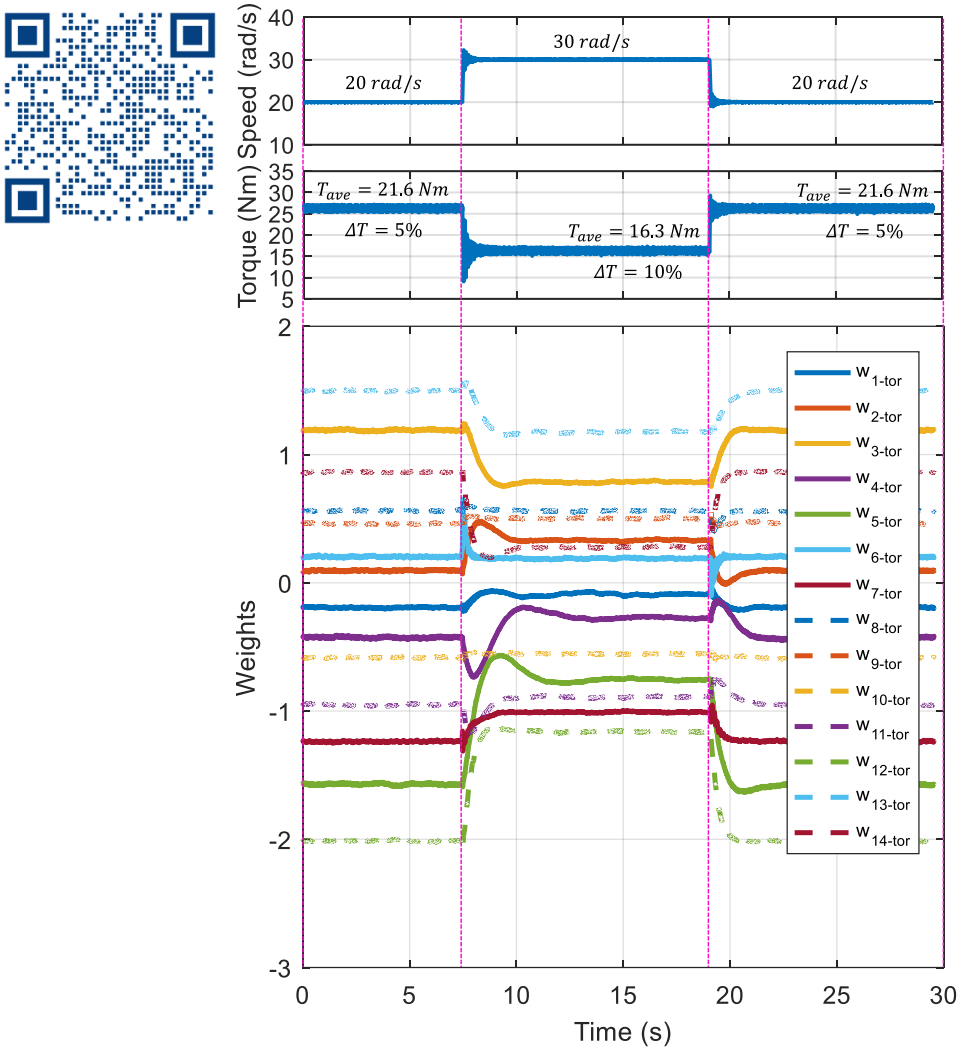

Fig. 3.25. (Experimental result) Torque and harmonic weights (η=0.001) when the rotating speed changes from 20 to 30 rad/s and then returns to 20 rad/s under an OC fault in phase *A*.

3.3.2. Current control improvements in faulty mode with method (II)-RCA

3.3.2.A. *Time-variant current references*

Method (II) in **section 2.3.3** of **Chapter 2** applies new transformation matrices $[\boldsymbol{T}^{\mathbf{1}}_{\boldsymbol{Clarke}}]$ and $[\boldsymbol{T}^{\mathbf{3}}_{\boldsymbol{Clarke}}]$ to find new current references when phase *A* is open-circuited. These current references with method (II)-RCA are calculated based on Fig. 3.26. It is noted that the total d-q current references for the pre-fault control scheme are time-variant in the first and third fictitious machines. Ideally, if the constant references (i_{d11}, i_{q11}, i_{d91}, i_{q91}, i_{x1}) and (i_{d33}, i_{q33}, i_{d93}, i_{q93}, i_{x3}) are directly used for current controllers, their measured values, as feedback signals, need to be determined from measured phase currents. However, the measured phase currents cannot be

directly transformed into d-q frames by using $[\boldsymbol{T}^{\mathbf{1}}_{\boldsymbol{Clarke}}]$ and $[\boldsymbol{T}^{\mathbf{3}}_{\boldsymbol{Clarke}}]$ if the first and third harmonic components of the measured phase currents are not separated. The time-variant current references reduce the control quality at high speed as shown in **section 2.3.3.F.2**. Therefore, a solution to separate harmonics of measured phase currents is necessary.

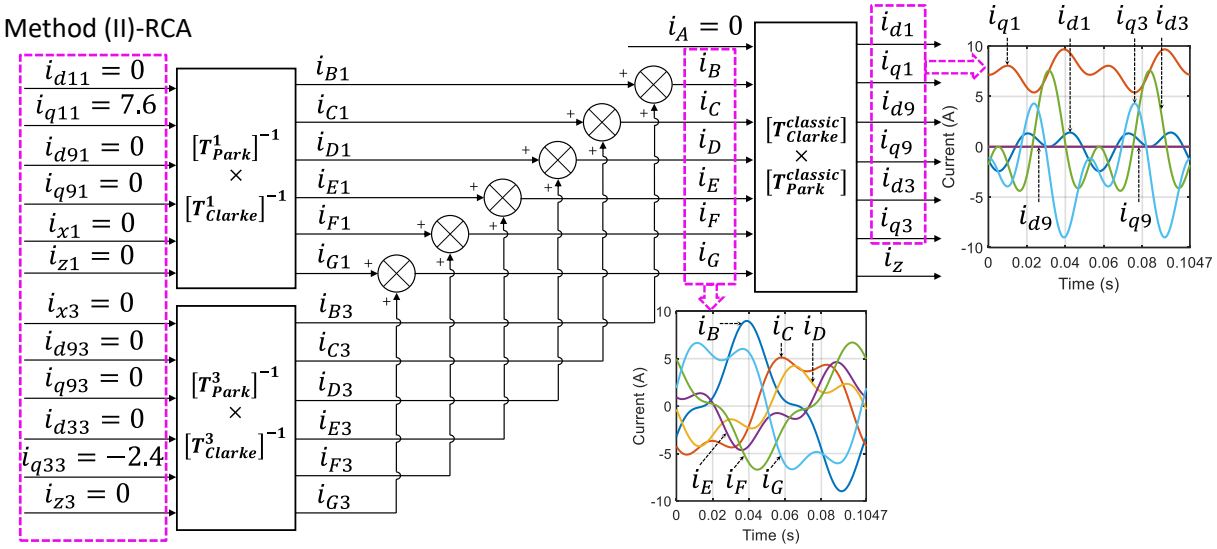

Fig. 3.26. Time-variant d-q current references generated with method (II)-RCA for the pre-fault control scheme.

3.3.2.B. *Proposed control structure to use time-constant d-q current references*

In [177], a PLL based on ADALINE has been proposed and it has been concluded that the ADALINE-based PLL gives a better performance compared to the conventional PLL. That is thanks to several advantages of neural networks such as online self-learning, fast convergence, and simple implementation in real time. Therefore, an ADALINE is a good option to separate harmonic components of measured phase currents, allowing to use more constant d-q current references for control.

In this doctoral thesis, a real-time current learning (RTCL) using an ADALINE is proposed. RTCL is to learn and separate measured phase currents into several harmonic components, for example the 1st and 3rd harmonics. These separated harmonics are transformed into d-q frames by using $[\boldsymbol{T}^{\mathbf{1}}_{\boldsymbol{Clarke}}]$ and $[\boldsymbol{T}^{\mathbf{3}}_{\boldsymbol{Clarke}}]$ to obtain constant d-q currents in method (II). Therefore, the new control structure for method (II) is represented by EMR in Fig. 3.27 in which the offline optimization considering constraints on RMS current and peak voltage is implemented. It is noted that, the new control structure has 10 PI controllers instead of 6 PI controllers in the pre-fault control scheme in Fig. 2.21 of **Chapter 2**.

The details of RTCL are described in the block diagram of the new control structure in Fig. 3.28. The real-time current learning RTCL aims at separating harmonics of measured phase currents to estimate useful current harmonics in natural frame. The harmonic separation allows to obtain constant d-q currents used as feedback signals of PI controllers. The most important part of RTCL is a simple ADALINE to estimate the measured current of only a single arbitrary phase among the remaining healthy phases. Then, the other phase currents are derived from their mathematical relationships with the ADALINE-based estimated current by using current design options RCA and SCL (see **sections 2.3.3.B** and **2.3.3.C** of **Chapter 2**). The

minimization of the number of ADALINEs avoids the calculation burden, enabling to easily implement RTCL in real time.

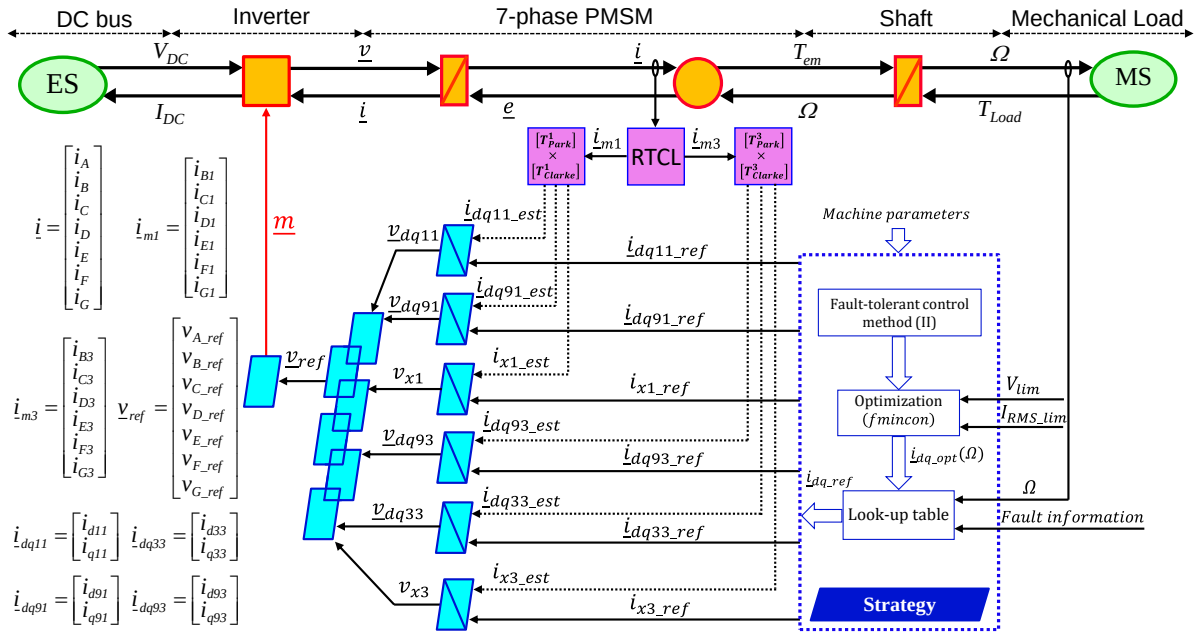

Fig. 3.27. The new control structure using real-time current learning RTCL for an OC fault with method (II) represented by EMR.

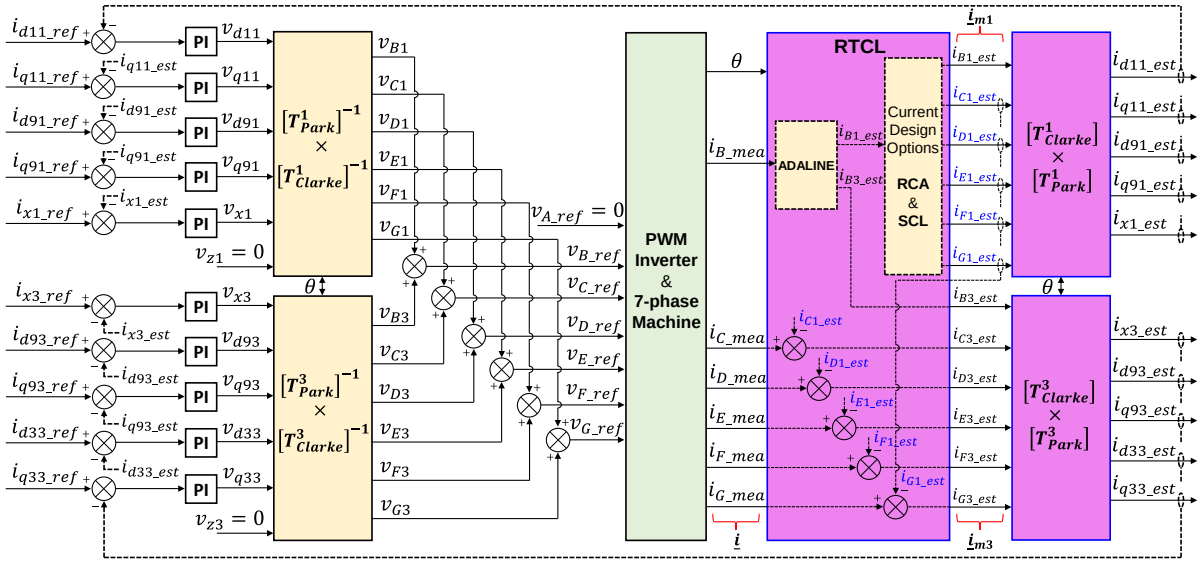

Fig. 3.28. The detailed structure of RTCL in the new control structure represented by a block diagram.

For example, if phase *B* is chosen, the ADALINE-based estimation for the measured current of phase *B* is presented in Fig. 3.29. The estimated current i_{B_est} is equal to the sum of several main harmonics depending on the back-EMF harmonic distribution as follows:

$$i_{B\_est} = [w_1 \cos(\theta) + w_2 \sin(\theta)] + [w_3 \cos(3\theta) + w_4 \sin(3\theta)] + [w_5 \cos(9\theta) + w_6 \sin(9\theta)] \quad (3.18)$$

where (w_1, w_2) are weights for harmonic θ; (w_3, w_4) are weights for harmonic for 3θ; and (w_5, w_6) are weights for harmonic for 9θ. In the considered seven-phase machine, the 1st, 3rd, and 9th harmonics are considered with the idea of using one harmonic per two-phase fictitious machine. In Fig. 3.29, estimated current i_{B_est} is compared to measured current i_{B_mea} to obtain current

error i_{error}. The weights are online updated by a learning process with learning rate η, current error i_{error}, and ADALINE inputs with current harmonics.

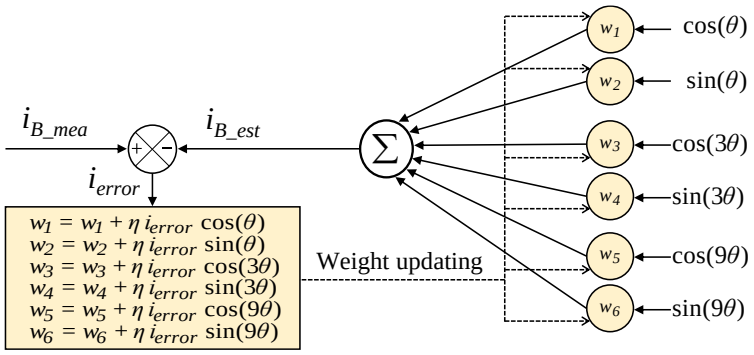

Fig. 3.29. The structure of the ADALINE used in RTCL.

To sum up, the principle to implement RTCL when phase *B* is chosen to be estimated by the ADALINE is described as follows:

1) Estimate the measured current of phase *B* by using the ADALINE in Fig. 3.29. Due to the back-EMF assumption, the 1st and 3rd harmonics of current are considered as useful harmonics to be obtained. Therefore, the 1st and 3rd harmonic currents of phase *B* in natural frame (i_{B1_est} and i_{B3_est}) are estimated.
2) Then, i_{B1_est} is used to calculate the 1st harmonic currents of the other phases (i_{C1_est}, i_{D1_est}, i_{E1_est}, i_{F1_est}, i_{G1_est}) by exploiting their mathematical relationships as described in current design options RCA and SCL in **sections 2.3.3.B** and **2.3.3.C** of **Chapter 2**.
3) Finally, the 3rd harmonic currents in natural frame (i_{C3_est}, i_{D3_est}, i_{E3_est}, i_{F3_est}, i_{G3_est}) are determined from differences between the measured phase currents and the estimated 1st harmonic currents as described in RTCL block of Fig. 3.28.

The flowchart for dynamic performances is described in Fig. 3.30 with changes in rotating speed or current references. With fixed current references, the harmonic weights of the ADALINE do not change when the rotating speed varies because current waveforms are unchanged at all speeds. Therefore, the new current control structure using RTCL can be applied to variable-speed applications with a given torque.

When current references ($\underline{i}_{dq\_ref}$ means i_{q11_ref} and i_{q33_ref}) (as well as the torque reference) are required to change, the drive needs to return to the pre-fault control scheme in Fig. 2.21 with time-variant current references in Fig. 3.26 as discussed in **section 2.3.3** of **Chapter 2**. Without returning to the pre-fault control scheme, the drive will be unstable because the ADALINE is an inner loop of the current control, providing the false feed-back signals for current controllers. After switching to the pre-fault control scheme, the learning process of phase-*B* current is activated with the ADALINE to determine new values of the harmonic weights. After that, the new control scheme can be re-applied to improve the control quality of the drive. In this doctoral thesis, the switch of these two schemes is manually made. This point can be considered as a drawback of the new control scheme.

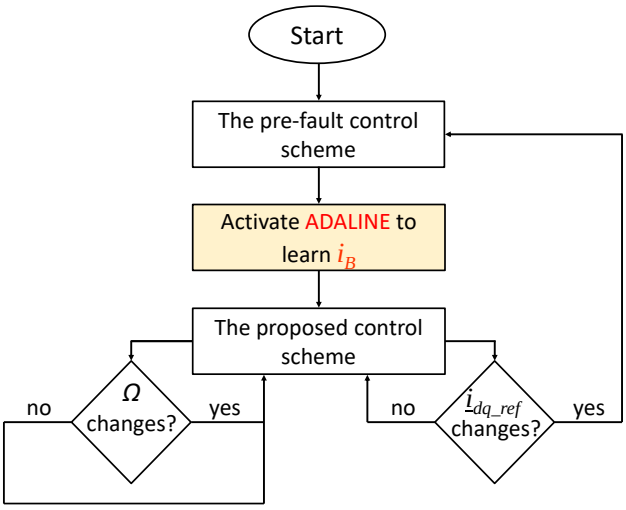

Fig. 3.30. The flowchart of the ADALINE learning process in response to changes of the rotating speed and current references.

3.3.2.C. *Verification with experimental results*

The new control structure to improve current control quality can be applied to methods (II)-RCA and SCL. However, as previously mentioned, only method (II)-RCA will be verified in this chapter, and the verification for method (II)-SCL is similar.

The experimental drive in **section 2.1.4** of **Chapter 2** continues to be applied. To validate the effectiveness of the proposed control scheme, the speed of the electric drive is limited to 35 rad/s although the maximum speed of the original characteristic presented in **Chapter 2** is 49 rad/s. The reason is that the voltage references slightly increase compared to the original ones, reducing the speed range. The experimental machine has been designed for wind turbines with a smaller speed range compared to automotive applications. The following results demonstrate the idea of this work. If the speed could increase to higher values, the proposed strategies would be more effective.

At low speed, there are no differences in the current control and torque performances between the original method (II)-RCA (the pre-fault control structure) and method (II)-RCA with RTCL (the new control structure). However, at 35 rad/s, the new control structure with RTCL generates lower torque ripples compared to the pre-fault control structure as described in Fig. 3.31. Indeed, in the third and final stages of the 4-stage operation, torque ripples reduce from 26% to 15% when the new control structure with RTCL is activated. Phase current waveforms in different stages are presented in Fig. 3.32 in which the constraint on RMS current is always respected in method (II)-RCA. Meanwhile, the peak values of phase currents slightly increase when the new control structure is used.

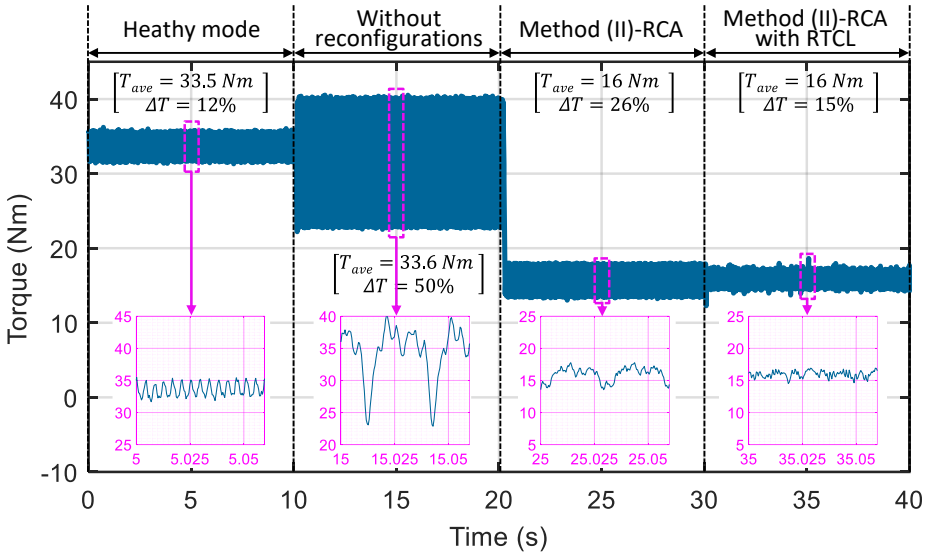

Fig. 3.31. (Experimental result) Torque in healthy mode, an OC fault without any reconfigurations, with method (II)-RCA in the pre-fault control structure, and with method (II)-RCA in the new control structure using RTCL at 35 rad/s.

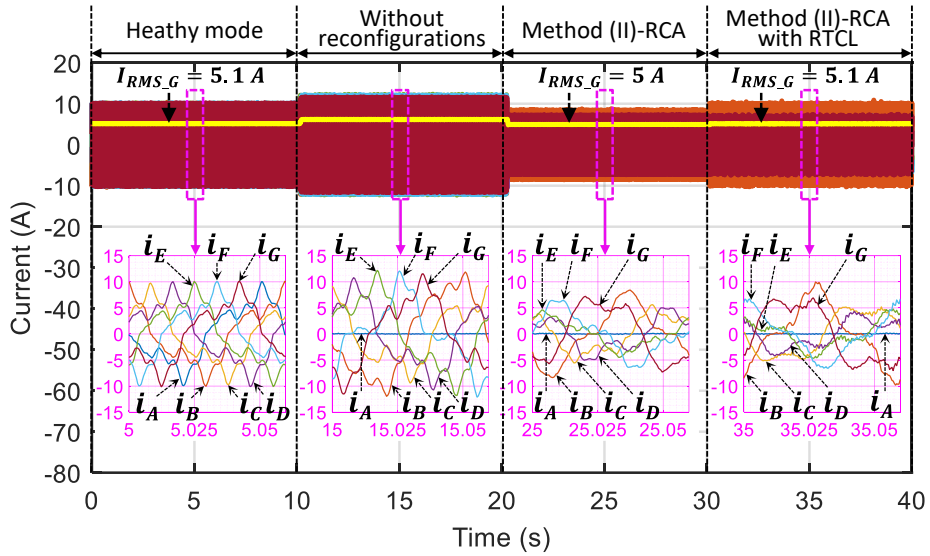

Fig. 3.32. (Experimental result) Phase currents in healthy mode, an OC fault without any reconfigurations, with method (II)-RCA in the pre-fault control structure, and with method (II)-RCA in the new control structure using RTCL at 35 rad/s.

To activate the new control structure in the final operating stage, the learning process of phase *B* has been previously taken from the 25th second when the pre-fault control scheme is still active. The harmonic weights converge within 4 s as described in Fig. 3.33a when the learning rate η is 0.001. When the learning process of phase-*B* current is done as in Fig. 3.33b, the new control scheme can be activated. The real-time current learning RTCL will continue to determine currents of the other healthy phases in real time based on the harmonic separation in Fig. 3.33c.

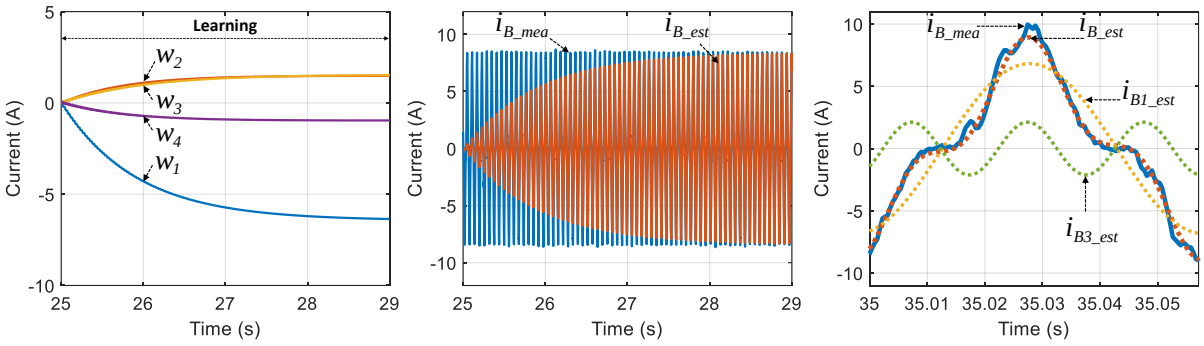

(a) (b) (c)

Fig. 3.33. (Experimental result) The learning process of phase-*B* current with harmonic weights (η=0.001) (a), phase current convergence (b), separated harmonics (c) by RTCL at 35 rad/s.

After all measured phase currents are analyzed with the estimated first and third harmonic components, 10 PI controllers for constant d-q currents (i_{d11}, i_{q11}, i_{d91}, i_{q91}, i_{x1}, i_{d33}, i_{q33}, i_{93}, i_{93}, i_{x3}) are used in the new control scheme. Current control performances are described in Fig. 3.34 with the estimated values obtained from RTCL to make comparisons with their reference values.

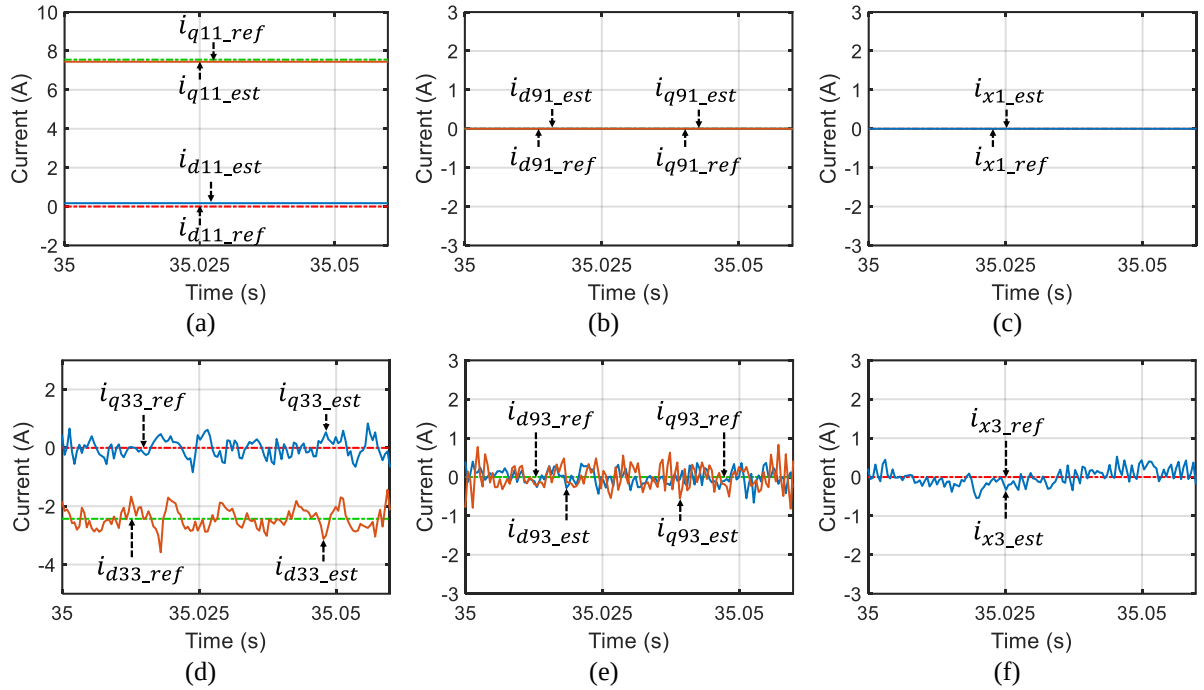

(a) (b) (c)

(d) (e) (f)

Fig. 3.34. (Experimental result) Control performances with the new control structure using RTCL at 35 rad/s: (i_{d11}, i_{q11}) (a), (i_{d91}, i_{q91}) (b), i_{x1} (c), (i_{d33}, i_{q33}) (d), (i_{d93}, i_{q93}) (e), i_{x3} (f).

It is noted that currents (i_{B1}, i_{C1}, i_{D1}, i_{E1}, i_{F1}, i_{G1}) and (i_{d11}, i_{q11}, i_{d91}, i_{q91}, i_{x1}) are directly estimated from the ADALINE and mathematical calculations. Therefore, these values are perfectly constant without high frequencies of the experimental drive. Meanwhile, currents (i_{B3}, i_{C3}, i_{D3}, i_{E3}, i_{F3}, i_{G3}) and (i_{d33}, i_{q33}, i_{d93}, i_{q93}, i_{x3}) contain high frequencies because these currents are derived from the subtraction of the measured phase currents and the estimated first harmonic components. The proper control performances of the first harmonic components, generating most of the torque, make the torque quality higher compared to the pre-fault control scheme.

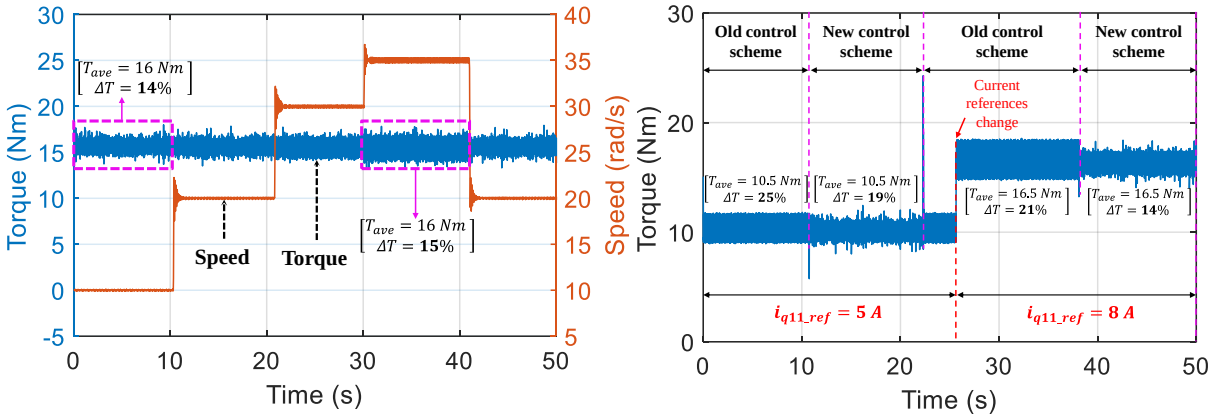

(a) (b)

Fig. 3.35. (Experimental result) Dynamic performances with method (II)-RCA in the new control structure using RTCL: variable rotating speed (a), variable current references at 26 rad/s (b).

The dynamic performances of the new control scheme, as previously described in Fig. 3.30, are verified in Fig. 3.35. Variations of the rotating speed in Fig. 3.35a do not have any significant influences on torque quality (a ripple from 14 to 15%). As previously discussed, variations of current references Fig. 3.35b (i_{q11_ref} from 5 to 8 A) require a switch from the new control scheme to the pre-fault control scheme to guarantee the stability of the drive. It is worth noting that the torque quality is improved whenever the new control scheme with RTCL is activated, specifically reductions from 25 to 19% (i_{q11_ref} =5 A) and from 21 to 14% (i_{q11_ref} =8 A). To see demonstration videos, please click on this link: https://youtu.be/pnWGwRDVfxg or scan the nearest QR code in this page.

3.4. Conclusions

This chapter has presented enhancements of the quality of current control and torque in a multiphase drive by using a simple type of artificial intelligence, ADALINE. The knowledge of harmonics in the drive has helped ADALINEs reduce the weight updating time and avoid the calculation burden. However, the number of used ADALINEs can be flexible according to the computation power of processors. ADALINEs for the control of parameters in the main fictitious machines that generate most of the torque should be prioritized.

In healthy mode, ADALINEs have been applied to eliminate current harmonics in d-q frames caused by unwanted back-EMF harmonics and inverter nonlinearity. In addition, torque ripples generated by the unwanted back-EMF harmonics have been directly nullified by a single ADALINE. By using these (seven) ADALINEs, every machine can generate a constant torque with high quality current control. However, the speed range should be reduced to respect the constraint on peak voltage.

In faulty mode, torque ripples in the proposed fault-tolerant methods in **Chapter 2** have been directly eliminated by the same way as in healthy mode with a shorter speed range. An ADALINE has been applied to eliminate torque ripples in the post-fault operation using method (III)-2 where the highest average torque is obtained. As healthy mode, the most important step of torque ripple eliminations using ADALINEs is to determine harmonic components of the torque, allowing to avoid the calculation burden.

A new control scheme using a single ADALINE has improved current control quality of the post-fault drive with method (II), indirectly improving the torque quality. Time-variant current references for control have been replaced by time-constant values. The key part of the new control structure is a real-time current learning (RTCL) that allows to separate harmonic components from measured phase currents, providing feedback signals of constant d-q currents. With a robustness to the back-EMF harmonic components in the second fictitious machine (9^{th}, for example), method (II)-RCA has been chosen to verify the effectiveness of the new control scheme.

General conclusions and Perspectives

General conclusions

Electrified vehicles have been considered as alternatives of ICE vehicles to cope with the shortage of fossil energy sources and the air pollution. In general, all types of electrified vehicles are driven by electric drives. To ensure high-performance electromechanical conversions, several requirements for the electric drives such as high efficiency, high volume densities, low-cost but safe-to-touch, high functional reliability, high torque quality, and flux-weakening control need to be met. In this context, multiphase PMSM drives are suitable candidates to meet the above requirements from electrified vehicles.

This doctoral thesis has proposed, systemized, and refined fault-tolerant control strategies for non-sinusoidal multiphase PMSM drives. Besides several advantages such as easy-to-manufacture, low production costs, high torques, and electromagnetic pole changing, non-sinusoidal back-EMFs of electric machines in the considered drives make the control more complicated but interesting to study. In addition, in this doctoral thesis, limits of RMS current and peak voltage have been always considered from healthy to faulty operations; hence, flux-weakening operations can be guaranteed. A case study with seven-phase machines and a single-phase OC fault has been used for verifications of the proposed strategies. Two-phase OC faults are briefly described in **Appendix B**. Most results in this doctoral thesis have been obtained from an experimental test bench.

The doctoral thesis has been organized into three chapters. In **Introduction** and **Chapter 1**, the context and state of the art have been discussed to clarify the necessary of this doctoral research. In **Chapter 2**, the mathematical modeling has been described to develop control strategies based on FOC for the seven-phase PMSM drive. In healthy mode, the current control and torque performances with the current and voltage constraint consideration have been presented. Although, there are no faults happening in the drive but measured currents in d-q frames and the electromagnetic torque consist of harmonic components. When one phase is open-circuited, a post-fault operation without any reconfigurations leads to very high torque ripples and the breaking of the electrical limits. Therefore, three main fault-tolerant control strategies have been cohesively proposed with the exploitation of the mathematical model of the drive. Method (I) with three options has provided constant d-q currents in the first and third fictitious machines, creating most of the torque. This feature allows the drive to obtain smooth torques if the back-EMF harmonics in the second fictitious machine are small. Method (II) has applied new transformation matrices to generate new current references. Especially, method (II)-SCL can obtain the similar average torque as in method (I)-2. Meanwhile, method (II)-RCA proves its robustness when its torque is unaffected by the harmonics in the second fictitious machine. However, method (II) generates time-variant d-q current references in the first and third fictitious machines, reducing current control quality as well as torque quality at high speed. Methods (I) and (II) can generate a maximum average post-fault torque equal to 65% of the torque in healthy mode. Therefore, method (III) has been proposed with the aim of improving the average torque to 79% under the constraints on current and voltage. Indeed, the uniformity

of current waveforms enables to maximize currents in all remaining phases within their limit. This current maximization allows to generate more torques, especially when the phase current and back-EMF waveforms are similar as described in method (III)-2. However, the fixed waveforms of phase currents in method (III) lead to inevitable torque ripples.

Chapter 3 has tackled the existing problems presented in **Chapter 2** by using a simple type of artificial intelligence, ADALINE. ADALINEs have eliminated current harmonics in d-q frames as well as torque ripples in healthy mode. By the same way, the post-fault torque ripples in method (III) have been nullified. One of the drawbacks of the torque ripple elimination is a reduction in the speed range as well as the base speed due to more harmonics injected into phase voltage references. Another application of ADALINEs is to separate harmonic components of measured phase currents in method (II) by using a real-time current learning. This harmonic separation provides time-constant feedback signals for current control in a new control scheme. Therefore, controllers such as PI of time-constant d-q currents can have good quality even at high speed. Variations of the rotating speed do not affect the control quality of the new control scheme. However, the new control scheme needs to deal with instability when current references vary. Therefore, the switch of the pre-fault and new control schemes has been made before any variations of current references.

Finally, this doctoral thesis contributes to enriching the control field of multiphase PMSM drives for automotive applications, especially in faulty conditions. A PMSM with multi-harmonics in its back-EMFs can generate a smooth torque regardless of the operating modes without exceeding current and voltage limits, avoiding the oversizing of the drive.

Publications associated with this doctoral thesis are listed as follows:

1) Journal papers:
   - D. T. Vu, N. K. Nguyen, E. Semail, and T. J. d. S. Moraes, “Control strategies for non-sinusoidal multiphase PMSM drives in faulty modes under constraints on copper losses and peak phase voltage,” *IET Electric Power Applications*, vol. 13, no. 11, pp. 1743-1752, 2019 [165].
   - D. T. Vu, N. K. Nguyen, E. Semail, and T. J. d. S. Moraes, “Torque optimisation of seven-phase BLDC machines in normal and degraded modes with constraints on current and voltage,” *The Journal of Engineering*, vol. 2019, no. 17, pp. 3818-3824, 2019 [164].
   - D. T. Vu, N. K. Nguyen, E. Semail, “A Fault-tolerant Control scheme based on Adaptive Linear Neurons for Non-sinusoidal multiphase drives,” *IEEE Transactions on Power Electronics*, UNDER REVIEW.
2) Conference papers:
   - D. T. Vu, N. K. Nguyen, and E. Semail, "Sensitivity of Torque Control for Seven-phase BLDC Machine with One Opened Phase under Constraints on Voltage and Current," in *International Symposium on Power Electronics, Electrical Drives, Automation and Motion (SPEEDAM)*, Amalfi, Italy, 2018, pp. 142-148 [169].
   - B. Zhao, J. Gong, D. T. Vu, N. K. Nguyen, and E. Semail, "Fault Tolerant 7-phase Hybrid Excitation Permanent Magnet Machine," in *The Eighteenth Biennial IEEE Conference on Electromagnetic Field Computation CEFC 2018*, Hangzhou, China, 2018, pp. 1-5 [170].
   - D. T. Vu, N. K. Nguyen, and E. Semail, "An Overview of Methods using Reduced-Ordered Transformation Matrices for Fault-Tolerant Control of 5-phase Machines with an Open Phase," in *IEEE International Conference on Industrial Technology (ICIT)*, Melbourne, Australia, 2019, pp. 1557-1562 [166].
   - D. T. Vu, N. K. Nguyen, E. Semail, and W. Lhomme, "Electric Vehicles Driven by 5-Phase Open-End Winding Machines Fed by Battery and Supercapacitors," in *IEEE Vehicle Power and Propulsion Conference (VPPC)*, Hanoi, Vietnam, 2019, pp. 1-6 [178].

- K. Yanagihara, D. T. Vu, N. K. Nguyen, J. Gong, E. Semail, and T. J. d. S. Moraes, "Fault-tolerant Control for 7-phase Non-sinusoidal Permanent Magnet Machines with One Opened Phase," in *International Symposium on Electrical and Electronics Engineering (ISEE)*, Ho Chi Minh city, Vietnam, 2019, pp. 292-297 [163].
- H. Zhang, B. Zhao, J. Gong, Y. Xu, D. T. Vu, N. K. Nguyen, E. Semail, and T. J. d. S. Moraes,"Torque Optimization of a Seven-Phase Bi-harmonic PMSM in Healthy and Degraded Mode," in *The 22nd International Conference on Electrical Machines and Systems (ICEMS)*, Harbin, China, 2019, pp. 1-6 [168].
- T. J. d. S. Moraes, H. L. Wu, E. Semail, N. K. Nguyen, D. T. Vu, "Optimal torque/speed characteristics of a Five-Phase Synchronous Machine under Peak or RMS current control strategies," in *The 22nd European Conference on Power Electronics and Applications (EPE)*, Lyon, France, 2020 [179].
- D. T. Vu, N. K. Nguyen, E. Semail, "Eliminations of Low-frequency Current Harmonics for Five-phase Open-end Winding Non-sinusoidal Machine Drives applying Neural Networks," in *The 46th Annual Conference of the IEEE Industrial Electronics Society (IECON)*, Singapore, 2020 [180].
- D. T. Vu, N. K. Nguyen, E. Semail, "Current Harmonic Eliminations for Seven-phase Non-sinusoidal PMSM Drives applying Artificial Neurons," in *The 3rd International Conference on Engineering and Research Application (ICERA)*, Thai Nguyen, Vietnam, 2020 [181].

Perspectives

Among the presented studies in the three chapters of this doctoral thesis, there are several issues that have not been solved yet. These issues could be studied in the future as follows:

1) It would be interesting to research on a general approach to find reduced-order matrices, as in method (II) in **Chapter 2**, corresponding to each opened phase.
2) An automatic solution to replace the manual switch between the new and old control schemes in method (II), as discussed in **section 3.3.2.B** of **Chapter 3**, in response to the variation of current references should be found.
3) The proposed control strategies could be more interesting when they are applied to multiphase machines with a higher maximum speed. The high-speed machines are suitable for automotive applications instead of a low-speed machine for wind turbines that has been considered in this doctoral thesis.
4) Fault-tolerant control with SC faults in transistors or machine windings (turns) could be interesting to study.

References

[1] C. C. Chan, "The State of the Art of Electric, Hybrid, and Fuel Cell Vehicles," *Proceedings of the IEEE,* vol. 95, no. 4, pp. 704-718, 2007.

[2] A. E.-. Refaie, "Toward a Sustainable More Electrified Future: The Role of Electrical Machines and Drives," *IEEE Electrification Magazine,* vol. 7, no. 1, pp. 49-59, 2019.

[3] C. C. Chan and K. T. Chau, "An overview of power electronics in electric vehicles," *IEEE Transactions on Industrial Electronics,* vol. 44, no. 1, pp. 3-13, 1997.

[4] C. C. Chan and K. T. Chau, "An advanced permanent magnet motor drive system for battery-powered electric vehicles," *IEEE Transactions on Vehicular Technology,* vol. 45, no. 1, pp. 180-188, 1996.

[5] Z. Q. Zhu and D. Howe, "Electrical Machines and Drives for Electric, Hybrid, and Fuel Cell Vehicles," *Proceedings of the IEEE,* vol. 95, no. 4, pp. 746-765, 2007.

[6] A. Cavagnino, A. Tenconi, and S. Vaschetto, "Experimental Characterization of a Belt-Driven Multiphase Induction Machine for 48-V Automotive Applications: Losses and Temperatures Assessments," *IEEE Transactions on Industry Applications,* vol. 52, no. 2, pp. 1321-1330, 2016.

[7] S. K. T. Dörsam, A. Klinkig, A. Radon, O. Sirch, "The New Voltage Level 48 V for Vehicle Power Supply," *ATZ Electronik Worldwide,* vol. 7, no. 1, pp. 10-14, 2/2012.

[8] C. Pawsey, "48V technology on the Automotive Horizon," in *the 3rd international conference automotive 48 V power supply systems*, Duesseldorf, Germany, 11/2015.

[9] M. Sattler, T. Smetana, T. Meyerhofer, and L. Kuhlkamp, "48 V minihybrid—A new solution for the minimal hybridization of vehicles," in *the 22nd Aachen Colloquium Automobile and Engine Technology*, Aachen, Germany, 10/2013, pp. 995-1008.

[10] B. K. W. Hackmann, C. Gotte, R. Schmid, F. X. Pujol, "48 V—The way to a high volume electrification," in *the 22nd Aachen Colloquium Automobile and Engine Technology*, Aachen, Germany, 10/2013, pp. 1009-1030.

[11] F. G. S. Lauer, M. Springer, S. Wechler, "48 Volt Hybrid with e-drive features - Excellent fuel efficiency and drivability," in *Electric & Electronic Systems in Hybrid and Electric Vehicles and Electrical Energy Management*, Bamberg, Germany, 5/2017, pp. 1-11.

[12] P. Els, "48 Volt Electrification: the next step to achieving 2020 emissions," in *the 3rd international conference automotive 48 V power supply systems*, Duesseldorf, Germany, 11/2015.

[13] T. M. Jahns, "Improved Reliability in Solid-State AC Drives by Means of Multiple Independent Phase Drive Units," *IEEE Transactions on Industry Applications,* vol. IA-16, no. 3, pp. 321-331, 1980.

[14] F. Meinguet, P. Sandulescu, X. Kestelyn, and E. Semail, "A Method for Fault Detection and Isolation Based on the Processing of Multiple Diagnostic Indices: Application to Inverter Faults in AC Drives," *IEEE Transactions on Vehicular Technology,* vol. 62, no. 3, pp. 995-1009, 2013.

[15] S. Yang, A. Bryant, P. Mawby, D. Xiang, L. Ran, and P. Tavner, "An Industry-Based Survey of Reliability in Power Electronic Converters," *IEEE Transactions on Industry Applications,* vol. 47, no. 3, pp. 1441-1451, 2011.

[16] S. Yang, D. Xiang, A. Bryant, P. Mawby, L. Ran, and P. Tavner, "Condition Monitoring for Device Reliability in Power Electronic Converters: A Review," *IEEE Transactions on Power Electronics,* vol. 25, no. 11, pp. 2734-2752, 2010.

[17] Z. Zhong, S. Jiang, Y. Zhou, and S. Zhou, "Active torque ripple reduction based on an analytical model of torque," *IET Electric Power Applications,* vol. 11, no. 3, pp. 331-341, 2017.

[18] Z. Azar, Z. Q. Zhu, and G. Ombach, "Influence of Electric Loading and Magnetic Saturation on Cogging Torque, Back-EMF and Torque Ripple of PM Machines," *IEEE Transactions on Magnetics,* vol. 48, no. 10, pp. 2650-2658, 2012.

[19] E. E. Ward and H. Härer, "Preliminary investigation of an invertor-fed 5-phase induction motor," *Proceedings of the Institution of Electrical Engineers,* vol. 116, no. 6, pp. 980-984, 1969.

[20] L. Parsa and H. A. Toliyat, "Five-phase permanent-magnet motor drives," *IEEE Transactions on Industry Applications*, vol. 41, no. 1, pp. 30-37, 2005.

[21] E. Levi, "Multiphase Electric Machines for Variable-Speed Applications," *IEEE Transactions on Industrial Electronics*, vol. 55, no. 5, pp. 1893-1909, 2008.

[22] E. Levi, R. Bojoi, F. Profumo, H. A. Toliyat, and S. Williamson, "Multiphase induction motor drives - a technology status review," *IET Electric Power Applications*, vol. 1, no. 4, pp. 489-516, 2007.

[23] M. J. Duran, E. Levi, and F. Barrero, "Multiphase Electric Drives: Introduction," in *Wiley Encyclopedia of Electrical and Electronics Engineering*, 2017, pp. 1-26.

[24] E. A. Klingshirn, "High Phase Order Induction Motors - Part I-Description and Theoretical Considerations," *IEEE Transactions on Power Apparatus and Systems*, vol. PAS-102, no. 1, pp. 47-53, 1983.

[25] M. Slunjski, O. Dordevic, M. Jones, and E. Levi, "Symmetrical/Asymmetrical Winding Reconfiguration in Multiphase Machines," *IEEE Access*, vol. 8, pp. 12835-12844, 2020.

[26] F. Barrero and M. J. Duran, "Recent Advances in the Design, Modeling, and Control of Multiphase Machines Part I," *IEEE Transactions on Industrial Electronics*, vol. 63, no. 1, pp. 449-458, 2016.

[27] R. Bojoi, S. Rubino, A. Tenconi, and S. Vaschetto, "Multiphase electrical machines and drives: A viable solution for energy generation and transportation electrification," in *International Conference and Exposition on Electrical and Power Engineering (EPE)*, Iasi, Romania, 2016, pp. 632-639.

[28] R. Rui, "AN-Power stage of 48 V BSG inverter," ed. Munich, Germany: Infineon Technologies AG, 2018.

[29] F. Locment, A. Bruyere, E. Semail, X. Kestelyn, A. Bouscayrol, and J. M. Dubus, "Comparison of 3-, 5- and 7-leg Voltage Source Inverters for low voltage applications," in *IEEE International Electric Machines & Drives Conference*, Antalya, Turkey, 2007, vol. 2, pp. 1234-1239.

[30] S. Runde, A. Baumgardt, O. Moros, B. Rubey, and D. Gerling, "ISCAD — Design, control and car integration of a 48 volt high performance drive," *CES Transactions on Electrical Machines and Systems*, vol. 3, no. 2, pp. 117-123, 2019.

[31] M. J. Duran and F. Barrero, "Recent Advances in the Design, Modeling, and Control of Multiphase Machines Part II," *IEEE Transactions on Industrial Electronics*, vol. 63, no. 1, pp. 459-468, 2016.

[32] A. Boglietti *et al.*, "Electrical Machine Topologies: Hottest Topics in the Electrical Machine Research Community," *IEEE Industrial Electronics Magazine*, vol. 8, no. 2, pp. 18-30, 2014.

[33] A. M. E.-. Refaie, "Fractional-Slot Concentrated-Windings Synchronous Permanent Magnet Machines: Opportunities and Challenges," *IEEE Transactions on Industrial Electronics*, vol. 57, no. 1, pp. 107-121, 2010.

[34] E. Semail, A. Bouscayrol, and J. P. Hautier, "Vectorial formalism for analysis and design of polyphase synchronous machines," *Eur. Phys. J. AP*, 10.1051/epjap:2003034 vol. 22, no. 3, pp. 207-220, 2003.

[35] E. Semail, X. Kestelyn, and A. Bouscayrol, "Right harmonic spectrum for the back-electromotive force of an n-phase synchronous motor," in *the 39th IEEE Industry Applications Conference*, Seattle, WA, USA, 10/2004, vol. 1, pp. 71-78.

[36] T. M. Jahns and W. L. Soong, "Pulsating torque minimization techniques for permanent magnet AC motor drives-a review," *IEEE Transactions on Industrial Electronics*, vol. 43, no. 2, pp. 321-330, 1996.

[37] J. Y. Hung, "Design of the most efficient excitation for a class of electric motor," *IEEE Transactions on Circuits and Systems I: Fundamental Theory and Applications*, vol. 41, no. 4, pp. 341-344, 1994.

[38] N. K. Nguyen, "Approches neuromimétiques pour l'identification et la commande des systèmes électriques : application au filtrage actif et aux actionneurs synchrones," 2010.

[39] F. Mekri, S. B. Elghali, and M. E. H. Benbouzid, "Fault-Tolerant Control Performance Comparison of Three- and Five-Phase PMSG for Marine Current Turbine Applications," *IEEE Transactions on Sustainable Energy*, vol. 4, no. 2, pp. 425-433, 2013.

[40] K. Gopakumar, S. Sathiakumar, S. K. Biswas, and J. Vithayathil, "Modified current source inverter fed induction motor drive with reduced torque pulsations," *IEE Proceedings B - Electric Power Applications*, vol. 131, no. 4, pp. 159-164, 1984.

[41] W. L. Soong and T. J. E. Miller, "Field-weakening performance of brushless synchronous AC motor drives," *IEE Proceedings - Electric Power Applications*, vol. 141, no. 6, pp. 331-340, 1994.

[42] G. R. Slemon, "Achieving a constant power speed range for PM drives," *IEEE Transactions on Industry Applications*, vol. 31, no. 2, pp. 368-372, 1995.

[43] J. Wai and T. M. Jahns, "A new control technique for achieving wide constant power speed operation with an interior PM alternator machine," in *Conference Record of the 2001 IEEE Industry Applications Conference*, Chicago, IL, USA, USA, 10/2001, vol. 2, pp. 807-814 vol.2.

[44] R. F. Schiferl and T. A. Lipo, "Power capability of salient pole permanent magnet synchronous motors in variable speed drive applications," *IEEE Transactions on Industry Applications*, vol. 26, no. 1, pp. 115-123, 1990.

[45] S. Sadeghi, L. Guo, H. A. Toliyat, and L. Parsa, "Wide Operational Speed Range of Five-Phase Permanent Magnet Machines by Using Different Stator Winding Configurations," *IEEE Transactions on Industrial Electronics*, vol. 59, no. 6, pp. 2621-2631, 2012.

[46] N. K. Nguyen, E. Semail, F. Meinguet, P. Sandulescu, X. Kestelyn, and B. Aslan, "Different virtual stator winding configurations of open-end winding five-phase PM machines for wide speed range without flux weakening operation," in *15th European Conference on Power Electronics and Applications (EPE)*, Lille, France, 9/2013, pp. 1-8.

[47] M. M. Swamy, T. Kume, A. Maemura, and S. Morimoto, "Extended high-speed operation via electronic winding-change method for AC motors," *IEEE Transactions on Industry Applications*, vol. 42, no. 3, pp. 742-752, 2006.

[48] M. Osama and T. A. Lipo, "A new inverter control scheme for induction motor drives requiring wide speed range," *IEEE Transactions on Industry Applications*, vol. 32, no. 4, pp. 938-944, 1996.

[49] M. Osama and T. A. Lipo, "Modeling and analysis of a wide-speed-range induction motor drive based on electronic pole changing," *IEEE Transactions on Industry Applications*, vol. 33, no. 5, pp. 1177-1184, 1997.

[50] M. Osama and T. A. Lipo, "Experimental and finite-element analysis of an electronic pole-change drive," *IEEE Transactions on Industry Applications*, vol. 36, no. 6, pp. 1637-1644, 2000.

[51] M. v. d. Giet, K. Hameyer, and S. Risse, "Induction motor with pole-changing winding for variable supply frequency," in *IEEE International Electric Machines & Drives Conference*, Antalya, Turkey, 5/2007, vol. 2, pp. 1484-1489.

[52] A. Gautam and J. O. Ojo, "Variable speed multiphase induction machine using pole phase modulation principle," in *The 38th Annual Conference on IEEE Industrial Electronics Society (IECON)*, Montreal, QC, Canada, 10/2012, pp. 3659-3665.

[53] H. Zahr, F. Scuiller, and E. Semail, "Five-phase SPM machine with electronic pole changing effect for marine propulsion," in *International Conference on Electrical Systems for Aircraft, Railway, Ship Propulsion and Road Vehicles & International Transportation Electrification Conference (ESARS-ITEC)*, Toulouse, France, 11/2016, pp. 1-6.

[54] J. Gong, H. Zahr, E. Semail, M. Trabelsi, B. Aslan, and F. Scuiller, "Design Considerations of Five-Phase Machine With Double p/3p Polarity," *IEEE Transactions on Energy Conversion*, vol. 34, no. 1, pp. 12-24, 2019.

[55] H. Zahr, E. Semail, B. Aslan, and F. Scuiller, "Maximum Torque Per Ampere strategy for a biharmonic five-phase synchronous machine," in *International Symposium on Power Electronics, Electrical Drives, Automation and Motion (SPEEDAM)*, Anacapri, Italy, 6/2016, pp. 91-97.

[56] X. Kestelyn, "Modélisation vectorielle multimachines pour la commande des ensembles convertisseurs-machines polyphasés," PhD, Université de Lille 1, 2003.

[57] H. T. Le Luong, "Optimal Design of Modular High Performance Brushless Wound Rotor Synchronous Machine for embedded systems," 2018.

[58] *Motorbrain final review: presentation at ZF Friedrichshafen*. Available: https://www.motorbrain.eu/

[59] *The integrated smart energy converter project CE2I*. Available: http://ce2i.pole-medee.com/the-project/

[60] Z. Liu, Y. Li, and Z. Zheng, "A review of drive techniques for multiphase machines," *CES Transactions on Electrical Machines and Systems*, vol. 2, no. 2, pp. 243-251, 2018.

[61] M. B. Guzman, "Novel control techniques in multiphase drives: Direct control methods (DTC and MPC) under limit situations," PhD, École Nationale Supérieure d'Arts et Métiers, 2018.

[62] G. K. Singh, "Multi-phase induction machine drive research—a survey," *Electric Power Systems Research,* vol. 61, no. 2, pp. 139-147, 2002.

[63] K. Haase, "Zur Dynamik drehzahlgeregelter Antriebe mit stromrichtergespeisten Asynchron-Kurzschlußläufermaschinen (On dynamic of the speed controlled static AC drive with squirrel-cage induction machine)," Darmstadt, Germany, 1969.

[64] F. Blaschke, "The principle of field orientation as applied to the new transvector closed loop control for rotating machine," *Siemens Review,* vol. 34, no. 3, pp. 217-220, 1972.

[65] E. Semail, "Outils et méthodologie d'étude des systèmes électriques polyphasés - Généralisation de la méthode des vecteurs d'espace," PhD, Université de Lille 1, 2000.

[66] M. Jones, S. N. Vukosavic, D. Dujic, and E. Levi, "A Synchronous Current Control Scheme for Multiphase Induction Motor Drives," *IEEE Transactions on Energy Conversion,* vol. 24, no. 4, pp. 860-868, 2009.

[67] H. S. Che, E. Levi, M. Jones, W. Hew, and N. A. Rahim, "Current Control Methods for an Asymmetrical Six-Phase Induction Motor Drive," *IEEE Transactions on Power Electronics,* vol. 29, no. 1, pp. 407-417, 2014.

[68] A. G. Yepes, J. Malvar, A. Vidal, O. López, and J. Doval-Gandoy, "Current Harmonics Compensation Based on Multiresonant Control in Synchronous Frames for Symmetrical n-Phase Machines," *IEEE Transactions on Industrial Electronics,* vol. 62, no. 5, pp. 2708-2720, 2015.

[69] A. Abdelkhalik, M. Masoud, and W. Barry, "Eleven-phase induction machine: steady-state analysis and performance evaluation with harmonic injection," *IET Electric Power Applications,* vol. 4, no. 8, pp. 670-685, 2010.

[70] A. S. Abdel-Khalik, S. M. Gadoue, M. I. Masoud, and B. W. Wiliams, "Optimum Flux Distribution With Harmonic Injection for a Multiphase Induction Machine Using Genetic Algorithms," *IEEE Transactions on Energy Conversion,* vol. 26, no. 2, pp. 501-512, 2011.

[71] L. Zheng, J. E. Fletcher, B. W. Williams, and X. He, "Dual-Plane Vector Control of a Five-Phase Induction Machine for an Improved Flux Pattern," *IEEE Transactions on Industrial Electronics,* vol. 55, no. 5, pp. 1996-2005, 2008.

[72] A. S. Abdel-Khalik, M. I. Masoud, and B. W. Williams, "Improved Flux Pattern With Third Harmonic Injection for Multiphase Induction Machines," *IEEE Transactions on Power Electronics,* vol. 27, no. 3, pp. 1563-1578, 2012.

[73] A. S. Abdel-Khalik, M. I. Masoud, S. Ahmed, and A. M. Massoud, "Effect of Current Harmonic Injection on Constant Rotor Volume Multiphase Induction Machine Stators: A Comparative Study," *IEEE Transactions on Industry Applications,* vol. 48, no. 6, pp. 2002-2013, 2012.

[74] M. Mengoni, L. Zarri, A. Tani, L. Parsa, G. Serra, and D. Casadei, "High-Torque-Density Control of Multiphase Induction Motor Drives Operating Over a Wide Speed Range," *IEEE Transactions on Industrial Electronics,* vol. 62, no. 2, pp. 814-825, 2015.

[75] L. Lu, E. Semail, L. Kobylanski, and X. Kestelyn, "Flux-weakening strategies for a five-phase PM synchronous machine," in *Proceedings of the 14th European Conference on Power Electronics and Applications*, Birmingham, UK, 8/2011, pp. 1-7.

[76] P. Sandulescu *et al.*, "FPGA implementation of a general Space Vector approach on a 6-leg voltage source inverter," in *The 37th Annual Conference of the IEEE Industrial Electronics Society (IECON)*, Melbourne, VIC, Australia, 11/2011, pp. 3482-3487.

[77] L. Lu *et al.*, "Computation of optimal current references for flux-weakening of multi-phase synchronous machines," in *the 38th Annual Conference on IEEE Industrial Electronics Society (IECON)*, Montreal, QC, Canada, 10/2012, pp. 3610-3615.

[78] P. Sandulescu, F. Meinguet, X. Kestelyn, E. Semail, and A. Bruyère, "Control Strategies for Open-End Winding Drives Operating in the Flux-Weakening Region," *IEEE Transactions on Power Electronics,* vol. 29, no. 9, pp. 4829-4842, 2014.

[79] A. Bruyere, E. Semail, A. Bouscayrol, F. Locment, J. M. Dubus, and J. C. Mipo, "Modeling and control of a seven-phase claw-pole integrated starter alternator for micro-hybrid automotive applications," in *IEEE Vehicle Power and Propulsion Conference (VPPC)*, Harbin, China, 9/2008, pp. 1-6.

[80] A. Bruyere, "Modélisation et commande d'un alterno-demarreur hetaphase pour application automobile micro-hybride," PhD, École Nationale Supérieure d'Arts et Métiers, 2009.

[81] P. Sandulescu, "Modélisation et commande d'un système à trois phases indépendantes à double fonctionnalité : Traction électrique et chargeur forte puissance pour application automobile," PhD, École Nationale Supérieure d'Arts et Métiers, 2013.

[82] F. Scuiller, H. Zahr, and E. Semail, "Maximum Reachable Torque, Power and Speed for Five-Phase SPM Machine With Low Armature Reaction," *IEEE Transactions on Energy Conversion*, vol. 31, no. 3, pp. 959-969, 2016.

[83] H. Zahr, "Machine pentaphasée a double polarité pour électrification du domaine des transports par effet boite de vitesse électromagnétique," PhD, École Nationale Supérieure d'Arts et Métiers, 2016.

[84] Y. Hu, Z. Zhu, and K. Liu, "Current Control for Dual Three-Phase Permanent Magnet Synchronous Motors Accounting for Current Unbalance and Harmonics," *IEEE Journal of Emerging and Selected Topics in Power Electronics*, vol. 2, no. 2, pp. 272-284, 2014.

[85] N. K. Nguyen, E. Semail, F. D. Belie, and X. Kestelyn, "Adaline Neural Networks-based sensorless control of five-phase PMSM drives," in *The 42nd Annual Conference of the IEEE Industrial Electronics Society (IECON)*, Florence, Italy, 10/2016, pp. 5741-5746.

[86] D. Flieller, N. K. Nguyen, P. Wira, G. Sturtzer, D. O. Abdeslam, and J. Mercklé, "A Self-Learning Solution for Torque Ripple Reduction for Nonsinusoidal Permanent-Magnet Motor Drives Based on Artificial Neural Networks," *IEEE Transactions on Industrial Electronics*, vol. 61, no. 2, pp. 655-666, 2014.

[87] O. Fall, N. K. Nguyen, J. F. Charpentier, P. Letellier, E. Semail, and X. Kestelyn, "Variable speed control of a 5-phase permanent magnet synchronous generator including voltage and current limits in healthy and open-circuited modes," *Electric Power Systems Research*, vol. 140, pp. 507-516, 2016.

[88] O. Fall, "Contribution à l'étude de machines électriques polyphasées à aimants permanents en vue d'une meilleure gestion de la commande en modes dégradés pour des applications liées aux energies renouvelables marines," PhD, École Nationale Supérieure d'Arts et Métiers, 2017.

[89] T. J. d. S. Moraes, E. Semail, N. K. Nguyen, F. Meinguet, and M. Guerin, "New Electrical Inversed-Series Connection for Even-Phase Symmetrical PMSMs," *IEEE Transactions on Power Electronics*, vol. 33, no. 9, pp. 7938-7947, 2018.

[90] T. J. D. S. Moraes, M. Trabelsi, H. Zahr, and E. Semail, "Homopolar Current's Copper Losses Analysis for Different Modulations in Open-End Winding Five-Phase Drives," in *XIII International Conference on Electrical Machines (ICEM)*, Alexandroupoli, Greece, 2018, pp. 1538-1544.

[91] I. Takahashi and T. Noguchi, "A New Quick-Response and High-Efficiency Control Strategy of an Induction Motor," *IEEE Transactions on Industry Applications*, vol. IA-22, no. 5, pp. 820-827, 1986.

[92] M. Depenbrock, "Direct self-control (DSC) of inverter-fed induction machine," *IEEE Transactions on Power Electronics*, vol. 3, no. 4, pp. 420-429, 1988.

[93] G. S. Buja and M. P. Kazmierkowski, "Direct torque control of PWM inverter-fed AC motors - a survey," *IEEE Transactions on Industrial Electronics*, vol. 51, no. 4, pp. 744-757, 2004.

[94] R. Karampuri, J. Prieto, F. Barrero, and S. Jain, "Extension of the DTC Technique to Multiphase Induction Motor Drives Using Any Odd Number of Phases," in *IEEE Vehicle Power and Propulsion Conference (VPPC)*, Coimbra, Portugal, 10/2014, pp. 1-6.

[95] L. Zheng, J. E. Fletcher, B. W. Williams, and X. He, "A Novel Direct Torque Control Scheme for a Sensorless Five-Phase Induction Motor Drive," *IEEE Transactions on Industrial Electronics*, vol. 58, no. 2, pp. 503-513, 2011.

[96] L. Gao, J. E. Fletcher, and L. Zheng, "Low speed control improvements for classic Direct Torque Control of a 2-level 5-phase inverter-fed induction machine," in *IEEE International Symposium on Industrial Electronics*, Bari, Italy, 7/2010, pp. 2172-2177.

[97] A. Taheri, A. Rahmati, and S. Kaboli, "Efficiency Improvement in DTC of Six-Phase Induction Machine by Adaptive Gradient Descent of Flux," *IEEE Transactions on Power Electronics*, vol. 27, no. 3, pp. 1552-1562, 2012.

[98] X. Kestelyn, E. Semail, and D. Loroil, "Direct torque control of multi-phase permanent magnet synchronous motor drive: application to a five-phase," in *IEEE International Conference on Electric Machines and Drives*, San Antonio, TX, USA, 5/2005, pp. 137-143.

[99] L. Parsa and H. A. Toliyat, "Sensorless Direct Torque Control of Five-Phase Interior Permanent-Magnet Motor Drives," *IEEE Transactions on Industry Applications*, vol. 43, no. 4, pp. 952-959, 2007.

[100] T. G. Habetler, F. Profumo, M. Pastorelli, and L. M. Tolbert, "Direct torque control of induction machines using space vector modulation," *IEEE Transactions on Industry Applications*, vol. 28, no. 5, pp. 1045-1053, 1992.

[101] R. Bojoi, F. Farina, G. Griva, F. Profumo, and A. Tenconi, "Direct torque control for dual three-phase induction motor drives," *IEEE Transactions on Industry Applications*, vol. 41, no. 6, pp. 1627-1636, 2005.

[102] P. Cortes, M. P. Kazmierkowski, R. M. Kennel, D. E. Quevedo, and J. Rodriguez, "Predictive Control in Power Electronics and Drives," *IEEE Transactions on Industrial Electronics*, vol. 55, no. 12, pp. 4312-4324, 2008.

[103] M. R. Arahal, F. Barrero, S. Toral, M. Duran, and R. Gregor, "Multi-phase current control using finite-state model-predictive control," *Control Engineering Practice*, vol. 17, no. 5, pp. 579-587, 2009.

[104] F. Barrero, M. R. Arahal, R. Gregor, S. Toral, and M. J. Duran, "A Proof of Concept Study of Predictive Current Control for VSI-Driven Asymmetrical Dual Three-Phase AC Machines," *IEEE Transactions on Industrial Electronics*, vol. 56, no. 6, pp. 1937-1954, 2009.

[105] M. J. Duran, J. A. Riveros, F. Barrero, H. Guzman, and J. Prieto, "Reduction of Common-Mode Voltage in Five-Phase Induction Motor Drives Using Predictive Control Techniques," *IEEE Transactions on Industry Applications*, vol. 48, no. 6, pp. 2059-2067, 2012.

[106] C. S. Lim, E. Levi, M. Jones, N. A. Rahim, and W. P. Hew, "FCS-MPC-Based Current Control of a Five-Phase Induction Motor and its Comparison with PI-PWM Control," *IEEE Transactions on Industrial Electronics*, vol. 61, no. 1, pp. 149-163, 2014.

[107] C. Martín, M. Bermúdez, F. Barrero, M. R. Arahal, X. Kestelyn, and M. J. Durán, "Sensitivity of predictive controllers to parameter variation in five-phase induction motor drives," *Control Engineering Practice*, vol. 68, pp. 23-31, 2017.

[108] X. Kestelyn, O. Gomozov, J. Buire, F. Colas, N. K. Nguyen, and E. Semail, "Investigation on model predictive control of a five-phase permanent magnet synchronous machine under voltage and current limits," in *IEEE International Conference on Industrial Technology (ICIT)*, Seville, Spain, 3/2015, pp. 2281-2287.

[109] M. Bermudez, O. Gomozov, X. Kestelyn, F. Barrero, N. K. Nguyen, and E. Semail, "Model predictive optimal control considering current and voltage limitations: Real-time validation using OPAL-RT technologies and five-phase permanent magnet synchronous machines," *Mathematics and Computers in Simulation*, vol. 158, pp. 148-161, 2019.

[110] W. Cao, B. C. Mecrow, G. J. Atkinson, J. W. Bennett, and D. J. Atkinson, "Overview of Electric Motor Technologies Used for More Electric Aircraft (MEA)," *IEEE Transactions on Industrial Electronics*, vol. 59, no. 9, pp. 3523-3531, 2012.

[111] A. Wintrich, U. Nicolai, W. Tursky, and T. Reimann, *Application Manual Power Semiconductors*, 2nd ed. SEMIKRON International GmbH, 2015.

[112] M. Trabelsi, N. K. Nguyen, and E. Semail, "Real-Time Switches Fault Diagnosis Based on Typical Operating Characteristics of Five-Phase Permanent-Magnetic Synchronous Machines," *IEEE Transactions on Industrial Electronics*, vol. 63, no. 8, pp. 4683-4694, 2016.

[113] M. Trabelsi, E. Semail, and N. K. Nguyen, "Experimental Investigation of Inverter Open-Circuit Fault Diagnosis for Biharmonic Five-Phase Permanent Magnet Drive," *IEEE Journal of Emerging and Selected Topics in Power Electronics*, vol. 6, no. 1, pp. 339-351, 2018.

[114] M. J. Duran, I. Gonzalez-Prieto, N. Rios-Garcia, and F. Barrero, "A Simple, Fast, and Robust Open-Phase Fault Detection Technique for Six-Phase Induction Motor Drives," *IEEE Transactions on Power Electronics*, vol. 33, no. 1, pp. 547-557, 2018.

[115] M. Salehifar, R. S. Arashloo, J. M. Moreno-Equilaz, V. Sala, and L. Romeral, "Fault Detection and Fault Tolerant Operation of a Five Phase PM Motor Drive Using Adaptive Model Identification Approach," *IEEE Journal of Emerging and Selected Topics in Power Electronics*, vol. 2, no. 2, pp. 212-223, 2014.

[116] F. Meinguet, "Fault-tolerant permanent-magnet synchronous machine drives: Fault detection and isolation, control reconfiguration and design considerations," PhD, Université Libre de Bruxelles, 2012.

[117] F. Meinguet, E. Semail, and J. Gyselinck, "An on-line method for stator fault detection in multi-phase PMSM drives," in *IEEE Vehicle Power and Propulsion Conference (VPPC)*, Lille, France, 9/2010, pp. 1-6.

[118] N. K. Nguyen, F. Meinguet, E. Semail, and X. Kestelyn, "Fault-Tolerant Operation of an Open-End Winding Five-Phase PMSM Drive With Short-Circuit Inverter Fault," *IEEE Transactions on Industrial Electronics*, vol. 63, no. 1, pp. 595-605, 2016.

[119] R. Kianinezhad, B. Nahid-Mobarakeh, L. Baghli, F. Betin, and G. Capolino, "Modeling and Control of Six-Phase Symmetrical Induction Machine Under Fault Condition Due to Open Phases," *IEEE Transactions on Industrial Electronics*, vol. 55, no. 5, pp. 1966-1977, 2008.

[120] F. Locment, E. Semail, and X. Kestelyn, "Vectorial Approach-Based Control of a Seven-Phase Axial Flux Machine Designed for Fault Operation," *IEEE Transactions on Industrial Electronics*, vol. 55, no. 10, pp. 3682-3691, 2008.

[121] X. Kestelyn and E. Semail, "A Vectorial Approach for Generation of Optimal Current References for Multiphase Permanent-Magnet Synchronous Machines in Real Time," *IEEE Transactions on Industrial Electronics*, vol. 58, no. 11, pp. 5057-5065, 2011.

[122] S. Dwari and L. Parsa, "Fault-Tolerant Control of Five-Phase Permanent-Magnet Motors With Trapezoidal Back EMF," *IEEE Transactions on Industrial Electronics*, vol. 58, no. 2, pp. 476-485, 2011.

[123] H. S. Che, M. J. Duran, E. Levi, M. Jones, W. Hew, and N. A. Rahim, "Postfault Operation of an Asymmetrical Six-Phase Induction Machine With Single and Two Isolated Neutral Points," *IEEE Transactions on Power Electronics*, vol. 29, no. 10, pp. 5406-5416, 2014.

[124] S. Dwari and L. Parsa, "An Optimal Control Technique for Multiphase PM Machines Under Open-Circuit Faults," *IEEE Transactions on Industrial Electronics*, vol. 55, no. 5, pp. 1988-1995, 2008.

[125] A. Mohammadpour and L. Parsa, "A Unified Fault-Tolerant Current Control Approach for Five-Phase PM Motors With Trapezoidal Back EMF Under Different Stator Winding Connections," *IEEE Transactions on Power Electronics*, vol. 28, no. 7, pp. 3517-3527, 2013.

[126] H. Guzmán, M. J. Durán, and F. Barrero, "A comprehensive fault analysis of a five-phase induction motor drive with an open phase," in *15th International Power Electronics and Motion Control Conference (EPE/PEMC)*, Novi Sad, Serbia, 2012, pp. LS5b.3-1-LS5b.3-6.

[127] R. Hyung-Min, K. Ji-Woong, and S. Seung-Ki, "Synchronous-frame current control of multiphase synchronous motor under asymmetric fault condition due to open phases," *IEEE Transactions on Industry Applications*, vol. 42, no. 4, pp. 1062-1070, 2006.

[128] H. Guzman *et al.*, "Comparative Study of Predictive and Resonant Controllers in Fault-Tolerant Five-Phase Induction Motor Drives," *IEEE Transactions on Industrial Electronics*, vol. 63, no. 1, pp. 606-617, 2016.

[129] H. Zhou, W. Zhao, G. Liu, R. Cheng, and Y. Xie, "Remedial Field-Oriented Control of Five-Phase Fault-Tolerant Permanent-Magnet Motor by Using Reduced-Order Transformation Matrices," *IEEE Transactions on Industrial Electronics*, vol. 64, no. 1, pp. 169-178, 2017.

[130] H. Zhou, G. Liu, W. Zhao, X. Yu, and M. Gao, "Dynamic Performance Improvement of Five-Phase Permanent-Magnet Motor With Short-Circuit Fault," *IEEE Transactions on Industrial Electronics*, vol. 65, no. 1, pp. 145-155, 2018.

[131] A. Seck, L. Moreau, M. F. Benkhoris, and M. Machmoum, "Automatic generation of optimal phase currents for five-phase PMSG control under open phase condition," in *The 43rd Annual Conference of the IEEE Industrial Electronics Society (IECON)*, Beijing, China, 10/2017, pp. 3847-3852.

[132] B. Tian, Q. T. An, J. D. Duan, D. Semenov, D. Y. Sun, and L. Sun, "Cancellation of Torque Ripples With FOC Strategy Under Two-Phase Failures of the Five-Phase PM Motor," *IEEE Transactions on Power Electronics*, vol. 32, no. 7, pp. 5459-5472, 2017.

[133] B. Tian, Q. T. An, J. D. Duan, D. Y. Sun, L. Sun, and D. Semenov, "Decoupled Modeling and Nonlinear Speed Control for Five-Phase PM Motor Under Single-Phase Open Fault," *IEEE Transactions on Power Electronics*, vol. 32, no. 7, pp. 5473-5486, 2017.

[134] G. Liu, Z. Lin, W. Zhao, Q. Chen, and G. Xu, "Third Harmonic Current Injection in Fault-Tolerant Five-Phase Permanent-Magnet Motor Drive," *IEEE Transactions on Power Electronics*, vol. 33, no. 8, pp. 6970 - 6979, 2018.

[135] C. Xiong, H. Xu, T. Guan, and P. Zhou, "Fault-tolerant FOC for five-phase SPMSM with non-sinusoidal back EMF," *IET Electric Power Applications*, vol. 13, no. 11, pp. 1734-1742, 2019.

[136] M. Bermudez, I. Gonzalez-Prieto, F. Barrero, H. Guzman, X. Kestelyn, and M. J. Duran, "An Experimental Assessment of Open-Phase Fault-Tolerant Virtual-Vector-Based Direct Torque Control in Five-Phase Induction Motor Drives," *IEEE Transactions on Power Electronics*, vol. 33, no. 3, pp. 2774-2784, 2018.

[137] F. Jen-Ren and T. A. Lipo, "Disturbance-free operation of a multiphase current-regulated motor drive with an opened phase," *IEEE Transactions on Industry Applications*, vol. 30, no. 5, pp. 1267-1274, 1994.

[138] A. Tani, M. Mengoni, L. Zarri, G. Serra, and D. Casadei, "Control of Multiphase Induction Motors With an Odd Number of Phases Under Open-Circuit Phase Faults," *IEEE Transactions on Power Electronics*, vol. 27, no. 2, pp. 565-577, 2012.

[139] M. A. Fnaiech, F. Betin, G. Capolino, and F. Fnaiech, "Fuzzy Logic and Sliding-Mode Controls Applied to Six-Phase Induction Machine With Open Phases," *IEEE Transactions on Industrial Electronics*, vol. 57, no. 1, pp. 354-364, 2010.

[140] Z. Sun, J. Wang, G. W. Jewell, and D. Howe, "Enhanced Optimal Torque Control of Fault-Tolerant PM Machine Under Flux-Weakening Operation," *IEEE Transactions on Industrial Electronics*, vol. 57, no. 1, pp. 344-353, 2010.

[141] Y. Sui, P. Zheng, Z. Yin, M. Wang, and C. Wang, "Open-Circuit Fault-Tolerant Control of Five-Phase PM Machine Based on Reconfiguring Maximum Round Magnetomotive Force," *IEEE Transactions on Industrial Electronics*, vol. 66, no. 1, pp. 48-59, 2019.

[142] R. S. Arashloo, J. L. R. Martinez, M. Salehifar, and M. Moreno-Eguilaz, "Genetic algorithm-based output power optimisation of fault tolerant five-phase brushless direct current drives applicable for electrical and hybrid electrical vehicles," *IET Electric Power Applications*, vol. 8, no. 7, pp. 267-277, 2014.

[143] A. Mohammadpour, S. Sadeghi, and L. Parsa, "A Generalized Fault-Tolerant Control Strategy for Five-Phase PM Motor Drives Considering Star, Pentagon, and Pentacle Connections of Stator Windings," *IEEE Transactions on Industrial Electronics*, vol. 61, no. 1, pp. 63-75, 2014.

[144] X. Kestelyn, Y. Crevits, and E. Semail, "Fault tolerant control of a seven-phase drive by degrees of freedom adaptation," in *IEEE International Conference on Industrial Technology (ICIT)*, Vina del Mar, Chile, 3/2010, pp. 1513-1518.

[145] X. Kestelyn, F. Locment, Y. Crevits, and E. Semail, "Easy-to-Implement Integral Numerical Simulation of Multi-phase Drives under Fault Supply Condition," in *IEEE International Electric Machines & Drives Conference*, Antalya, Turkey, 5/2007, vol. 2, pp. 1131-1135.

[146] X. Kestelyn, E. Semail, and Y. Crevits, "Generation of on-line optimal current references for Multi-phase Permanent Magnet Machines with open-circuited phases," in *IEEE International Electric Machines and Drives Conference*, Miami, FL, USA, 5/2009, pp. 689-694.

[147] N. K. Nguyen, D. Flieller, X. Kestelyn, T. J. d. S. Moraes, and E. Semail, "Analytical optimal currents for multiphase PMSMs under fault conditions and saturation," in *The 40th Annual Conference of the IEEE Industrial Electronics Society (IECON)*, 10/2014, pp. 3197-3203.

[148] M. Bermudez, I. Gonzalez-Prieto, F. Barrero, H. Guzman, M. J. Duran, and X. Kestelyn, "Open-Phase Fault-Tolerant Direct Torque Control Technique for Five-Phase Induction Motor Drives," *IEEE Transactions on Industrial Electronics*, vol. 64, no. 2, pp. 902-911, 2017.

[149] C. Xiong, T. Guan, P. Zhou, and H. Xu, "A Fault-Tolerant FOC Strategy for Five-Phase SPMSM With Minimum Torque Ripples in the Full Torque Operation Range Under Double-Phase Open-Circuit Fault," *IEEE Transactions on Industrial Electronics*, vol. 67, no. 11, pp. 9059-9072, 2020.

[150] Y. Zhao and T. A. Lipo, "Modeling and control of a multi-phase induction machine with structural unbalance," *IEEE Transactions on Energy Conversion*, vol. 11, no. 3, pp. 570-577, 1996.

[151] H. Guzman, F. Barrero, and M. J. Duran, "IGBT-Gating Failure Effect on a Fault-Tolerant Predictive Current-Controlled Five-Phase Induction Motor Drive," *IEEE Transactions on Industrial Electronics*, vol. 62, no. 1, pp. 15-20, 2015.

[152] H. Guzman, M. J. Duran, F. Barrero, B. Bogado, and S. Toral, "Speed Control of Five-Phase Induction Motors With Integrated Open-Phase Fault Operation Using Model-Based Predictive Current Control Techniques," *IEEE Transactions on Industrial Electronics*, vol. 61, no. 9, pp. 4474-4484, 2014.

[153] L. Parsa and H. A. Toliyat, "Fault-Tolerant Interior-Permanent-Magnet Machines for Hybrid Electric Vehicle Applications," *IEEE Transactions on Vehicular Technology*, vol. 56, no. 4, pp. 1546-1552, 2007.

[154] A. Mohammadpour and L. Parsa, "Global Fault-Tolerant Control Technique for Multiphase Permanent-Magnet Machines," *IEEE Transactions on Industry Applications*, vol. 51, no. 1, pp. 178-186, 2015.

[155] A. S. Abdel-Khalik, A. S. Morsy, S. Ahmed, and A. M. Massoud, "Effect of Stator Winding Connection on Performance of Five-Phase Induction Machines," *IEEE Transactions on Industrial Electronics*, vol. 61, no. 1, pp. 3-19, 2014.

[156] Z. Liu, Z. Zheng, and Y. Li, "Enhancing Fault-Tolerant Ability of a Nine-Phase Induction Motor Drive System Using Fuzzy Logic Current Controllers," *IEEE Transactions on Energy Conversion*, vol. 32, no. 2, pp. 759-769, 2017.

[157] F. Betin and G. Capolino, "Shaft Positioning for Six-Phase Induction Machines With Open Phases Using Variable Structure Control," *IEEE Transactions on Industrial Electronics*, vol. 59, no. 6, pp. 2612-2620, 2012.

[158] *EMR Website*. Available: http://www.emrwebsite.org.

[159] A. Bouscayrol, J.-P. Hautier, and B. Lemaire-Semail, "Graphic formalisms for the control of multi-physical energetic systems," in *Systemic Design Methodologies for Electrical Energy: Analysis, Synthesis and Management*X. Roboam, Ed. Hoboken, NJ, USA: Wiley, Oct. 2012, pp. 89-124.

[160] *fmincon*. Available: https://uk.mathworks.com/help/optim/ug/fmincon.html

[161] F. Locment, "Conception et modélisation d'une machine synchrone à 7 phases à aimants permanents et flux axial : commande vectorielle en modes normal et dégradé," PhD, Université des sciences et technologies de Lille, 2006.

[162] F. Locment, E. Semail, and F. Piriou, "Design and study of a multiphase axial-flux machine," *IEEE Transactions on Magnetics*, vol. 42, no. 4, pp. 1427-1430, 2006.

[163] K. Yanagihara, D. T. Vu, N. K. Nguyen, J. Gong, E. Semail, and T. J. d. S. Moraes, "Fault-tolerant Control for 7-phase Non-sinusoidal Permanent Magnet Machines with One Opened Phase," in *2019 International Symposium on Electrical and Electronics Engineering (ISEE)*, Ho Chi Minh city, Vietnam, 2019, pp. 292-297.

[164] D. T. Vu, N. K. Nguyen, E. Semail, and T. J. d. S. Moraes, "Torque optimisation of seven-phase BLDC machines in normal and degraded modes with constraints on current and voltage," *The Journal of Engineering*, vol. 2019, no. 17, pp. 3818-3824, 2019.

[165] D. T. Vu, N. K. Nguyen, E. Semail, and T. J. d. S. Moraes, "Control strategies for non-sinusoidal multiphase PMSM drives in faulty modes under constraints on copper losses and peak phase voltage," *IET Electric Power Applications*, vol. 13, no. 11, pp. 1743-1752, 2019.

[166] D. T. Vu, N. K. Nguyen, and E. Semail, "An Overview of Methods using Reduced-Ordered Transformation Matrices for Fault-Tolerant Control of 5-phase Machines with an Open Phase," in *2019 IEEE International Conference on Industrial Technology (ICIT)*, Melbourne, Australia, 2019, pp. 1557-1562.

[167] H. Chuan, S. M. Fazeli, Z. Wu, and R. Burke, "Mitigating the Torque Ripple in Electric Traction using Proportional Integral Resonant Controller," *IEEE Transactions on Vehicular Technology*, pp. 1-1, 2020.

[168] H. Zhang *et al.*, "Torque Optimization of a Seven-Phase Bi-harmonic PMSM in Healthy and Degraded Mode," in *The 22nd International Conference on Electrical Machines and Systems (ICEMS)*, Harbin, China, 2019, pp. 1-6.

[169] D. T. Vu, N. K. Nguyen, and E. Semail, "Sensitivity of Torque Control for Seven-phase BLDC Machine with One Opened Phase under Constraints on Voltage and Current," in *International Symposium on Power Electronics, Electrical Drives, Automation and Motion (SPEEDAM)*, Amalfi, Italy, 2018, pp. 142-148.

[170] B. Zhao, J. Gong, D. T. Vu, N. K. Nguyen, and E. Semail, "Fault Tolerant 7-phase Hybrid Excitation Permanent Magnet Machine," in *The Eighteenth Biennial IEEE Conference on Electromagnetic Field Computation CEFC 2018*, Hangzhou, China, 2018, pp. 1-5.

[171] S. Haykin, *Neural networks: A comprehensive foundation*, Second ed. Delhi 110 092, India: Prentice Education, 1999.

[172] B. Widrow and E. Walach, *Adaptive Inverse Control*. Prentice-Hall, 1996.

[173] B. Widrow and M. A. Lehr, "Adaptive neural networks and their applications," *International Journal of Intelligent Systems*, vol. 8, no. 4, pp. 453-507, 1993.

[174] L. Wang, Z. Q. Zhu, H. Bin, and L. M. Gong, "Current Harmonics Suppression Strategy for PMSM with Non-Sinusoidal Back-EMF Based on Adaptive Linear Neuron Method," *IEEE Transactions on Industrial Electronics*, pp. 1-1, 2019.

[175] H. Sediki, A. Bechouche, D. O. Abdeslam, and S. Haddad, "ADALINE approach for induction motor mechanical parameters identification," *Mathematics and Computers in Simulation*, vol. 90, pp. 86-97, 2013.

[176] G. Grandi and J. Loncarski, "Analysis of dead-time effects in multi-phase voltage source inverters," in *6th IET International Conference on Power Electronics, Machines and Drives (PEMD 2012)*, 2012, pp. 1-6.

[177] N. K. Nguyen, D. Flieller, P. Wira, and D. O. Abdeslam, "Neural networks for phase and symmetrical components estimation in power systems," in *2009 35th Annual Conference of IEEE Industrial Electronics*, Porto, Portugal, 2009, pp. 3252-3257.

[178] D. T. Vu, N. K. Nguyen, E. Semail, and W. Lhomme, "Electric Vehicles Driven by 5-Phase Open-End Winding Machines Fed by Battery and Supercapacitors," in *IEEE Vehicle Power and Propulsion Conference (VPPC)*, Hanoi, Vietnam, 2019, pp. 1-6.

[179] T. J. d. S. Moraes, H. L. Wu, E. Semail, N. K. Nguyen, and D. T. Vu, "Optimal torque/speed characteristics of a Five-Phase Synchronous Machine under Peak or RMS current control strategies," in *The 22nd European Conference on Power Electronics and Applications (EPE)*, Lyon, France, 2020.

[180] D. T. Vu, N. K. Nguyen, and E. Semail, "Eliminations of Low-frequency Current Harmonics for Five-phase Open-end Winding Non-sinusoidal Machine Drives applying Neural Networks," in *The 46th Annual Conference of the IEEE Industrial Electronics Society (IECON)*, Singapore, 2020.

[181] D. T. Vu, N. K. Nguyen, and E. Semail, "Current Harmonic Eliminations for Seven-phase Non-sinusoidal PMSM Drives applying Artificial Neurons," in *The International Conference on Engineering and Research Application (ICERA)*, Thai Nguyen, Vietnam, 2020.

Appendices

Appendix A. Energetic Macroscopic Representation

Energetic Macroscopic Representation (EMR) is a graphical formalism for modeling and control of energetic systems [159]. Specifically, EMR is a tool to organize the model of an energetic system, then the control scheme for this system is easily developed.

A.1. Representation of the system model

The system model is represented in EMR according to the two principles:

1) *Principle of causality:* inputs and outputs of an energetic system must follow the integral causality in which the outputs are functional integrals of the inputs. The outputs are delayed with respect to the inputs. For example, if a system contains a capacitor, the capacitor current must be the input while the capacitor voltage must be the output to respect the principle of causality. The reason is that the capacitor voltage is an integral of the capacitor current. A model which imposes a voltage on the capacitor violates the principle of causality.
2) *Principle of interaction:* subsystems of an energetic system interact with each other via pairs of action and reaction variables in which the product of these variables is the instantaneous power exchanged between these subsystems. For example, when a battery is connected to a resistor, they interact with each other by a pair of variables current and voltage. The battery imposes a voltage on the resistor as an action while the resistor enforces a current to the battery as a reaction.

Several EMR elements of the system model are described in TABLE A.1. More information and the EMR library can be found in the official website of EMR [158].

TABLE A.1. Several EMR elements in the model of an energetic system.

Element	Pictogram	Description
Source	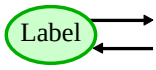	Terminal of the system which supplies or dissipates energy. Name of the source can be written in the label such as energy source (ES) and mechanical source (MS).
Accumulation	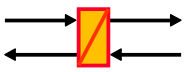	Accumulation of energy which introduces delay to the system and represents dynamics of the system. For example, it can be an inductor which cause current dynamic delay, or a shaft that connects the rotor of a motor to a mechanical load.
Mono-physical conversion	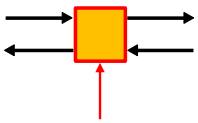	Mono-domain conversion of energy which can be with or without tuning input (red line). For example, an inverter with modulation functions converts electrical DC energy to electrical AC energy.

Multi-physical conversion	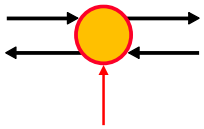	Multi-domain conversion of energy which can be with or without tuning input (red line). For example, an electrical machine converts electrical energy to mechanical energy (and vice versa).
Coupling	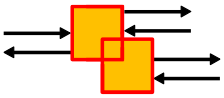	Mono-domain coupling or distribution of energy between more than two subsystems. For example, the coupling can be the distribution of energy to fictitious machines of a multiphase machine, or the coupling of torques from fictitious machine to create the total electromagnetic torque.

A.2. The control scheme of the system

The control scheme obtained from the model representation in EMR is based on *the principle of inversion*. The control is considered as a functional inversion of the model. TABLE A.2 gives details of several EMR elements in the control scheme of the system. More information and the EMR library can be found in the official website of EMR [158].

TABLE A.2. Several EMR elements in the control scheme of an energetic system.

Element	Pictogram	Description
Conversion inversion	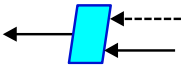	Direct inversion of an energy conversion element in which the output is the reference of the next control block. Information from the system model (dash line) can be used. For example, this element can be a calculation of current references from a torque reference and back-EMFs in a fictitious machine of a multiphase drive.
Accumulation inversion	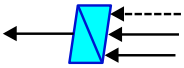	Indirect inversion of an accumulation element to control its output. It is a closed-loop control with reference, output feedback (mandatory), and disturbance rejection (optional). For example, it can be the closed-loop control of current or speed.
Coupling inversion	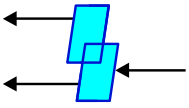	Direct inversion of a coupling element (both mono-domain and multi-domain). A distribution or weighting factor must be introduced to manage the power flow. For example, this element distributes a torque reference to fictitious machines of a multiphase drive according to a repartition rate.
Strategy		Strategy block to impose references, distributions, and/or weighting factors on the control scheme. For example, a strategy to maximize torque under constraints on current and voltage.
Estimation	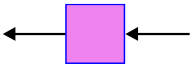	Model copy of the system implemented in the control program, playing the role of estimation of reference model. For example, the estimation of current harmonic components existing in phase currents of an electric machine.

Appendix B. Two-phase OC faults

When two phases of a seven-phase machine are open-circuited and there are no constraints on the winding configuration, the number of DoF for control reduces from 7 in heathy mode to 5 under these faulty conditions. If the stator windings are wye-connected, the number of DoF is equal to 4. In other words, only 4 currents can be independently imposed on the machine. Like method (I) in **Chapter 2** for a single-phase OC fault, currents (i_{d1}, i_{q1}) and (i_{d3}, i_{q3}) are imposed as constant values to facilitate conventional PI controllers. Therefore, in case of two-phase OC faults, the 4 imposed currents are determined from the optimal strategy considering constraints on RMS current and peak voltage as in Fig. 2.21 of **Chapter 2**. Two open-circuited phases can be adjacent (phases (*A*-*B*), for example) and non-adjacent (phases (*A*-*C*) and (*A*-*D*), for example). Current references for two-phase OC faults in phases (*A*-*B*) can be determined as follows:

$$\begin{bmatrix} i_{d1} \\ i_{q1} \\ i_{d9} \\ i_{q9} \\ i_{d3} \\ i_{q3} \\ 0 \end{bmatrix} = [\boldsymbol{T}_{\boldsymbol{Park}}] \begin{bmatrix} i_{\alpha 1} \\ i_{\beta 1} \\ i_{\alpha 2} \\ i_{\beta 2} \\ i_{\alpha 3} \\ i_{\beta 3} \\ 0 \end{bmatrix} = [\boldsymbol{T}_{\boldsymbol{Park}}][\boldsymbol{T}_{\boldsymbol{Clarke}}] \begin{bmatrix} 0 \\ 0 \\ i_C \\ i_D \\ i_E \\ i_F \\ i_G \end{bmatrix} \tag{B.1}$$

$$\begin{bmatrix} 0 \\ 0 \\ i_C \\ i_D \\ i_E \\ i_F \\ i_G \end{bmatrix} = \sqrt{\frac{2}{7}} \begin{bmatrix} 1 & 0 & 1 & 0 & 1 & 0 & 1/\sqrt{2} \\ \cos(\delta) & \sin(\delta) & \cos(2\delta) & \sin(2\delta) & \cos(3\delta) & \sin(3\delta) & 1/\sqrt{2} \\ \cos(2\delta) & \sin(2\delta) & \cos(4\delta) & \sin(4\delta) & \cos(6\delta) & \sin(6\delta) & 1/\sqrt{2} \\ \cos(3\delta) & \sin(3\delta) & \cos(6\delta) & \sin(6\delta) & \cos(9\delta) & \sin(9\delta) & 1/\sqrt{2} \\ \cos(4\delta) & \sin(4\delta) & \cos(8\delta) & \sin(8\delta) & \cos(12\delta) & \sin(12\delta) & 1/\sqrt{2} \\ \cos(5\delta) & \sin(5\delta) & \cos(10\delta) & \sin(10\delta) & \cos(15\delta) & \sin(15\delta) & 1/\sqrt{2} \\ \cos(6\delta) & \sin(6\delta) & \cos(12\delta) & \sin(12\delta) & \cos(18\delta) & \sin(18\delta) & 1/\sqrt{2} \end{bmatrix} \begin{bmatrix} i_{\alpha 1} \\ i_{\beta 1} \\ i_{\alpha 2} \\ i_{\beta 2} \\ i_{\alpha 3} \\ i_{\beta 3} \\ 0 \end{bmatrix} \tag{B.2}$$

$$\begin{cases} i_{\alpha 2} = -\{i_{\alpha 1} + i_{\alpha 3}\} \\ i_{\beta 2} = -\dfrac{1}{\sin(2\delta)}\{i_{\alpha 1}[\cos(\delta) - \cos(2\delta)] + i_{\beta 1}\sin(\delta) + i_{\alpha 3}[\cos(3\delta) - \cos(2\delta)] + i_{\beta 3}\sin(3\delta)\} \end{cases} \tag{B.3}$$

$$\begin{cases} i_C = \sqrt{\dfrac{2}{7}}\{i_{\alpha 1}\cos(2\delta) + i_{\beta 1}\sin(2\delta) + i_{\alpha 2}\cos(4\delta) + i_{\beta 2}\sin(4\delta) + i_{\alpha 3}\cos(6\delta) + i_{\beta 3}\sin(6\delta)\} \\ i_D = \sqrt{\dfrac{2}{7}}\{i_{\alpha 1}\cos(3\delta) + i_{\beta 1}\sin(3\delta) + i_{\alpha 2}\cos(6\delta) + i_{\beta 2}\sin(6\delta) + i_{\alpha 3}\cos(9\delta) + i_{\beta 3}\sin(9\delta)\} \\ i_E = \sqrt{\dfrac{2}{7}}\{i_{\alpha 1}\cos(4\delta) + i_{\beta 1}\sin(4\delta) + i_{\alpha 2}\cos(8\delta) + i_{\beta 2}\sin(8\delta) + i_{\alpha 3}\cos(12\delta) + i_{\beta 3}\sin(12\delta)\} \\ i_F = \sqrt{\dfrac{2}{7}}\{i_{\alpha 1}\cos(5\delta) + i_{\beta 1}\sin(5\delta) + i_{\alpha 2}\cos(10\delta) + i_{\beta 2}\sin(10\delta) + i_{\alpha 3}\cos(15\delta) + i_{\beta 3}\sin(15\delta)\} \\ i_G = \sqrt{\dfrac{2}{7}}\{i_{\alpha 1}\cos(6\delta) + i_{\beta 1}\sin(6\delta) + i_{\alpha 2}\cos(12\delta) + i_{\beta 2}\sin(12\delta) + i_{\alpha 3}\cos(18\delta) + i_{\beta 3}\sin(18\delta)\} \end{cases} \tag{B.4}$$

Current reference calculations for the other cases with two-phase OC faults in phases (*A*-*C*) and (*A*-*D*) can be easily obtained by the same way.

The optimal calculated torque-speed characteristics in the three cases of faults are presented in FIG. B.1. It is noted that the fault-tolerant control strategy in the three cases generates different average torques (0.45, 0.36, and 0.27 pu before base speeds). FIG. B.2 describes the experimental torque-speed characteristic and instantaneous torques at 20 rad/s when phases (*A*-*B*) are open-circuited. The torque ripple in the post-fault operation reduces from 81% to 47% when the fault-tolerant strategy is applied. FIG. B.3 show that phase currents and phase voltage references always respect the limits of RMS current and peak voltage (5.1 A and 100 V, respectively).

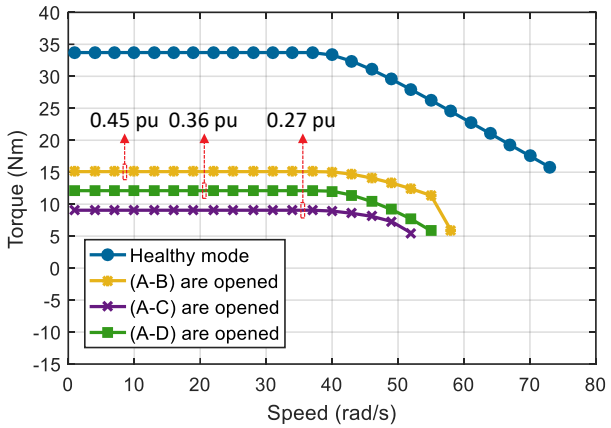

FIG. B.1. (Calculated result) Torque-speed characteristics under constraints on RMS current and peak voltage when two phases are open-circuited.

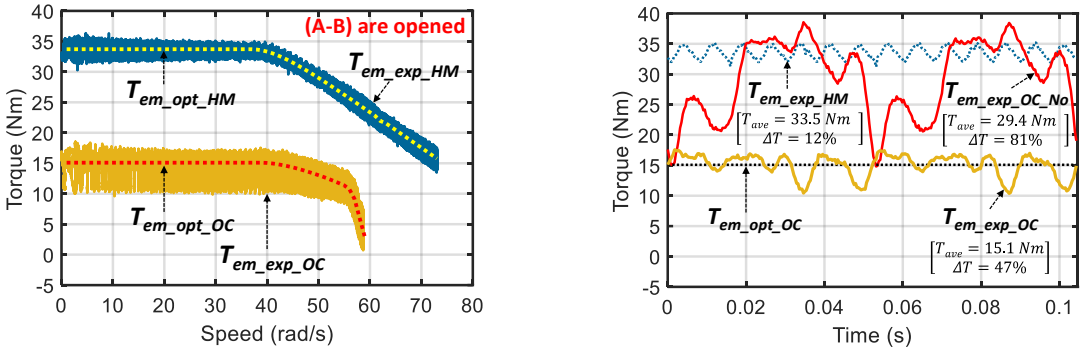

(a) (b)

FIG. B.2. (Experimental result) Torque-speed characteristics (a), torques in terms of time at 20 rad/s without and with new current references (b) for an OC fault in phases (*A*-*B*).

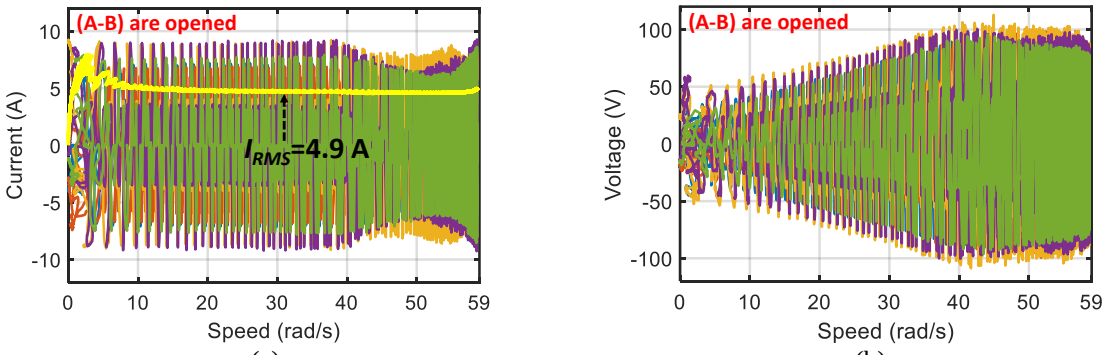

(a) (b)

FIG. B.3. (Experimental result) Measured phase currents (a), and phase voltage references (b) with new current references for an OC fault in phases (*A*-*B*).

Appendix C. Résumé étendu en Français

C.1. Exigences dans les applications automobiles

Dans les années 1830, l'idée d'utiliser des machines électriques pour la traction des véhicules automobiles, également appelées véhicules électrifiés (EV), a été introduite. Cependant, des contraintes sur le coût, le volume et la masse des batteries ont entravé leur processus de commercialisation. Au cours des dernières décennies, les sources d'énergie fossile ont fortement diminué et la pollution de l'environnement est devenue un problème mondial très sérieux. Pendant ce temps, des améliorations significatives sur les batteries ont été réalisées. Par conséquent, depuis les années 1990, les véhicules électriques émergent lentement et deviennent une solution commerciale efficace pour faire face aux crises énergétiques et environnementales. Un EV peut être soit une combinaison d'une propulsion électrique et d'un moteur thermique dans un véhicule électrique hybride (HEV), soit un véhicule purement électrique. Le véhicule électrique pur est un véhicule à pile à combustible (FCV en anglais) ou un véhicule électrique à batterie (BEV). Alors que les BEV et les FCV à émission nulle ont des contraintes de coût et de technologie, les HEV à faibles émissions deviennent plus intéressants dans l'industrie automobile en raison du taux d'hybridation qu'il est possible d'ajuster [1].

En général, un véhicule électrique est une combinaison sophistiquée d'ingénierie électrique et d'ingénierie automobile. Les entraînements électriques jouent un rôle important dans les performances des EV. Ils se composent de machines électriques, de convertisseurs d'électronique de puissance, de systèmes d'alimentation en énergie, de contrôle et de gestion de l'énergie. Les technologies des entraînements électriques appliquées dans les véhicules électriques dépendent principalement des technologies utilisées dans les machines électriques : DC, AC induction (IM) et AC synchrone. On constate que la technologie DC n'est plus attractive en raison de ses contraintes de maintenance et de ses limitations mécaniques. Actuellement, les machines synchrones à aimants permanents (PMSM en anglais) sont plus présentes dans les HEV où les contraintes spatiales sont importantes. Pendant ce temps, des IM et des machines synchrones à excitation séparée à rotor bobiné, sans aimants permanents coûteux, sont observés dans les BEV [2].

Plusieurs exigences principales des entraînements électriques dans les véhicules électriques sont indiquées comme suit :

1) Le rendement élevé pour une utilisation optimale de l'alimentation en énergie intégrée. Les entraînements électriques à haut rendement peuvent augmenter l'autonomie ou réduire le besoin en capacité de batterie dans les EV.
2) Les densités volumiques élevées de puissance et de couple en raison des espaces limités dans les EV, en particulier les HEV.
3) Le faible coût pour obtenir des véhicules électriques abordables sur le marché de masse et sans danger pour les humains (l'alimentation par une tension faible de 48 V, par exemple, requiert moins de dispositifs de protection qu'une tension de bus de 500 V).
4) La fiabilité fonctionnelle élevée avec la capacité de tolérance aux défauts pour le transport (des défauts dans les convertisseurs de puissance ou les enroulements de

machines électriques, par exemple). La possibilité de fonctionner correctement à puissance réduite en cas de défaut rend plus admissible l'idée d'un défaut et permet d'éviter des marges de sécurité couteuses dans le contexte d'un marché de masse.

5) La qualité élevée de couple pour les véhicules électriques confortables avec de faibles vibrations et bruits (pour assurer une conduite confortable et précise particulièrement aux faibles vitesses).
6) Le contrôle de défluxage pour la conduite à grande vitesse sans entraînements électriques surdimensionnés.

Lorsque ces exigences sont satisfaites, des conversions électromécaniques hautes performances des EV à des vitesses et des couples variables peuvent être garanties. Cependant, ces exigences sont considérées comme des défis qui peuvent être contradictoires avec les solutions classiques. Par conséquent, des compromis flexibles doivent être faits. Pour pallier ces contradictions, la recherche de nouvelles solutions avec plus de degrés de liberté est intéressante. Dans cette thèse, les entraînements électriques avec plus de degrés de liberté que les entraînements triphasés classiques seront considérés pour le contrôle et la conception.

C.2. L'applicabilité des entraînements polyphasés

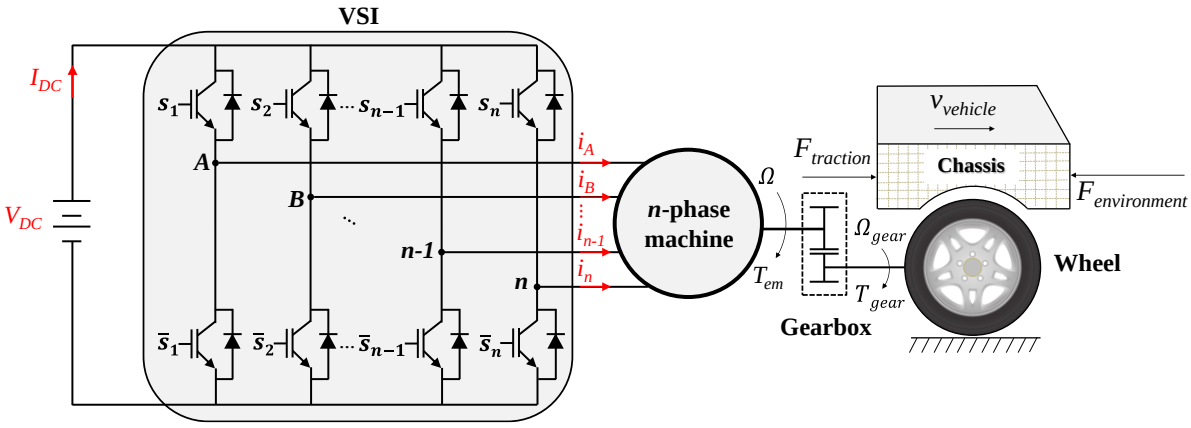

FIG. C.1. Une machine à *n* phases alimentée par un onduleur de source de tension à *n* bras dans un EV.

Selon les six principales exigences relatives aux entraînements électriques dans les EV de la **section C.1**, les six propriétés spéciales suivantes permettent aux entraînements polyphasés (FIG. C.1) d'être un choix privilégié dans les applications automobiles :

1) La faible puissance nominale par phase pour des véhicules électriques sûrs. Le courant nominal par phase des convertisseurs et des enroulements de machine est inférieur à celui des entraînements triphasés conventionnels avec la même tension DC et la même puissance. Cela facilite l'utilisation la conception d'entrainements à faible tension de bus 48 V et de puissance supérieure à 10 KW, valeur minimale pour une hybridation.
2) La capacité de tolérance aux défauts pour la fiabilité fonctionnelle. La capacité de tolérance aux défauts des entraînements polyphasés est due à plus de degrés de liberté de contrôle que les entraînements triphasés conventionnels qui ne supportent pas le défaut d'alimentation d'une des trois phases qui mène à l'arrêt.
3) Les couples pulsatoires faibles pour des véhicules électriques confortables aux basses vitesses. Une augmentation du nombre de phases se traduit par la possibilité de

travailler avec des machines à forces électromotrices non-sinusoïdales donc avec moins de contrainte lors de la conception et de fait un coût moindre.

4) Plus de possibilités de configuration d'enroulement de stator grâce à plus de phases (permettent de faire varier la caractéristique couple-vitesse).
5) Changement de pôle électromagnétique avec les harmoniques de courant. Cela permet d'avoir un effet équivalent à une boite de vitesse et donc de disposer d'une plage de vitesse à puissance maximale quasi-constante bien adaptée au cahier des charges d'une automobile moyenne gamme (milieu de segment), élément important pour le coût. En plus, une conduite plus confortable peut être obtenue avec la boîte de vitesses électromagnétique.

En particulier, les machines PMSM polyphasées sont plus intéressantes que les IM polyphasées en raison de leur rendement élevé, leurs densités élevées de couple et de puissance. Cependant, pour remplacer complètement les homologues triphasés utilisés majoritairement dans les véhicules électriques, les entraînements polyphasés, en particulier les entraînements de machines PMSM polyphasées, doivent surmonter quelques handicaps : des ressources en temps de calcul augmentant avec le nombre de phases, une plus grande complexité de conception du contrôle notamment pour un fonctionnement de qualité en mode de défaut, et une méconnaissance des spécificités de ces entrainements électriques.

C.3. Etat de l'art des entraînements polyphasés

C.3.1. Techniques de contrôle des entraînements polyphasés en mode sain

Comme analysé dans [21-23, 26, 31, 60-62], les techniques de contrôle pour les entraînements polyphasés peuvent être généralement classées en trois types principales : contrôle vectoriel orienté (FOC), contrôle direct du couple (DTC), et contrôle prédictif basé sur un modèle (MPC). Seules boucles internes pour le contrôle du courant, du couple et du flux sont analysées car la boucle externe pour le contrôle de la vitesse dans les trois techniques de contrôle est la même.

C.3.2. Stratégies de contrôle pour des opérations avec défauts

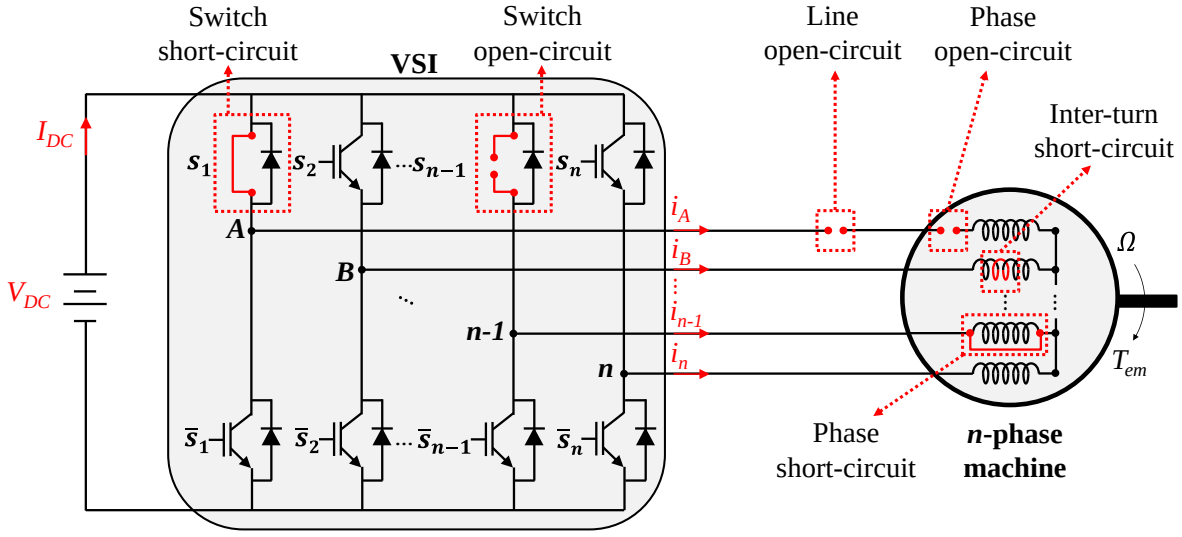

FIG. C.2. Différents types de défauts dans un entraînement à *n* phases.

Sur la FIG. C.2, différents types de défauts dans un entraînement polyphasé incluent le court-circuit (SC) ou le circuit ouvert (OC) dans les interrupteurs de l'onduleur, les enroulements de phase ou les lignes de connexion entre la machine et l'onduleur. En fonctionnement post-défaut, le nombre de phases actives est plus faible et les phases restantes ne sont plus réparties symétriquement dans la machine. Si les références de courant avant défaut ne sont pas modifiées, il y aura des courants incontrôlables et des couples pulsatoires [78, 118-121]. Les récentes études de contrôle tolérant aux défauts peuvent être classées comme suit :

1) Classement basé sur les critères pour élaborer de nouvelles références pour les opérations tolérantes aux défauts : contraintes sur les limites de courant [61, 87, 122, 123] et de tension [61, 74, 87], en optimisant les pertes de cuivre [120, 121, 124-138].
2) Classement basé sur la conservation de force magnétomotrices pour les opérations tolérantes aux défauts : machines sinusoïdales [87, 119, 123, 126-133, 137-141] et machines non-sinusoïdales [61, 120-122, 124, 125, 134-136, 142-149].
3) Classement basé sur la modélisation des entraînements polyphasés pour des opérations tolérantes aux défauts. La transformation de Clarke en mode sain est préservée mais les références actuelles dans les repères de référence du rotor doivent être redéfinies [87, 120, 123, 138]. Une autre option est que des matrices de transformation d'ordre réduit avec des dimensions équivalentes au nombre de phases saines sont appliquées [126-129, 132-135, 149].
4) Classement basé sur les techniques de contrôle pour les opérations tolérantes aux défauts : correcteurs PI [87, 120], MPC et DTC [109, 128, 136, 148, 151, 152], correcteurs d’hystérésis [121, 122, 125, 153, 154], correcteurs résonants proportionnels [123, 135, 138, 149, 155], et contrôle robuste [139, 156, 157].

C.4. Objectifs de thèse

Cette thèse de doctorat est dédiée à l'enrichissement des approches existantes de contrôle pour les entraînements polyphasés, dans le but de mettre en évidence l’intérêt des entraînements polyphasés dans les applications automobiles. Les entraînements polyphasés peuvent répondre de manière significative aux exigences des véhicules électrifiés de la **section C.1** uniquement lorsque ces entrainements sont correctement contrôlés dans des diverses conditions de fonctionnement. Par exemple, un véhicule électrique entraîné par des entraînements polyphasés avec deux modes de conduite est décrit dans la FIG. C.3. La référence de couple peut être générée soit à partir de la pédale d'accélérateur (contrôlée par le conducteur), soit du régulateur de vitesse (une opération autonome, par exemple). Le mode économique permet généralement aux véhicules électriques de fonctionner avec un rendement élevé dans la région à faible couple de la caractéristique couple-vitesse. Pendant ce temps, le mode haute performance permet aux véhicules électriques de fonctionner avec des couples maximaux à chaque vitesse pour les accélérations. Un basculement entre ces deux modes de conduite se produit lorsque le couple requis entraîne un dépassement des limites électriques (courants et tensions). Cette thèse de doctorat portera sur le mode haute performance dans des conditions saines ou dégradés. Le couple électromagnétique sera maximisé dans les limites des courants et des tensions.

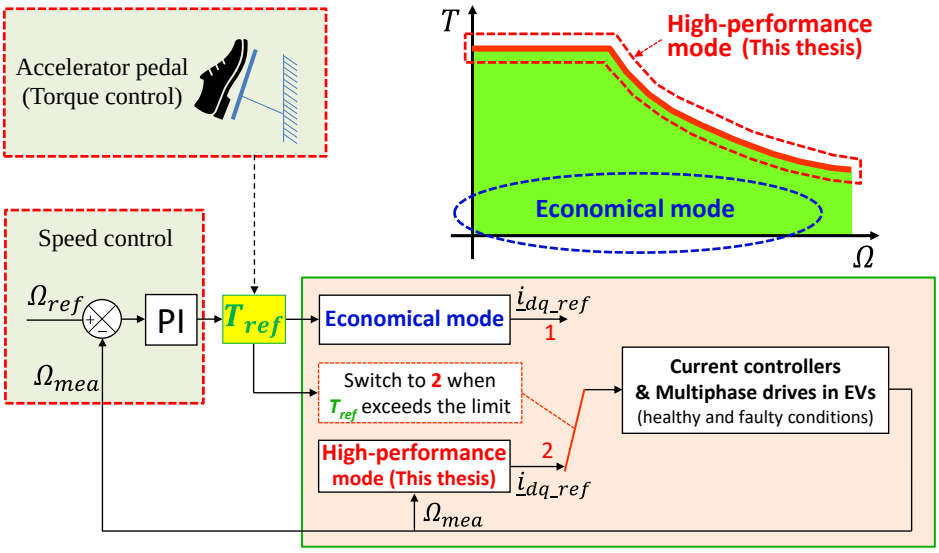

FIG. C.3. Les entraînements polyphasés dans les véhicules électriques avec deux modes de conduite.

Ainsi, en fonction des analyses ci-dessus et de l'état de l'art dans le domaine de la commande des entraînements polyphasés, l'objectif principal de cette thèse de doctorat est de proposer des stratégies de contrôle des entraînements PMSM polyphasés non-sinusoïdales dans des conditions de circuit ouvert. Surtout, les contraintes de courant et de tension seront toujours prises en compte dans tous les modes de fonctionnement. Un autre objectif de cette thèse est de valoriser les performances, notamment la qualité du couple et du contrôle, sous les impacts d'incertitudes et d'imperfections des entraînements électriques en utilisant l'intelligence artificielle.

Plusieurs points principaux de ces objectifs de cette thèse de doctorat peuvent être justifiés et plus expliqués comme suit :

1) Concernant le type de machine électrique, les PMSM polyphasés non-sinusoïdale sont l'objet contrôlé de cette thèse de doctorat. Outre les propriétés générales du concept polyphasé, les PMSM polyphasés sont choisis pour cette thèse de doctorat en raison de leur rendement élevé et de leurs densités volumiques élevées. Ces avantages répondent aux deux premières exigences des EV. De plus, les forces électromotrices non-sinusoïdales sont pris en compte en raison de plusieurs avantages tels que la facilité de fabrication, les faibles coûts de production, les densités de couple élevées, et la capacité de changement de pôle électromagnétique. Le contrôle des machines non-sinusoïdales est plus difficile et intéressant en raison des harmoniques élevés des forces électromotrices.
2) Concernant la technique de contrôle dans cette thèse de doctorat, les stratégies de contrôle proposées dans tous les modes de fonctionnement seront basées sur la technique FOC et les contrôleurs PI comme mode sain. Outre les techniques récentes MPC et DTC, la technique FOC classique avec contrôleurs PI reste intéressante, notamment pour l'industrie en raison de sa qualité, sa simplicité, et sa robustesse (moins dépendante du modèle de machine). De plus, ce FOC classique a été largement utilisé dans l'industrie. Par conséquent, les stratégies de contrôle proposées dans cette thèse sont dérivées du modèle mathématique utilisant la théorie des cadres multi-

références [35]. Les courants dans les cadres de référence rotatifs devront être constants ou varier lentement, en particulier les courants générant la majeure partie du couple.

3) Concernant les contraintes de courant et de tension, ces contraintes garantissent une grande fiabilité de fonctionnement et des opérations d'affaiblissement du flux des entraînements. D'après l'état de l'art, peu d'études ont été menées sur la commande tolérante aux défauts et les forces électromotrices non-sinusoïdales sous contraintes de courant et de tension, sauf [61] avec les techniques MPC et DTC pour les machines 5 phasées.
4) Concernant les améliorations des performances de contrôle et de couple sous impacts d'incertitudes et d'imperfections des entraînements électriques par l'intelligence artificielle, ADALINE (ADAptive LInear NEuron), type simple de réseaux de neurones artificiels, est retenu. L'une des incertitudes peut être les tensions «dead-time» (la non-linéarité de l'onduleur) tandis que la présence de multi-harmoniques dans les forces électromotrices provoque une imperfection dans la conception de la machine. Les ADALINE sont choisis dans cette thèse de doctorat grâce à leur capacité d'auto-apprentissage et leur mise en œuvre facile. Par ailleurs, la connaissance des composants harmoniques dans les signaux que doivent compenser les ADALINE permet leur convergence rapide et d'éviter la charge de calcul, augmentant l'applicabilité aux entraînements électriques industriels. En effet, cette connaissance est facilement obtenue et généralement proportionnelle au nombre de phases. Les ADALINES ont juste besoin de trouver les bonnes amplitudes de ces harmoniques. Ces avantages rendent les ADALINE plus favorables par rapport à d'autres approches telles que FL, PIR, etc. Le contrôle FL nécessite l'expérience d'experts tandis que le contrôle PIR nécessite de multiples ajustements de paramètres et nécessite de la connaissance de la fréquence. En utilisant des ADALINE, la qualité du contrôle du courant et la qualité du couple seront considérablement améliorées, soit en mode sain, soit en mode dégradé.

C.5. Plan de la thèse

Cette thèse de doctorat se compose de 3 chapitres comme suit :

C.5.1. Chapitre 1-Les entraînements polyphasés : opportunités et état de l'art

Section C.1 a abordé les principales exigences des entraînements électriques pour les véhicules électrifiés, motivant cette thèse de doctorat. Grâce aux propriétés spéciales des entraînements polyphasés présentés dans le premier chapitre, les EV pilotés par des entraînements polyphasés, en particulier les entraînements de machines PMSM, ont un fort potentiel de commercialisation dans un proche avenir. Cependant, les entraînements polyphasés présentent certains inconvénients en ce qui concerne le temps de calcul élevé, le coût plus élevé de l'électronique de commande en raison du nombre élevé de bras de VSI à piloter, la complexité de la modélisation et du contrôle, et l'inertie sociale. Ces inconvénients peuvent être surmontés par les progrès des microprocesseurs, les productions de masse, les améliorations des technologies

d'électronique de puissance ainsi que les investissements à long terme des entreprises industrielles, etc.

De plus, la modélisation générale d'une machine PMSM polyphasée a été brièvement décrite pour donner un aperçu du modèle mathématique d'une machine polyphasée. Cette modélisation est présentée pour faciliter les analyses des études récentes sur le domaine de contrôle des entraînements polyphasés pour les modes sains et dégradés. A partir de ces analyses, les objectifs de cette thèse de doctorat sont clarifiés. Plus précisément, la technique de FOC pour machine non-sinusoïdale est appliquée dans cette étude en raison de sa qualité, sa simplicité et sa popularité. Le contrôle s'opère en mode sain et en modes dégradés sous contraintes de courant et de tension. Enfin, pour tenir compte de l'incertitude sur les modèles, l'utilisation de structure d'auto-apprentissage de type ADALINE est effectuée afin d'améliorer la qualité de contrôle du couple dans tous les modes de fonctionnement.

C.5.2. Chapitre 2- Modélisation et contrôle des entraînements polyphasés

Ce chapitre est dédié à la modélisation et au contrôle des entraînements de machines PMSM polyphasées avec des forces électromotrices non-sinusoïdales en mode sain et en modes dégradés. Les contraintes sur le courant RMS et la tension de crête ont été prises en compte dans les modes sains et dégradés. Une étude d'un cas de machine non-sinusoïdale à sept phases est choisie pour illustrer les théories de cette thèse de doctorat.

Dans un premier temps, la modélisation et le contrôle de l'entraînement en mode sain sont présentés. Les contraintes sur le courant RMS et la tension crête sont appliquées. Dans un second temps, les qualités de courant et de couple de l'entraînement en fonctionnement post-défaut sont examinés montrant une forte détérioration sur les ondulations de couple ainsi qu'une augmentation importante de la valeur RMS de courants. Le problème de couplage empêche l'entraînement de continuer à utiliser les références actuelles du mode sain pour le fonctionnement après défaut.

Par conséquent, une reconfiguration avec des stratégies de commandes tolérantes aux défauts est nécessaire pour garantir des performances de couple peu ondulé et des opérations post-défaut sûres pour l'entraînement ainsi que pour les EV. Trois principales stratégies proposées de commandes tolérantes aux défauts avec sept options sont présentées en exploitant le modèle mathématique de la machine polyphasée (FIG. C.4). Plus précisément, des nouvelles références de courants peuvent être conçues dans :

1) Les repères découplés (α-β ou d-q) avec les méthodes (I)-1-2-3.
2) L'utilisation de nouvelles matrices de transformation avec les méthodes (II)-RCA-SCL.
3) Le repère naturel avec les méthodes (III)-1-2.

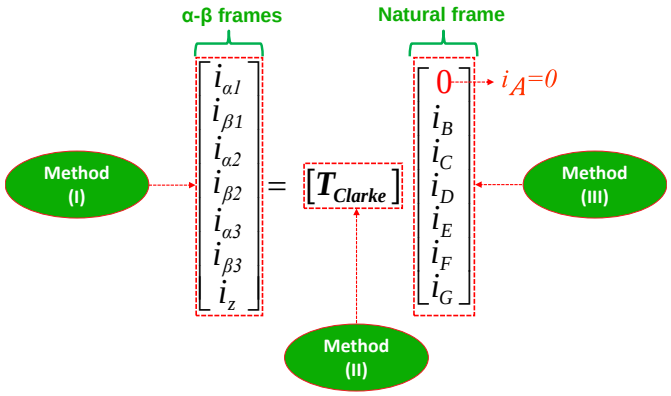

FIG. C.4. Schéma général des méthodes de commande tolérante aux défauts lorsque la phase A est ouverte.

Les méthodes (I) et (II) peuvent permettre théoriquement d'obtenir des couples constants lorsque le premier et le troisième harmonique de back-EMF de la machine sont considérés. Cependant, leurs couples moyens sont relativement faibles si le courant de phase RMS est limité (0.65 pu). Par conséquent, la méthode (III) est proposée pour obtenir des couples moyens plus élevés (0.79 pu) en utilisant des courants de phase identiques mais déphasés. Sous la contrainte de courant, ces courants de forme d'onde identique peuvent être efficacement exploités pour produire plus de couple. Cependant, les ondulations de couple sont inévitables dans la méthode (III) (19%). Finalement, il y a théoriquement un compromis entre des couples moyens élevés avec des ondulations de couple, et des couples sans ondulations avec des valeurs moyennes faibles. De plus, une combinaison de plusieurs stratégies en fonction de la charge utile des véhicules électriques peut tirer parti de chaque méthode (FIG. C.5).

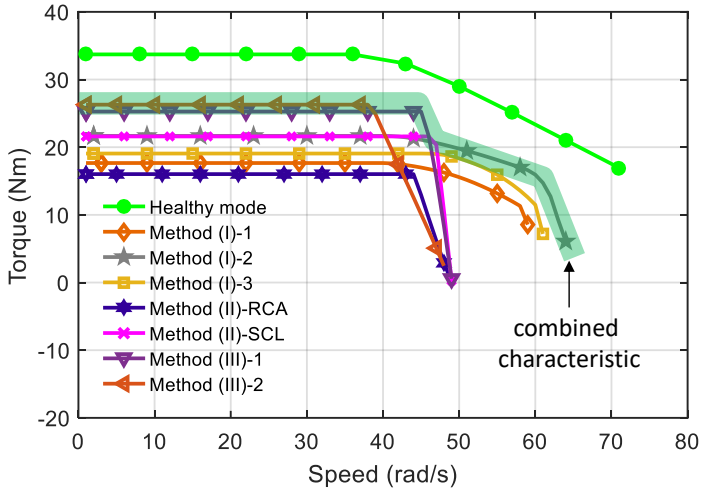

FIG. C.5. (Résultat numérique) Caractéristiques couple-vitesse en mode sain et en mode dégradé de circuit ouvert en phase A, en appliquant les sept méthodes de commande proposées.

La qualité de la commande d'entraînement peut être améliorée en appliquant un type simple d'intelligence artificielle nommé ADALINE dans le prochain chapitre de cette thèse de doctorat. En effet, les effets négatifs des harmoniques indésirables de back-EMF sur les couples et les courants peuvent être éliminés.

C.5.3. Chapitre 3- Les améliorations des performances des entraînements polyphasés par les neurones linéaires adaptatifs

Ce chapitre a présenté les améliorations de la qualité du couple et du contrôle de courant d'un entraînement polyphasé en utilisant un type simple de contrôle issu de l'Intelligence Artificielle nommé ADALINE (neurone linéaire adaptatif). En mode sain, les ADALINE sont appliqués pour éliminer les harmoniques de courant dans les repères d-q causés par des harmoniques indésirables de force électromotrice et la non-linéarité de l'onduleur. De plus, les ondulations de couple générées par les harmoniques indésirables de force électromotrice sont directement annulées par un seul ADALINE. En utilisant ces ADALINE, chaque machine peut générer un couple constant avec un contrôle de courant de haute qualité. Cependant, la plage de vitesse doit être réduite pour respecter la contrainte de tension de crête.

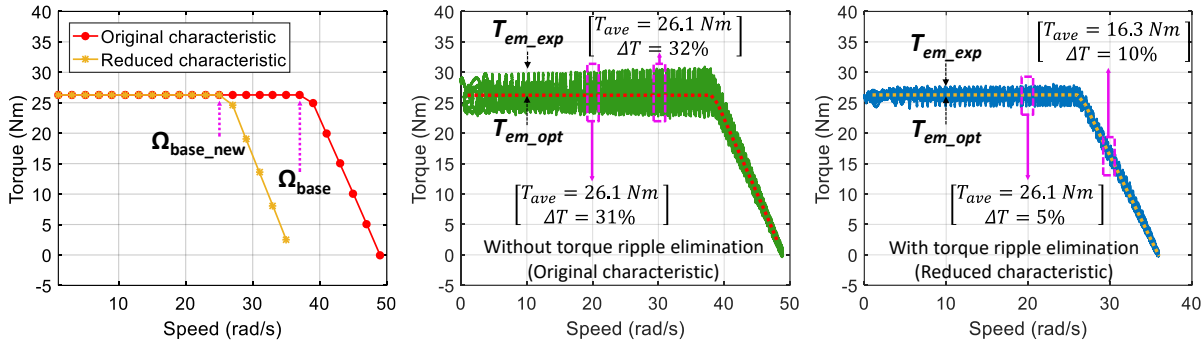

(a) (b) (c)

FIG. C.6. (Résultat expérimental) Les caractéristiques couple-vitesse calculées optimales (a), les caractéristiques couple-vitesse expérimentales sans (b) et avec (c) l'élimination d'ondulation de couple lorsque la phase A est ouverte.

En mode dégradé, les ondulations de couple dans les méthodes tolérantes aux défauts proposées au chapitre 2 peuvent être directement éliminées ou réduites (31% à 5% à 20 rad/s dans la FIG. C.6) de la même manière qu'en mode sain avec une plage de vitesse plus courte. Un ADALINE est appliquée pour éliminer les ondulations de couple dans le fonctionnement post-défaut en utilisant la méthode (III)-2 où le couple moyen le plus élevé est obtenu. L'étape la plus importante de l'élimination des ondulations de couple à l'aide des ADALINE est de déterminer les composantes harmoniques du couple, ce qui permet d'éviter un temps de calcul très élevé.

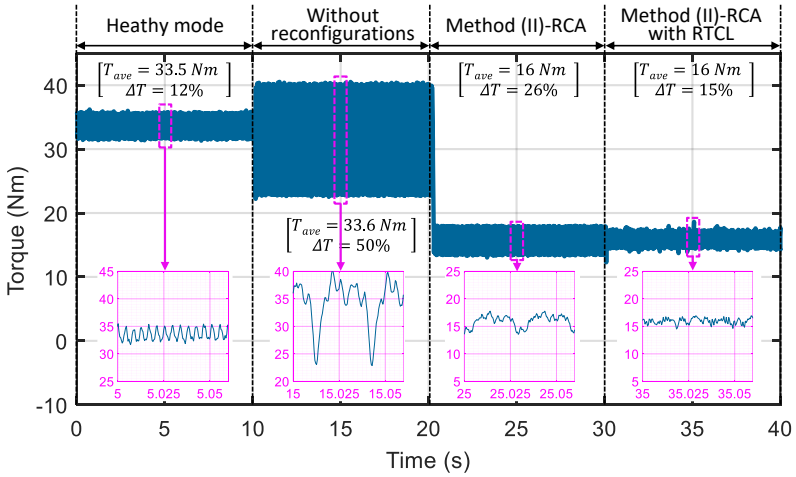

FIG. C.7. (Résultat expérimental) Couple en mode sain, en mode dégradé sans des reconfigurations, en mode dégradé avec la méthode (II)-RCA dans l'ancienne structure de contrôle, et en mode dégradé avec la méthode (II)-RCA dans la nouvelle structure de contrôle en utilisant RTCL à 35 rad/s.

Un nouveau schéma de contrôle en utilisant un seul ADALINE améliore la qualité de contrôle du courant de l'entraînement post-défaut avec la méthode (II), améliorant indirectement la qualité du couple (26% à 15% à 35 rad/s dans la FIG. C.7). Les références de courant variant dans le temps pour le contrôle sont alors remplacées par des valeurs constantes dans le temps. L'élément clé de la nouvelle structure de contrôle est un apprentissage du courant en temps réel qui permet de séparer les composants harmoniques des courants de phase mesurés, en fournissant des signaux de retour de courants d-q constants. Avec une robustesse aux composants harmoniques de force électromotrice dans la deuxième machine fictive (le $9^{ème}$ harmonique, par exemple), la méthode (II)-RCA est choisie pour vérifier le nouveau schéma de contrôle. Lorsque les références de courant sont fixes, la méthode (II)-RCA avec la nouvelle structure de commande n'est pas affectée par la vitesse de rotation. En d'autres termes, la région de fonctionnement avant la vitesse de base est idéale pour appliquer la nouvelle structure afin d'améliorer la qualité du couple. Cependant, si le couple ou les références de courant doivent changer, le fonctionnement doit revenir à l'ancien schéma de commande dans lequel un nouveau processus d'apprentissage est activé pour estimer le nouveau courant de la phase *B*. Par la suite, le nouveau schéma de commande peut être utilisé. Cela peut être considéré comme un inconvénient du nouveau schéma de contrôle.

C.6. Conclusions générales et perspectives

C.6.1. Conclusions générales

Les véhicules électrifiés ont été considérés comme des alternatives aux véhicules utilisant un moteur à combustion interne (ICE) pour faire face à la pénurie de sources d'énergie fossile et à la pollution de l'air. En général, tous les types de véhicules électrifiés sont entraînés par des moteurs électriques. Pour garantir des conversions électromécaniques de haute performance, plusieurs exigences des entraînements électriques tels qu'un rendement élevé, des densités volumiques élevées, un coût faible mais sûr, une fiabilité fonctionnelle élevée, une qualité de couple élevée, et un contrôle de défluxage doivent être satisfaites. Dans ce contexte, les entraînements de machines PMSM polyphasées sont devenus des candidats appropriés pour répondre aux exigences ci-dessus des véhicules électrifiés.

Cette thèse de doctorat a proposé systématiquement et affiné des stratégies de contrôle tolérantes aux défauts pour les entraînements de machines PMSM polyphasées non-sinusoïdales. Outre plusieurs avantages tels que facile-à-fabriquer, des faibles coûts de production, des densités de couple élevées, et des changements de pôles électromagnétiques, les forces électromotrices non-sinusoïdales des machines électriques dans les entraînements considérés ont rendu le contrôle plus compliqué mais intéressant à étudier. De plus, dans cette thèse de doctorat, les limites du courant RMS et de la tension de crête ont toujours été considérées dans les modes de fonctionnement sain et dégradés. Par conséquent, les opérations de défluxage peuvent être garanties. Une étude d'un cas d'une machine à sept phases et un défaut monophasé en circuit ouvert a été utilisée pour les vérifications des stratégies proposées. Les défauts biphasés en circuit ouvert sont brièvement décrits à l'annexe B. Les résultats présentés dans cette thèse de doctorat ont été obtenus à partir d'un banc d'essai expérimental.

Les publications associées à cette thèse de doctorat sont répertoriées comme suit :

1) Articles dans des revues avec comité de lecture internationales :
   - D. T. Vu, N. K. Nguyen, E. Semail, and T. J. d. S. Moraes, “Control strategies for non-sinusoidal multiphase PMSM drives in faulty modes under constraints on copper losses and peak phase voltage,” *IET Electric Power Applications*, vol. 13, no. 11, pp. 1743-1752, 2019 [165].
   - D. T. Vu, N. K. Nguyen, E. Semail, and T. J. d. S. Moraes, “Torque optimisation of seven-phase BLDC machines in normal and degraded modes with constraints on current and voltage,” *The Journal of Engineering*, vol. 2019, no. 17, pp. 3818-3824, 2019 [164].
   - D. T. Vu, N. K. Nguyen, E. Semail, “A Fault-tolerant Control scheme based on Adaptive Linear Neurons for Non-sinusoidal multiphase drives,” *IEEE Transactions on Power Electronics*, UNDER REVIEW.
2) Conférences internationales avec actes :
   - D. T. Vu, N. K. Nguyen, and E. Semail, "Sensitivity of Torque Control for Seven-phase BLDC Machine with One Opened Phase under Constraints on Voltage and Current," in *International Symposium on Power Electronics, Electrical Drives, Automation and Motion (SPEEDAM)*, Amalfi, Italy, 2018, pp. 142-148 [169].
   - B. Zhao, J. Gong, D. T. Vu, N. K. Nguyen, and E. Semail, "Fault Tolerant 7-phase Hybrid Excitation Permanent Magnet Machine," in *The Eighteenth Biennial IEEE Conference on Electromagnetic Field Computation CEFC 2018*, Hangzhou, China, 2018, pp. 1-5 [170].
   - D. T. Vu, N. K. Nguyen, and E. Semail, "An Overview of Methods using Reduced-Ordered Transformation Matrices for Fault-Tolerant Control of 5-phase Machines with an Open Phase," in *IEEE International Conference on Industrial Technology (ICIT)*, Melbourne, Australia, 2019, pp. 1557-1562 [166].
   - D. T. Vu, N. K. Nguyen, E. Semail, and W. Lhomme, "Electric Vehicles Driven by 5-Phase Open-End Winding Machines Fed by Battery and Supercapacitors," in *IEEE Vehicle Power and Propulsion Conference (VPPC)*, Hanoi, Vietnam, 2019, pp. 1-6 [178].
   - K. Yanagihara, D. T. Vu, N. K. Nguyen, J. Gong, E. Semail, and T. J. d. S. Moraes, "Fault-tolerant Control for 7-phase Non-sinusoidal Permanent Magnet Machines with One Opened Phase," in *International Symposium on Electrical and Electronics Engineering (ISEE)*, Ho Chi Minh city, Vietnam, 2019, pp. 292-297 [163].
   - H. Zhang, B. Zhao, J. Gong, Y. Xu, D. T. Vu, N. K. Nguyen, E. Semail, and T. J. d. S. Moraes,"Torque Optimization of a Seven-Phase Bi-harmonic PMSM in Healthy and Degraded Mode," in *The 22nd International Conference on Electrical Machines and Systems (ICEMS)*, Harbin, China, 2019, pp. 1-6 [168].
   - T. J. d. S. Moraes, H. L. Wu, E. Semail, N. K. Nguyen, D. T. Vu, “Optimal torque/speed characteristics of a Five-Phase Synchronous Machine under Peak or RMS current control strategies,” in *The 22nd European Conference on Power Electronics and Applications (EPE)*, Lyon, France, 2020 [179].
   - D. T. Vu, N. K. Nguyen, E. Semail, “Eliminations of Low-frequency Current Harmonics for Five-phase Open-end Winding Non-sinusoidal Machine Drives applying Neural Networks,” in *The 46th Annual Conference of the IEEE Industrial Electronics Society (IECON)*, Singapore, 2020 [180].
   - D. T. Vu, N. K. Nguyen, E. Semail, “Current Harmonic Eliminations for Seven-phase Non-sinusoidal PMSM Drives applying Artificial Neurons,” in *The 3rd International Conference on Engineering and Research Application (ICERA)*, Thai Nguyen, Vietnam, 2020 [181].

C.6.2. Perspectives

Parmi les études présentées dans cette thèse de doctorat, il y a plusieurs problèmes qui n'ont pas encore été résolus. Ces problèmes pourraient être étudiés à l'avenir comme suit :

1) Il serait intéressant de rechercher une approche générale pour trouver des matrices d'ordre réduit, comme dans la méthode (II) du chapitre 2, correspondant à chaque phase ouverte.
2) Une solution automatique pour remplacer le basculement manuel entre les nouveaux et anciens schémas de contrôle dans la méthode (II), comme discuté dans la section

3.3.2.B du chapitre 3, en réponse à la variation des références actuelles doit être trouvée.

3) Les stratégies de contrôle proposées pourraient être plus intéressantes lorsqu'elles sont appliquées à des machines polyphasées avec une vitesse maximale plus élevée. Les machines à grande vitesse conviennent aux applications automobiles au lieu d'une machine à basse vitesse (destinée aux éoliennes) qui a été considérée dans cette thèse de doctorat.
4) Une commande tolérante aux défauts avec des défauts de court-circuit dans les transistors ou les enroulements de machine (spires) pourrait être intéressante à étudier.

Duc Tan VU

Fault-tolerant control of non-sinusoidal multiphase permanent magnet synchronous machine drives under constraints on current and voltage for automotive applications

Résumé : Les entraînements électriques pour les véhicules électrifiés doivent répondre à certaines exigences spécifiques des marchés automobiles, tels qu'un rendement élevé, des densités volumiques élevées de puissance et de couple, un coût faible avec une protection contre les risques électriques, une fiabilité fonctionnelle élevée, une qualité de couple élevée, et un contrôle de défluxage. Dans ce contexte, les entraînements de machines synchrones à aimants permanents (PMSM) polyphasées sont devenus des candidats appropriés pour répondre aux exigences citées ci-dessus. L'objectif principal de cette thèse de doctorat vise à proposer et affiner des stratégies de commandes tolérantes aux défauts pour les entraînements de machines PMSM polyphasées non-sinusoïdales qui requièrent moins de contraintes lors de leur conception. Par ailleurs, les contraintes de courant et de tension définies par l'onduleur et la machine sont prises en compte pour optimiser en régime non-sinusoïdal le contrôle de la machine sans dépasser leurs limites admissibles. Cela permet idéalement un dimensionnement au plus juste et cela tout particulièrement dans la zone de défluxage. Les stratégies proposées de commandes tolérantes aux défauts, basées sur le modèle mathématique des entraînements polyphasés, enrichissent le domaine de contrôle des entraînements polyphasés en offrant de diverses options de contrôle. Le choix de l'une des options proposées de commande peut être un compromis entre un couple de haute qualité mais avec une valeur moyenne faible, et un couple moyen élevé mais avec une ondulation relativement élevée. Les performances de contrôle et de couple peuvent être affinées en utilisant l'intelligence artificielle avec un type simple de réseaux de neurones artificiels nommé ADALINE (neurone linéaire adaptatif). Grâce à leur capacité d'auto-apprentissage, à leur convergence rapide, et à leur simplicité, les ADALINE peuvent être appliqués aux entraînements polyphasés industriels. Toutes les stratégies de contrôle proposées dans cette thèse de doctorat sont validées avec un entraînement d'une machine PMSM à sept phases. La force électromotrice non-sinusoïdale de la machine PMSM à sept phases, relevée expérimentalement, est complexe avec la présence de plusieurs harmoniques. Les résultats expérimentaux vérifient l'efficacité des stratégies proposées, et leur applicabilité dans une machine polyphasée avec une force électromotrice non-sinusoïdale complexe.

Mots clés : Machine polyphasée, machine à sept phases, force électromotrice non-sinusoïdale, commande tolérante aux défauts, commande optimale sous contrainte, intelligence artificielle, neurone linéaire adaptatif,

Abstract: Electric drives for electrified vehicles need to fulfil some specific requirements from automotive markets such as high efficiency, high volume power and torque densities, low-cost but safe-to-touch, high functional reliability, high torque quality, and flux-weakening control. In this context, multiphase permanent magnet synchronous machine (PMSM) drives have become suitable candidates to meet the above requirements. The main objective of this doctoral thesis is to propose and refine fault-tolerant control strategies for non-sinusoidal multiphase PMSM drives that require less constraints on their design. In addition, constraints on current and voltage defined by the inverter and the machine are considered to optimize the machine control under the non-sinusoidal condition without exceeding their allowable limits. Therefore, the system sizing is guaranteed, especially in flux-weakening operations. The proposed fault-tolerant control strategies, based on the mathematical model of multiphase drives, enrich the control field of multiphase drives by providing various control options. The selection of one of the proposed control options can be a trade-off between a high quality torque but a low average value and a high average torque but a relatively high ripple. The control and torque performances of the drives can be refined by using artificial intelligence with a simple type of artificial neural networks named ADALINE (ADAptive LInear NEuron). With self-learning ability, fast convergence, and simplicity, ADALINEs can be applied to industrial multiphase drives. All proposed control strategies in this doctoral thesis are validated with an experimental seven-phase PMSM drive. The non-sinusoidal back electromotive force (back-EMF) of the experimental seven-phase PMSM is complex with the presence of multi-harmonics. Experimental results verify the effectiveness of the proposed strategies, and their applicability in a multiphase machine with a complex non-sinusoidal back-EMF.

Keywords: Multiphase machine, seven-phase machine, non-sinusoidal back-EMF, fault-tolerant control, optimal control under constraint, artificial intelligence, adaptive linear neuron, ADALINE.